

# Design Rules and Models for the Synthesis and Optimization of Cylindrical Flexures

by

Maria J. Telleria

S.M. Mechanical Engineering  
Massachusetts Institute of Technology, 2010

S.B. Mechanical Engineering  
Massachusetts Institute of Technology, 2008

SUBMITTED TO THE DEPARTMENT OF MECHANICAL ENGINEERING IN PARTIAL  
FULFILLMENT OF THE REQUIREMENTS FOR THE DEGREE OF

DOCTOR OF PHILOSOPHY IN MECHANICAL ENGINEERING  
AT THE  
MASSACHUSETTS INSTITUTE OF TECHNOLOGY

JUNE 2013

© 2013 Massachusetts Institute of Technology  
All rights reserved.

Signature of Author.....  
Department of Mechanical Engineering  
May 10<sup>th</sup>, 2013

Certified by.....  
Martin L. Culpepper IV  
Associate Professor of Mechanical Engineering  
Thesis Supervisor

Accepted by.....  
David E. Hardt  
Professor of Mechanical Engineering  
Graduate Officer



Design Rules and Models for the Synthesis and Optimization of Cylindrical Flexures  
by

Maria J. Telleria

Submitted to the Department of Mechanical Engineering  
on May 10<sup>th</sup>, 2013 in Partial Fulfillment of the  
Requirements for the Degree of Doctor of Philosophy in  
Mechanical Engineering

## ABSTRACT

Cylindrical flexures (CFs) are defined as systems composed of flexural elements whose length is defined by the product of their radius of curvature,  $R$ , and sweep angle,  $\phi$ . CFs may be constructed out of a cylindrical stock which leads to geometry, manufacturability, and compatibility advantages over planar flexures. However, CFs present a challenge because their mechanics differ from those of straight beams, and although the modeling of curved beams has been researched in detail [1–4], it has yet to be distilled into compliant element and system creation rules. The lack of relevant design rules has inhibited the process of concept generation and optimization of CF systems, preventing these systems from becoming pervasive in engineering applications. The design guidelines and models developed in this work enable (i) the rapid generation of multiple concepts, (ii) the efficient analysis of different designs and selection of the best design, and (iii) the effective optimization of the chosen concept.

The CF synthesis approach presented in this thesis has three components: (i) analysis of element mechanics models to reveal key parameters, (ii) understanding of how the key parameters affect the flexure performance and (iii) guidelines as to how to assemble and optimize CF systems. With the knowledge generated designers will be able to rapidly layout possible designs using the element building blocks and system creation rules, and then use the identified key parameters to optimize a design. The synthesis guidelines were established and tested through the development of two case study flexures: a CF linear guide and an x-y- $\theta_z$  stage. The case studies demonstrate the increased design space of CF systems, which makes it possible for these new flexure mechanisms to meet functional requirements that could not be met using traditional straight-beam flexures.

Thesis Supervisor: Martin L. Culpepper  
Title: Professor of Mechanical Engineering



# ACKNOWLEDGEMENTS

---

I am extremely grateful for Prof. Culpepper's guidance, support, and encouragement. From the first time I worked in his lab as a UROP he encouraged me to pursue research and later on graduate school. I cannot say thank you enough for the 5 years that he has served as my advisor. His advice and encouragement were instrumental in my application for the National Science Foundation Graduate Fellowship. The NSF fellowship made it possible for me to pursue my work in Cylindrical Flexures. I am extremely grateful for NSF's support in my education and sincerely hope that the fellowship continues promoting the advancement of new fields.

Prof. Sangbae Kim and Dr. Mark Schattenburg graciously accepted to join my committee, and I am sincerely grateful for their valuable time, advice, and questions. Every committee meeting was stimulating, and I always walked away with exciting questions and ideas. My entire committee constantly probed at my progress, and insisted that I consider new avenues of thinking during my investigation. I was also extremely fortunate to have Prof. Evelyn Wang as a mentor. Our numerous lunch meetings were always refreshing and uplifting.

Further, I am sincerely thankful to all of my present and past colleagues at the Precision Compliant Systems Lab. Regardless of their immense workloads, they were always ready and eager to help: whether it was a lively discussion of instrumentation or lending an extra hand when one was needed. In particular, I would like to thank Robert Panas, Jon Hopkins, and Chris DiBiasio for their help and friendship.

Throughout my time in graduate school I had the wonderful opportunity of working with several undergraduate students (UROPs). I am thankful for the time and effort that each of my UROPs invested in their projects. I have enjoyed serving as their mentor and have learned a considerable amount from our time in research. I am especially grateful to Laura Matloff who worked with me on Cylindrical Flexures and who was the first guinea pig for the models and rules that I developed. Laura always impressed me with how quickly she picked up the new material and how she always asked the right question. I am also extremely thankful to have Julie Wang work with me on the SQUISHbot project. For two years, she has been instrumental in the project's development through her work on ER valves. During these two years I have gotten to

see Julie grow as an engineer, she has expanded her understanding of fluids, electronics, design, and manufacturing with ease.

During my graduate career I had the privilege of working with the MIT SQUISHbot team on creating cm-scale, low-cost robotics. Working with this group of students, professors, and Boston Dynamics engineers has been a highlight of my years at MIT. The project was and continues to be extremely challenging but I'm continually amazed by the strides the team has achieved. Led by Prof. Hosoi, Prof. McKinley, Prof. Culpepper, Dr. Iagnemma and the work of numerous students, this team was able to produce multiple cm-scale robots. I am very thankful for the guidance and advice I received from all of the professors and engineers. It was a pleasure to work alongside students like Nadia Cheng and Ahmed Helal whose work I admire and whose friendship I value even more.

This work would not have been possible without Prof. Hunter's BioInstrumentation lab or the machine shop in building 35. The CF linear guides created for this thesis were machined in the BioInstrumentation Lab with the help of Jean Chang, Ashin Modak, and Adam Wahab. I would not have been able to make these prototypes without their assistance and patience. Similarly, the staff in the shop has been so helpful throughout my entire time at MIT, from helping me make my undergraduate thesis to giving me advice on how to manufacture the CF systems. Pat, Dave, and Bill make it possible for all students to excel in their research. Their help and experience has been essential for countless theses, and I will always value their friendship.

My experiences in the laboratory of manufacturing and productivity, LMP, have been a highlight of my studies at MIT. The students and the faculty in LMP are truly amazing colleagues and friends. I cannot imagine a graduate career without the lively and supportive environment that LMP promotes. There are countless friends that deserve thanks for their support, and for simply listening and being available. In the final push to graduate, I am so grateful to have had Melinda, Bob, Maia, Caitlin, and many others working in our shared office. I always looked forward to returning lab and seeing them; they are the reason I never wanted to work from home. This sentiment extends to the mechanical engineering department. I can think of countless number of faculty and staff who were always willing to help. In particular, I'd like to thank Leslie Reagan for her support and for keeping the department running smoothly.

Finally I am eternally grateful for the support of my family and friends. My mom, dad, and sister have been with me through all the highs and lows, and have always provided the

necessary love and support regardless of the situation. They were the ones who had to deal with my endless questions as a child and who encouraged me to pursue engineering. Los quiero muchisimo y muchas gracias por todo. I would also like to thank Asiri for his love and support. There have been many days when taking a shortcut was too tempting and yet he always knew how to encourage and help me so that I always did my best. To Joy Johnson and Monica Orta I would like to say thanks for your friendship and support. It has been an amazing experience getting to know you and getting to work with you for four years. I know that the impact of our work will be felt for many years to come. To my friends who have been with me through all my MIT years, thank you for your help and more importantly for making these 9 years so much fun. Jean, Connie, Buddy, and my trivia team, you guys have always been there after work to listen and provide memorable distractions from work. When people asked me why I have stayed at MIT for so long, I can't help to think of all the people who made this time fly by. Thank you!





# CONTENTS

---

<b>Abstract.....</b>	<b>3</b>
<b>Acknowledgements .....</b>	<b>5</b>
<b>Contents .....</b>	<b>9</b>
<b>Figures.....</b>	<b>13</b>
<b>Tables .....</b>	<b>29</b>
<b>1 Introduction.....</b>	<b>31</b>
1.1    Cylindrical Flexures.....	32
1.1.1    Definition .....	33
1.2    Cylindrical Flexure Challenges.....	34
1.2.1    Element Level Challenges.....	34
1.2.2    System Level Challenges .....	36
1.2.3    Stress Concentration.....	37
1.3    Design Process .....	38
1.4    Advantages of Cylindrical Flexures.....	40
1.5    Compliant Mechanisms Synthesis Approaches .....	42
1.6    Thesis Overview .....	46
1.6.1    Flexure Performance Metrics .....	47
1.6.2    Case Studies .....	48
<b>2 Prior Art .....</b>	<b>51</b>
2.1    Curved-Beam Models .....	51
2.2    Examples of Flexures with Curved Beams.....	52
2.3    Technology Gap.....	53
<b>3 Element Rules and Models.....</b>	<b>55</b>
3.1    Element description .....	55

3.2	Compliance Matrix .....	56
3.2.1	Corroboration with FEA.....	58
3.3	Curvature Adjustment Factor.....	61
3.4	Sweep angle and beta parameter effect.....	64
3.4.1	Sweep angle, $\phi$ .....	64
3.4.2	Beta parameter, $\beta$ .....	65
3.5	Stiffness ratios.....	67
3.5.1	Sweep angle effect .....	68
3.5.2	Taper angle effect.....	72
3.6	Parasitic Motion Ratios.....	73
3.6.1	Sweep angle effect .....	74
3.6.2	Taper angle effect.....	77
3.6.3	Eigenvalue Parasitic Ratios.....	78
3.7	Sensitivity Analysis .....	83
3.7.1	Sensitivity to sweep angle tolerance .....	83
3.7.2	Taper angle tolerance sensitivity.....	86
3.7.3	Sensitivity to off-neutral position.....	88
3.8	Boundary Conditions .....	90
3.8.1	Effect on Stiffness Ratios.....	91
3.8.2	Parasitic Ratios.....	93
3.9	Load location effect .....	95
3.10	Stress Model.....	99
3.10.1	$r$ -Compliance and $\theta$ -Compliance .....	100
3.10.2	$z$ -compliance .....	106
3.11	Summary of Element Design Rules .....	114
<b>4</b>	<b>System Rules and Models.....</b>	<b>117</b>
4.1	Parallel System Rules .....	118
4.1.1	Stiffness Ratios.....	119
4.1.2	Parasitic Rotation Ratios .....	120
4.1.2.1	Load Location Effect.....	129
4.1.2.2	Flexure Spacing Effect.....	132

4.1.3	Parasitic Displacement Ratios .....	134
4.1.4	Stress Model .....	136
4.2	Serial System Rules .....	138
4.2.1	Stiffness Ratios .....	139
4.2.2	Parasitic Rotation Ratios .....	142
4.2.3	Parasitic Displacement Ratios .....	142
4.3	Summary of System Design Rules .....	144
<b>5</b>	<b>CF Linear Guide .....</b>	<b>147</b>
5.1	Application .....	148
5.2	First Prototype .....	149
5.3	Second Prototype .....	156
5.4	Fabrication and Testing .....	160
<b>6</b>	<b>CF x-y-<math>\theta_z</math> Stage .....</b>	<b>169</b>
6.1	Application .....	170
6.2	CF Design Process .....	172
6.2.1	Concept Generation .....	172
6.2.2	Concept Analysis and Optimization .....	174
6.3	Fabrication and Testing .....	187
<b>7</b>	<b>Conclusions .....</b>	<b>191</b>
7.1	Future Work .....	193
	<b>References .....</b>	<b>195</b>
	<b>Appendix A: FEA Corroboration of CF Compliance Matrix .....</b>	<b>199</b>
	<b>Appendix B: Torsional Stiffness Constant for an r-compliance Element .....</b>	<b>205</b>
	<b>Appendix C: Element Compliance Matrices for Different Boundary Conditions .....</b>	<b>207</b>
	<b>Appendix D: CF Four-bar Compliance Matrix .....</b>	<b>209</b>



# FIGURES

---

Figure 1.1: Two cylindrical flexure system examples: (A) linear guide and (B) x-y- $\theta_z$  stage. .... 32

Figure 1.2: Cylindrical flexure elements are defined by their direction of greatest compliance. Their coordinate system is given in cylindrical coordinates at the tip of the flexure. The flexure blade element is described by its radius,  $R$ , sweep angle,  $\phi$ , radial thickness,  $t_r$ , and z-axis thickness,  $t_z$ . Z-compliance elements are differentiated from r-compliance elements by the relative magnitude of their area moments of inertia. .... 34

Figure 1.3: Element level challenges. Straight-beam flexure elements (A) under a z-axis load,  $F_z$ , suffer from one parasitic rotation,  $\alpha_x$ , in addition to the desired displacement,  $\Delta z$ . The straight flexure experiences a single bending moment,  $m_x$ . Cylindrical flexure z-compliance elements (B) under a z-axis load,  $F_z$ , suffer from two parasitic rotations,  $\alpha_r$  and  $\alpha_\theta$ , in addition to the desired displacement,  $\Delta z$ . The curved beam is subjected to a twisting moment,  $m_\theta$ , and a bending moment,  $m_r$  [7]. .... 35

Figure 1.4: Sweep angle effect,  $\phi$ , on the ratio of r-axis stiffness,  $K_r$ , to  $\theta$ -axis stiffness,  $K_\theta$ , for an r-compliance element. The graph shows that the ratio is larger than 1 for  $\phi > 123^\circ$ , indicating that beyond that sweep angle the flexure can no longer be considered a  $\theta$ -axis constraint.... 36

Figure 1.5: A) A Straight-beam compound four-bar system nests two four-bars to remove the y-axis parasitic displacement of the input stage,  $\Delta y$ , while increasing the range of the system,  $\Delta z$ . The nesting also reduces the parasitic rotation of the each of the stages,  $\alpha_x$ . B) In a curved compound four-bar the input and floating stages are located on different planes, as a result the parasitic displacements of the input stage,  $\Delta r$  and  $\Delta \theta$ , are not directly cancelled by the nesting. The parasitic rotations of the two stages,  $\alpha_r$  and  $\alpha_\theta$ , are also affected by the nesting. The range of the system is increased [7]. .... 37

Figure 1.6: A) Resulting VonMises stress on a straight-beam flexure compared to the stress of a curved-beam flexure of the same dimensions under the same loading. The figure shows that the curved beam experiences a stress concentration at the inner radius. This stress concentration has to be captured by the stress model to ensure the designer calculates the maximum stress on the beam [7]. .... 38

Figure 1.7: Simplified design process flowchart followed by the research components necessary to enable the design process for cylindrical flexure systems.....	39
Figure 1.8: Comparison between the straight-beam version of a system (A) and its cylindrical flexure counterpart (B). Cylindrical flexures can lead to a more compact design. The wrapping of the beams leads to footprint and volume reductions. ....	41
Figure 1.9: Assembly of concentric cylinders allows for a compact system design [10].....	41
Figure 1.10: Cylindrical flexures can be fabricated using a variety of methods including: A) Lathe with actuated tool (Turning center), B) abrasive water-jet with a rotary axis [11], and C) 3Dprinter. ....	42
Figure 1.11: Common flexure synthesis approaches include: topology synthesis, pseudo-rigid-body modeling, and exact constraint design. The building block approach and FACT are based on the exact constraint design methodology.....	43
Figure 1.12: Stiffness Ellipses are a visual representation of stiffness ratios. The relative lengths of the ellipse axis are representative of the magnitude of the stiffness ratio. ....	45
Figure 1.13: Planar and CF element and system examples. ....	46
Figure 1.14: The arc displacement of a straight four-bar is the result of the sum of two parasitic displacements (purple), $\Delta y$ and $\alpha_x$ , in addition to the desired displacement (green), $\Delta z$ . A parasitic displacement is an undesired displacement.....	48
Figure 1.15: CAD model depicting the actuation of the final CF linear guide design. ....	48
Figure 1.16: CAD model depicting the $\Delta x$ actuation of the CF x-y- $\theta_z$ stage.....	49
Figure 2.1: Examples of Smith’s hinges of rotational symmetry: A) Disk coupling and B) Rotationally symmetric hinge [6]. ....	53
Figure 2.2: Awatar and Slocum’s diaphragm single DOF linear bearing [28].....	53
Figure 2.3: Chart shows the current knowledge available on curved-beams and the technology required to enable the design process for cylindrical flexures. This thesis fills the technology gap which has prevented cylindrical flexures from becoming prevalent. ....	54
Figure 3.1: Flexure element coordinate systems. Figure defines the direction of positive displacements, rotations, as well as the direction of positive loads and moments. ....	56
Figure 3.2: ADINA Finite Element Models used to corroborate the analytical compliance matrix. A) FEA model created using 10 straight beam elements in series to represent the curved beam element. B) 3D solid model.....	59

Figure 3.3: FEA corroboration of compliance matrix, predicted displacements under  $-0.2N F_z$  load vs. sweep angle,  $\phi$ . The plot compares the curved beam model to an FEA Beam Element model and an FEA 3D solid model. (L=60mm,  $t_r=6.35\text{mm}$ ,  $t_z=1\text{mm}$ , 7075Aluminum)..... 60

Figure 3.4: Curvature adjustment factors,  $\zeta$ , vs. Sweep Angle,  $\phi$ , for a  $z$ -compliance flexure. The plot shows that as the sweep angle approaches zero the curved-beam behaves like a straight-beam. The curvature adjustment factor can be used to define the value of sweep angle below which a beam can be modeled as a straight beam,  $\phi_s$ . Below  $\phi=34^\circ$  the value of the two dominant displacements,  $\Delta z$  and  $\alpha_r$ , are within 5% of the straight-beam value. While for  $\phi<14^\circ$  the additional parasitic rotation,  $\alpha_\theta$ , is less than  $1/10^{\text{th}}$  the value of the dominant parasitic motion,  $\alpha_r$ . ..... 63

Figure 3.5: Curvature adjustment factors,  $\zeta$ , vs. Sweep Angle,  $\phi$ , for an  $r$ -compliance flexure. The plot shows that as the sweep angle approaches zero the curved-beam behaves like a straight-beam. The curvature adjustment factor can be used to define the value of sweep angle below which a beam can be modeled as a straight beam,  $\phi_s$ . Below  $\phi=29^\circ$  the value of the two dominant displacements,  $\Delta r$  and  $\alpha_z$ , are within 5% of the straight-beam value. While below  $\phi=15^\circ$  the additional parasitic displacement,  $\Delta\theta$ , is less than  $1/10^{\text{th}}$  the value of the dominant parasitic displacement,  $\Delta r$ . ..... 64

Figure 3.6: Fixed length flexures with increasing sweep angle,  $\phi$ ..... 65

Figure 3.7: A) Flexure beam cross-sectional area indicating the taper angle,  $\Psi$ , or deviation from the desired rectangular cross-section. B) Location of bend axis of the area moments of inertia,  $I_z$  and  $I_r$ , of a  $z$ -compliance element and an  $r$ -compliance element. The taper angle shifts the location of the bend axis of  $I_z$ . ..... 66

Figure 3.8: Normalized taper angle effect on the area moments of inertia,  $I_z$  and  $I_r$ , and the torsional stiffness constant,  $k_t$ , of a  $z$ -compliance CF with  $\phi=120^\circ$ . Effect is normalized using the values for  $\Psi=0^\circ$ . ..... 67

Figure 3.9: Sweep angle,  $\phi$ , effect on the stiffness ratios for a  $z$ -compliance flexure with a radial-thickness,  $t_r$ , to  $z$ -thickness,  $t_z$ , ratio of 10. The stiffness ratios are equal when  $\phi=122.56^\circ$ . (L=60mm,  $t_r=10\text{mm}$ ,  $t_z=1\text{mm}$ , 6061 Aluminum). ..... 68

Figure 3.10: Effect of  $t_r/t_z$  ratio on the magnitude of the stiffness ratios for a  $z$ -compliance flexure ( $\phi=122.56^\circ$ ). Plot shows that regardless of the value of  $t_r/t_z$  the stiffness ratios are equal when

$\phi=122.56^\circ$ and their magnitude is less than that the ratio of $K_z/K_r$ for a straight-beam of the same dimensions. ( $L=60\text{mm}$ , 6061 Aluminum). .....	69
Figure 3.11: Sweep angle, $\phi$ , effect on the stiffness ratios for an $r$ -compliance flexure with a $z$ -thickness, $t_z$ to radial-thickness, $t_r$ , ratio of 10. The $K_r/K_\theta$ stiffness ratio is equal to 1 when $\phi = 122.56^\circ$ . When the $K_r/K_\theta$ is greater than 1 the flexure should be considered $\theta$ -compliant because this is its lowest stiffness. ( $L=60\text{mm}$ , $t_z=10\text{mm}$ , $t_r=1\text{mm}$ , 7075 Aluminum). .....	70
Figure 3.12: Effect of $t_z/t_r$ ratio on the magnitude of the stiffness ratios for an $r$ -compliance flexure ( $\phi = 122.56^\circ$ ). Plot shows that regardless of the value of $t_z/t_r$ the $K_r/K_\theta$ stiffness ratio is equal to 1 when $\phi = 122.56^\circ$ . ( $L=60\text{mm}$ , 7075 Aluminum). .....	71
Figure 3.13: $t_z/t_r$ effect on the stiffness ratios of an $r$ -compliance flexure ( $\phi = 122.56^\circ$ ). Plot shows that $t_z/t_r$ has a significantly greater effect on the $K_r/K_z$ stiffness ratio of a straight-beam flexure compared to a curved-beam $r$ -compliance element. ( $L=60\text{mm}$ , 7075 Aluminum). ...	71
Figure 3.14 Taper angle effect on the stiffness ratios for a $z$ -compliance flexure ( $\phi=120^\circ$ ). Plot shows that increasing $\Psi$ increases the value of the stiffness ratios. ( $L=60\text{mm}$ , $t_r=10\text{mm}$ , $t_z=1\text{mm}$ , 7075Aluminum). .....	72
Figure 3.15 Taper angle effect on the stiffness ratios for an $r$ -compliance flexure ( $\phi=60^\circ$ ). Plot shows that increasing $\Psi$ decreases the value of the $K_r/K_z$ stiffness ratio but has no effect on $K_r/K_\theta$ . ( $L=60\text{mm}$ , $t_z=10\text{mm}$ , $t_r=1\text{mm}$ , 7075Aluminum). .....	73
Figure 3.16 Definition of parasitic (purple) and desired (green) motions for the three types of cylindrical flexures: A) $z$ -compliance, B) $r$ -compliance, and C) $\theta$ -compliance. ....	74
Figure 3.17 Sweep angle, $\phi$ , effect on the parasitic ratios of a $z$ -compliance flexure. The two parasitic ratios, $\alpha_\theta/\Delta z$ and $\alpha_r/\Delta z$ , are equal when $\phi = 118^\circ$ . ( $L=60\text{mm}$ , $t_r=10\text{mm}$ , $t_z=1\text{mm}$ , 6061 Aluminum) .....	75
Figure 3.18 Sweep angle, $\phi$ , effect on the parasitic ratios of an $r$ -compliance flexure. The shaded region highlights the sweep angles ( $215.5^\circ > \phi > 132.5^\circ$ ) for which the desired motion, $\Delta r$ , is less than the parasitic motion, $\Delta \theta$ . ( $L=60\text{mm}$ , $t_z=10\text{mm}$ , $t_r=1\text{mm}$ , 7075Aluminum) .....	76
Figure 3.19 Sweep angle, $\phi$ , effect on the parasitic ratios of a $\theta$ -compliance flexure. Above $\phi=115^\circ$ the desired motion, $\Delta \theta$ , is less than the parasitic motion, $\Delta r$ . ( $L=60\text{mm}$ , $t_z=10\text{mm}$ , $t_r=1\text{mm}$ , 7075Aluminum) .....	77
Figure 3.20 Taper angle, $\Psi$ , effect on the parasitic ratios of a $z$ -compliance flexure with $\phi=120^\circ$ . ( $L=60\text{mm}$ , $t_r=10\text{mm}$ , $t_z=1\text{mm}$ , 7075Aluminum) .....	78



Figure 3.21 Linearization of tip rotations for a $z$ -compliance flexure (A), and an $r$ -compliance flexure (B).....	80
Figure 3.22 Sweep angle, $\phi$ , effect on the eigenvalue parasitic ratios of $z$ -compliance flexure with $t_r/t_z=10$ . ( $L=60\text{mm}$ , $t_r=5\text{mm}$ , $t_z=0.5\text{mm}$ , 7075 Aluminum).....	81
Figure 3.23 Sweep angle, $\phi$ , effect on the eigenvalue parasitic ratios of an $r$ -compliance flexure with $t_z/t_r=10$ . ( $L=60\text{mm}$ , $t_z=5\text{mm}$ , $t_r=0.5\text{mm}$ , 7075 Aluminum).....	82
Figure 3.24 Stiffness ratios sensitivity to sweep angle, $\phi$ , tolerance for a $z$ -compliance flexure vs. desired sweep angle. Plot shows the percent error from desired value per degree of sweep angle tolerance. ( $L=60\text{mm}$ , $t_r=10\text{mm}$ , $t_z=1\text{mm}$ , 6061 Aluminum) .....	83
Figure 3.25 Stiffness ratios sensitivity to sweep angle, $\phi$ , tolerance for an $r$ -compliance flexure vs. desired sweep angle, $\phi$ . Plot shows the percent error from predicted value per degree of sweep angle tolerance. ( $L=60\text{mm}$ , $t_z=10\text{mm}$ , $t_r=1\text{mm}$ , 7075 Aluminum) .....	84
Figure 3.26 Parasitic ratios sensitivity to sweep angle, $\phi$ , tolerance for a $z$ -compliance flexure vs. desired sweep angle. Plot shows the percent error from predicted value per degree of sweep angle tolerance. ( $L=60\text{mm}$ , $t_r=10\text{mm}$ , $t_z=1\text{mm}$ , 6061 Aluminum) .....	85
Figure 3.27 Parasitic ratios sensitivity to sweep angle, $\phi$ , tolerance for an $r$ -compliance flexure vs. desired sweep angle. Plot shows the percent error from predicted value per degree of sweep angle tolerance. ( $L=60\text{mm}$ , $t_z=10\text{mm}$ , $t_r=1\text{mm}$ , 7075 Aluminum) .....	85
Figure 3.28 Stiffness ratios sensitivity to taper angle, $\Psi$ , tolerance for a $z$ -compliance flexure vs. sweep angle, $\phi$ . Plot shows that the percent error from predicted value depends on the sweep angle of the flexure. ( $L=60\text{mm}$ , $t_r=6.35\text{mm}$ , $t_z=1\text{mm}$ , 7075 Aluminum) .....	86
Figure 3.29 Stiffness ratios sensitivity to taper angle, $\Psi$ , tolerance for an $r$ -compliance flexure vs. sweep angle, $\phi$ . Plot shows that the percent error from predicted value depends on the sweep angle of the flexure. ( $L=60\text{mm}$ , $t_z=6.35\text{mm}$ , $t_r=1\text{mm}$ , 7075 Aluminum) .....	87
Figure 3.30 Parasitic ratios sensitivity to taper angle, $\Psi$ , tolerance for a $z$ -compliance flexure vs. sweep angle, $\phi$ . Plot shows that the percent error from predicted value depends on the sweep angle of the flexure. ( $L=60\text{mm}$ , $t_r=10\text{mm}$ , $t_z=1\text{mm}$ , 7075 Aluminum) .....	88
Figure 3.31 ADINA FEA beam models used to determine $K_\theta$ . A) Neutral position and B) Off-neutral position $\Delta z=1\text{mm}$ . .....	89

Figure 3.32 Off-neutral position effect on the stiffness of a  $z$ -compliance flexure vs. sweep angle,  $\phi$ . Plot shows the ratio of the off-neutral position ( $\Delta z=1\text{mm}$ ) stiffness to the neutral position ( $\Delta z=0$ ) stiffness. ( $L=60\text{mm}$ ,  $t_r=10\text{mm}$ ,  $t_z=1\text{mm}$ , 7075 Aluminum) ..... 90

Figure 3.33 Gauss elimination is used to eliminate degrees of freedom, creating the compliance matrices for elements under different boundary conditions. .... 91

Figure 3.34 Boundary conditions effect on stiffness ratios vs. sweep angle,  $\phi$ , for a  $z$ -compliance flexure. Plot shows that the stiffness ratios are always equal when  $\phi=122.56^\circ$ . ( $L=60\text{mm}$ ,  $t_r=10\text{mm}$ ,  $t_z=1\text{mm}$ , 7075 Aluminum)..... 92

Figure 3.35 Boundary conditions effect on stiffness ratios vs. sweep angle,  $\phi$ , for an  $r$ -compliance flexure. Plot shows that when the parasitic rotation  $\alpha_z$  is constrained, the sweep angle at which the stiffness ratio  $K_r/K_\theta=1$  decreases from  $\phi=122.6^\circ$  to  $\phi=90^\circ$ . ( $L=60\text{mm}$ ,  $t_z=10\text{mm}$ ,  $t_r=1\text{mm}$ , 7075 Aluminum)..... 93

Figure 3.36 Boundary conditions effect on the parasitic ratios vs. sweep angle,  $\phi$ , for a  $z$ -compliance flexure. Plot shows the effect that constraining one parasitic rotation has on the other parasitic ratio. ( $L=60\text{mm}$ ,  $t_r=10\text{mm}$ ,  $t_z=1\text{mm}$ , 7075 Aluminum) ..... 94

Figure 3.37 Boundary conditions effect on the parasitic ratios vs. sweep angle,  $\phi$ , for an  $r$ -compliance flexure. Plot shows the effect that constraining the one parasitic motion,  $\alpha_z$  or  $\Delta\theta$ , has on the other parasitic ratio. For a  $\alpha_z$ -constrained element the region for which  $\Delta r > \Delta\theta$  is now limited by  $96^\circ > \phi > 150^\circ$ . ( $L=60\text{mm}$ ,  $t_z=10\text{mm}$ ,  $t_r=1\text{mm}$ , 7075 Aluminum)..... 94

Figure 3.38 Load location can be used to remove parasitic rotations. A) A straight-beam loaded along the  $z$ -axis experiences a desired motion,  $\Delta z$ , and a parasitic rotation,  $\alpha_x$ . B) Loading the beam with a Moment about the  $x$ -axis,  $M_x$ , at the tip of the flexure, produces a rotation,  $\alpha_x$ , and a displacement,  $\Delta z$ . C) By applying an  $F_z$  load on a stage that measures half the length,  $L$ , of the beam, an  $M_x$  moment is exerted at the tip cancelling the  $\alpha_x$  rotation. The resulting motion is a pure  $\Delta z$  displacement..... 95

Figure 3.39 Location of applied load on a  $z$ -compliance element. The loading point is defined by the radius to the load location,  $R_L$ , and the angle between the tip of the flexure and the loading point,  $\gamma$ . .... 96

Figure 3.40  $F_z$  load location required to remove each parasitic rotation given  $R_L=R$ . Plot shows the ratio of  $\gamma/\phi$  vs. sweep Angle,  $\phi$ , for a  $z$ -compliance element.  $\gamma$  is measured from the tip of the flexure. .... 97

Figure 3.41  $F_z$  load location required to remove the element's parasitic rotations,  $\alpha_\theta$  and  $\alpha_r$ . Plot gives the ratios of  $\gamma/\phi$  and  $R_L/R$  vs. Sweep Angle,  $\phi$ , for a  $z$ -compliance element.  $\gamma$  is measured from the tip of the flexure..... 98

Figure 3.42  $F_r$  load location required to remove the element's parasitic rotation given  $R_L=R$ . Plot gives the ratio of  $\gamma/\phi$  vs. Sweep Angle,  $\phi$ , for an  $r$ -compliance element.  $\gamma$  is measured from the tip of the flexure..... 99

Figure 3.43 Resulting moments on  $r$ -compliance and  $\theta$ -compliance elements as a result of loading at the tip. Both elements experience a single bending moment,  $m_z$ , when loaded under  $F_r$  and  $F_\theta$  respectively. The bending moment varies along the length of the beam. The position of the resulting moments is given by  $R\lambda$ , where  $\lambda$  is measured from the tip of the beam..... 100

Figure 3.44 Maximum stress location,  $\lambda_{max}$ , vs. sweep angle,  $\phi$ , for an  $r$ -compliance element under a pure  $F_r$  load. .... 101

Figure 3.45 Maximum stress location,  $\lambda_{max}$ , vs. sweep angle,  $\phi$ , for a  $\theta$ -compliance element under a pure  $F_\theta$  load..... 101

Figure 3.46 Normalized VonMises stress vs. sweep angle,  $\phi$ , for an  $r$ -compliance element. Stress is normalized using the 3D-solid FEA stress value for a straight-beam of the same dimensions under the same load. .... 102

Figure 3.47 Normalized VonMises stress vs. sweep angle,  $\phi$ , for a  $\theta$ -compliance element. Stress is normalized using the 3D-solid FEA stress value for a straight-beam of the same dimensions under the same load. .... 103

Figure 3.48 Normalized range vs. sweep angle,  $\phi$ , for an  $r$ -compliance element under an  $F_r$  load. Range is normalized using the range value for a straight-beam of the same dimensions. ... 104

Figure 3.49 Normalized range vs. sweep Angle,  $\phi$ , for a  $\theta$ -compliance element under an  $F_\theta$  load. Stress is normalized using the range value for a  $\phi=5^\circ$  element. .... 104

Figure 3.50 Range/ $R$  vs. sweep angle,  $\phi$ , for an  $r$ -compliance element under  $F_r$ . Dotted line shows the range/ $L$  for a straight-beam element of the same dimensions..... 106

Figure 3.51 Range/ $R$  vs. sweep angle,  $\phi$ , for a  $\theta$ -compliance element under  $F_\theta$ . .... 106

Figure 3.52 Resulting moments on  $z$ -compliance element as a result of loading at the tip. Element experience a bending moment,  $m_r$ , and a twisting moment,  $m_\theta$ , when loaded under

$F_z$ . The resulting moments vary along the length of the beam. The position of the resulting moments is given by  $R\lambda$ , where  $\lambda$  is measured from the tip of the beam..... 107

Figure 3.53 Maximum stress location,  $\lambda_{max}$ , vs. sweep angle,  $\phi$ , for a  $z$ -compliance element under a pure  $F_z$  load. ( $L=60\text{mm}$ ,  $t_r=6.4\text{mm}$ ,  $t_z=0.6\text{mm}$  7075 Aluminum) ..... 108

Figure 3.54 Normalized maximum VonMises stress vs. sweep angle,  $\phi$ , for a  $z$ -compliance element. Stress is normalized using the 3D-solid FEA stress value for a straight-beam of the same dimensions under the same load. Plot compares the FEA stress values to the stress calculated by a stress model that considers the bending axial stress and the torsion shear stress on the beam at the base of the beam (Bending & Torsion) and a stress model that gives the stress at  $\lambda_{max}$  (Bending & Torsion  $\lambda_{max}$ ). ..... 109

Figure 3.55 ADINA FEA images showing the major stress components on a straight-beam under a A) bending moment and B) a torsional moment. The axial stress,  $\sigma_{\theta\theta-m\theta}$ , due to twisting is highlighted because it is the missing component from the original stress model,  $\sigma_{von1-z}$ . ..... 110

Figure 3.56 Normalized maximum Von Mises stress vs. sweep angle,  $\phi$ , for a  $z$ -compliance element. Stress is normalized using the 3D-solid FEA stress value for a straight-beam of the same dimensions under the same load. Plot compares the FEA stress values to the stress calculated by the three stress models: (i) the bending axial and the torsion shear stress on the beam at the base of the flexure (Bending & Torsion), (ii) the bending and shear stress at  $\lambda_{max}$ ,  $\sigma_{von1-z}$  (Bending & Torsion  $\lambda_{max}$ ), and (iii) bending and shear stress at  $\lambda_{max}$  with the presented warping correction,  $\sigma_{von2-z}$  (Warping Correction  $\lambda_{max}$ ). ..... 112

Figure 3.57 VonMises stress for a  $\phi=120^\circ$   $z$ -compliance element. The FEA values for different length to radial-thickness,  $L/t_r$ , and radial to  $z$ -axis thickness,  $t_r/t_z$ , are plotted along the presented warping corrected stress model. .... 112

Figure 3.58 Normalized range vs. sweep angle,  $\phi$ , for a  $z$ -compliance element. Stress is normalized using the range value for a straight-beam element of the same dimensions under the same loading. .... 113

Figure 3.59 Range/R vs. sweep angle,  $\phi$ , for a  $z$ -compliance element. Dotted line shows the range/L for a straight-beam element of the same dimensions. .... 114

Figure 4.1: Flexure system types: A) In a parallel system the load is split between the flexural elements. The total stiffness of the system is given by the sum of the element stiffnesses. A

four-bar is an example of a parallel system. B) Serial systems are characterized by a shared load path. The compliance of the system ( $1/K_{sys}$ ) is equal to the sum of the element compliances. A compound four-bar is created by nesting two four-bars in series. .... 117

Figure 4.2: Four-bar system parameters and motions.  $F_z$  indicates load along the  $z$ -axis and  $\Delta z$  is the desired displacement. A) Straight four-bar system: The parasitic motions are given by  $\alpha_x$  and  $\Delta y$ .  $a$  indicates the location of  $F_z$  relative to ground, and  $b$  is the distance between the two flexures. B) The curved four-bar has four undesired motions,  $\alpha_r$ ,  $\alpha_\theta$ ,  $\Delta r$ ,  $\Delta\theta$ . The location of  $F_z$  is specified using  $R_L$  and  $\gamma$ . .... 119

Figure 4.3: Curved compliant four-bar mechanisms. Image shows the coordinate systems for the two flexures. .... 120

Figure 4.4: Straight four-bar force and moment diagram. Loads and moments on the flexures and input stage are shown.  $F_z$  is the applied load, while  $M_x$  is the moment resulting from constraining the flexure tip. The axial forces,  $F_y$ , balance the  $M_x$  moments on the input stage. .... 121

Figure 4.5: Curved four-bar force and moment diagram. Loads and moments on one end of the flexures and input stage are shown.  $F_z$  is the applied load, while  $M_r$  and  $M_\theta$  are the moments resulting from constraining each flexure tip. The radial forces,  $F_r$ , balance the  $M_\theta$  and the axial forces,  $F_\theta$ , balance the  $M_r$  moment on the input stage. .... 122

Figure 4.6: Curved four-bar parasitics vs. sweep angle,  $\phi$ . The FEA values were calculated using a 3D-solid model. The two rotations are normalized using the FEA calculated value for  $\phi = 30^\circ$ . The plot shows that the beam-based model is inaccurate for low  $\phi$ . ( $L=60\text{mm}$ ,  $t_r=6\text{mm}$ ,  $t_z=0.6\text{mm}$ ,  $L_{stage}=6\text{mm}$ , 7075 Aluminum). .... 123

Figure 4.7: Stage length effect on the curved four-bar parasitics vs.  $\phi$ . Values were calculated using an FEA 3D-solid model. The parasitics are normalized using the value for the  $\phi = 30^\circ$  four-bar with a 2mm stage. .... 124

Figure 4.8: The curvature of the beam leads to a difference in length between the inner and outer radiuses. This effect in addition to the length of the stage leads to the rotation of the  $r$ -axis of the four-bar away from the  $r$ -axis of the elements. The rotation angle is given by  $\omega$ . .... 125

Figure 4.9:  $\omega$  adjustment vs.  $L/t_r$  for three different stage sizes. The plot gives the fitted values for  $p$  and the model values.  $\omega$  is given by  $p\phi$ . .... 125

Figure 4.10: Corrected curved four-bar parasitics vs. $\phi$ . The rotations are normalized using the FEA values for $\phi=30^\circ$ . The dotted lines show the $\omega=0^\circ$ model values for $\alpha_r$ and $\alpha_\theta$ . ( $L=60\text{mm}$ , $t_r=6\text{mm}$ , $t_z=0.6\text{mm}$ $L_{stage}=6\text{mm}$ 7075 Aluminum). .....	127
Figure 4.11: Corrected curved four-bar $\alpha_\theta$ vs. $\phi$ for different $L/t_r$ ratios. $\alpha_\theta$ is normalized using the FEA value for $\phi=30^\circ$ . ( $L_{stage} = 6\text{mm}$ ).....	127
Figure 4.12: Corrected curved four-bar $\alpha_r$ vs. $\phi$ for different $L/t_r$ ratios. $\alpha_r$ is normalized using the FEA value for $\phi=30^\circ$ . ( $L_{stage} = 6\text{mm}$ ).....	128
Figure 4.13: Corrected curved four-bar $\alpha_\theta$ vs. $\phi$ for different stage lengths. $\alpha_\theta$ is normalized using the FEA value for $\phi=30^\circ$ with a 2mm stage. The dotted line shows the $\omega=0^\circ$ predicted values. ( $L/t_r=10$ ) .....	128
Figure 4.14: Corrected curved four-bar $\alpha_r$ vs. $\phi$ for different stage lengths. $\alpha_r$ is normalized using the FEA value for $\phi=30^\circ$ with a 2mm stage. The dotted line shows the $\omega=0^\circ$ predicted values. ( $L/t_r=10$ ) .....	129
Figure 4.15: Load location effect on the curved four-bar parasitics. Plot gives the normalized rotations vs. the ratio of $R_L$ to $R$ ( $\gamma=0^\circ$ ). Rotations are normalized using the FEA values for $R_L/R=1/6$ .....	130
Figure 4.16: Load location effect on curved four-bar parasitics. Plot gives the normalized rotations vs. the ratio of $\gamma/\phi$ . Rotations are normalized using the FEA values for $\gamma=0^\circ$ . ....	130
Figure 4.17: Applied-moment error effect on $\alpha_\theta$ . Plot gives the ratio of $\alpha_{\theta\text{-resulting}}/\alpha_{\theta\text{-desired}}$ vs. the ratio of the $M$ -applied to $M$ -desired. ....	131
Figure 4.18: Applied-moment error effect on $\alpha_r$ . Plot gives the ratio of $\alpha_{r\text{-resulting}}/\alpha_{r\text{-desired}}$ vs. the ratio of the $M$ -applied to $M$ -desired. The dotted line gives the straight four-bar sensitivity to applied-moment error. ....	132
Figure 4.19: Symmetry may be used to cancel the curved four-bar parasitic rotations.....	132
Figure 4.20: Flexure spacing, $b$ , effect on curved four-bar parasitic motions. Rotations are normalized using the FEA values for $b=10\text{mm}$ . ( $\phi=60^\circ$ ) .....	133
Figure 4.21: Input stage $\Delta y$ displacement for a straight four-bar under $F_z$ . The four-bar's input stage can deform during operation when the spacing between the flexures is too large and the stage is not stiff enough. ....	134
Figure 4.22: A straight-beam flexure suffers from a $\Delta y$ displacement when loaded along $z$ . The schematic shows the relationship between $\Delta y$ , $\Delta z$ , $L$ and $\alpha_x$ . ....	135

Figure 4.23: The  $\Delta r$  and  $\Delta\theta$  parasitic motions of a curved four-bar can be estimated by modeling the curved flexure as a series of straight beams..... 135

Figure 4.24: Curved four-bar input stage parasitic displacement ratios vs. sweep angle,  $\phi$ . The plot also compares the FEA calculated parasitic ratios to the model approximations..... 136

Figure 4.25: Loading conditions on a CF four-bar flexural element.  $M_r$  and  $M_\theta$  are the moments applied by the stage constraint on the flexure tip.  $F_z$  is the half the load applied on the four-bar.  $F_z$ ,  $M_r$ , and  $M_\theta$ , produce a bending moment,  $m_r$ , and a twisting moment,  $m_\theta$ , on the beam. The resulting moments vary along the length of the beam. The position of the resulting moments is given by  $R\lambda$ , where  $\lambda$  is measured from the tip of the beam..... 137

Figure 4.26: Curved four-bar Von Mises stress vs.  $\phi$ . Stress is normalized using the stress of a straight four-bar of the same dimensions under the same load. Plot shows the FEA calculated values, the stress given by a no-warp model and the values given by the full model which includes the warping correction..... 137

Figure 4.27: A CF compound four-bar is assembled by nesting two four-bars. The input and floating four-bars have different coordinate systems. If the coordinates of the input four-bar are chosen as the system coordinates, the compliance matrix of the floating four-bar must be transformed to match the system's new coordinate system ( $r'_2, \theta'_2, z'_2$ )...... 139

Figure 4.28: In a compound four-bar each four-bar has a different coordinate system; therefore, an applied radial force,  $F_{r1}$ , on the input four-bar results in radial and axial forces,  $f_{r2}$  and  $f_{\theta2}$ , and a moment about  $z$ ,  $m_z$ , on the floating four-bar..... 140

Figure 4.29: Sweep angle,  $\phi$ , effect on the CF compound four-bar's  $K_z/K_r$  stiffness ratio. Plot shows that the ratio decreases with increasing  $\phi$ . The CF's ratio is compared to the  $K_z/K_r$  of a straight compound four-bar of the same dimensions. The graph demonstrates the importance of accounting for the effect of the  $\alpha_z$  rotation of the floating stage. .... 141

Figure 4.30: Sweep angle,  $\phi$ , effect on the curved compound four-bar's  $K_z/K_\theta$  stiffness ratio. Plot shows that the ratio increases with increasing  $\phi$ . The CF's ratio is compared to the  $K_z/K_\theta$  of a straight compound four-bar of the same dimensions. The graph demonstrates the importance of accounting for the effect of the  $\alpha_z$  rotation of the floating stage. .... 141

Figure 4.31: Curved compound four-bar parasitic ratios vs.  $\phi$ . Plot compares the parasitic ratios for a compound four-bar to those of a single four-bar..... 142

Figure 4.32: Curved compound four-bar parasitic ratios vs. $\phi$ . Plot compares the parasitic ratios for a compound four-bar to those of a single four-bar.....	143
Figure 4.33: A symmetric system design may be used to reduce or remove the parasitic displacements, $\Delta r$ and $\Delta\theta$ , of a compound four-bar. A) In a design with two compound four-bars separated by $180^\circ$ , the $\Delta r$ displacements cancel out and the $\Delta\theta$ motions result in an $\alpha_z$ -rotation. B) Using two double-compound four-bars leads to the cancellation of all the parasitic displacements. ....	144
Figure 4.34: Steps used to establish a CF system's compliance matrix. <sup>+</sup> For serial systems it may be necessary to account for the compliance due to rotations of the secondary stages.....	145
Figure 5.1: Linear guide prototypes: A) MIT Lincoln Lab's FTS linear guide, B) First CF linear guide, C) Second CF prototype designed using CF guidelines. ....	148
Figure 5.2: Michelson Interferometer illustration. A linear guide is used to translate the moving mirror. ....	149
Figure 5.3: The first CF linear guide prototype was conceived by wrapping two double compound four-bars. The floating stages of the compound four-bars were joined to create a single cylinder. The CF image highlights the four compound four-bars.....	150
Figure 5.4: Mechanism used to hold cylindrical stock in place during the machining process used to create the CF. The future flexure (1) is slipped onto a piece of cylindrical stock (2) which radially supports the work piece. The support stock is attached to a base (3) which is held by the lathe's spindle. The flexure stock is constrained axially with a cap (4) which is connected to the base using a bolt.....	152
Figure 5.5: First prototype measurement setup. A) The CF (4) is attached to a grounding cylinder (3) which is then attached to the optical table. The flexure is actuated using a depth micrometer (1) which pushes on a stage attached to the two input stages of the CF. The inset shows the tip of the micrometer (2) and the actuation stage. B) A cap with scales was attached to the flexure. The displacements of the CF were measured using optical linear encoders: (5) top, (6) center, (7) side.....	153
Figure 5.6: Tilt angle vs. axial displacement ( $\Delta z$ ) for the first CF linear guide prototype. The dotted lines indicate the functional requirement of $\pm 10\mu\text{radians}$ . A moving average filter ( $\Delta z \pm 0.3175\text{mm}$ ) was used to remove the cyclic behavior imposed by the rotation of the micrometer head.....	154



Figure 5.7: Tip angle vs. axial displacement ( $\Delta z$ ) for the first CF linear guide prototype. The dotted line indicates the functional requirement of  $10\mu\text{radians}$ . A moving average filter ( $\Delta z \pm 0.3175\text{mm}$ ) was used to remove the cyclic behavior imposed by the rotation of the micrometer head..... 154

Figure 5.8: FEA analysis of one of the compound four-bars of the first CF linear guide design shows that the input stage deforms during actuation..... 155

Figure 5.9: Range vs. sweep angle,  $\phi$ , for a 6061 Aluminum four-bar with  $R=32\text{mm}$ ,  $t_r=6.35\text{mm}$ , and  $t_z=0.5\text{mm}$ . The minimum range required for the FTS system is  $5\text{mm}$  per four-bar which is achieved for  $\phi > 91^\circ$ . An  $R$  of  $31.75\text{mm}$  corresponds to an outer diameter of  $69.85\text{mm}$  ( $2.75''$ )..... 157

Figure 5.10: Input stage parasitic rotation ratios vs. sweep angle,  $\phi$ , for a 6061 Aluminum compound four-bar with  $R=32\text{mm}$ ,  $t_r=6.35\text{mm}$ , and  $t_z=0.5\text{mm}$ . Angles below  $91^\circ$  are shaded because they do not meet the minimum  $5\text{mm}$  range constraint. The dotted line indicates the FTS  $5e-4 \text{ rad/m}$  parasitic ratio requirement..... 158

Figure 5.11: CAD model of the second CF linear guide design. The concept is composed of two compound four-bars which are labeled in the picture. The design allows for the floating stages to translate and rotate freely. The two compound four-bars' input stages are joined using connecting rings at the front and back of the cylinder..... 159

Figure 5.12: Each pocket of the second prototype was filled with putty before the next one was cut. The putty helps reduce the vibrations of the flexure elements during cutting..... 160

Figure 5.13: Second prototype measurement setup. A) The CF (4) is attached to a grounding cylinder (3) which is then attached to the optical table. The flexure is actuated using a depth micrometer (1) which pushes on a cap attached to the connecting ring of the CF. The inset shows the tip of the micrometer (2) and the actuation cap. B) Another cap with scales was attached to the front of the flexure. The displacements of the CF were measured using optical linear encoders: (5) top, (6) center, (7) side..... 161

Figure 5.14: Tilt angle,  $\alpha_{tilt}$ , vs. axial displacement ( $\Delta z$ ) for the second CF linear guide prototype. The dotted lines indicate the functional requirement of  $\pm 10\mu\text{radians}$ . The flexure was actuated using a micrometer. A moving average filter ( $\Delta z \pm 0.3175\text{mm}$ ) was used to remove the cyclic behavior imposed by the rotation of the micrometer head..... 162

Figure 5.15: Tip angle,  $\alpha_{tip}$ , vs. axial displacement ( $\Delta z$ ) for the second CF linear guide prototype. The dotted lines indicate the functional requirement of  $\pm 10\mu\text{radians}$ . The flexure was actuated using a micrometer. A moving average filter ( $\Delta z \pm 0.3175\text{mm}$ ) was used to remove the cyclic behavior imposed by the rotation of the micrometer head. .... 162

Figure 5.16: Weight loading measurement setup. The flexure (2) is attached to the table using a grounding cylinder (1). The CF is loaded using a mass (5) on a low-friction pulley (4). The displacements are measured using the same three optical linear encoders (3). .... 163

Figure 5.17: Tilt angle,  $\alpha_{tilt}$ , vs. axial displacement ( $\Delta z$ ) for the second CF linear guide prototype. The dotted lines indicate the functional requirement of  $\pm 10\mu\text{radians}$  from the average tilt error. The flexure was actuated by hanging masses. .... 164

Figure 5.18: Tip angle,  $\alpha_{tip}$ , vs. axial displacement ( $\Delta z$ ) for the second CF linear guide prototype. The dotted lines indicate the functional requirement of  $\pm 10\mu\text{radians}$  from the average tip error. The flexure was actuated by hanging masses. .... 164

Figure 5.19: Machining errors: A) Tool lead-in error resulted in some of the flexure elements being thinner at their base. B) The back connecting ring is larger than the front because of the machine's travel limit. .... 166

Figure 5.20: Linear guide constructed using two CF bearings. .... 167

Figure 6.1: A) Thomas' current straight-beam x-y- $\theta_z$  stage [35]. B) Proposed CF  $r$ -compliance x-y- $\theta_z$  stage. .... 170

Figure 6.2: DPN alignment mechanism with the straight-beam x-y- $\theta_z$ -stage [35]. The camera is used to determine the position of the DPN tip, while the voice coil actuators are used to position the tip. .... 171

Figure 6.3: Preliminary CF x-y- $\theta_z$  stage concepts. The table compares the motions of the three layouts under  $F_y$  and  $M_z$  loads. The desired displacements are indicated in green, while the parasitic motions are given in purple. .... 173

Figure 6.4: 4-Flexure spider concept. Axi-symmetric layout of the flexures reduces  $K_{\theta_z}$ . In this design the flexures are not concentric which allows for  $\phi > 90^\circ$ . .... 174

Figure 6.5: 4-flexure spider concept system and element parameters.  $R_{sys}$  and  $R_{stage}$  define the radius of the system and stage respectively. The element span gives the maximum distance between the tip of flexure and any point along the beam. The element parameters are the

sweep angle of the flexure,  $\phi$ , the radial thickness,  $t_r$ , and the  $z$ -axis thickness,  $t_z$ . The figure also shows the system and element coordinate systems. .... 175

Figure 6.6: Spider concept stiffness ratios vs. element sweep angle,  $\phi$ . Plot shows that  $K_x/K_z = K_{\theta_z}/K_{\theta_x}$  when  $\phi = 60^\circ$ . ( $R_{sys}=3''$ ,  $R_{stage}=0.5''$ ,  $t_z=0.5''$ ,  $t_r=0.03''$ , 6061-T6 Al). .... 177

Figure 6.7: Spider concept in-plane stiffnesses vs. element sweep angle,  $\phi$ . The stiffnesses are normalized using the desired stiffness value,  $K_x\text{-desired}=1700\text{N/m}$ ,  $K_{\theta_z}\text{-desired}=2\text{Nm/rad}$ . ( $R_{sys}=3''$ ,  $R_{stage}=0.5''$ ,  $t_z=0.5''$ ,  $t_r=0.03''$ , 6061-T6 Al). .... 177

Figure 6.8: Serial spider concept design. System is composed of two spider designs connected in series. The top stage is actuated while the bottom stage is grounded. Each leg of the system is composed of two  $r$ -compliance elements connected in series. .... 178

Figure 6.9: Single plane serial spider design. The attachment angle between the serial flexures is given by  $\nu$ . The coordinate system for the input-flexure is given by  $r_i\theta_i-z_i$ , while  $r_g\theta_g-z_g$  designate the coordinate system for the ground-flexure. The dotted lines delineate the subsystem for which the analysis and optimization was performed. .... 179

Figure 6.10: Flexure attachment angle,  $\nu$ , effect on the serial spider concept subsystem in-plane stiffnesses. The stiffnesses are normalized using the corresponding stiffness value for  $\nu = 0^\circ$ .  $\nu$  must be less than or equal to  $60^\circ$  for both flexures to fit within  $R_{sys}$ . The plot corresponds to a design with  $\phi = 60^\circ$ . .... 181

Figure 6.11: Flexure attachment angle,  $\nu$ , effect on the serial spider concept subsystem stiffness ratios. The ratios are normalized using the corresponding ratio value for  $\nu = 0^\circ$ .  $\nu$  must be less than or equal to  $60^\circ$  for both flexures to fit within  $R_{sys}$ . The plot corresponds to a design with  $\phi = 60^\circ$ . .... 181

Figure 6.12: Flexure attachment angle,  $\nu$ , effect on the serial spider concept subsystem in-plane range. The ranges are normalized using the corresponding range value for  $\nu = 0^\circ$ .  $\nu$  must be less than or equal to  $60^\circ$  for both flexures to fit within  $R_{sys}$ . The plot corresponds to a design with  $\phi = 60^\circ$ . .... 182

Figure 6.13: A) Subsystem  $\Delta z$  displacement under an  $F_z$  load. FEA image shows the  $\theta_x$  and  $\theta_y$  rotations of the subsystem's stage. B) Full system  $\Delta z$  displacement under an  $F_z$  load. The system's stage does not experience a  $\theta_x$  or  $\theta_y$  rotation. .... 183

Figure 6.14: Stage attachment angle definition. The attachment angle between the stage and the input-flexure is given by  $\eta$ . .... 184

Figure 6.15: Stage attachment angle,  $\eta$ , effect on the serial spider concept subsystem in-plane stiffnesses. The stiffnesses are normalized using the corresponding stiffness value for  $\eta = 0^\circ$ . The plot corresponds to a design with  $\phi = 60^\circ$  and  $\nu = 60^\circ$ . ..... 184

Figure 6.16: Stage attachment angle,  $\eta$ , effect on the serial spider concept subsystem stiffness ratios. The ratios are normalized using the corresponding ratio value for  $\eta = 0^\circ$ . The plot corresponds to a design with  $\phi = 60^\circ$  and  $\nu = 60^\circ$ . ..... 185

Figure 6.17: CF stage first four frequency modes: A) Original design, B) Design with four radial arms, and C) Design with four arms with masses. .... 187

Figure 6.18: Final CF x-y- $\theta_z$  DPN stage prototype. System was fabricated using an abrasive water-jet. .... 188

Figure 6.19: CF x-y- $\theta_z$  DPN stage measurement setup. Six capacitance probes (1-6) are used to measure the three displacements,  $\Delta x$ ,  $\Delta y$ , and  $\Delta z$ , and three rotations,  $\theta_x$ ,  $\theta_y$ , and  $\theta_z$ , of the stage. The system is actuated by hanging masses off the stage. .... 189

Figure A.1: FEA corroboration of compliance matrix, predicted displacements under  $-0.2N F_\theta$  load vs. sweep angle,  $\phi$ . The plot compares the curved beam model to an FEA Beam Element model and an FEA 3D solid model. (L=60mm,  $t_r=6.35\text{mm}$ ,  $t_z=1\text{mm}$ , 7075Aluminum)..... 199

Figure A.2: FEA corroboration of compliance matrix, predicted displacements under  $-0.2N F_r$  load vs. sweep angle,  $\phi$ . The plot compares the curved beam model to an FEA Beam Element model and an FEA 3D solid model. (L=60mm,  $t_r=6.35\text{mm}$ ,  $t_z=1\text{mm}$ , 7075Aluminum)..... 200

Figure A.3: FEA corroboration of compliance matrix, predicted displacements under  $3.175\text{Nmm } M_z$  vs. sweep angle,  $\phi$ . The plot compares the curved beam model to an FEA Beam Element model and an FEA 3D solid model. (L=60mm,  $t_r=6.35\text{mm}$ ,  $t_z=1\text{mm}$ , 7075Aluminum)..... 201

Figure A.4: FEA corroboration of compliance matrix, predicted displacements under  $10\text{Nmm } M_r$  vs. sweep angle,  $\phi$ . The plot compares the curved beam model to an FEA Beam Element model and an FEA 3D solid model. (L=60mm,  $t_r=6.35\text{mm}$ ,  $t_z=1\text{mm}$ , 7075Aluminum)..... 202

Figure A.5: FEA corroboration of compliance matrix, predicted displacements under  $10\text{Nmm } M_\theta$  vs. sweep angle,  $\phi$ . The plot compares the curved beam model to an FEA Beam Element model and an FEA 3D solid model. (L=60mm,  $t_r=6.35\text{mm}$ ,  $t_z=1\text{mm}$ , 7075Aluminum)..... 203

Figure B.1:  $r$ -compliance element cross-section parameter definitions. The taper angle is given by  $\Psi$ . .... 205

# TABLES

---

Table 3.1: Average model error and standard deviation for each displacement.....	60
Table 3.2: Primary (PCV) and secondary compliance vectors (SCV) for a $z$ -compliance flexure. Vectors depend on the sweep angle, $\phi$ . ( $L=60\text{mm}$ , $t_r=5\text{mm}$ , $t_z=0.5\text{mm}$ , 7075 Aluminum)....	81
Table 3.3: Primary (PCV) and secondary compliance vectors (SCV) for an $r$ -compliance flexure. Vectors depend on the sweep angle, $\phi$ . ( $L=60\text{mm}$ , $t_z=5\text{mm}$ , $t_r=0.5\text{mm}$ , 7075 Aluminum)....	82
Table 3.4: Range of values used for each of the components included in the stress model parametric study.....	111
Table 5.1: FTS linear guide functional requirements. ....	149
Table 5.2: First CF linear guide prototype dimensions.....	151
Table 5.3: First CF linear guide prototype performance. <sup>+</sup> Error over 5mm range. ....	156
Table 5.4: Second CF linear guide prototype dimensions.....	159
Table 5.5: Second CF linear guide prototype performance. <sup>+</sup> Error over 5mm range. ....	165
Table 5.6: Possible sources of tip/tilt error. <sup>+</sup> Error over 5mm range. ....	166
Table 6.1: DPN $x$ - $y$ - $\theta_z$ -stage attributes. ....	171
Table 6.2: Advantages and disadvantages of the preliminary CF $x$ - $y$ - $\theta_z$ stage concepts. ....	173
Table 6.3: Final CF $x$ - $y$ - $\theta_z$ -stage element and system parameters.....	185
Table 6.4: Performance comparison for the straight-beam and CF $x$ - $y$ - $\theta_z$ -stages. ....	186
Table 6.5: CF DPN $x$ - $y$ - $\theta_z$ stage performance. ....	189



# INTRODUCTION

---

## 1.1 Synopsis

Compliant mechanisms, or flexures, guide motion through member compliance. They are powerful machine elements, because unlike rigid mechanisms they have no sliding joints therefore they do not experience stick and slip due to friction. Compliant mechanisms are prevalent in engineering because design guidelines have been developed that inform the engineer as to how to design the flexure to obtain the correct kinematics and ensure that the system achieves the desired range. No such rules exist for guiding the design of the curved-beam elements utilized in cylindrical flexures (CFs). The focus of this research is to develop the design rules and models necessary to enable to synthesis and optimization of CFs. These new flexures systems may be utilized to create more compact, lower cost solutions, which are particularly necessary for applications constrained to a cylindrical geometry.

This thesis presents the four fundamental contributions required to enable the design process for CFs: (i) analysis of element mechanics models to reveal key parameters, (ii) development of an accurate stress model to predict element and system range, (iii) understanding of how the key parameters affect the flexure performance and (iv) guidelines as to how to assemble and optimize CF systems. The impact of this work is demonstrated through two case studies, shown in Figure 1.1. The need for design rules and models is most evident when one attempts to design a CF system using the available straight-beam models and finds that they are inadequate. Without design rules the engineer is forced to rely on FEA and blind iteration. The contributions of this thesis enabled the rapid design and optimization of these CF systems, reducing the design process timeline from months to weeks.

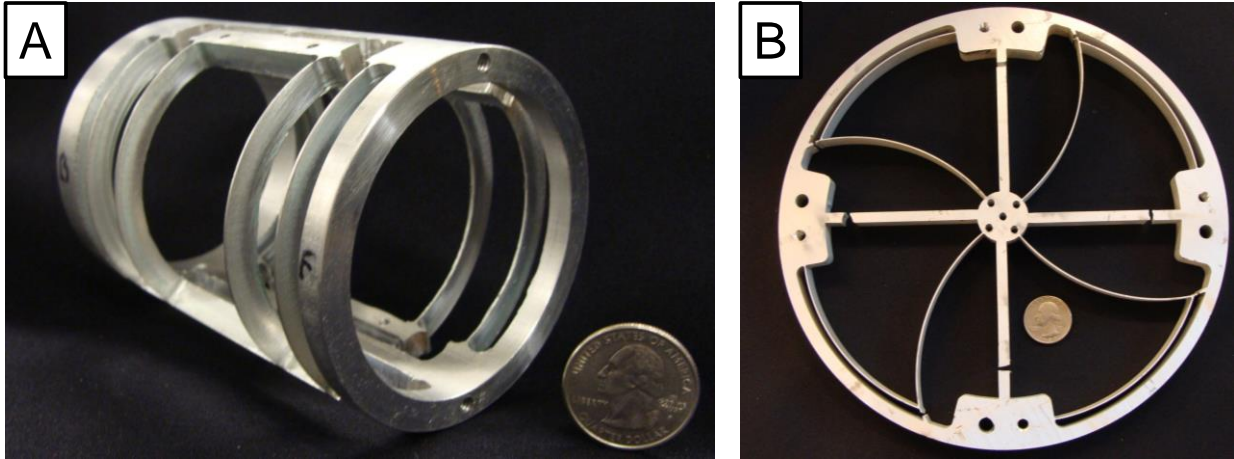


**Figure 1.1: Two cylindrical flexure system examples: (A) linear guide and (B) x-y- $\theta_z$  stage.**

## 1.2 Cylindrical Flexures

The resolution of sliding joints is limited to 100s of nanometers because of the stick-slip phenomenon, making friction bearings inadequate for precision motion applications. Flexures on the other hand can attain angstrom level resolution because they achieve motion through member compliance; therefore they do not suffer from friction. Compliant mechanisms must operate within their elastic deformation range to ensure the repeatability of the system. As a result, flexure elements must be operated below their yield stress which limits a flexure's range and load capacity [5], [6]. Another advantage of compliant mechanisms is that they can preclude assembly and fabrication costs because they can be created from a single piece of stock.

Current flexure systems are mostly planar; this limits their uses and their impact. Straight-beam flexures are common because design rules have been established which enable their effective design. However, no such rules exist for CFs, and therefore the design process is impeded. Cylindrical compliant mechanisms could fill the gaps that current planar flexures fail to meet. Some of the CF benefits include: (i) the availability of precision round stock, means reduced fabrication variations and (ii) reduced cost, (iii) compatibility with cylindrical applications, (iv) higher stability due to symmetry, (v) ease of assembly of concentric tubes, (vi) larger range to footprint ratio, and (vii) an increased design space which can lead to designs that meet currently unreachable functional requirements.



### 1.2.1 Definition

Herein I define CFs as systems with flexure elements that have only one finite radius of curvature, in other words, systems composed of flexure beams that are curved in a single plane. Figure 1.1 shows two examples of CF systems, a linear guide and an  $x$ - $y$ - $\theta_z$  stage. Chapter 5 presents how the design rules developed in this work were used to improve the performance of the CF linear guide. The conception of the curved-beam  $x$ - $y$ - $\theta_z$  stage is covered in Chapter 6. Past works have given different names to flexures that fall under the CF description. The most applicable definition is Smith's "hinges of rotational symmetry", which he characterizes as flexures constructed from solids of revolution [6]. In this work Smith's definition is expanded to allow CFs to be fractions of a solid of revolution. The thesis is scoped by constraining CFs to systems formed by elements with a single finite radius. Finally, the system must have well-defined distortions for it to be classified as a CF.

Two types of flexural blade elements may be constructed under the given CF definition. The element types, shown in Figure 1.2, are classified by their direction of least stiffness, (A)  $z$ -compliance and (B)  $r$ -compliance. The coordinate system of the element is defined at its tip using cylindrical coordinates. The length of the flexure is given by  $R\phi$ , where  $R$  is the radius of curvature and  $\phi$  defines the sweep angle of the element. The flexure's radial thickness is given by  $t_r$ , and its  $z$ -axis thickness by  $t_z$ . The two element types are differentiated by the relative magnitude of their two area moments of inertia,  $I_r$  and  $I_z$ . A  $z$ -compliance element is more compliant in the  $z$ -direction because  $I_r \ll I_z$ ; while an  $r$ -compliance CF is characterized by  $I_z \ll I_r$ .

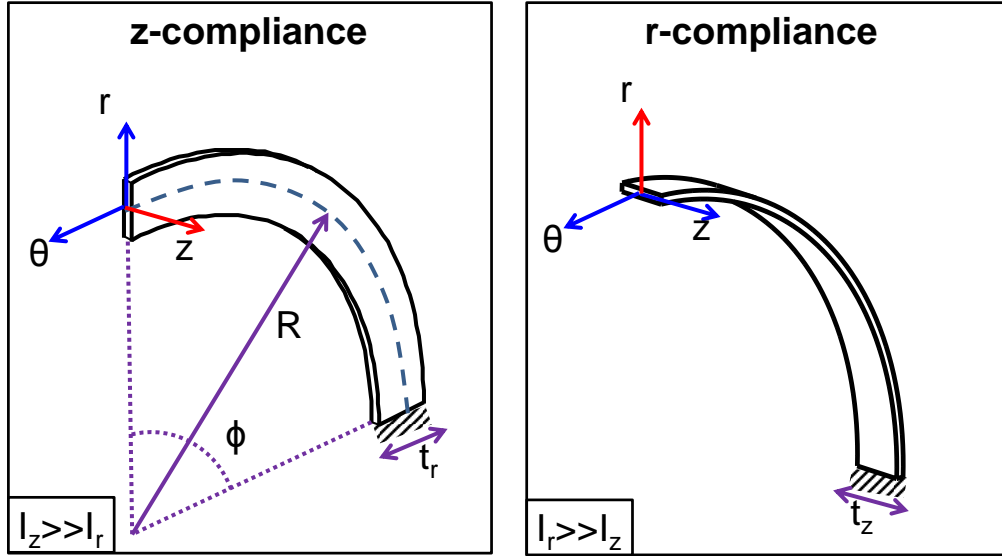


**Figure 1.2: Cylindrical flexure elements are defined by their direction of greatest compliance. Their coordinate system is given in cylindrical coordinates at the tip of the flexure. The flexure blade element is described by its radius,  $R$ , sweep angle,  $\phi$ , radial thickness,  $t_r$ , and  $z$ -axis thickness,  $t_z$ .  $Z$ -compliance elements are differentiated from  $r$ -compliance elements by the relative magnitude of their area moments of inertia.**

## 1.3 Cylindrical Flexure Challenges

### 1.3.1 Element Level Challenges

This section presents a couple of examples of how CF elements behave differently than straight-beam flexures. These differences make current design guidelines inadequate for the effective creation of CF concepts. An example of how the behavior of a curved-beam diverges from that of a straight-beam is given in Figure 1.3 [7]. The image shows the motions of a  $z$ -compliance cantilever curved beam loaded at its free-end. In this case, the desired motion is a displacement along the cylinder's axis,  $\Delta z$ . All other displacements are defined as parasitic motions. The curvature of the beam leads to two parasitic rotations,  $\alpha_r$  and  $\alpha_\theta$ , compared to one for a straight-beam flexure,  $\alpha_x$ . In addition, instead of the beam experiencing a single bending moment,  $m_x$ , the curved blade is subjected to both a bending moment,  $m_r$ , and a twisting moment,  $m_\theta$ . The straight-beam design rules give no information on the magnitude of  $\alpha_\theta$ , or how the element's curvature affects  $\Delta z$  and  $\alpha_r$ . Furthermore, the straight-beam flexure stress-model needs to be supplemented to account for  $m_\theta$ .

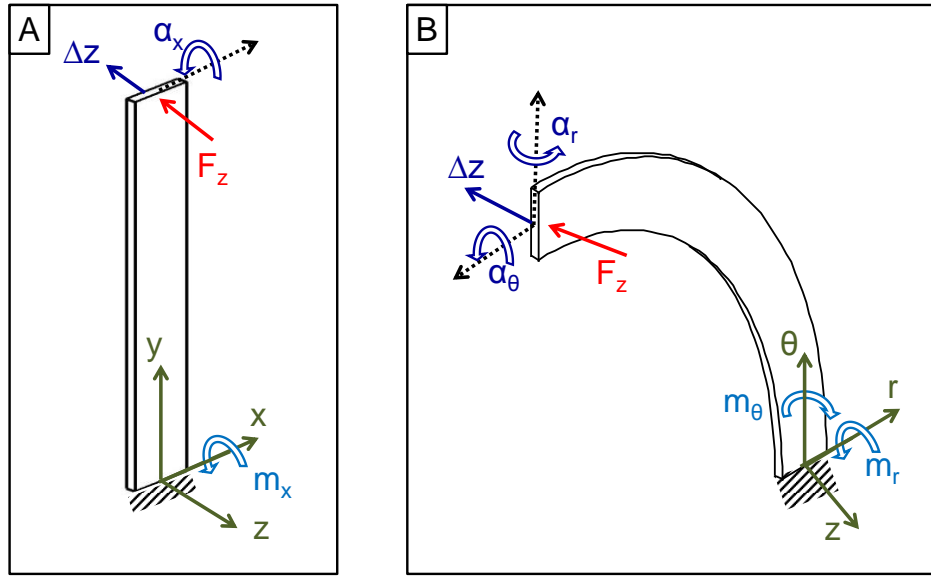


**Figure 1.3: Element level challenges. Straight-beam flexure elements (A) under a z-axis load,  $F_z$ , suffer from one parasitic rotation,  $\alpha_x$ , in addition to the desired displacement,  $\Delta z$ . The straight flexure experiences a single bending moment,  $m_x$ . Cylindrical flexure z-compliance elements (B) under a z-axis load,  $F_z$ , suffer from two parasitic rotations,  $\alpha_r$  and  $\alpha_\theta$ , in addition to the desired displacement,  $\Delta z$ . The curved beam is subjected to a twisting moment,  $m_\theta$ , and a bending moment,  $m_r$  [7].**

Planar flexure blades are characterized by having a single translational degree-of-freedom (DOF). Analysis of the kinematics of an  $r$ -compliance CF element provides another example of how the behavior of the curved-blade is different from its straight-beam counterpart. Figure 1.4 plots the ratio of  $K_r$  to  $K_\theta$  stiffnesses vs.  $\phi$  for an  $r$ -compliance element. The plot shows that for  $\phi > 123^\circ$  the stiffness of the blade along the  $\theta$ -axis is less than its  $r$ -stiffness. In fact, at  $\phi = 122.56^\circ$   $K_r = K_\theta$ , which means that the CF blade has two translational DOF. In order to capture the kinematics of the  $r$ -compliance element using straight-beam models, the curved-beam would have to be approximated as a series of two straight-blades attached at  $90^\circ$ . The analytical models in this thesis present a more accurate way to model the behavior of the  $r$ -compliance curved blade.

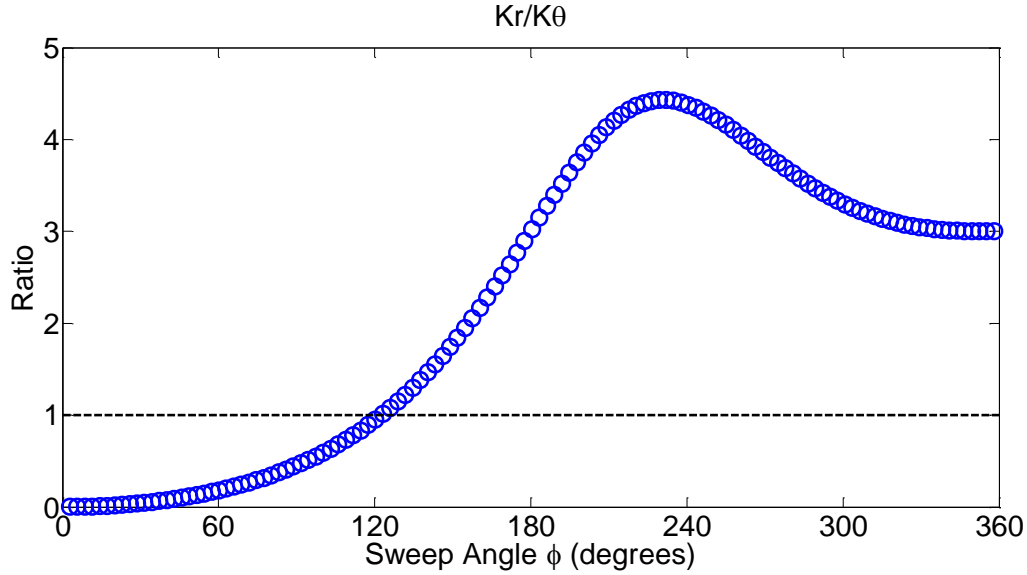


**Figure 1.4: Sweep angle effect,  $\phi$ , on the ratio of  $r$ -axis stiffness,  $K_r$ , to  $\theta$ -axis stiffness,  $K_\theta$ , for an  $r$ -compliance element. The graph shows that the ratio is larger than 1 for  $\phi > 123^\circ$ , indicating that beyond that sweep angle the flexure can no longer be considered a  $\theta$ -axis constraint.**

### 1.3.2 System Level Challenges

The curvature of the flexure beams also leads to challenges in the assembly of CF systems. The need for system creation rules is demonstrated by analyzing the behavior of a curved compound four-bar system [7]. A planar compound four-bar, shown in Figure 1.5a, is an example of a parallel and a serial flexure system. The mechanism utilizes two nested four-bar flexure systems to increase the range of the system and mitigate the parasitic displacement,  $\Delta y_I$ , of the input stage as shown in Figure 1.5a. The  $\Delta y$  motion of the floating stage cancels the  $\Delta y$  of the input stage. The nesting of the four-bars also reduces the parasitic rotation,  $\alpha_x$ , of the input stage. In the curved compound four-bar system, shown in Figure 1.5b, the floating and input stages are located on different planes due to the curvature of the beams. As a result of the location of the stages the parasitic displacements,  $\Delta r_I$  and  $\Delta \theta_I$ , of the input stage are not directly cancelled by the  $\Delta r$  and  $\Delta \theta$  of the floating stage.

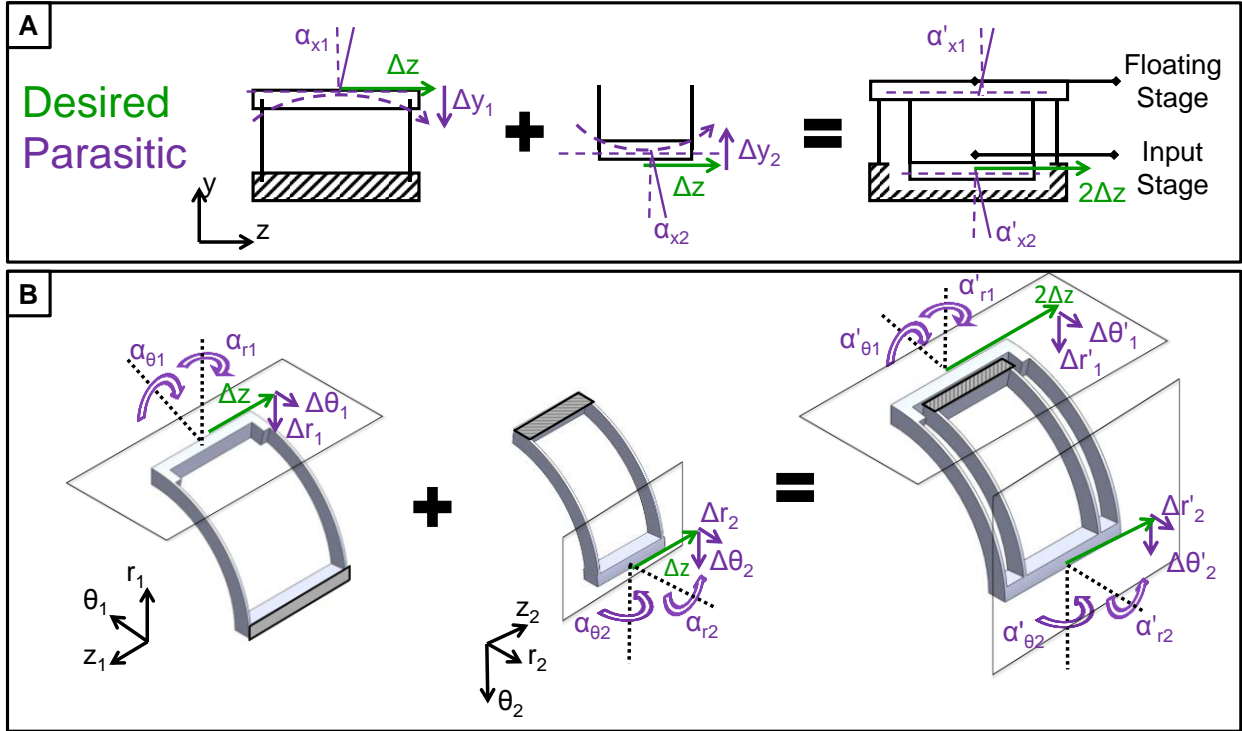


**Figure 1.5: A) A Straight-beam compound four-bar system nests two four-bars to remove the y-axis parasitic displacement of the input stage,  $\Delta y$ , while increasing the range of the system,  $\Delta z$ . The nesting also reduces the parasitic rotation of the each of the stages,  $\alpha_x$ . B) In a curved compound four-bar the input and floating stages are located on different planes, as a result the parasitic displacements of the input stage,  $\Delta r$  and  $\Delta \theta$ , are not directly cancelled by the nesting. The parasitic rotations of the two stages,  $\alpha_r$  and  $\alpha_\theta$ , are also affected by the nesting. The range of the system is increased [7].**

The mitigation of the parasitic rotations of the input stage,  $\alpha_{r1}$  and  $\alpha_{\theta1}$ , is also not straight forward. For example, in the case where  $\phi=90^\circ$  the  $\alpha_r$  of the floating stage corresponds to a  $\alpha_\theta$  of the input stage and vice versa. This leads to having to manage eight parasitic motions (four for each stage) on two different planes. The matter of mitigating these motions is no longer clear; the rules that have been established for straight-beam systems are inadequate for CFs. This work presents models and guidelines that enable the efficient design of curved parallel and serial CF systems like the curved compound four-bar.

### 1.3.3 Stress Concentration

In order to determine the range of a system both the displacement under a given load and the resulting stress must be considered. The curvature of a z-compliance element leads to a

twisting moment on the fixed end of the cantilever beam. This moment will affect the resulting stress calculation. Using energy conservation principles it can be identified that an added twisting moment requires that there be a decrease in the original resulting bending moment. Both of these effects will change the magnitude and distribution of the stress along the beam. Figure 1.6 shows that a stress concentration is observed at the base on the inner radius of the z-compliance curved element [7]. The stress model for the straight-beam flexure does not predict the stress concentration and therefore underestimates the stress level in the deflected beam. A stress model for the curved-beam flexure needs to be developed to ensure the accurate assessment of the range of the CF.

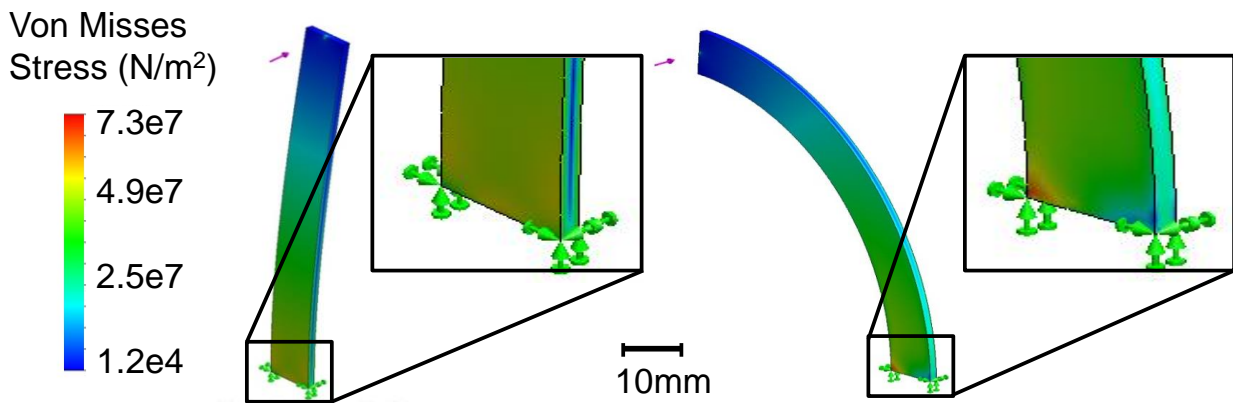


**Figure 1.6: A) Resulting VonMises stress on a straight-beam flexure compared to the stress of a curved-beam flexure of the same dimensions under the same loading. The figure shows that the curved beam experiences a stress concentration at the inner radius. This stress concentration has to be captured by the stress model to ensure the designer calculates the maximum stress on the beam [7].**

## 1.4 Design Process

The main steps of the engineering design process are summarized in Figure 1.7. First the designer must establish the functional requirements for the system. Once the requirements have been formulated the next step is to generate possible concepts that would meet those needs. This step is often called preliminary design because the designer is generating abstract embodiments of a possible concept; at this point time should not be spent on figuring out all the details for the different ideas. The sketched concepts should then be analyzed and the most promising design selected. Now detailed engineering of the selected design may begin [8], [9]. The concept generation phase of the process is particularly important to ensure that the designer is

considering different solutions and continuing with the least limiting design. During the detailed design step the selected concept is optimized given a set of criteria. Finally, once the design is complete the system can be fabricated.

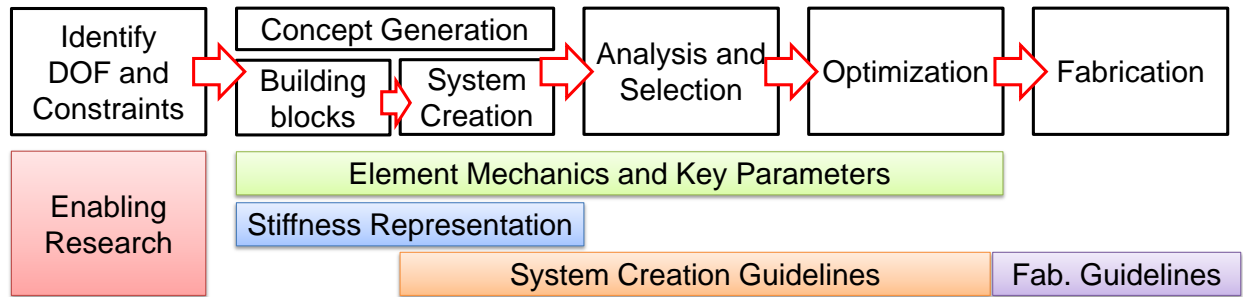


**Figure 1.7: Simplified design process flowchart followed by the research components necessary to enable the design process for cylindrical flexure systems.**

Design rules play a significant role in the compliant mechanism design process. In planar flexure design the generation of concepts is facilitated by using guidelines that establish the degrees-of-freedom (DOF) and constraints of a flexure element. This knowledge allows the designer to quickly layout different compliant elements to achieve the desired system motions. The straight-beam design rules are used in the concept analysis and selection phase to establish order of magnitude estimates of parasitic motions and range to footprint ratios. These assessments are used to efficiently compare the performance of a concept relative to the other ideas. Once the most promising concept has been selected the straight-beam models provide the engineer with the knowledge required for the effective optimization of the concept. Optimization can be a tedious process if the designer does not understand the effect of the different flexure parameters on the system performance metrics.

Section 1.2 established that the current straight-beam flexure design rules and models are insufficient for the successful design of CFs. The lack of design guidelines restricts the CF design process. Figure 1.7 summarizes the research that must be conducted to enable the design process. Foremost, the kinematic behavior of a curved-beam element has to be understood and modeled. The analytical models may then be used to characterize the effect of different parameters on the behavior of the beam. The parameters that differentiate the behavior of the curved-beam from that of a straight-beam must be identified as key parameters. The concept

generation phase of the design process will be facilitated by establishing the stiffness ratios for a flexure. The stiffness ratios establish the DOF and constraints of a compliant element; therefore they enable the layout of the beam elements required to achieve the desired system motions. The layout of the elements also requires the use of system creation rules which establish how the elements behave in serial and parallel systems. Finally, fabrication guidelines need to be developed to ease the manufacturing of CF systems. This work establishes the pieces of knowledge required to enable the design process for CFs. Chapter 3 presents the curved-beam design rules and models, as well as an analysis of the stiffness ratios of the two types of CF elements. The system creation guidelines are given in Chapter 4. Two case studies were used to help guide the work; they are presented in Chapters 5 and 6. Helpful fabrication tips are presented in the context of the creation of the two CF system prototypes.

## **1.5 Advantages of Cylindrical Flexures**

Cylindrical flexures present compatibility, geometry, and manufacturability advantages over planar flexure systems. CF's most attractive quality is their compatibility with applications that benefit from a cylindrical geometry, for instance rotating systems, optical mechanisms, and laparoscopic tools. The axial symmetry of cylindrical systems may be used to achieve thermocentricity, and it serves to decrease the effects of manufacturing and load placement errors. Monolithic CF systems can be created out of a single piece of round stock reducing assembly cost and errors. The cylindrical geometry may also serve to reduce the footprint and therefore the volume of the system. Figure 1.8 compares the volume of a planar system (A) to the cylindrical version of the system (B). The wrapping of the beams reduces the footprint of the system and as a result its volume. Chapters 3 and 4 will demonstrate that CF systems may achieve a greater range to footprint ratio than its planar counterparts. Furthermore the use of concentric cylinders facilitates the assembly of the overall system into a compact design, as shown in Figure 1.9.



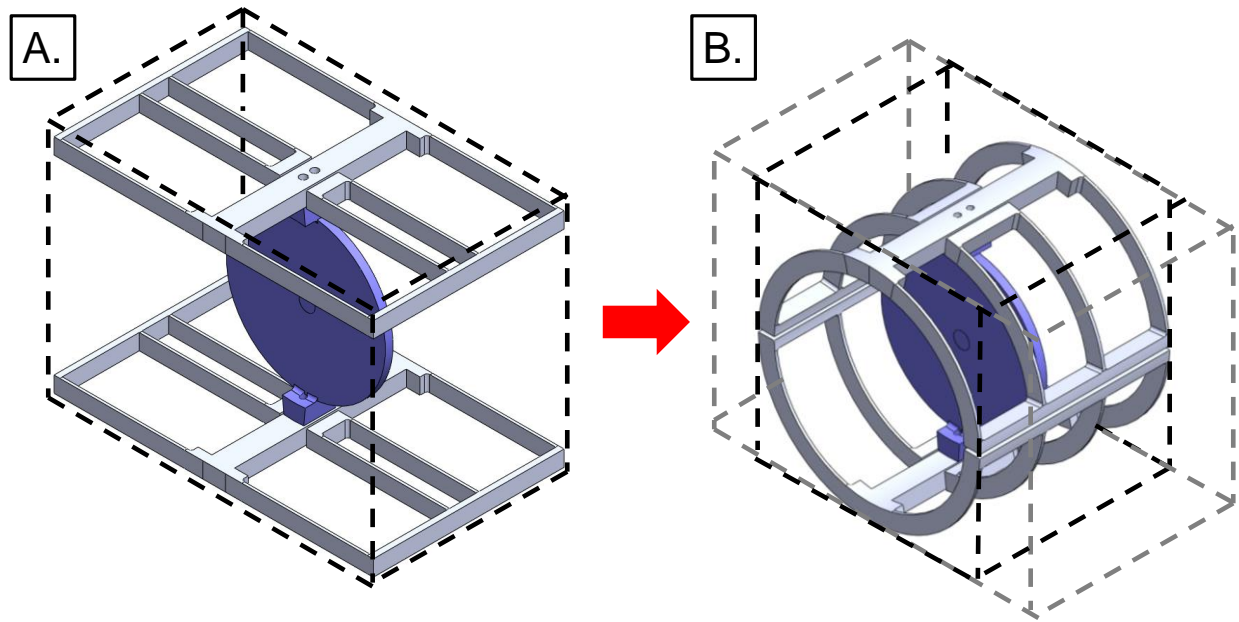


**Figure 1.8: Comparison between the straight-beam version of a system (A) and its cylindrical flexure counterpart (B). Cylindrical flexures can lead to a more compact design. The wrapping of the beams leads to footprint and volume reductions.**

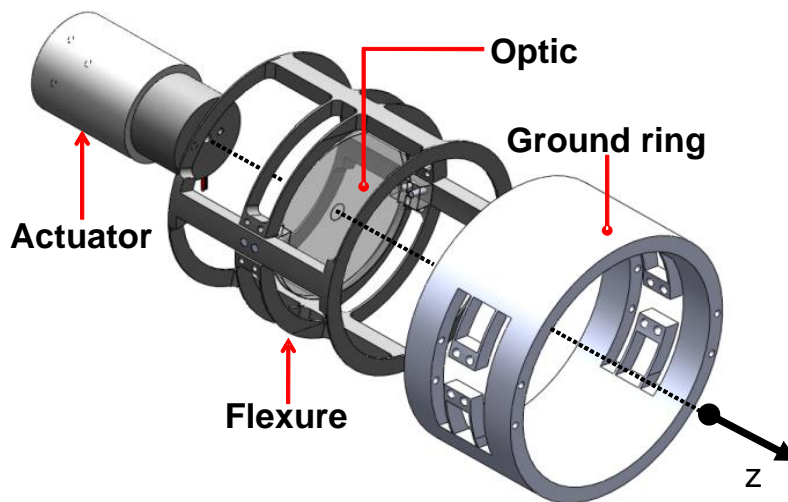


**Figure 1.9: Assembly of concentric cylinders allows for a compact system design [10].**

CF fabrication is facilitated by the availability of accurate round stock. CFs can be manufactured at low cost by using traditional machining methods such as a 4<sup>th</sup> axis lathe, 5-axis mill, and a laser cutter or abrasive water-jet with a rotary axis. Figure 1.10 shows images of three manufacturing techniques that may be used to fabricate CFs. The first is the Mazak turning

center which was used to machine the CF linear guide in Figure 1.1a. Next is an abrasive water-jet with a rotary axis. The rotary axis for a water-jet provides a low-cost, low-stress way of manufacturing the CF systems. Finally, the last image shows a cylindrical linear guide that was constructed using a 3D printer. 3D printers provide a way to assess different CF concepts; however, the printed flexures are unsuitable for precision applications because of creep.

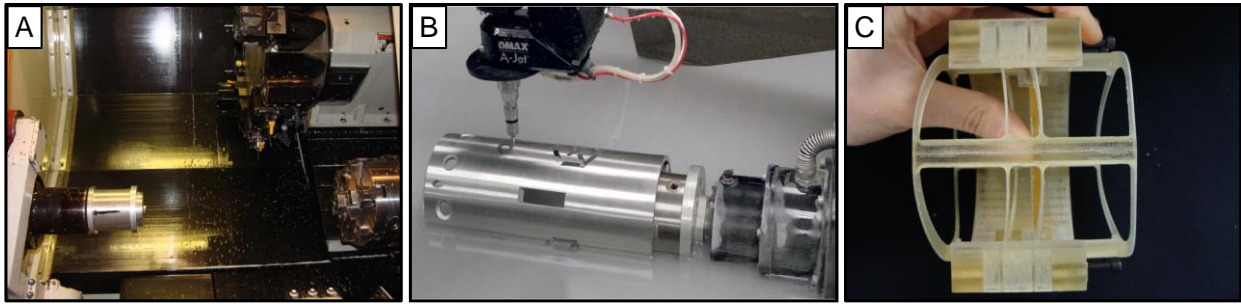


**Figure 1.10: Cylindrical flexures can be fabricated using a variety of methods including: A) Lathe with actuated tool (Turning center), B) abrasive water-jet with a rotary axis [11], and C) 3Dprinter.**

Machining of precision flexure systems presents a challenge due to the vibrations induced by the tool on the thin flexure systems. The tradeoff is that flexure performance improves with reduced flexure thickness, but the ease of fabrication declines as the thickness decreases. This thesis presents ways on how to support the stock during machining to minimize vibrations [12], [13]. An exciting area of future research that new 5-axis machines enable is the contouring of the beams of the cylindrical flexure. Previous work has shown contouring to be a successful way to distribute stress along the length of a beam [14]. By contouring the CF's beams at different locations, the stress concentrations on the beam may be reduced and as a result the range of the system may be increased.

## 1.6 Compliant Mechanisms Synthesis Approaches

The chief compliant mechanism synthesis approaches to this date are topology synthesis, pseudo-rigid-body modeling, and exact-constraint design. Figure 1.11 outlines the three schools of thought in compliant mechanism synthesis. Topology synthesis designs compliant mechanisms through computer iteration of the design parameters [15]. The software takes the

users designate design domain and break it up into a set of nodes, which are connected to form beam elements. The computer uses FEA to identify which nodes to add or remove to meet the user specified objective function, such as maximizing output deflection for a specified input load while minimizing the mean compliance under other loading conditions. Once the general layout of the beam elements has been identified the software iterates on the different beam parameters to maximize the objective function and/or meet a secondary constraint such as minimizing weight. The iterative loop is performed until the software is able to reach convergence and the result is a design that has been optimized to meet the user's objective functions [15]. The challenge with topology synthesis is that the designer is unaware of the design trade-offs. As a result the user is unable to assess how different parameters affect the performance and will have to re-run the program if any functional requirement changes. Another difficulty is that all functional requirements need to be specified as objective functions and ranked such that the system can optimize to the most important requirement [16]. This synthesis approach limits the rapid concept generation of the design process, for an objective function the computer will find the optimal design.

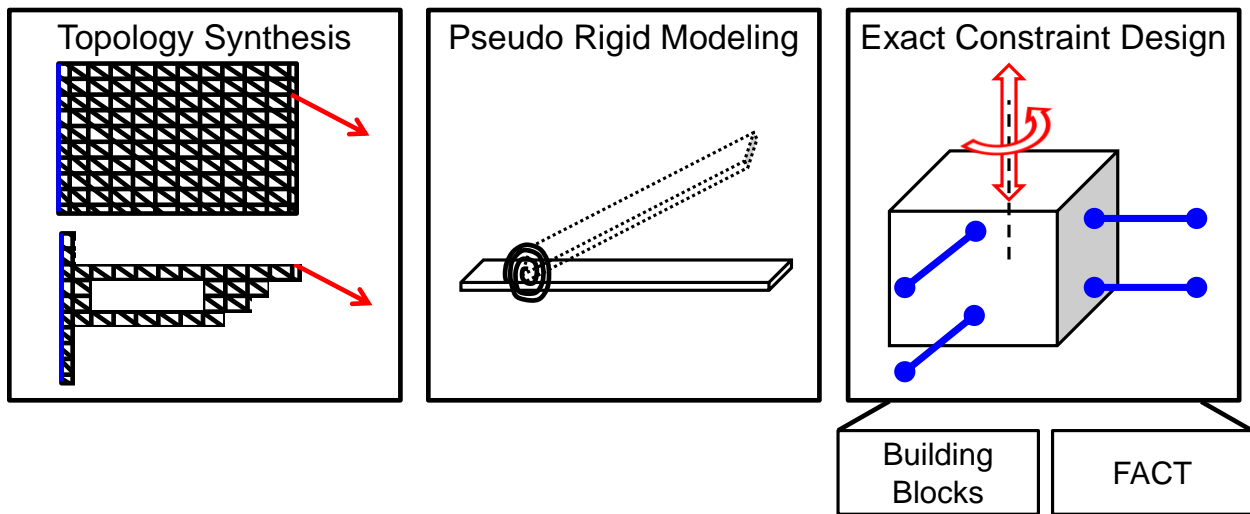


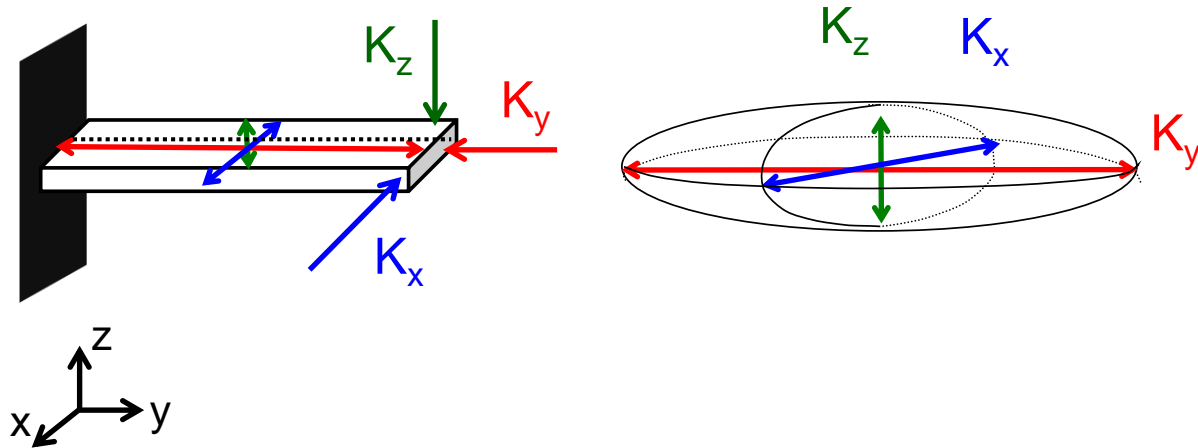
**Figure 1.11: Common flexure synthesis approaches include: topology synthesis, pseudo-rigid-body modeling, and exact constraint design. The building block approach and FACT are based on the exact constraint design methodology.**

Pseudo-rigid-body modeling creates a rigid-link representation of a compliant mechanism in order to utilize common rigid-linkage models to analyse the kinematics of the flexure system

[17]. In the pseudo-rigid-body model the flexure's compliance is simulated by connecting two rigid links with a spring mechanism. The stiffness of the springs is set by the flexure's compliance. Once the compliant mechanism has been modelled as a set of springs and links the designer can use rigid-link tools to analyse and optimize the performance of the system. The pseudo-rigid-body model is very powerful if the compliant mechanism is accurately represented as a rigid system, in order to do this the kinematics of the flexure need to be well-understood.

The foundation for exact-constraint design is that the permitted motions or degrees-of-freedom (DOF) of a rigid-body are dictated by the constraints placed on the body [18], [19]. A rigid-body without any constraints has six DOF: three translations and three rotations. Exact-constraint dictates that the number of DOF of a body is equal to six minus the number of independent constraints. In using exact-constraint design in compliant mechanisms the designer must be able to identify the constraints imposed by a flexure linkage on the rigid-body. This process is facilitated by the use of building blocks. Building blocks are flexural elements or subsystems whose kinematics are well-understood. The designer can assemble these building blocks to create more complex systems relying on established series and parallel system rules [20][21].

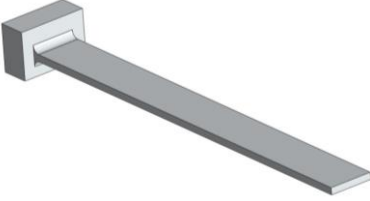
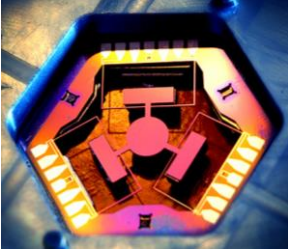


The challenge with flexures is that all of their DOF have a finite stiffness; therefore the challenge becomes how to establish if the flexure acts as a constraint in a particular direction. One way to differentiate constraints from DOF is by looking at the ratio of their stiffnesses. For example in the beam shown in Figure 1.12 the  $K_y$  stiffness is orders of magnitude greater than the  $K_z$  stiffness, as a result the beam is considered a  $\Delta y$ -constraint. Compliance or stiffness ellipsoids facilitate this analysis by providing a visual representation of the stiffness ratios [22], [23]. The stiffness ellipsoid in Figure 1.12 illustrates the relative magnitude of the stiffnesses allowing the designer to quickly identify  $K_z$  as the lowest stiffness; given  $K_x \gg K_z$  the flexure blade element has  $\Delta z$  as a DOF. The ellipsoid is a characterization of the kinematics of the flexure element [23].



**Figure 1.12: Stiffness Ellipses are a visual representation of stiffness ratios. The relative lengths of the ellipse axis are representative of the magnitude of the stiffness ratio.**

A new synthesis approach Freedom Actuation and Constraint Topologies (FACT) proposes using freedom, constraint, and actuation topologies to design any flexure system [24], [25]. FACT utilizes the principles of exact-constraint based design and the mathematics of screw theory to create visual spaces for where constraints should be placed to achieve the desired DOF. The design process is enhanced by FACT because it presents the designer with a quick way to consider all possible constraint locations.

A building block approach derived from constraint based design principles is proposed as the most appropriate synthesis methodology for CFs at this stage. The plan is to first develop a full understanding of the parameters that affect the element's behavior. This element then becomes a building block for CF systems. The next step is to develop rules for how these blocks interact when assembled together. The desired outcome of the research consists of (i) models that allow the designer to quickly understand how different parameters will affect the behavior of an element, and (ii) design guidelines for the assembly of CF systems. Figure 1.13 gives element and system examples for planar and CF systems.

	Element	System
Planar		 [16]
Curved		

**Figure 1.13: Planar and CF element and system examples.**

A constraint based design approach has been chosen because it is intuitive for precision engineers. This synthesis approach presents a quick way to determine how a system created from a set of building blocks will behave. Building blocks make the rapid concept generation phase of the design process very efficient as the designer can use the stiffness representations and system rules to quickly lay out the elements required to achieve a desired performance, while being able to account for external constraints such as manufacturing. The knowledge gathered through the development of these building block rules can then be used to create arguments for the other synthesis methods.

## 1.7 Thesis Overview

The first step in the building block approach is to understand the flexure element mechanics. Chapter 3 begins by establishing the 6-DOF compliance ( $1/\text{stiffness}$ ) matrix for a curved-beam element. Once the matrix has been established we identify the effect of different parameters on the performance on the flexure. Section 3.7 presents an analysis of the performance sensitivity to fabrication tolerances of key parameters. Chapter 3 continues on to

explore the effect of boundary conditions and input load location on the performance metrics. This analysis is important because the assembly of elements into systems will impose different end-conditions on the tips of the flexures and will affect the location of the load relative to the element. In order to calculate the curved-beam's range an accurate stress model had to be developed. Chapter 3 concludes with a new stress model specific for  $z$ -compliance elements. The system creation guidelines describe the interaction between the element building blocks. These rules enable the designer to assemble the blocks together to achieve a desired system performance. Chapter 4 utilizes two flexure systems to help establish the system creation guidelines. The chapter covers the effect of system parameters on the performance metrics of parallel and serial systems.

### **1.7.1 Flexure Performance Metrics**

The challenge is to find a set of flexure performance metrics that characterize the CF and provide useful insight as to what parameters can be used to alter its kinematics. To this end, this thesis establishes the effect of different parameters on the CF's (i) stiffness ratios, (ii) parasitic ratios, and (iii) the ratio of range to footprint. Stiffness ratios are used to differentiate the flexure's DOF from its constraints. These ratios provide a quantitative measure of the stiffness ellipses introduced in section 1.5. A mechanism will have desired motions and undesired motions known as parasitics. Figure 1.14 shows the desired and parasitic motions for a straight-beam four-bar. In precision mechanism design the goal is to minimize the ratio of parasitic to desired displacement. Precision engineering applications require high accuracy flexure systems, microns of parasitic motion can cause a design to fail. Finally, considering only the range of a flexure mechanism can be deceiving because it gives no information on the size of the system. A better measure of the CF's performance is the ratio of its range to its radius. This ratio gives information on the range of the system relative to its footprint.

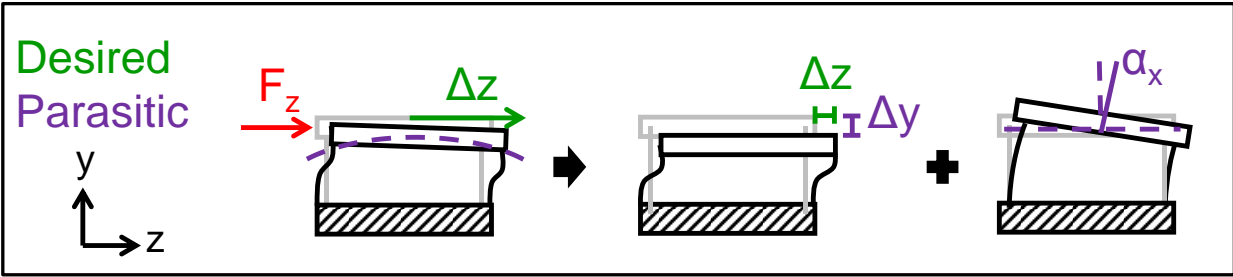


**Figure 1.14:** The arc displacement of a straight four-bar is the result of the sum of two parasitic displacements (purple),  $\Delta y$  and  $\alpha_x$ , in addition to the desired displacement (green),  $\Delta z$ . A parasitic displacement is an undesired displacement.

## 1.7.2 Case Studies

Two case studies were used to help guide the development of the design rules and to demonstrate their applicability. The first case involves the design of a precision linear guide flexure mechanism to be used to translate an optic in a Fourier Transform Spectrometer (FTS). The final design, shown in Figure 1.15, is fabricated out of a single aluminum tube and is composed of  $z$ -compliance curved-beam elements. Chapter 5 details the shortcomings of creating a CF linear guide using straight-beam flexure design rules. The CF rules and guidelines presented in this work were then used to redesign the linear guide. The redesign achieved an order of magnitude lower parasitic ratio compared to the original CF prototype.

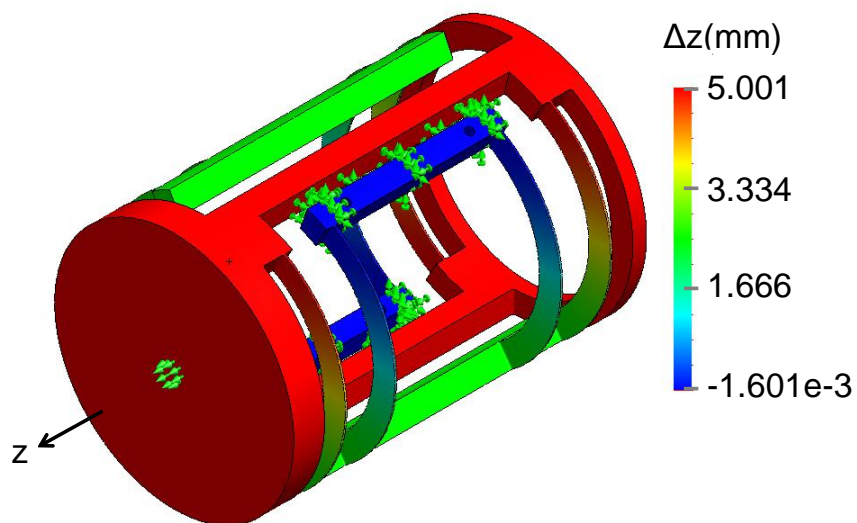


**Figure 1.15:** CAD model depicting the actuation of the final CF linear guide design.



Chapter 6 presents the design of a CF x-y- $\theta_z$  stage. The goal of this case study was to demonstrate the usability of the design rules during the creation of a CF with  $r$ -compliance elements. To ensure that the guidelines developed in this thesis would be useful to other engineers the design of the x-y- $\theta_z$  stage was led by Laura Matloff, an undergraduate student working in the PCSL lab on her senior thesis [26]. The author worked with the student to create the final design shown in Figure 1.16. Chapter 6 details the use of the design guidelines during the design process.

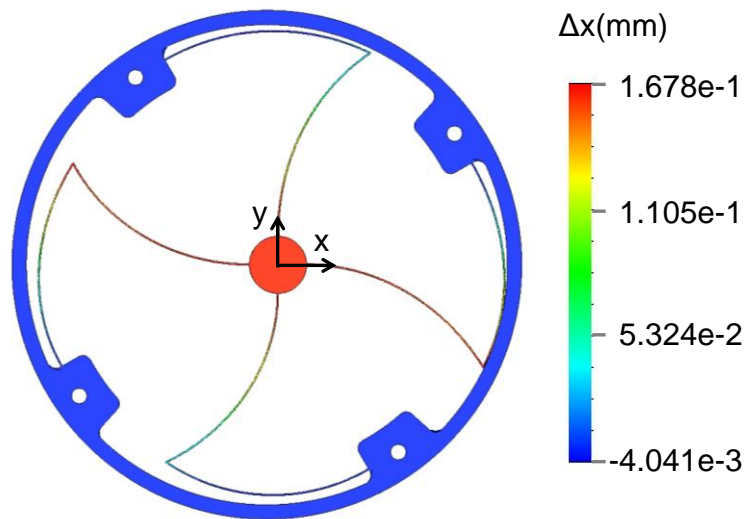


**Figure 1.16:** CAD model depicting the  $\Delta x$  actuation of the CF x-y- $\theta_z$  stage.



Past work that pertains to CFs has focused on two areas: (i) models for curved beams and (ii) the analysis of specific CF concepts. Detailed models for the design of structural curved-beams have been developed since the early 1900s [1],[2]. These structural beam models are used as the foundation for the modeling of the kinematics of CF flexures. The design of compliant mechanisms differs in two major aspects from that of structural beams: (i) in flexures the design seeks to maximize the deflection of the element, and (ii) parasitic motions are significant in the performance of precision compliant mechanisms. As a result of these two differences, structural models do not provide a designer with guidelines as to how to use curved flexures to achieve a set of functional requirements. This work will extract, from these analytical models, clear rules for the design of CF elements and systems.

## 2.1 Curved-Beam Models

The kinematics of a curved-beam are usually calculated using Castigliano's second theorem. Timoshenko utilizes the theorem to establish the deflection equations for curved-beams loaded in and out of the plane of curvature [1]. The in-plane loading condition corresponds to an  $r$ -compliance CF element, while a  $z$ -compliance element is actuated out-of-plane. Roark presents equations for both types of loading with different boundary conditions [27]. The formulas for the kinematics of curved elements can be compiled to create the stiffness or compliance matrix for the element. Martin presents the compliance matrix for the 3-DOF of a curved-beam loaded along its plane of curvature, while others have expanded the matrix to include all 6 DOF [2–4].

A more recent compliant curved-beam model is Kim et al.'s curved beam building block (CBB) [23]. The CBB is introduced as a building block for the creation of flexure systems. The publication focuses on creating a systematic way of assembling compliant mechanisms composed of both straight and curved beams. The authors present the compliance ellipsoids as a way of capturing the behavior of the building blocks; however, little information is given on what determines the kinematics of the beam. In their work the analysis of the CBB compliance ellipsoid is limited to in-plane motions. This work seeks to expand on the analysis of the curved-beam building block by capturing all 6-DOF, providing an in-depth examination of the effects of beam's parameters, and extracting clear guidelines on the design and optimization of CF systems.

## **2.2 Examples of Flexures with Curved Beams**

The other area of prior art pertains to the analysis of specific systems that fit within the CF definition. Smith presents a detailed analysis of the disk coupling and the rotationally symmetric hinge, shown in Figure 2.1 [6]. The examination of these two CF examples includes an exploration as to how different flexure parameters affect the behavior of these systems. Others have developed diaphragm flexures designs composed of curved-beams [28], [29], [30]. Figure 2.2 shows Awtar and Slocum's single-DOF linear bearing design. The difficulty with diaphragms is that they need to be assembled into systems; as a result, diaphragm flexures are burdened by assembly error and cost. The analysis of specific CF designs, such as these three examples, has produced useful flexure systems; however, there has been little overarching insight developed that could be used to create new CF concepts. In addition, in many cases the analysis of these systems has relied on FEA to determine the system's range. In some cases CF systems with flexures with a small sweep angle have been successfully designed using straight-beam models [31].

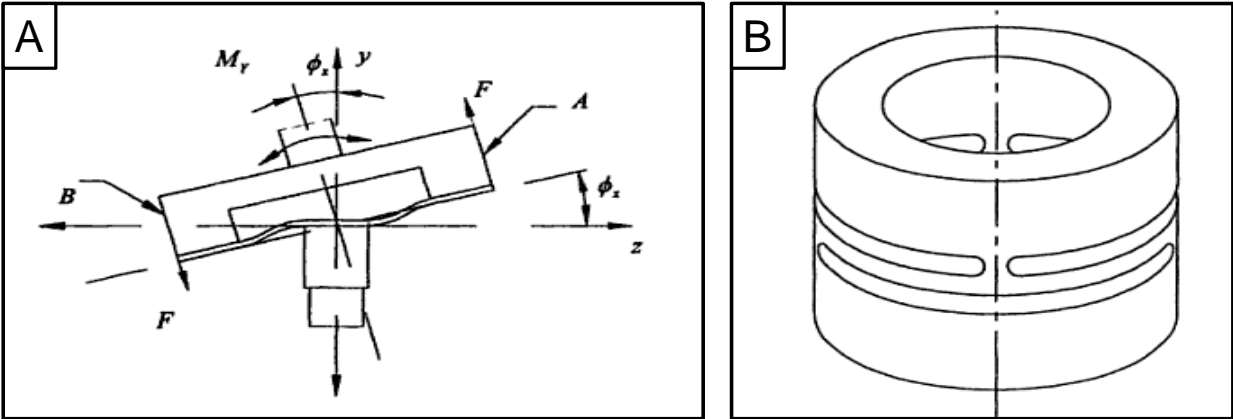


**Figure 2.1: Examples of Smith's hinges of rotational symmetry: A) Disk coupling and B) Rotationally symmetric hinge [6].**

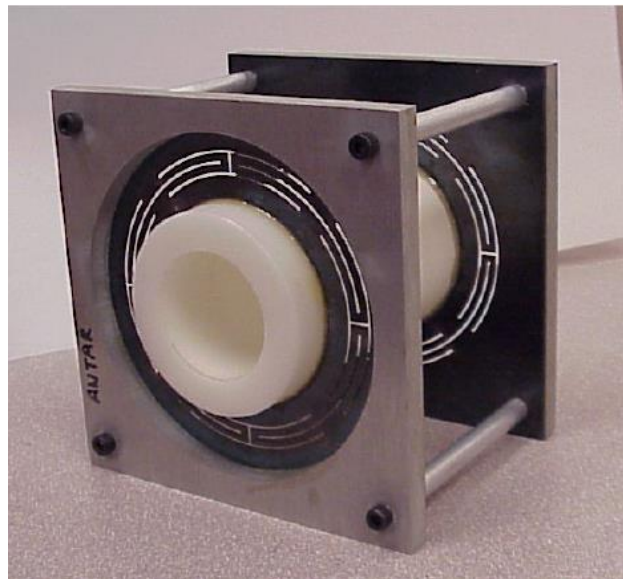


**Figure 2.2: Awtar and Slocum's diaphragm single DOF linear bearing [28].**

## 2.3 Technology Gap

Figure 2.3 summarizes the prior art knowledge and highlights the work necessary to enable the design process for CF systems. The current lack of design guidelines has restricted the design process which is apparent in the limited use of cylindrical flexures. The detailed analysis of specific CF examples has resulted in useful systems; however, the knowledge generated has not been generalized to help guide the design of new mechanisms. This work takes a step back and begins by creating guidelines for the design and optimization of the CF elements. The

system design rules presented in chapter 4 enable the use of these elements as building blocks for CF systems.

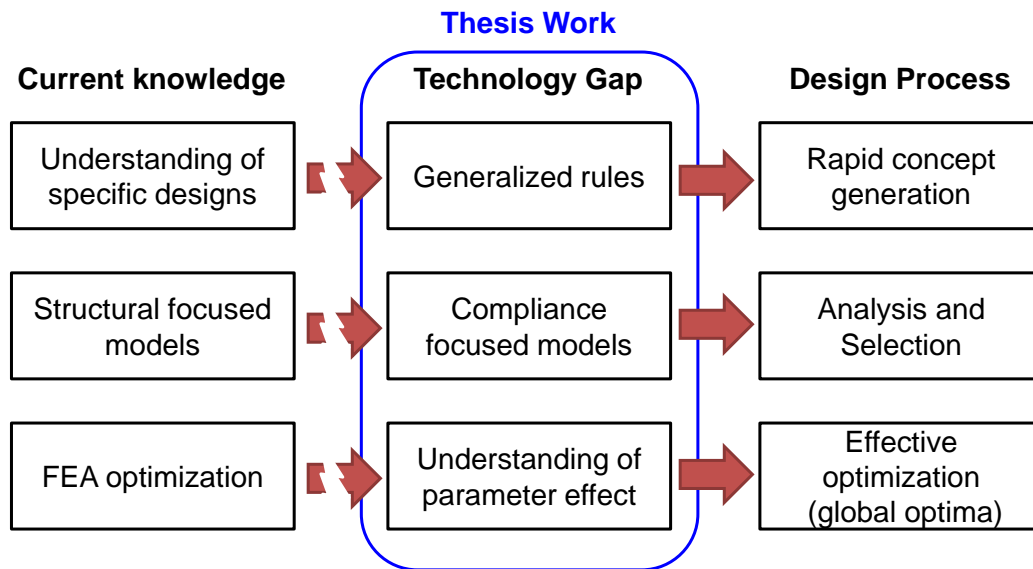


**Figure 2.3: Chart shows the current knowledge available on curved-beams and the technology required to enable the design process for cylindrical flexures. This thesis fills the technology gap which has prevented cylindrical flexures from becoming prevalent.**

An understanding of the effect of different parameters on the performance of a curved-beam is necessary during the analysis, selection, and optimization of CF concepts. This work utilizes the available analytical models to quantify the effect of the element and system attributes on the flexure’s performance metrics. Furthermore, this thesis identifies the parameters that differentiate the kinematics of a curved-beam flexure from those of a straight flexure. The identification of the differentiating parameters allows for the compliance matrix of the CF element to be presented as a function of the straight-beam equations. This presentation of the matrix allows the engineer to utilize their straight-flexure knowledge during the design of curved-beam flexures. Throughout the analysis of the CF elements and systems this thesis highlights the advantages and drawbacks of utilizing curved-beams over straight-beams.

# 3

## ELEMENT RULES AND MODELS

---

### 3.1 Element description

The first step in the building block approach is to understand the flexure element mechanics. The goal is to identify what the effect of different parameters is on the element's performance. The element's mechanics are described by its compliance matrix. The compliance matrix,  $[C]$ , relates the displacements and rotations,  $\Delta$  and  $\alpha$ , of the beam to the forces and moments,  $F$  and  $M$ , applied on the element, as shown in equation (3.1). In order to define the compliance matrix, it is necessary to establish the coordinate system for the matrix. The compliance matrix used in this thesis describes the six-DOF for the tip of a fixed-free curved-beam element. Figure 3.1 shows the coordinate system for the two types of CF elements, and establishes the positive direction for all displacements, rotations, forces, and moments.

$$\begin{bmatrix} \Delta\theta \\ \Delta r \\ \Delta z \\ \alpha_\theta \\ \alpha_r \\ \alpha_z \end{bmatrix} = [C] \begin{bmatrix} F_\theta \\ F_r \\ F_z \\ M_\theta \\ M_r \\ M_z \end{bmatrix} \quad (3.1)$$

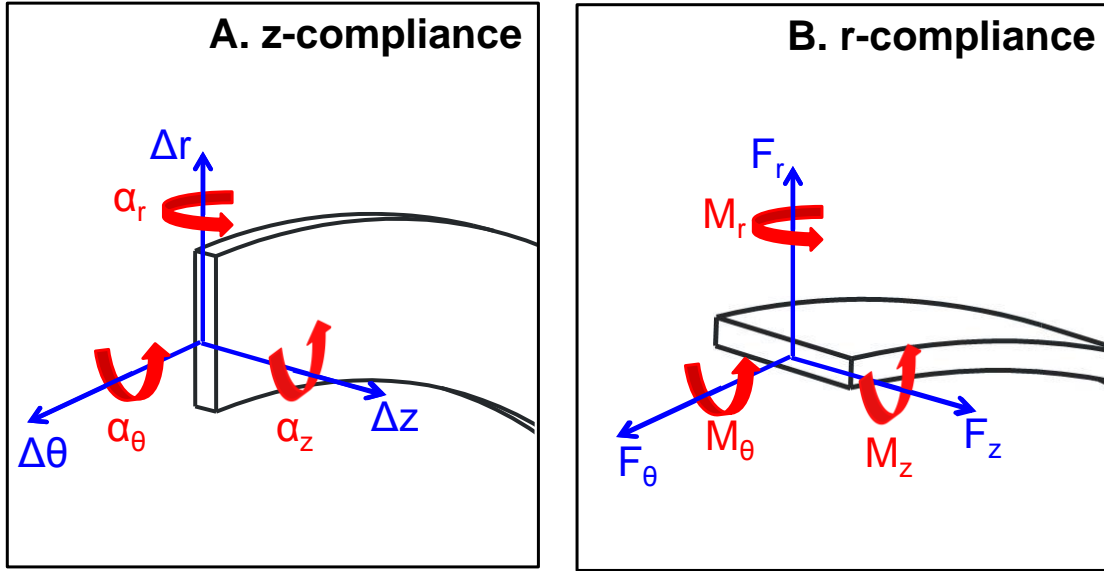


**Figure 3.1: Flexure element coordinate systems. Figure defines the direction of positive displacements, rotations, as well as the direction of positive loads and moments.**

## 3.2 Compliance Matrix

The foundation for the element analysis and optimization is the compliance matrix,  $[C]$ , for a CF element, given in Equation (3.3). The matrix has been derived from previous works [1–3], [27]. The compliance matrix of an element is established using Castigliano’s Second Theorem for displacements of a linearly elastic structure. The theorem states that a displacement,  $q_i$ , in the direction of the generalized force,  $Q_i$ , is given by the partial derivative of the strain energy,  $U$ , with respect to  $Q_i$ . Equation (3.2) expresses Castigliano’s Second Theorem. The analysis consists of establishing the strain energy resulting from all possible loading conditions and then taking the partial derivative with respect to each load [3]. It is important to note that the matrix accounts for the curvature of the beam element when establishing the strain energy resulting from a loading condition; however, the analysis does not consider that the beam’s length is shorter at the inner radius compared to the length at the outer radius. The effect of this omission is analyzed in section 3.2.1.

$$q_i = \frac{\partial U}{\partial Q_i} \quad (3.2)$$

The presented compliance matrix, which is the inverse of the stiffness matrix, corrects errors in previous works. The last row of the matrix is erroneously reported in Martin [2]. The



matrix has been corrected so that each entry has the correct units. In the compliance matrix,  $I_z$  and  $I_r$  correspond to area moment of inertia about the z-axis and r-axis respectively.  $L$  corresponds to the length of the beam, which in curved beams is defined by the product of the  $R$  and  $\phi$  as shown in Equation (3.4).  $\beta$  is the ratio of the bending to torsional properties of the beam as defined in Equation (3.5).  $E$  is the modulus of elasticity and  $G$  is shear modulus.  $k_t$  is the torsional stiffness constant for a given cross-section. Equation (3.6) gives  $k_t$  for a rectangular beam, where  $a$  and  $b$  are the lengths of the two sides of the rectangle [27]. For a z-compliance element  $t_r$  is greater than  $t_z$  and therefore corresponds to  $a$  ( $t_r=a$ ), similarly for an r-compliance beam  $a$  corresponds to  $t_z$  ( $t_z=a$ ).

$$[C] = \begin{bmatrix} \zeta_{11} \frac{L^3}{3EI_z} & \zeta_{12} \frac{L^3}{3EI_z} & 0 & 0 & 0 & \zeta_{16} \frac{L^2}{2EI_z} \\ \zeta_{21} \frac{L^3}{3EI_z} & \zeta_{22} \frac{L^3}{3EI_z} & 0 & 0 & 0 & \zeta_{26} \frac{L^2}{2EI_z} \\ 0 & 0 & \zeta_{33} \frac{L^3}{3EI_r} & \zeta_{34} \frac{L^2}{2EI_r} & \zeta_{35} \frac{L^2}{2EI_r} & 0 \\ 0 & 0 & \zeta_{43} \frac{L^2}{2EI_r} & \zeta_{44} \frac{L}{EI_r} & \zeta_{45} \frac{L}{EI_r} & 0 \\ 0 & 0 & \zeta_{53} \frac{L^2}{2EI_r} & \zeta_{54} \frac{L}{EI_r} & \zeta_{55} \frac{L}{EI_r} & 0 \\ \zeta_{61} \frac{L^2}{2EI_z} & \zeta_{62} \frac{L^2}{2EI_z} & 0 & 0 & 0 & \zeta_{66} \frac{L}{2EI_z} \end{bmatrix} \quad (3.3)$$

$$\zeta_{11} = \frac{3}{\phi^3} (1.5\phi - 2 \sin 2\phi + .25 \sin 2\phi)$$

$$\zeta_{12} = \zeta_{21} = \frac{3}{\phi^3} (\cos \phi + (.5 \sin \phi)^2 - 1)$$

$$\zeta_{16} = \zeta_{61} = \frac{2}{\phi^2} (\phi - \sin \phi)$$

$$\zeta_{22} = \frac{3}{\phi^3} (0.5\phi - 0.25 \sin 2\phi)$$

$$\zeta_{26} = \zeta_{62} = \frac{2}{\phi^2} (\cos \phi - 1)$$

$$\zeta_{33} = \frac{3}{\phi^3} [\phi(1.5\beta + .5) - 2\beta \sin \phi + \sin \phi \cos \phi (.5\beta - 1)]$$

$$\zeta_{34} = \zeta_{43} = \frac{2}{\phi^2} [\beta \sin \phi - .5(\beta + 1) + .5 \sin \phi \cos \phi (1 - \beta)]$$

$$\zeta_{35} = \zeta_{53} = \frac{2}{\phi^2} [\beta(1 - \cos \phi + .5 \sin^2 \phi) + .5 \sin^2 \phi]$$

$$\zeta_{44} = \frac{1}{\phi} [.5\phi(\beta + 1) + .5 \sin \phi \cos \phi (\beta - 1)]$$

$$\zeta_{45} = \zeta_{54} = \frac{1}{\phi} [(\beta - 1).5 \sin^2 \phi]$$

$$\zeta_{55} = 1/\phi [ .5\phi(\beta + 1) + .5\sin\phi \cos\phi (1 - \beta) ]$$

$$\zeta_{66} = 2$$

$$L = R \cdot \phi \quad (3.4)$$

$$\beta = \frac{EI_r}{Gk_t} \quad (3.5)$$

$$k_t = ab^3 \left[ \frac{1}{3} - .21\frac{b}{a} \left( 1 - \frac{b^4}{12a^4} \right) \right], \text{ for } a \geq b \quad (3.6)$$

In the past some authors have presented the 3x3 compliance matrices for curved elements separately because of the sparsity of the full 6x6 matrix [1], [2], [27]. The matrix in Equation (3.3) shows that there is essentially two separate matrices: one relates the loads  $F_\theta$ ,  $F_r$ , and  $M_z$  to the displacements  $\Delta\theta$ ,  $\Delta r$ , and  $\alpha_z$ , these loads have no effect on the other three displacements; the other matrix relates the loads  $F_z$ ,  $M_\theta$ , and  $M_r$  to the displacements  $\Delta z$ ,  $\alpha_\theta$ ,  $\alpha_r$ , with no effect on the other three displacements. The full 6x6 compliance matrix is presented because it describes the loading conditions of both types of CFs. The full matrix also allows the designer to analyze the effect of all extraneous loads on the performance of the flexure element.

### 3.2.1 Corroboration with FEA

The compliance matrix for a CF element was corroborated using ADINA finite element analysis (FEA). The analytical results were compared to the results from (i) a FEA model consisting of 10 straight beam elements in series and (ii) a 3D solid FEA model. An example of each of the two FEA models is shown in Figure 3.2. The matrix was corroborated for each of the six loading conditions. Figure 3.3 shows the displacements due to  $F_z$  calculated by the two FEA models, and compares them to the predicted analytical values. The rest of the corroboration plots are given in Appendix A. The error between the analytical model and the FEA models was calculated for each sweep angle, Table 3.1 gives the maximum error and standard deviation of the errors for all sweep angles. The beam model does not account for the difference in beam length between the inner radius and the outer radius, while the 3D solid model does. A 3D solid model is more accurate but it would be too inefficient to use in the design process.

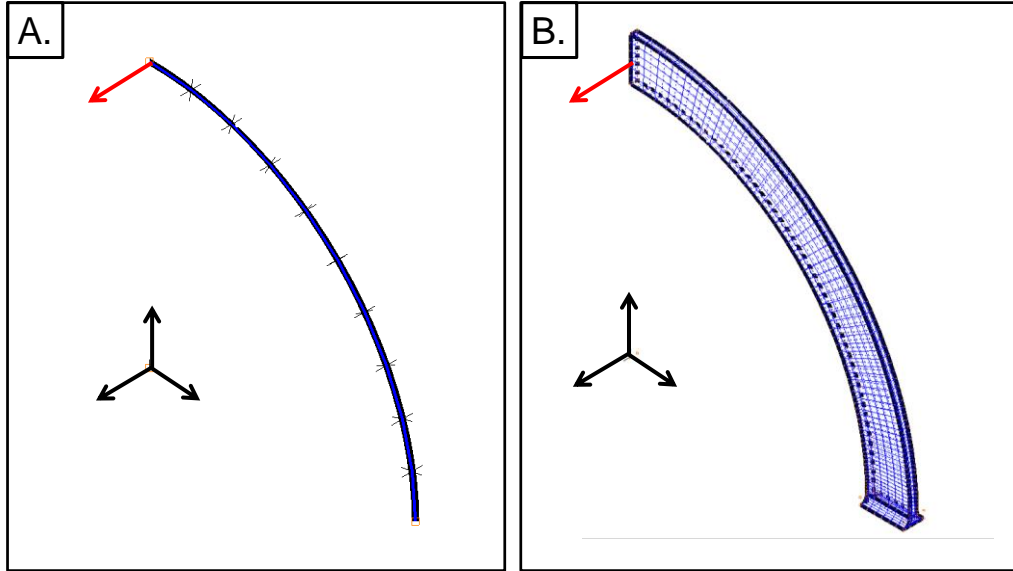


**Figure 3.2: ADINA Finite Element Models used to corroborate the analytical compliance matrix. A) FEA model created using 10 straight beam elements in series to represent the curved beam element. B) 3D solid model.**

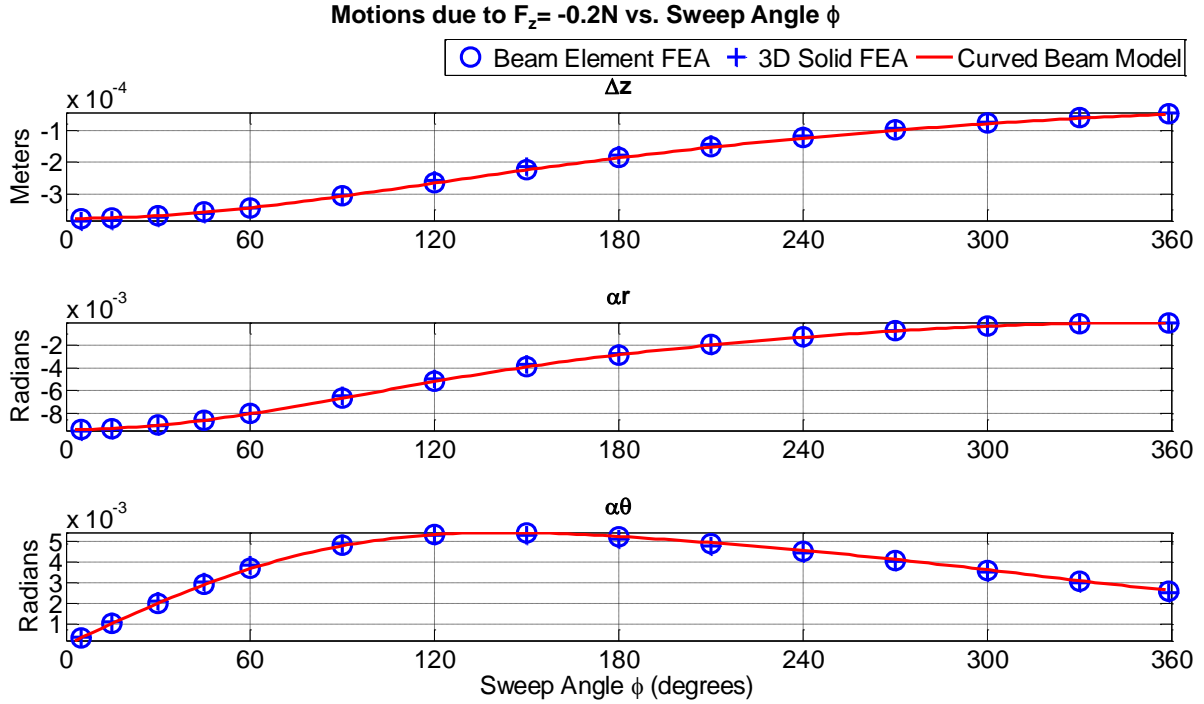


**Figure 3.3: FEA corroboration of compliance matrix, predicted displacements under  $-0.2N$   $F_z$  load vs. sweep angle,  $\phi$ . The plot compares the curved beam model to an FEA Beam Element model and an FEA 3D solid model. ( $L=60\text{mm}$ ,  $t_r=6.35\text{mm}$ ,  $t_z=1\text{mm}$ , 7075Aluminum).**

**Table 3.1: Average model error and standard deviation for each displacement**

Load	Motion	Average Model Error (standard deviation)		Notes
		3D Solid Model FEA	Beam Model FEA	
$F_\theta$	$\Delta\theta$	11.0% (17.1%)	6.3% (18.3%)	
	$\Delta r$	11.7% (26.8%)	5.0% (25.5%)	Max error $\Delta r \rightarrow 0$
	$\alpha_z$	3.1% (1.2%)	-0.3% (0.8%)	
$F_r$	$\Delta\theta$	10.9% (25.9%)	5.0% (25.5%)	Max error $\Delta\theta \rightarrow 0$
	$\Delta r$	3.9% (1.3%)	-1.2% (1.5%)	
	$\alpha_z$	8.3% (24.8%)	-0.7% (2.3%)	Max errors as $\alpha_z \rightarrow 0$

$F_z$	$\Delta z$	-3.7% (4.3%)	-1.2% (1.5%)	
	$\alpha_r$	4.5% (25.1%)	-0.1% (2.3%)	Max errors as $\alpha_r \rightarrow 0$
	$\alpha_\theta$	0.2% (3.9%)	-0.5% (0.7%)	
$M_\theta$	$\Delta z$	0.1% (3.9%)	-0.4% (0.8%)	
	$\alpha_r$	-39.1% (207.3%)	10.0% (24.9%)	Max errors as $\alpha_r \rightarrow 0$
	$\alpha_\theta$	-1.3% (1.3%)	-0.5% (0.5%)	Max errors as $\Delta z \rightarrow 0$
$M_r$	$\Delta z$	4.2% (25.7%)	5.8% (24.9%)	
	$\alpha_r$	-3.9% (1.7%)	-0.5% (0.6%)	
	$\alpha_\theta$	35.7% (115%)	5.6% (27.8%)	Max errors as $\alpha_\theta \rightarrow 0$
$M_z$	$\Delta \theta$	2.9% (1.3%)	-0.3% (0.8%)	
	$\Delta r$	2.7% (26.6%)	-0.7% (2.3%)	Max error $\Delta r \rightarrow 0$
	$\alpha_z$	4.6% (0.4%)	-0.5% (0.6%)	

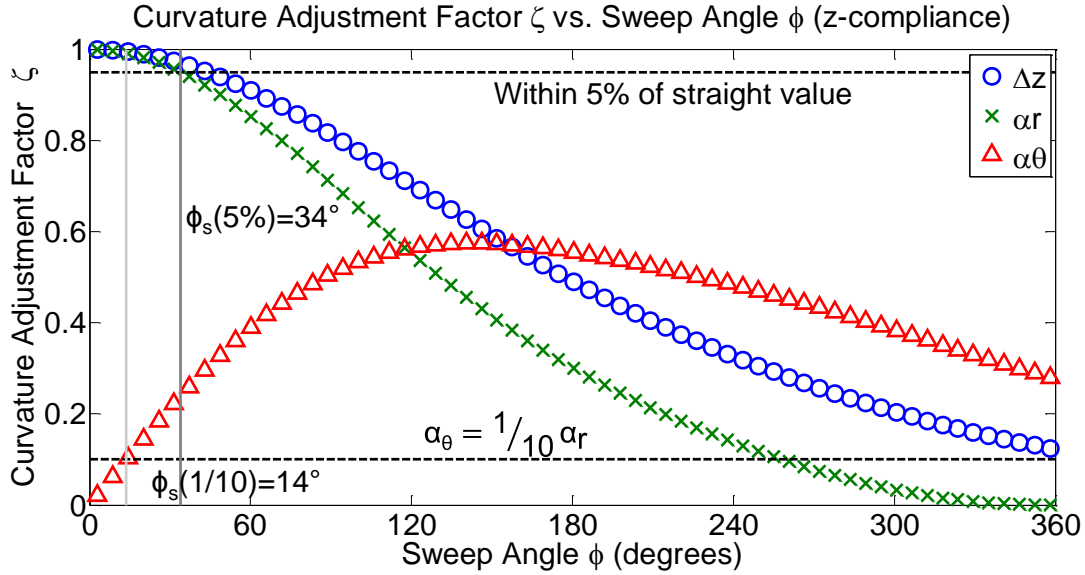
Once the compliance matrix for a CF element has been established and corroborated the next step is to extract useful information from the matrix to help establish design rules for CFs. The design rules need to provide the designer with tips on how different parameters will affect the flexure's performance. The first thing that needs to be established is what differentiates the performance of a curved-beam from that of a straight-beam. Then, the effect of these parameters on the different flexure performance metrics can be studied.

### 3.3 Curvature Adjustment Factor

Each entry of the compliance matrix in Equation (3.3) is factored into two components: (i) the straight-beam equation and (ii) a curvature adjustment factor,  $\zeta$  [7]. The matrix is presented in this manner because it allows the engineer to transfer their previous knowledge

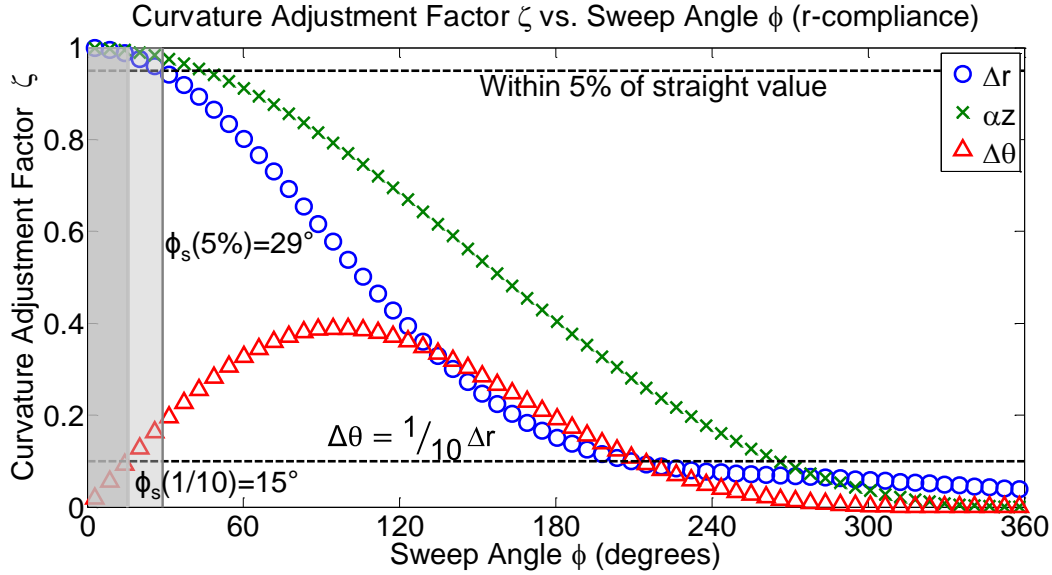
pertaining to straight-beam flexures towards analyzing the performance of CFs. This factorization also reveals that the two parameters that cause the kinematics of the curved-beam to differ from those of a straight beam are  $\phi$ , and  $\beta$ . This matrix allows the engineer to design a CF using his previous knowledge of straight-beam equations supplemented with an understanding of the effect of  $\phi$ , and  $\beta$ .

Figure 3.4 presents the effect of sweep angle on the curvature adjustment factors for a  $z$ -compliance element. The plot shows that as  $\phi$  approaches zero the curved beam behaves like a straight-beam:  $\zeta_{Az}$  and  $\zeta_{ar}$  approach 1 and  $\zeta_{a\theta}$  approaches zero because straight flexures do not have a  $\alpha_\theta$  parasitic motion. As the sweep angle increases the behavior of the CF deviates from the behavior of a straight-beam flexure. This analysis can be taken a step further to establish a maximum sweep angle,  $\phi_s$ , for when the straight-beam approximation is good enough to model the behavior of the curved-beam. The value for  $\phi_s$  can be established using a variety of performance metrics. For example, Figure 3.4 shows that for  $\phi \leq 34^\circ$  the value of the desired displacement,  $\Delta z$ , and dominant parasitic rotation,  $\alpha_r$ , will be within 5% of the value calculated using the straight-beam model. If the designer is most concerned with the new parasitic motion,  $\alpha_\theta$ , then the limit for  $\phi_s$  can be set for  $14^\circ$  when  $\alpha_\theta < 0.1\alpha_r$ .



**Figure 3.4: Curvature adjustment factors,  $\zeta$ , vs. Sweep Angle,  $\phi$ , for a z-compliance flexure. The plot shows that as the sweep angle approaches zero the curved-beam behaves like a straight-beam. The curvature adjustment factor can be used to define the value of sweep angle below which a beam can be modeled as a straight beam,  $\phi_s$ . Below  $\phi=34^\circ$  the value of the two dominant displacements,  $\Delta z$  and  $\alpha_r$ , are within 5% of the straight-beam value. While for  $\phi < 14^\circ$  the additional parasitic rotation,  $\alpha_\theta$ , is less than  $1/10^{\text{th}}$  the value of the dominant parasitic motion,  $\alpha_r$ .**

Similarly, Figure 3.5 presents the effect of sweep angle on the curvature adjustment factors for an  $r$ -compliance element. In this case the desired displacement of the CF and straight flexure is  $\Delta r$ . As  $\phi$  approaches zero, the two curvature adjustment factors for the two displacements associated with a straight-beam,  $\zeta_{\Delta r}$  and  $\zeta_{\alpha_z}$ , approach 1 and  $\zeta_{\Delta \theta}$  for the additional parasitic displacement goes to zero. The plot also shows that the straight-beam model may be used to calculate  $\Delta r$  and  $\alpha_z$  within 5% if  $\phi \leq 29^\circ$ . If  $\Delta \theta$  is a concern then below  $\phi = 15^\circ$  the value of  $\Delta \theta$  will be an order of magnitude smaller than the value of  $\Delta r$ .



**Figure 3.5: Curvature adjustment factors,  $\zeta$ , vs. Sweep Angle,  $\phi$ , for an  $r$ -compliance flexure. The plot shows that as the sweep angle approaches zero the curved-beam behaves like a straight-beam. The curvature adjustment factor can be used to define the value of sweep angle below which a beam can be modeled as a straight beam,  $\phi_s$ . Below  $\phi=29^\circ$  the value of the two dominant displacements,  $\Delta r$  and  $\alpha_z$ , are within 5% of the straight-beam value. While below  $\phi=15^\circ$  the additional parasitic displacement,  $\Delta\theta$ , is less than  $1/10^{\text{th}}$  the value of the dominant parasitic displacement,  $\Delta r$ .**

## 3.4 Sweep angle and beta parameter effect

### 3.4.1 Sweep angle, $\phi$

The factorization of the compliance matrix revealed that the sweep angle of a CF element affects the kinematics of the beam. In analyzing the effect of the sweep angle, it is important to keep the length of the element constant so as to explore only the additional effect of  $\phi$ . The length of the beam plays the same role in the curved element kinematics as it does in determining the behavior of a straight-flexure. Therefore, in the sweep angle analysis the length of the flexure,  $R\phi$ , is held constant to allow us to analyze the additional effect of  $\phi$  on the performance of the flexure. As  $\phi$  is increased,  $R$  decreases to maintain the same length. Figure 3.6 visually compares fixed length beams with different sweep angles. The sweep angle gives an additional design tuning knob and as a result creates a larger design space for CF elements as compared to the design space for straight-beam flexures. This new tuning knob may be used to create a design



that meets a set of functional requirements that cannot be met using straight-beam compliant elements.

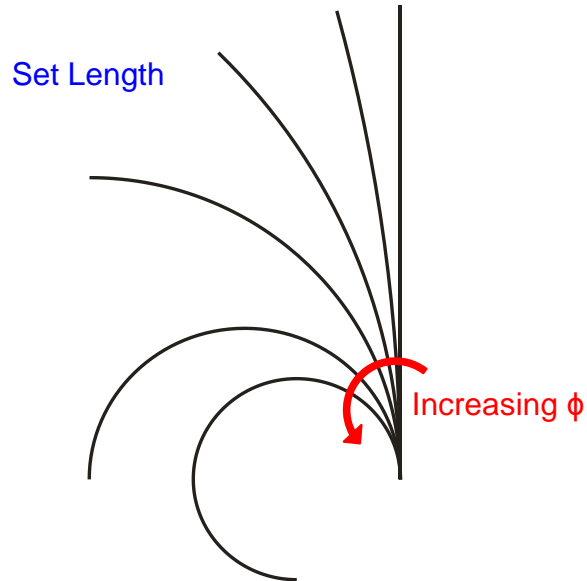


**Figure 3.6: Fixed length flexures with increasing sweep angle,  $\phi$ .**

### 3.4.2 Beta parameter, $\beta$

In a CF the ratio of elastic to shear properties of a beam,  $\beta$ , is important because the curvature of the element results in the application of both a bending,  $M_r$ , and twisting moment,  $M_\theta$ , when  $F_z$  is applied. As shown in Equation (3.5),  $\beta$  depends on the geometry of the beam,  $I_z$  and  $k_t$ , and the material properties of the beam,  $E$  and  $G$ . A material's  $E$  and  $G$  are related by Poisson's ratio, which is approximately 0.3 for most metals in their elastic regime. Given the majority flexures are constructed out of metal the analysis in this thesis focuses on the effect of the beam's cross-section on  $\beta$ . Specifically, the effect of taper angle,  $\Psi$ , defined in Figure 3.7a, on the performance of the flexure. Taper angle may be a direct result of the manufacturing method, e.g. abrasive water-jet cutting, or may be imposed during machining. The formulas for  $I_r$  and  $I_z$  for a trapezoid in terms  $\Psi$  are given in Equations (3.7) and (3.8) [27]. Two different formulas are used for  $k_t$  depending on whether the taper angle affects the cross-section's longer side, typically  $z$ -compliance elements, or its shorter side, typically  $r$ -compliance flexures. Roark provides Equation (3.9) which gives the torsional stiffness constant for a  $z$ -compliance CF,  $k_{t-zcomp}$ . The  $k_t$  for an  $r$ -compliance trapezoid was calculated by taking the torsional stiffness constant of a rectangle, (3.6), and adding the torsional stiffness constant of two right triangles

using the parallel axis theorem. The resulting equation for  $k_{t-rcomp}$  for an  $r$ -compliance flexure is given by (3.10). Appendix B gives the details on how (3.10) was calculated.

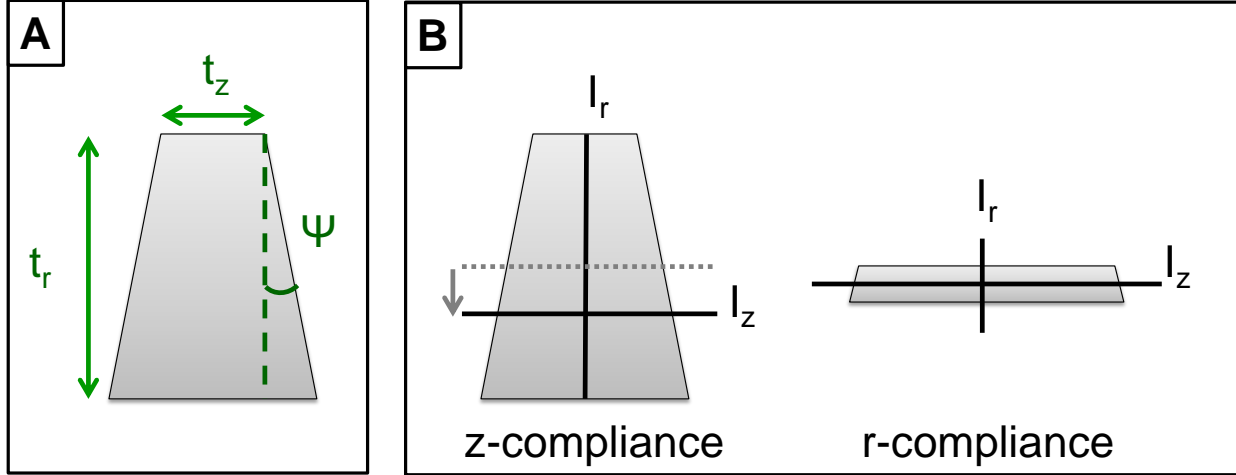


**Figure 3.7: A) Flexure beam cross-sectional area indicating the taper angle,  $\Psi$ , or deviation from the desired rectangular cross-section. B) Location of bend axis of the area moments of inertia,  $I_z$  and  $I_r$ , of a  $z$ -compliance element and an  $r$ -compliance element. The taper angle shifts the location of the bend axis of  $I_z$ .**

$$I_z = \frac{t_r^3}{36} \cdot \frac{d^2 + 4dt_z + t_z^2}{d + t_z} \quad (3.7)$$

$$c = t_r \sin \Psi, d = t_z + 2c$$

$$I_r = \frac{t_r}{36(b + t_z)} [d^4 + t_z^4 + 2dt_z(d^2 + t_z^2) - c(d^3 + 3d^2t_z - 3dt_z^2 - t_z^3) + c^2(d^2 + 4dt_z + t_z^2)] \quad (3.8)$$

$$k_{t-zcomp} = \frac{t_r}{12} (d + t_z)(d^2 + t_z^2) - V_L d^4 - V_S t_z^4$$

$$V_L = 0.10504 - 0.1s + 0.0848s^2 - 0.06746s^3 + 0.0515s^4 \quad (3.9)$$

$$V_S = 0.10504 + 0.1s + 0.0848s^2 + 0.06746s^3 + 0.0515s^4$$

$$s = d - t_z/t_r$$

$$k_{t-rcomp} = k_{t-rectangle} + 2k_{t-triangle} + 2 \left\{ A_{triangle} \cdot \left[ \left( \frac{t_z}{2} + \frac{c}{3} \right)^2 + \left( \frac{t_r}{6} \right)^2 \right] \right\} \quad (3.10)$$

Figure 3.8 presents the normalized effect of the taper angle on the area moments of inertia and the torsional stiffness of a curved  $z$ -compliance element. The effect of  $\Psi$  is normalized using the value for  $\Psi=0^\circ$ . The plot shows that  $\Psi$  has a smaller effect on  $I_z$  than on  $I_r$  or  $k_t$ . The reason for the reduced effect is that the beam's centroid will shift as the taper angle increases as shown in Figure 3.7b. As a result of the shift of the neutral  $z$ -axis, the effect of  $\Psi$  is decreased.

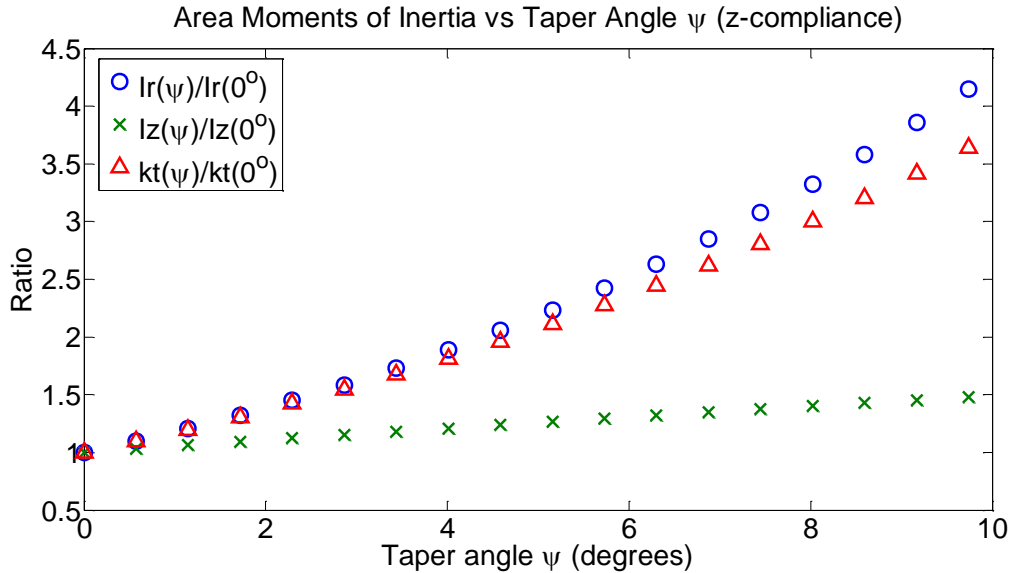


**Figure 3.8: Normalized taper angle effect on the area moments of inertia,  $I_z$  and  $I_r$ , and the torsional stiffness constant,  $k_t$ , of a  $z$ -compliance CF with  $\phi=120^\circ$ . Effect is normalized using the values for  $\Psi=0^\circ$ .**

### 3.5 Stiffness ratios

An important performance metric for a flexure element is the ratio of its stiffnesses. Good designs will decrease the stiffness in the desired DOF and maximize the stiffnesses in the other directions. For  $z$ -compliance element the goal is to minimize the ratio of  $K_z/K_r$  and  $K_z/K_\theta$ . A low stiffness ratio reduces undesired displacements resulting from extraneous loads. For an  $r$ -compliance flexure the design should minimize  $K_r/K_z$  and  $K_r/K_\theta$ . In the following sections the effect of the sweep angle and the taper angle on the stiffness ratios is analyzed.

### 3.5.1 Sweep angle effect

In the sweep angle analysis, the length of the flexure,  $L=R\phi$ , is held constant to analyze the additional role  $\phi$  plays in determining the stiffness ratios. Figure 3.9 shows how the  $z$ -compliance element stiffness ratios change with  $\phi$ ; the stiffness ratios for the curved beam are compared to those of a straight-beam of the same length and cross-section. The figure shows that  $\phi$  gives the designer an additional lever for developing a flexure with improved  $F_r$  load rejection capability. The two stiffness ratios are equal when  $\phi=122.56^\circ$  and lower than the straight beam  $K_z/K_r$  stiffness ratio. Increasing or decreasing  $\phi$  from this point will increase one of the stiffness ratios.

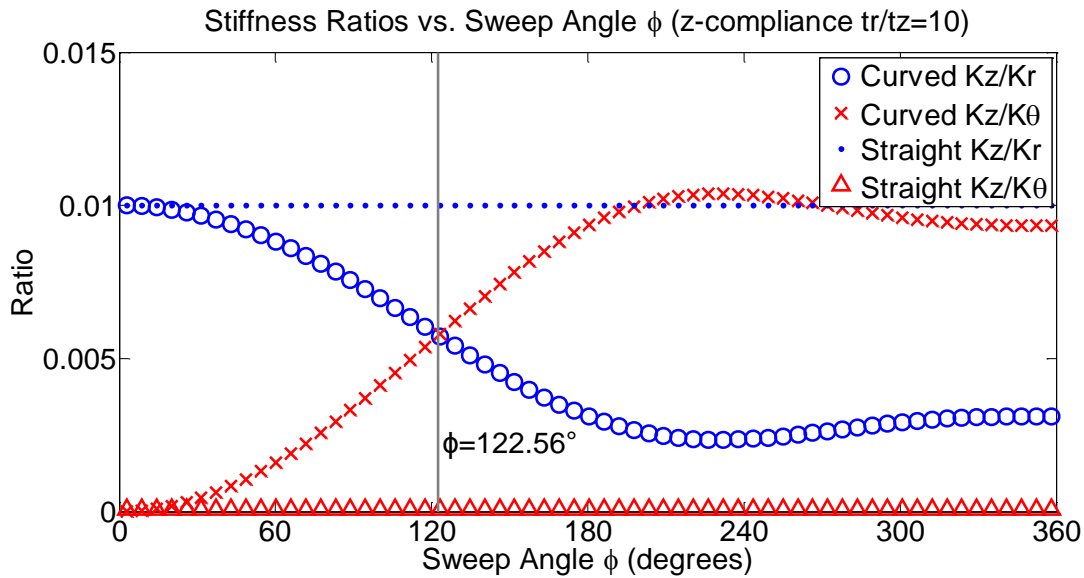


**Figure 3.9: Sweep angle,  $\phi$ , effect on the stiffness ratios for a  $z$ -compliance flexure with a radial-thickness,  $t_r$ , to  $z$ -thickness,  $t_z$ , ratio of 10. The stiffness ratios are equal when  $\phi=122.56^\circ$ . ( $L=60\text{mm}$ ,  $t_r=10\text{mm}$ ,  $t_z=1\text{mm}$ , 6061 Aluminum).**

The magnitude of the stiffness ratios depends on the cross-section of the beam, the beams in Figure 3.9 have a ratio of  $t_r/t_z=10$ . Figure 3.10 shows how the ratio of  $t_r/t_z$  affects the magnitude of the stiffness ratios for a  $z$ -compliance element with a  $\phi=122.56^\circ$ . The plot demonstrates that regardless of the cross-section dimensions the two stiffness ratios  $K_z/K_r$  and  $K_z/K_\theta$  for a  $z$ -compliance element are always equal when  $\phi=122.56^\circ$ . The magnitude of the stiffness ratios decreases as the ratio of  $t_r/t_z$  increases. For  $\phi=122.56^\circ$  both curved-beam stiffness ratios are always less than the value for the straight-beam  $K_z/K_r$  ratio.

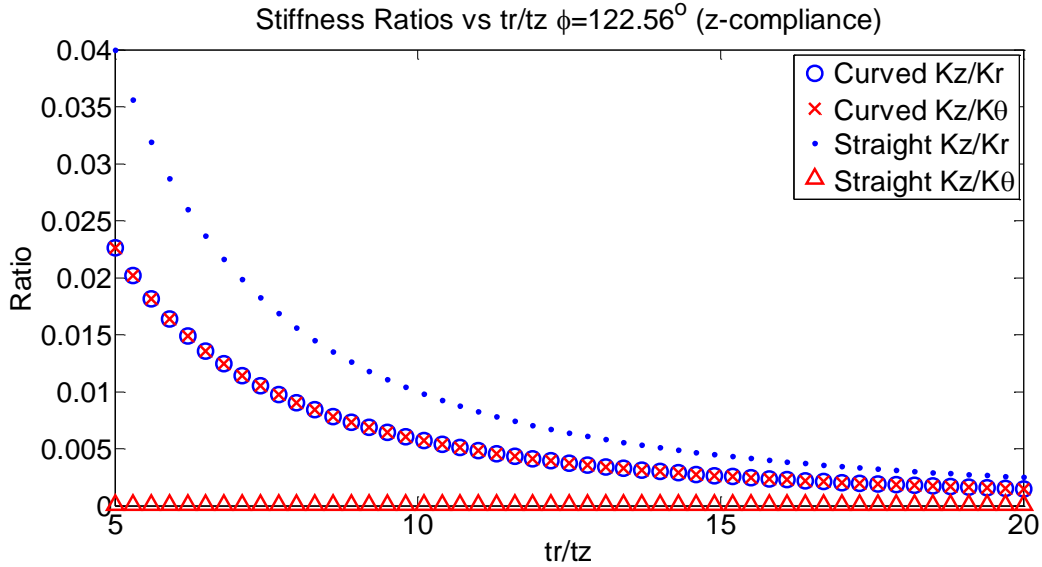


**Figure 3.10: Effect of  $t_r/t_z$  ratio on the magnitude of the stiffness ratios for a  $z$ -compliance flexure ( $\phi=122.56^\circ$ ). Plot shows that regardless of the value of  $t_r/t_z$  the stiffness ratios are equal when  $\phi=122.56^\circ$  and their magnitude is less than that the ratio of  $K_z/K_r$  for a straight-beam of the same dimensions. ( $L=60\text{mm}$ , 6061 Aluminum).**

When designing an  $r$ -compliance element the designer seeks to minimize the ratios of  $K_r/K_\theta$  and  $K_r/K_z$ , so as to maximize the desired displacement  $\Delta r$  per unit load  $F_r$ , and minimize the displacements due to extraneous loads  $F_\theta$  and  $F_z$ . Figure 3.11 shows how the sweep angle of an  $r$ -compliance element ( $t_z/t_r=10$ ) affects its stiffness ratios. The value for  $K_r/K_\theta$  is equal to 1 when  $\phi=122.56^\circ$ . Once again  $\phi=122.56^\circ$  is an important angle but for a different reason. When  $K_r/K_\theta > 1$  the flexure is more compliant in the  $\theta$ -direction than in the  $r$ -direction, this means that when  $\phi > 122.56^\circ$  the flexure should now be classified as a  $\theta$ -compliance element. Normally, flexure blades, such as the elements being analyzed in this work, are considered to have one linear DOF and two linear constraints, given that their stiffness ratios are much less than 1. In the case of  $r$ -compliance CF elements, the flexure blade cannot be considered a  $\theta$ -constraint for the majority of the sweep angles. This phenomenon can be exploited when a designer requires that the element provide two linear DOF, for this case a curved beam may be used instead of two straight-flexures in series.

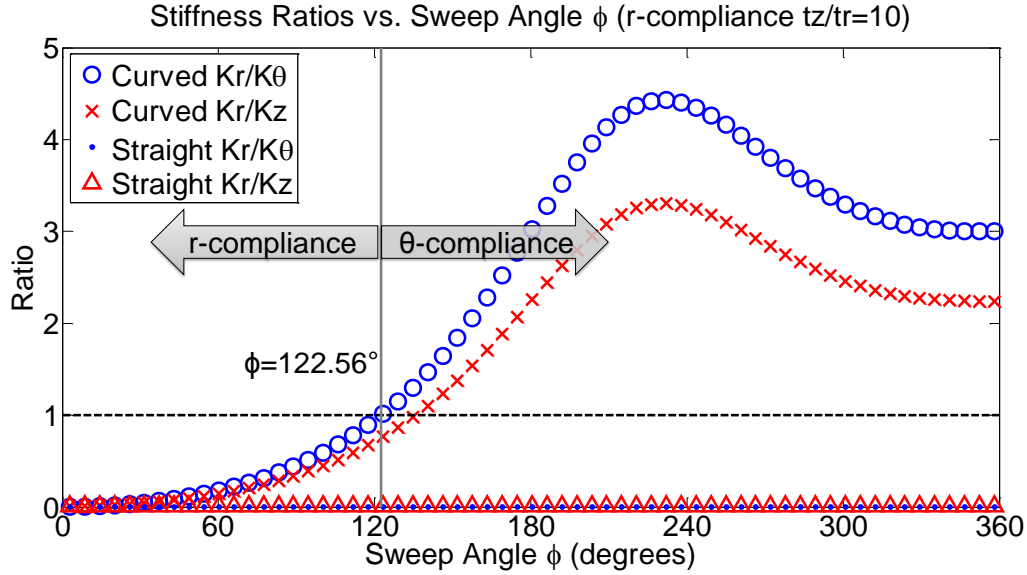


**Figure 3.11: Sweep angle,  $\phi$ , effect on the stiffness ratios for an  $r$ -compliance flexure with a  $z$ -thickness,  $t_z$  to radial-thickness,  $t_r$ , ratio of 10. The  $K_r/K_\theta$  stiffness ratio is equal to 1 when  $\phi = 122.56^\circ$ . When the  $K_r/K_\theta$  is greater than 1 the flexure should be considered  $\theta$ -compliant because this is its lowest stiffness. ( $L=60\text{mm}$ ,  $t_z=10\text{mm}$ ,  $t_r=1\text{mm}$ , 7075 Aluminum).**

Figure 3.12 shows the effect of the ratio of  $t_z/t_r$  on the magnitude of the stiffness ratios for the important sweep angle of  $122.56^\circ$ . At this  $\phi$ , the magnitude of  $K_r/K_\theta$  is always 1 for any  $t_z/t_r$  ratio. The relative magnitude of the dimensions of the cross-section of the beam has little effect on  $K_r/K_z$  because both  $K_z$  and  $K_r$  are functions of  $t_r^3$ .  $K_z$  is dictated by the sum of two components as highlighted in Equation (3.11). One component is a function of the torsional stiffness constant,  $k_t$ , which is a cubic function of the cross-sectional area's smallest dimension,  $t_r$  in this case. The other component is a function of  $I_r$ , therefore, an increase of  $t_z$  affects mainly this component. Figure 3.13 better illustrates the reduced effect of  $t_z/t_r$  on the  $K_r/K_z$  ratio by normalizing the straight-beam and curved-beam stiffness ratios using the corresponding stiffness ratio for  $t_z/t_r=5$ . The significant reduction in the effect of  $t_z/t_r$  is crucial because in straight-beam flexure design  $t_z/t_r$  is often used to decrease  $K_r/K_z$ .

$$K_z = \left( R^3 \left[ \frac{.5\phi - \sin \phi \cos \phi}{EI_r} + \frac{1.5\phi - 2 \sin \phi + .5 \sin \phi \cos \phi}{Gk_t} \right] \right)^{-1} \quad (3.11)$$

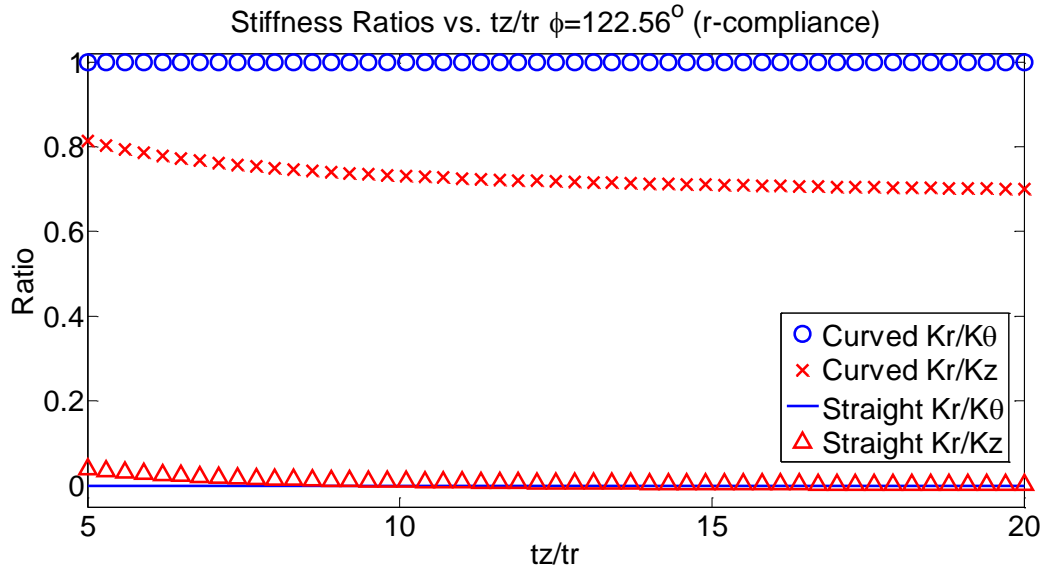


Figure 3.12: Effect of  $t_z/t_r$  ratio on the magnitude of the stiffness ratios for an  $r$ -compliance flexure ( $\phi = 122.56^\circ$ ). Plot shows that regardless of the value of  $t_z/t_r$  the  $K_r/K_\theta$  stiffness ratio is equal to 1 when  $\phi = 122.56^\circ$ . ( $L=60\text{mm}$ , 7075 Aluminum).

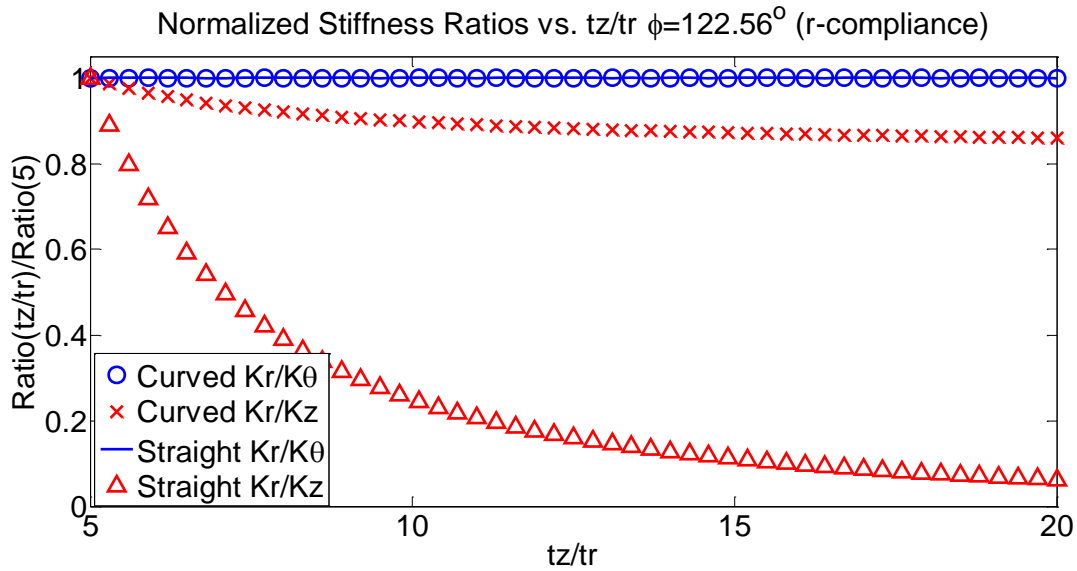
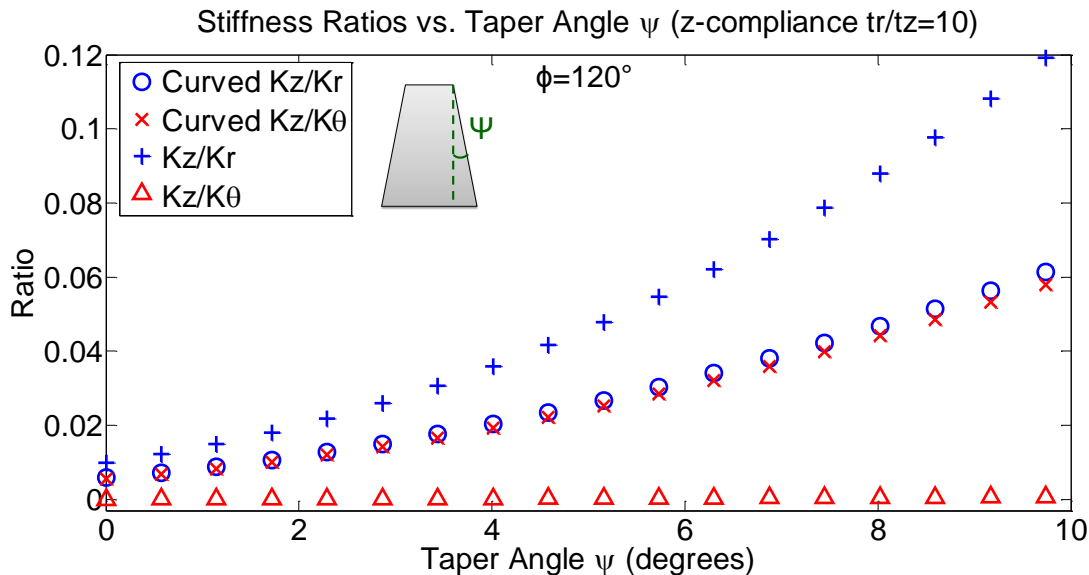


Figure 3.13:  $t_z/t_r$  effect on the stiffness ratios of an  $r$ -compliance flexure ( $\phi = 122.56^\circ$ ). Plot shows that  $t_z/t_r$  has a significantly greater effect on the  $K_r/K_z$  stiffness ratio of a straight-beam flexure compared to a curved-beam  $r$ -compliance element. ( $L=60\text{mm}$ , 7075 Aluminum).

### 3.5.2 Taper angle effect

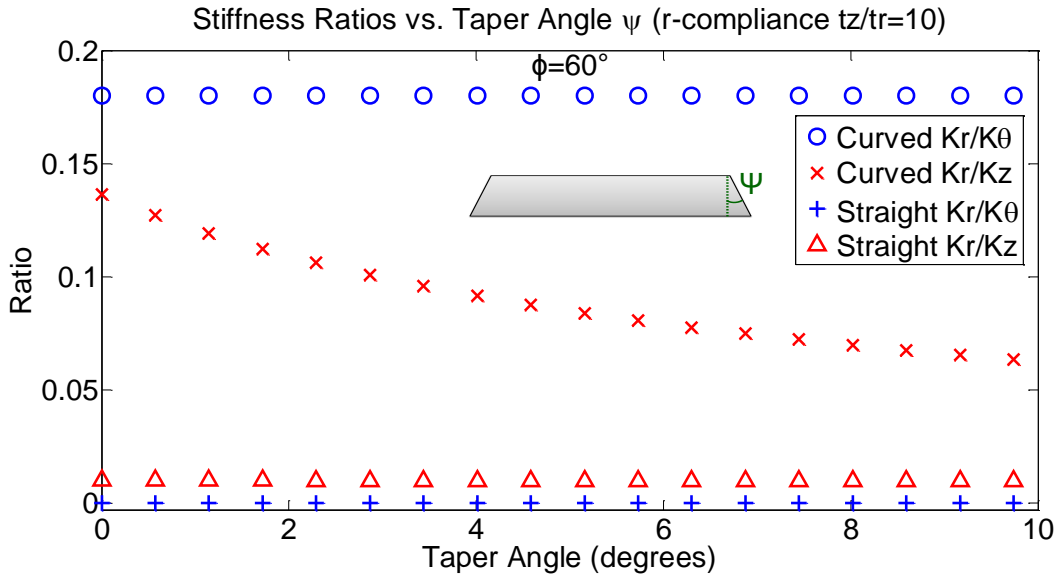
The taper angle,  $\Psi$ , of an element plays a role in determining the kinematics of the CF elements, because it affects  $I_r$ ,  $I_z$ , and  $k_t$ . For a  $z$ -compliance element the optimum sweep angle of  $\phi=122.56^\circ$  was used as the starting point for the taper angle analysis. Figure 3.14 shows the stiffness ratios for a  $z$ -compliance curved beam ( $\phi=120^\circ$ ) vs. taper angle. The model indicates that as the taper angle increases so do the stiffness ratios, and therefore, the optimum taper angle choice is  $\Psi=0^\circ$ . The plot shows that the straight-beam kinematics are also influenced by  $\Psi$ . The slope of the straight beam  $K_z/K_r$  is steeper than that of the curved beam indicating that a curved beam is less sensitive to the taper angle imposed by certain manufacturing methods. The sensitivity to taper angle manufacturing error is investigated in section 3.7.2.



**Figure 3.14 Taper angle effect on the stiffness ratios for a  $z$ -compliance flexure ( $\phi=120^\circ$ ). Plot shows that increasing  $\Psi$  increases the value of the stiffness ratios. ( $L=60\text{mm}$ ,  $t_r=10\text{mm}$ ,  $t_z=1\text{mm}$ , 7075Aluminum).**

Figure 3.15 shows the effect of  $\Psi$  on the stiffness ratios for an  $r$ -compliance element with  $\phi=60^\circ$ . The plot indicates that the ratio of  $K_r/K_z$  will decrease with increasing taper angle. There is no effect on  $K_r/K_\theta$  because they are both functions of  $I_z$ , and therefore the effect of  $\Psi$  on the stiffness ratio cancels.  $K_z$  on the other hand is a function of  $I_r$  and  $k_t$ , both of which are affected by taper angle. In the case of an  $r$ -compliance beam, a taper angle along the  $r$ -axis may be used to improve the performance of the flexural element.

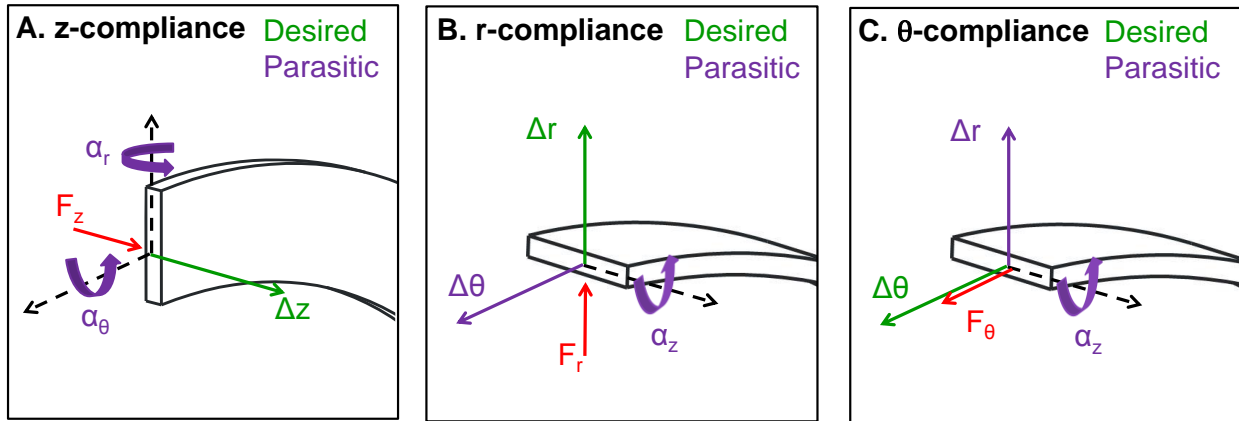




**Figure 3.15 Taper angle effect on the stiffness ratios for an  $r$ -compliance flexure ( $\phi=60^\circ$ ). Plot shows that increasing  $\Psi$  decreases the value of the  $K_r/K_z$  stiffness ratio but has no effect on  $K_r/K_\theta$ . ( $L=60\text{mm}$ ,  $t_z=10\text{mm}$ ,  $t_r=1\text{mm}$ , 7075Aluminum).**

### 3.6 Parasitic Motion Ratios

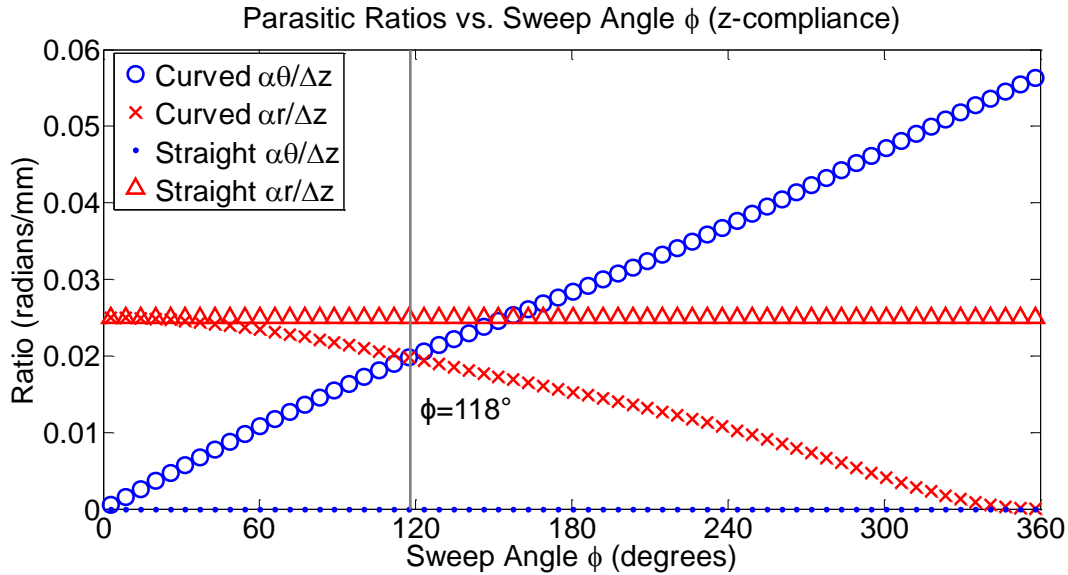
Another performance metric for a flexure element is the magnitude of the absolute value of its parasitic (undesired) displacements compared to the desired displacement along the direction of the applied force. A lower parasitic ratio indicates a better performance. Figure 3.16 defines the desired and parasitic displacements and rotations for each of the types of CF elements when loaded along their direction of greatest compliance. For a  $z$ -compliance CF under  $F_z$ , the desired displacement is  $\Delta z$  and the parasitic rotations associated with this loading are  $\alpha_r$  and  $\alpha_\theta$ . Therefore, the parasitic ratios of interest are  $\alpha_r/\Delta z$  and  $\alpha_\theta/\Delta z$ . An  $r$ -compliance element loaded with  $F_r$  has a desired displacement of  $\Delta r$  and the parasitic displacement  $\Delta \theta$  and rotation  $\alpha_z$ . In the previous section it was established that when  $\phi$  is greater than  $122.56^\circ$  the  $r$ -compliance element should be considered a  $\theta$ -compliance flexure. In the case of  $\theta$ -compliance element loaded under  $F_\theta$ , the desired displacement is  $\Delta \theta$  and the undesired displacement and rotation are  $\Delta r$  and  $\alpha_z$ , respectively.



**Figure 3.16** Definition of parasitic (purple) and desired (green) motions for the three types of cylindrical flexures: A)  $z$ -compliance, B)  $r$ -compliance, and C)  $\theta$ -compliance.

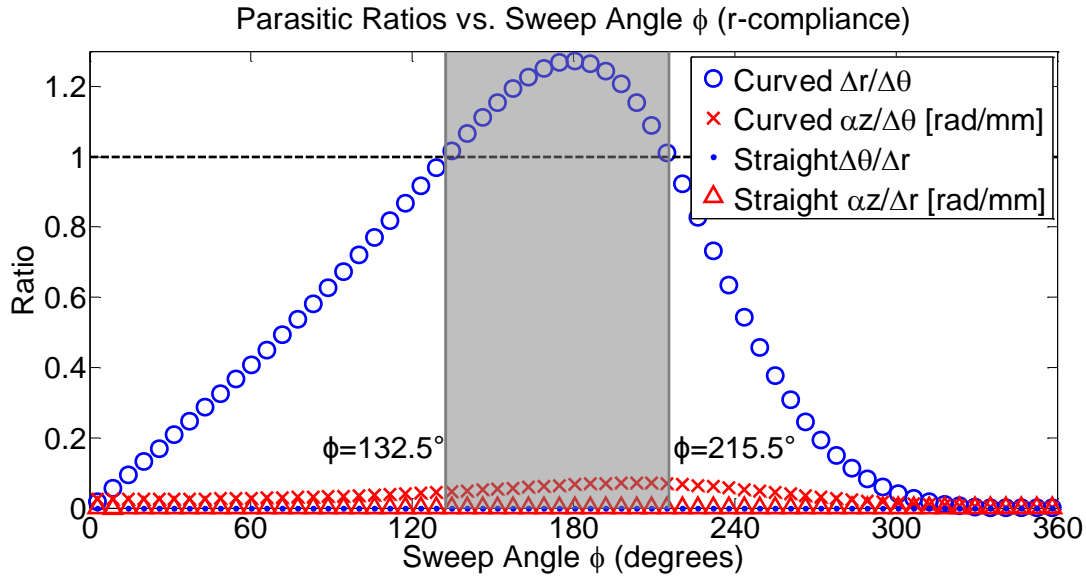
### 3.6.1 Sweep angle effect

Figure 3.17 shows the effect of sweep angle,  $\phi$ , on the parasitic ratios for a  $z$ -compliance element under  $F_z$ . The optimal sweep angle is found to be  $118^\circ$ , at which point the two parasitic ratios are equal. Deviation in either direction from this point results in the increase of one of the ratios. The plot indicates that at  $\phi = 118^\circ$  both parasitic ratios are less than the  $\alpha_r/\Delta z$  ratio of the straight-beam counterpart. If the parasitics of the flexure are of concern, a CF element can be used instead of a straight-beam to achieve a better performance. It is important to note that the sum of the absolute value of the two parasitic ratios of the  $z$ -compliance CF beam is always greater than the value of the single parasitic ratio of the straight flexure.



**Figure 3.17 Sweep angle,  $\phi$ , effect on the parasitic ratios of a z-compliance flexure. The two parasitic ratios,  $\alpha_\theta/\Delta z$  and  $\alpha_r/\Delta z$ , are equal when  $\phi = 118^\circ$ . ( $L=60\text{mm}$ ,  $t_r=10\text{mm}$ ,  $t_z=1\text{mm}$ , 6061 Aluminum)**

The effect of sweep angle on the parasitic ratios of an  $r$ -compliance element is shown in Figure 3.18. The chart reveals that the parasitic ratios for the  $r$ -compliance CF are greater than the corresponding values for a straight-beam regardless of  $\phi$ . The value of  $\Delta\theta/\Delta r$  is greater than 1 for  $215.5^\circ > \phi > 132.5^\circ$ . The shaded region highlights the sweep angles for which the parasitic displacement,  $\Delta\theta$ , will be larger than the desired displacement,  $\Delta r$ . When designing an  $r$ -compliance flexure the designer should be cognizant of this region and design the system such that the parasitic displacement is mitigated.



**Figure 3.18 Sweep angle,  $\phi$ , effect on the parasitic ratios of an  $r$ -compliance flexure. The shaded region highlights the sweep angles ( $215.5^\circ > \phi > 132.5^\circ$ ) for which the desired motion,  $\Delta r$ , is less than the parasitic motion,  $\Delta\theta$ . ( $L=60\text{mm}$ ,  $t_z=10\text{mm}$ ,  $t_r=1\text{mm}$ , 7075Aluminum)**

Similarly, Figure 3.19 displays the effect of sweep angle on the parasitic ratios of a  $\theta$ -compliance element. Once again the parasitic ratios for the CF element are greater than those of a straight-beam. The shaded region in the plot gives the sweep angles for which the parasitic motion,  $\Delta r$ , is greater than the desired displacement,  $\Delta\theta$ . Above  $\phi > 115^\circ$  the parasitic ratio  $\Delta r/\Delta\theta$  is less than 1 and quickly decreases with increasing  $\phi$ . The analysis indicates that a  $\theta$ -compliance element will have a better performance for large sweep angles, above  $\phi=115^\circ$ .

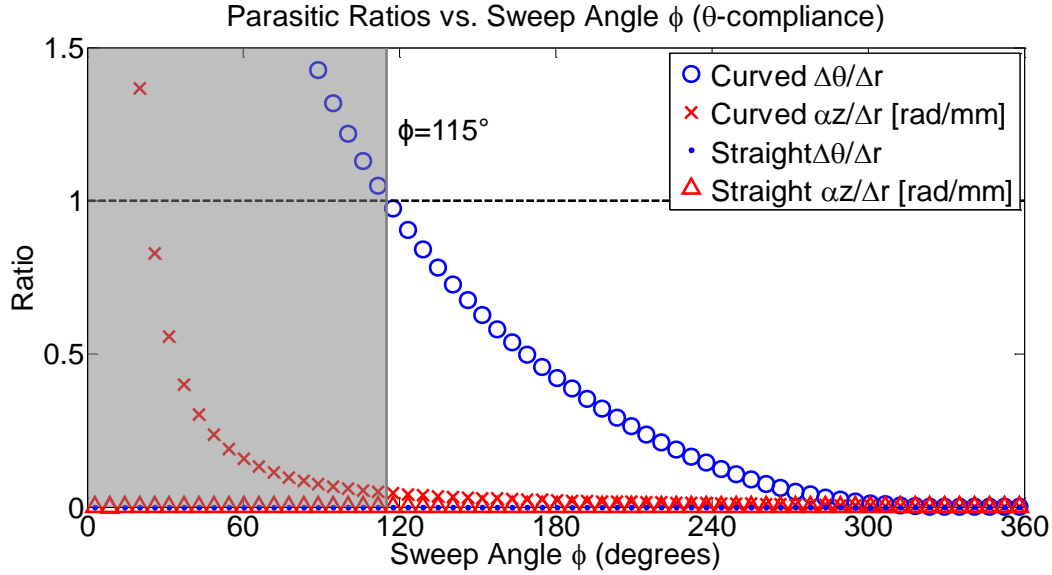


**Figure 3.19** Sweep angle,  $\phi$ , effect on the parasitic ratios of a  $\theta$ -compliance flexure. Above  $\phi=115^\circ$  the desired motion,  $\Delta\theta$ , is less than the parasitic motion,  $\Delta r$ . ( $L=60\text{mm}$ ,  $t_z=10\text{mm}$ ,  $t_r=1\text{mm}$ , 7075Aluminum)

### 3.6.2 Taper angle effect

The taper angle effect on the parasitic ratios of a CF element is limited because the desired and parasitic motions depend on the same area moments of inertia. In the case of both an  $r$ -compliance and a  $\theta$ -compliance beam, all displacements associated with an  $F_r$  or  $F_\theta$  load are dictated by  $1/I_z$  as shown in Equation (3.3). As a result, the effect of the taper angle on the parasitic ratios of these two types of elements cancels. The parasitic ratios of a  $z$ -compliance beam are given by  $1/I_r$  and different functions of  $\beta$ . Figure 3.20 shows that the  $\Psi$  effect on the parasitic ratios of a  $z$ -compliance curved beam with  $\phi=120^\circ$  is less than 5% for a  $10^\circ$  taper angle increase. The effect of taper angle for different sweep angles will be explored in section 3.7.2.

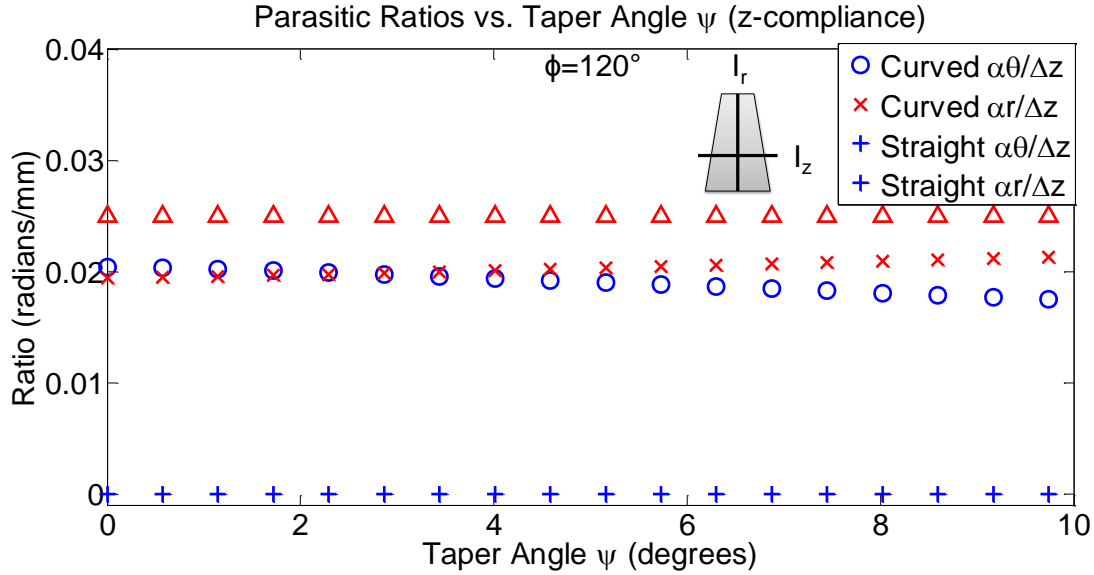


Figure 3.20 Taper angle,  $\Psi$ , effect on the parasitic ratios of a z-compliance flexure with  $\phi=120^\circ$ . ( $L=60\text{mm}$ ,  $t_r=10\text{mm}$ ,  $t_z=1\text{mm}$ , 7075Aluminum)

### 3.6.3 Eigenvalue Parasitic Ratios

In the previous section the parasitic displacements were defined as a displacement or rotation occurring solely about one of the prescribed axes. However, as the analysis showed, there are often displacements or rotations about more than one axis. This brings up the idea that a parasitic displacement can be defined as any combination of undesired displacements. The largest parasitic ratio can be established using the eigenvalues and eigenvectors of the compliance matrix [23]. Kim et al. define the parasitic ratio of a beam element,  $n_2$ , as ratio of the magnitude of the secondary compliance vector,  $|SCV|$ , to the magnitude of the primary compliance vector,  $|PCV|$ , as shown in Equation (3.12). This work calls this definition of the parasitic ratio of an element the eigenvalue parasitic ratio because the ratio is calculated using the eigenvalues of the compliance matrix.

$$n_2 = \frac{|SCV|}{|PCV|} \quad (3.12)$$

In order to calculate the eigenvalues of the compliance matrix the different entries of the matrix need to be unified [23]. Currently the matrix relates both forces and moments to displacements and rotations. The unified matrix needs to map only forces to displacements. To

unify the matrix characteristic lengths are used to convert rotations to displacements and moments to forces. Figure 3.21 shows the characteristic lengths that were selected to unify the compliance matrix. The lengths were selected such that for a given rotation the maximum displacement would be observed. The process used to change the rotations and moments into displacements and forces is shown in Equation (3.13). The characteristic length is given by  $l$ , while  $[\Delta]$  indicates the vector of displacements and  $[F]$  the vector of applied forces. Equation (3.14) is used to transform the compliance matrix,  $[C]$ , into the unified  $z$ -compliance matrix,  $[\hat{C}_z]$ . Similarly Equation (3.15) gives the unified compliance matrix for an  $r$ -compliance or  $\theta$ -compliance element,  $[\hat{C}_r]$ .

$$\begin{bmatrix} 1 & 0 & 0 & 0 & 0 & 0 \\ 0 & 1 & 0 & 0 & 0 & 0 \\ 0 & 0 & 1 & 0 & 0 & 0 \\ 0 & 0 & 0 & 1/l & 0 & 0 \\ 0 & 0 & 0 & 0 & 1/l & 0 \\ 0 & 0 & 0 & 0 & 0 & 1/l \end{bmatrix} [\Delta] = [C] \begin{bmatrix} 1 & 0 & 0 & 0 & 0 & 0 \\ 0 & 1 & 0 & 0 & 0 & 0 \\ 0 & 0 & 1 & 0 & 0 & 0 \\ 0 & 0 & 0 & l & 0 & 0 \\ 0 & 0 & 0 & 0 & l & 0 \\ 0 & 0 & 0 & 0 & 0 & l \end{bmatrix} [F] \quad (3.13)$$

$$[\hat{C}_z] = \begin{bmatrix} 1 & 0 & 0 & 0 & 0 & 0 \\ 0 & 1 & 0 & 0 & 0 & 0 \\ 0 & 0 & 1 & 0 & 0 & 0 \\ 0 & 0 & 0 & t_r & 0 & 0 \\ 0 & 0 & 0 & 0 & t_z & 0 \\ 0 & 0 & 0 & 0 & 0 & t_r \end{bmatrix} [C] \begin{bmatrix} 1 & 0 & 0 & 0 & 0 & 0 \\ 0 & 1 & 0 & 0 & 0 & 0 \\ 0 & 0 & 1 & 0 & 0 & 0 \\ 0 & 0 & 0 & t_r & 0 & 0 \\ 0 & 0 & 0 & 0 & t_z & 0 \\ 0 & 0 & 0 & 0 & 0 & t_r \end{bmatrix} \text{for } z\text{compliance} \quad (3.14)$$

$$[\hat{C}_r] = \begin{bmatrix} 1 & 0 & 0 & 0 & 0 & 0 \\ 0 & 1 & 0 & 0 & 0 & 0 \\ 0 & 0 & 1 & 0 & 0 & 0 \\ 0 & 0 & 0 & t_z & 0 & 0 \\ 0 & 0 & 0 & 0 & t_z & 0 \\ 0 & 0 & 0 & 0 & 0 & t_r \end{bmatrix} [C] \begin{bmatrix} 1 & 0 & 0 & 0 & 0 & 0 \\ 0 & 1 & 0 & 0 & 0 & 0 \\ 0 & 0 & 1 & 0 & 0 & 0 \\ 0 & 0 & 0 & t_z & 0 & 0 \\ 0 & 0 & 0 & 0 & t_z & 0 \\ 0 & 0 & 0 & 0 & 0 & t_r \end{bmatrix} \text{r}\&\theta\text{compliance} \quad (3.15)$$

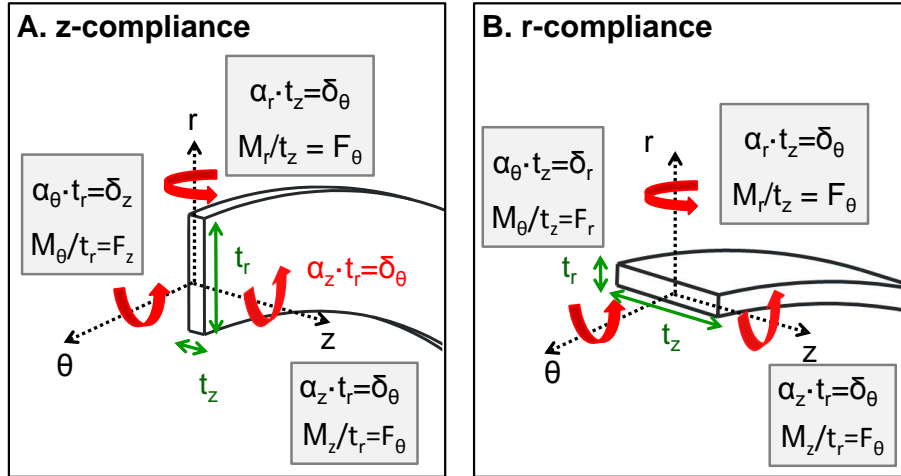


**Figure 3.21 Linearization of tip rotations for a  $z$ -compliance flexure (A), and an  $r$ -compliance flexure (B).**

Once the compliance matrix has been unified establishing the eigenvalue parasitic ratio of the element is as easy as finding the eigenvalues of the unified compliance matrix. The  $/PCV/$  corresponds to the highest eigenvalue and the  $/SCV/$  to the second highest eigenvalue. Figure 3.22 compares the eigenvalue parasitic ratio for a set of  $z$ -compliance element of varying  $\phi$  to that of a straight-beam element. An important part of the eigenvalue parasitic stiffness ratio analysis is to understand not only the effect of sweep angle on the magnitude of the ratio but also how the direction of the  $PCV$  and  $SCV$  changes with  $\phi$ . Table 3.2 shows how the eigenvectors for a  $z$ -compliance element change with increasing  $\phi$ . Figure 3.23 presents the effect of sweep angle on the eigenvalue parasitic ratio for an  $r$ -compliance element, while Table 3.3 lists the primary and secondary eigenvectors of the  $r$ -compliance matrix for several  $\phi$ .



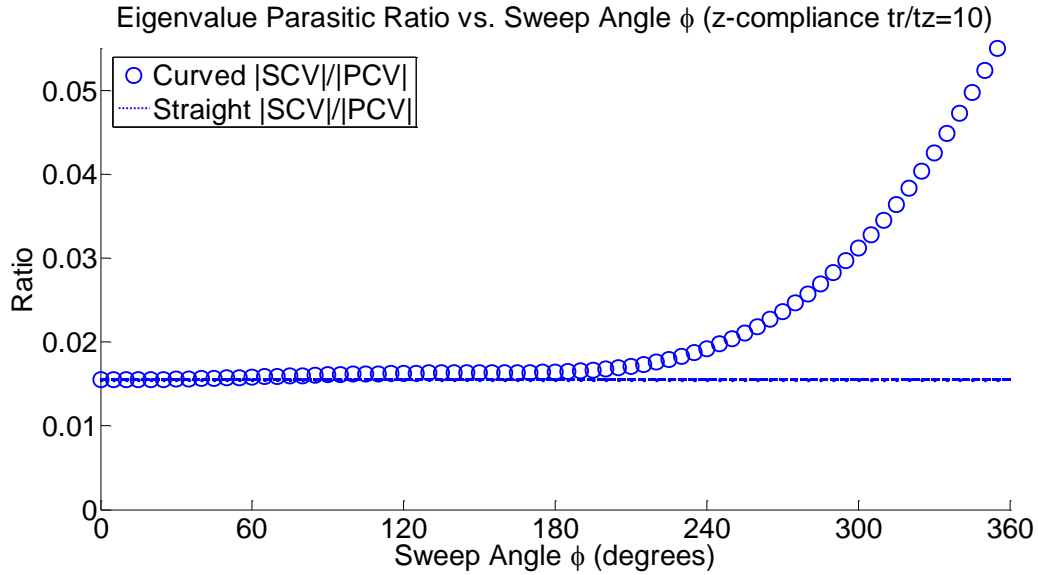


**Figure 3.22 Sweep angle,  $\phi$ , effect on the eigenvalue parasitic ratios of z-compliance flexure with  $t_r/t_z=10$ . ( $L=60\text{mm}$ ,  $t_r=5\text{mm}$ ,  $t_z=0.5\text{mm}$ , 7075 Aluminum)**

**Table 3.2: Primary (PCV) and secondary compliance vectors (SCV) for a z-compliance flexure. Vectors depend on the sweep angle,  $\phi$ . ( $L=60\text{mm}$ ,  $t_r=5\text{mm}$ ,  $t_z=0.5\text{mm}$ , 7075 Aluminum)**

	$\phi=0^\circ$		$\phi=60^\circ$		$\phi=90^\circ$		$\phi=180^\circ$		$\phi=300^\circ$	
	PCV	SCV	PCV	SCV	PCV	SCV	PCV	SCV	PCV	SCV
$\theta$	0	0	0	0	0	0	0	0	0	0
$r$	0	0	0	0	0	0	0	0	0	0
$z$	-0.999	0	-0.998	-0.054	-0.997	-0.079	-0.990	-0.141	-0.972	-0.236
$\alpha_\theta''$	0	1.000	0.054	-0.998	0.079	-0.996	0.142	-0.988	0.236	-0.972
$\alpha_r''$	-0.0013	0	-0.012	-0.027	-0.011	-0.040	-0.007	-0.066	-0.002	-0.010
$\alpha_z''$	0	0	0	0	0	0	0	0	0	0

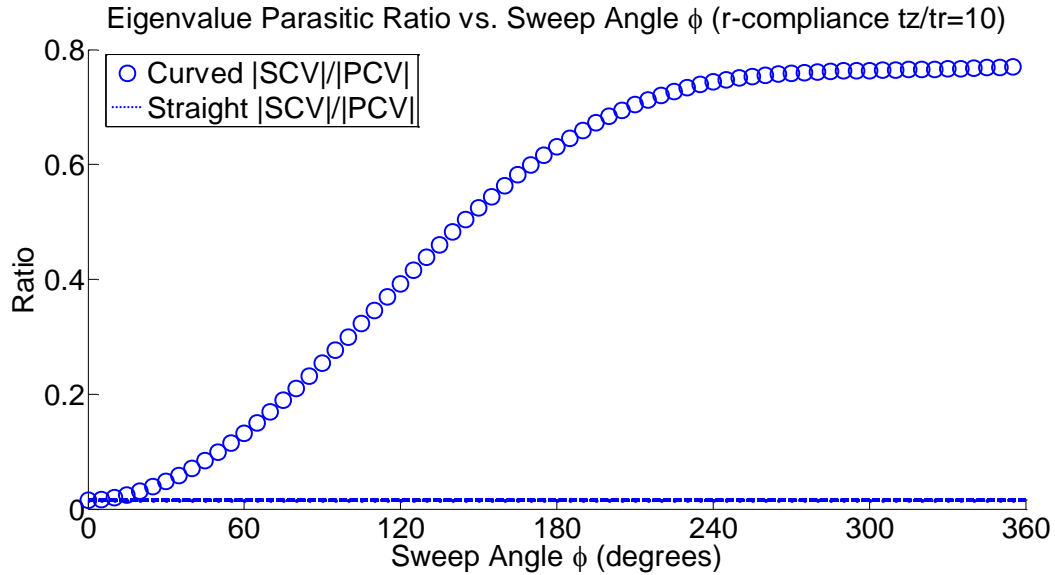


**Figure 3.23 Sweep angle,  $\phi$ , effect on the eigenvalue parasitic ratios of an  $r$ -compliance flexure with  $t_z/t_r=10$ . ( $L=60\text{mm}$ ,  $t_z=5\text{mm}$ ,  $t_r=0.5\text{mm}$ , 7075 Aluminum)**

**Table 3.3: Primary (PCV) and secondary compliance vectors (SCV) for an  $r$ -compliance flexure. Vectors depend on the sweep angle,  $\phi$ . ( $L=60\text{mm}$ ,  $t_z=5\text{mm}$ ,  $t_r=0.5\text{mm}$ , 7075 Aluminum)**

	$\phi=0^\circ$		$\phi=60^\circ$		$\phi=90^\circ$		$\phi=180^\circ$		$\phi=300^\circ$	
	PCV	SCV	PCV	SCV	PCV	SCV	PCV	SCV	PCV	SCV
$\theta$	0	0	0.3809	0	-0.554	0	0.899	0	-0.999	0
$r$	0	0	-0.925	0	0.835	0	-0.437	0	0.019	0
$z$	-0.999	0	0	-0.965	0	-0.981	0	-0.990	0	0.988
$\alpha_\theta''$	0	1.000	0	-0.186	0	-0.076	0	0.087	0	-0.155
$\alpha_r''$	0	0	0	-0.187	0	-0.179	0	-0.110	0	0.005
$\alpha_z''$	-0.013	0	0.013	0	-0.014	0	0.017	0	-0.028	0

### 3.7 Sensitivity Analysis

Design for manufacturing requires that the engineer understand the effect that the tolerance on each dimension will have on the expected performance of the flexure element. This section presents the sensitivity of the flexure performance metrics to sweep angle and taper angle tolerance. A robust design will be less sensitive to tolerances.

#### 3.7.1 Sensitivity to sweep angle tolerance

Like any other dimension the sweep angle of an element has an associated tolerance for a given manufacturing method. In the case of a machine with a rotary axis, the sweep angle tolerance is set by the resolution and repeatability of the rotary axis. Figure 3.24 shows the  $z$ -compliance element stiffness ratio sensitivity to the sweep angle tolerance vs.  $\phi$ . The vertical axis displays the percent error off of the desired value per degree of  $\phi$  tolerance. For this analysis the radius of each beam,  $R$ , is set by the desired  $L$  and  $\phi$ . The sweep angle is then increased by  $1^\circ$  while  $R$  is held constant. Figure 3.24 shows that for approximately  $\phi > 35^\circ$  the percent error off the predicted stiffness ratio per degree of  $\phi$  tolerance is less than  $\pm 2\%$ . The same is true for  $r$ -compliance element as shown in Figure 3.25.

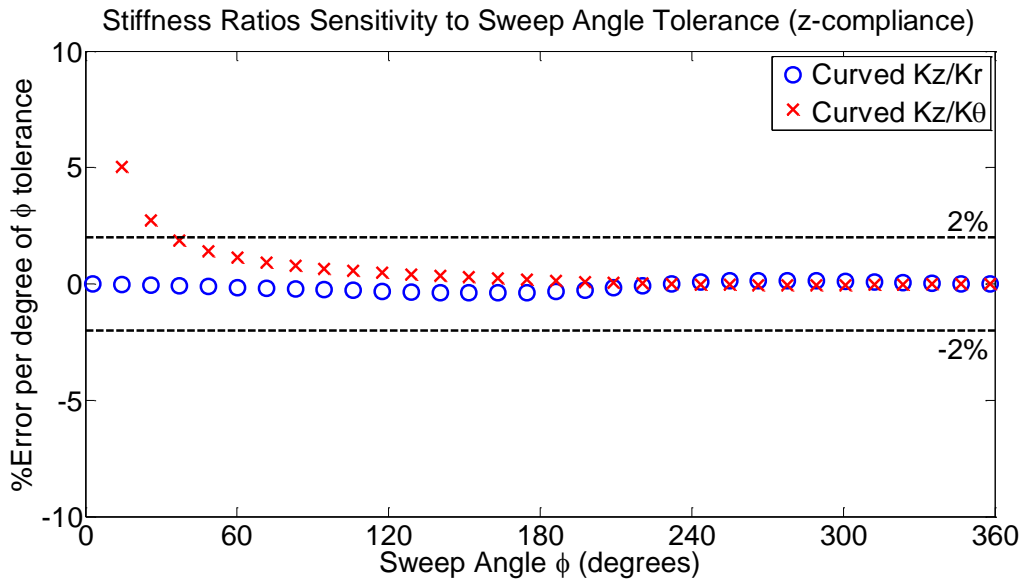


**Figure 3.24 Stiffness ratios sensitivity to sweep angle,  $\phi$ , tolerance for a  $z$ -compliance flexure vs. desired sweep angle. Plot shows the percent error from desired value per degree of sweep angle tolerance. ( $L=60\text{mm}$ ,  $t_r=10\text{mm}$ ,  $t_z=1\text{mm}$ , 6061 Aluminum)**

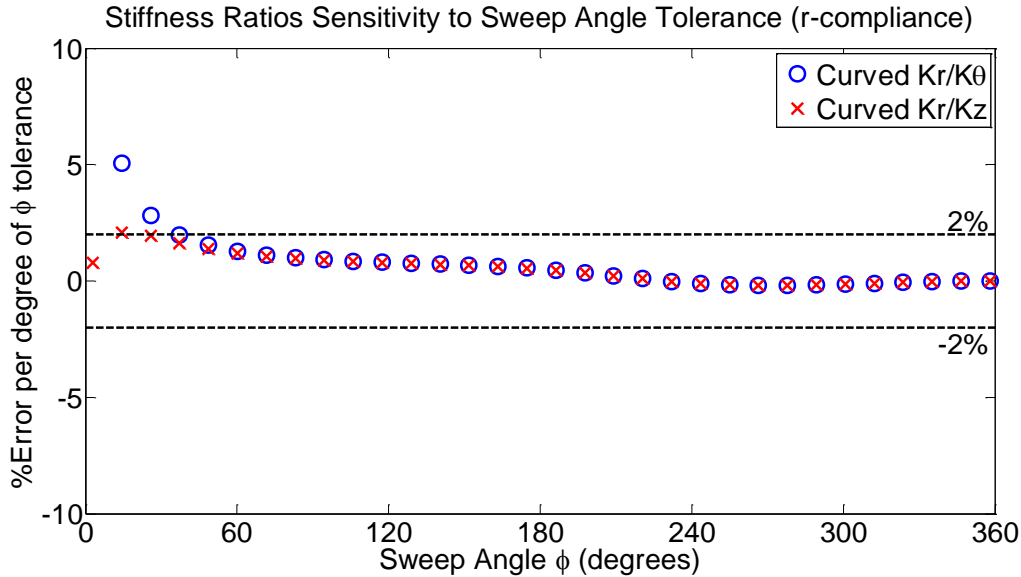


**Figure 3.25 Stiffness ratios sensitivity to sweep angle,  $\phi$ , tolerance for an  $r$ -compliance flexure vs. desired sweep angle,  $\phi$ . Plot shows the percent error from predicted value per degree of sweep angle tolerance. ( $L=60\text{mm}$ ,  $t_z=10\text{mm}$ ,  $t_r=1\text{mm}$ , 7075 Aluminum)**

The same analysis is performed to understand the effect of  $\phi$  tolerance on the parasitic ratios for the CF elements. The parasitic ratios sensitivity to the sweep angle tolerance for a  $z$ -compliance beam is plotted in Figure 3.26. The vertical axis gives the percent error off of the parasitic ratio for the desired  $\phi$  per degree of  $\phi$ -tolerance. The plot shows that for approximately  $15^\circ < \phi < 330^\circ$  the  $\phi$ -sensitivity of the element is low with an error of less than  $\pm 2\%$ . Figure 3.27 shows that for an  $r$ -compliance element the  $\phi$ -sensitivity is less than  $\pm 2\%$  for approximately  $20^\circ < \phi < 290^\circ$ . This sensitivity analysis is particularly important if the functional requirements call for a robust design and/or the manufacturing method has low resolution or repeatability.

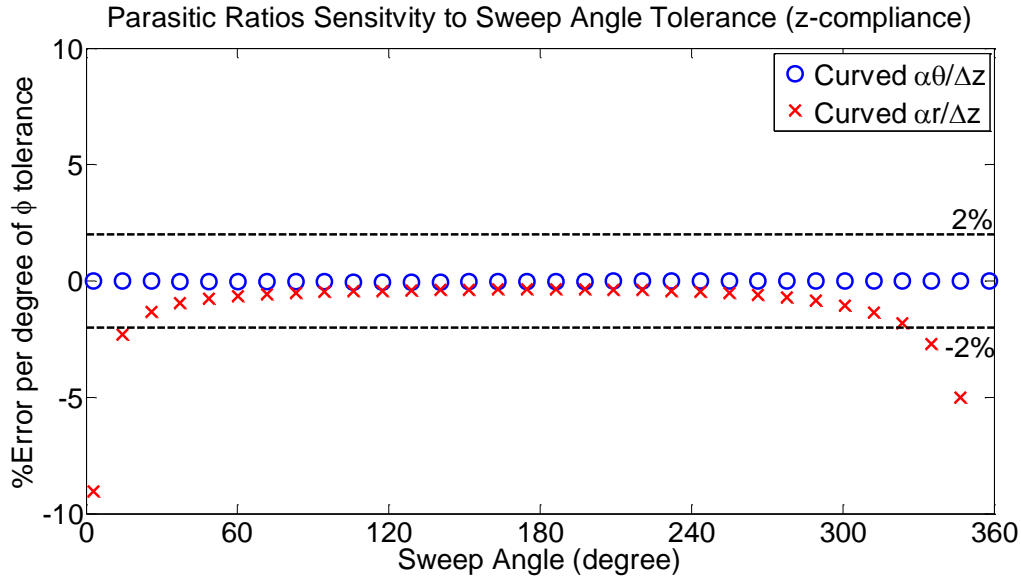


**Figure 3.26 Parasitic ratios sensitivity to sweep angle,  $\phi$ , tolerance for a z-compliance flexure vs. desired sweep angle. Plot shows the percent error from predicted value per degree of sweep angle tolerance. ( $L=60\text{mm}$ ,  $t_r=10\text{mm}$ ,  $t_z=1\text{mm}$ , 6061 Aluminum)**

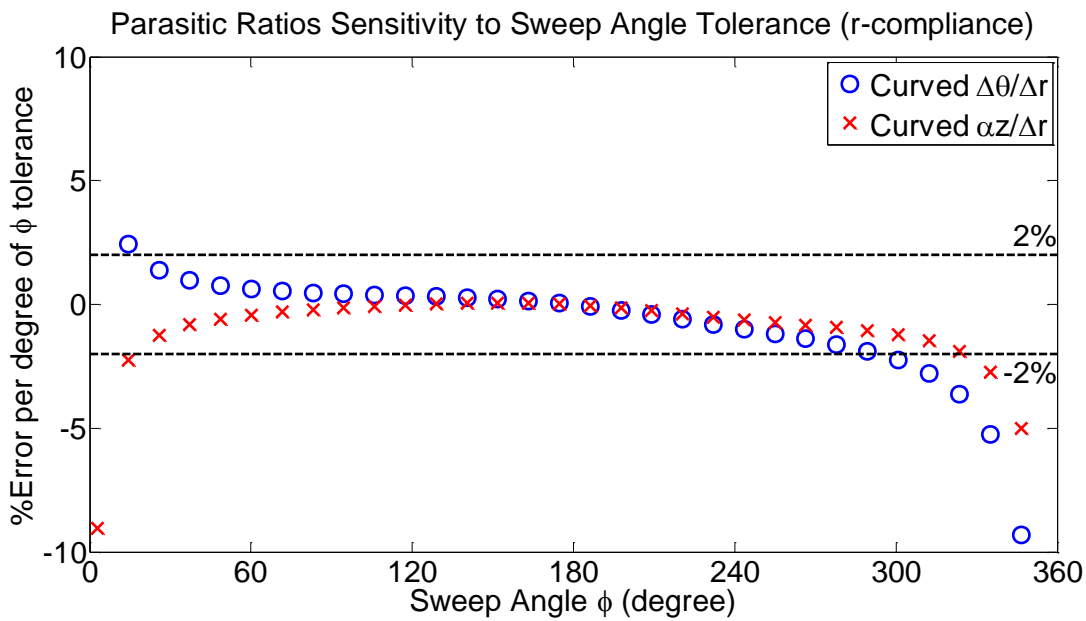


**Figure 3.27 Parasitic ratios sensitivity to sweep angle,  $\phi$ , tolerance for an r-compliance flexure vs. desired sweep angle. Plot shows the percent error from predicted value per degree of sweep angle tolerance. ( $L=60\text{mm}$ ,  $t_z=10\text{mm}$ ,  $t_r=1\text{mm}$ , 7075 Aluminum)**

### 3.7.2 Taper angle tolerance sensitivity

The analysis of the stiffness and parasitic ratios showed that the  $\Psi$ -effect is different for a curved-beam than for a straight-beam. This observation indicates that the sensitivity of the beam to a taper angle depends on  $\phi$ . The sensitivity of the beam to taper angle is important when dealing with a manufacturing method, such as abrasive water-jet, which results in a taper angle. Figure 3.28 plots the  $\Psi$ -sensitivity for a  $z$ -compliance element vs.  $\phi$ . The vertical axis shows the percent off of the desired stiffness ratio for every degree of  $\Psi$ . The chart indicates that the  $\Psi$ -sensitivity decreases with increasing  $\phi$ . In section 3.5.1 the analysis revealed  $\phi=122.56^\circ$  to be the optimal sweep angle to minimize the stiffness ratios. Figure 3.28 highlights the  $\Psi$ -sensitivity of a  $\phi=122.56^\circ$   $z$ -compliance element. An  $r$ -compliance element's taper angle sensitivity increases with  $\phi$ , as shown in Figure 3.29. The  $K_r/K_\theta$  ratio is insensitive to  $\Psi$  because the effect of  $\Psi$  on  $K_r$  is cancelled by its effect on  $K_\theta$ .

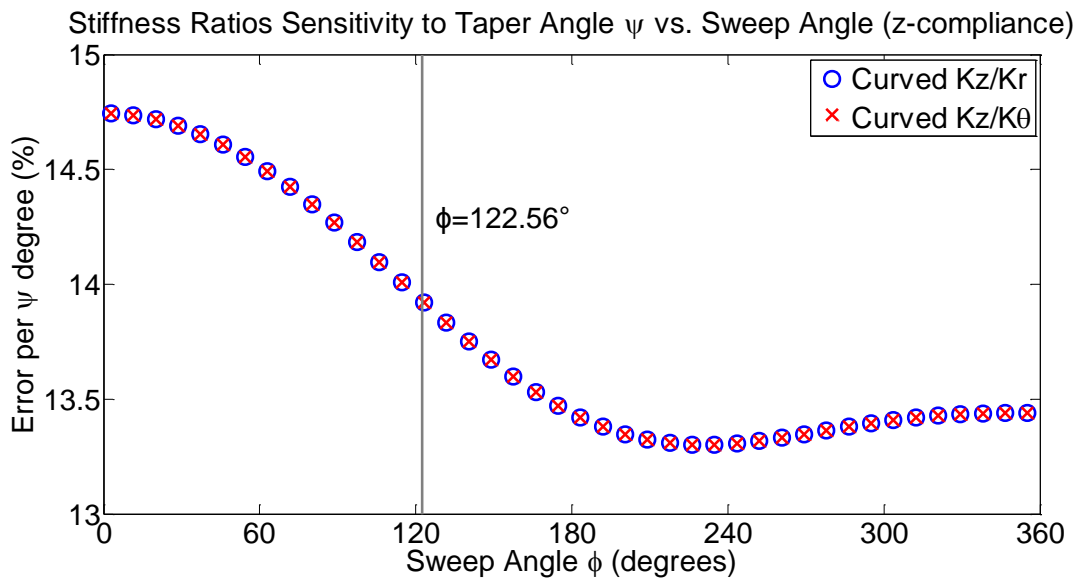


**Figure 3.28 Stiffness ratios sensitivity to taper angle,  $\Psi$ , tolerance for a  $z$ -compliance flexure vs. sweep angle,  $\phi$ . Plot shows that the percent error from predicted value depends on the sweep angle of the flexure. ( $L=60\text{mm}$ ,  $t_r=6.35\text{mm}$ ,  $t_z=1\text{mm}$ , 7075 Aluminum)**

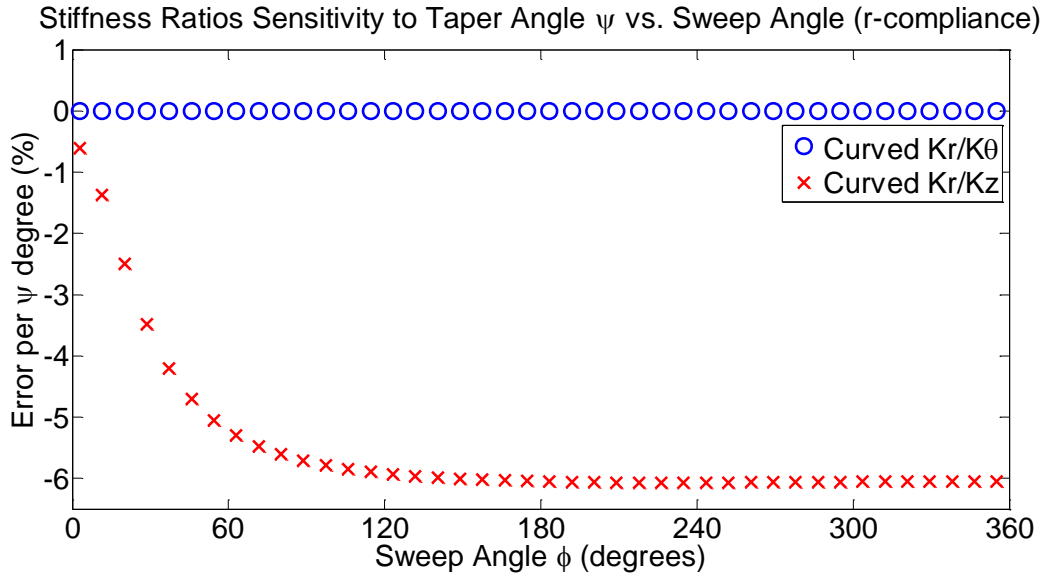


**Figure 3.29 Stiffness ratios sensitivity to taper angle,  $\Psi$ , tolerance for an  $r$ -compliance flexure vs. sweep angle,  $\phi$ . Plot shows that the percent error from predicted value depends on the sweep angle of the flexure. ( $L=60\text{mm}$ ,  $t_z=6.35\text{mm}$ ,  $t_r=1\text{mm}$ , 7075 Aluminum)**

Figure 3.20 shows that the parasitic ratios of a  $z$ -compliance element are sensitive to  $\Psi$ . The plot also demonstrates that  $\Psi$  has no effect on the parasitic ratios of a straight-beam flexure. Figure 3.30 plots the  $\Psi$ -sensitivity of  $z$ -compliance CF elements vs. the flexure's  $\phi$ . This analysis indicates that the parasitic ratios sensitivity per degree of  $\Psi$  varies with  $\phi$  but is always less than 1%. In section 3.6.2 it was established that the taper angle has no effect on the parasitic ratios for an  $r$ -compliance element, therefore, there is no  $\Psi$ -sensitivity.

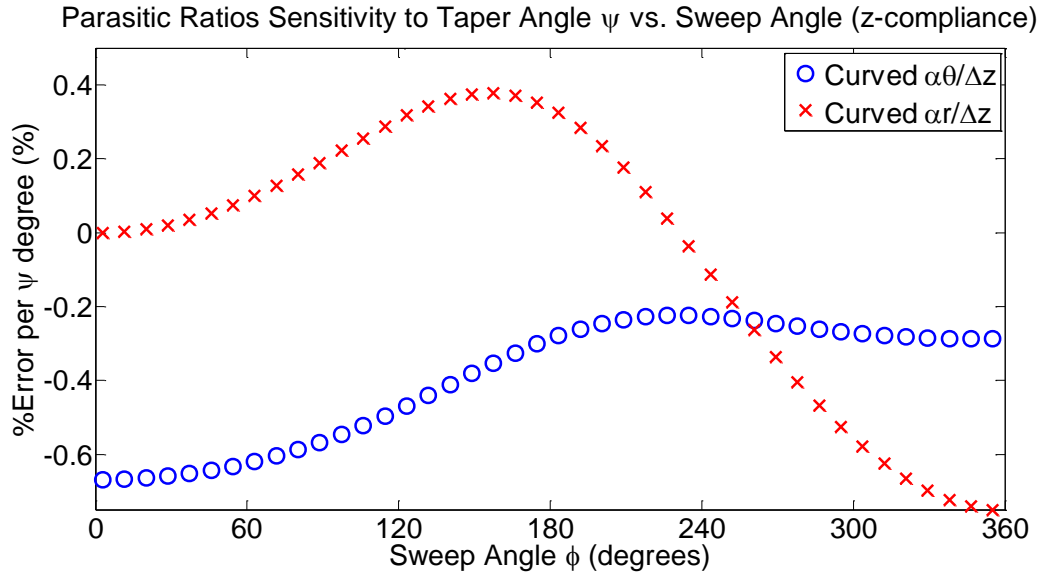


**Figure 3.30 Parasitic ratios sensitivity to taper angle,  $\Psi$ , tolerance for a  $z$ -compliance flexure vs. sweep angle,  $\phi$ . Plot shows that the percent error from predicted value depends on the sweep angle of the flexure. ( $L=60\text{mm}$ ,  $t_r=10\text{mm}$ ,  $t_z=1\text{mm}$ , 7075 Aluminum)**

### 3.7.3 Sensitivity to off-neutral position

The stiffness ratios for a flexure are established at the flexure's neutral position as defined in Figure 3.31a. Straight flexure elements are considered to be axial constraints because their  $K_\theta$  is orders of magnitude greater than their  $K_z$ . When the beam is actuated along its desired displacement,  $\Delta z$ , it moves away from its neutral position. The definition of the off-neutral position is shown in Figure 3.31b. The concern arises as to how the stiffness ratios, in particular  $K_z/K_\theta$ , change as the flexure is deflected away from its neutral position.  $K_z/K_\theta$  is of most interest because in the off-neutral position the beam is more sensitive to buckling. This same concern holds for  $z$ -compliance CFs which are also vulnerable to buckling in the  $\theta$ -direction as they are actuated along the  $z$ -direction. The off-neutral position analysis is not performed for  $r$ -compliance blade elements because it has already been shown they do not act as a  $\theta$ -constraint.



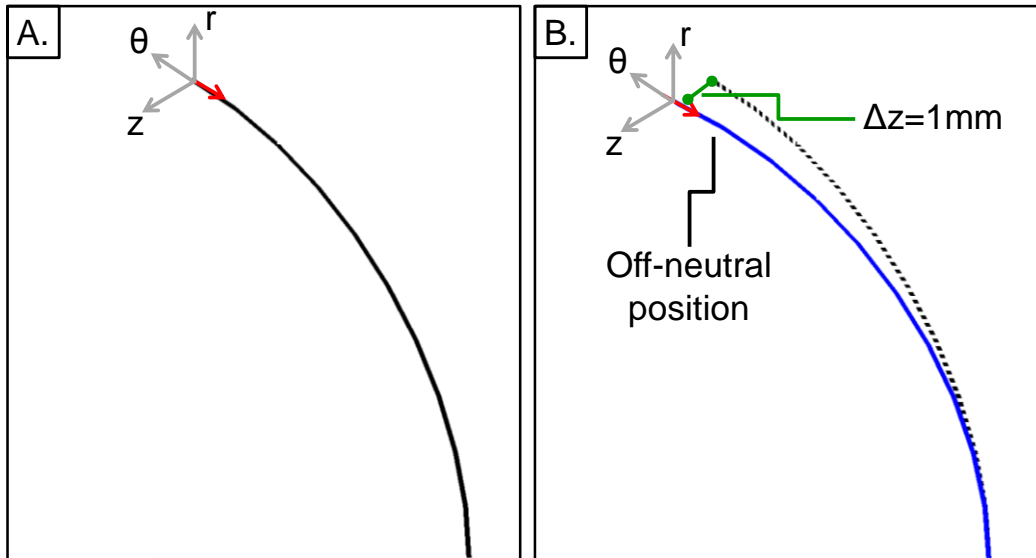


**Figure 3.31 ADINA FEA beam models used to determine  $K_\theta$ . A) Neutral position and B) Off-neutral position  $\Delta z=1\text{mm}$ .**

Figure 3.32 compares the ratio of off-neutral to neutral position stiffnesses for a  $z$ -compliance CF to those of a straight beam. In this analysis the off-neutral position is defined as  $\Delta z=1\text{mm}$ . The chart shows that the effect of the off-neutral position is most significant at large sweep angles. The study was performed using ADINA where the  $\Delta z$  displacement was first imposed and then the element was loaded with either an  $F_r$  or an  $F_\theta$  load to establish  $K_r$  and  $K_\theta$  respectively. For  $\phi \leq 330^\circ$  the off-neutral  $K_r$  and  $K_\theta$  stiffnesses are within 90% of the neutral position corresponding stiffnesses.

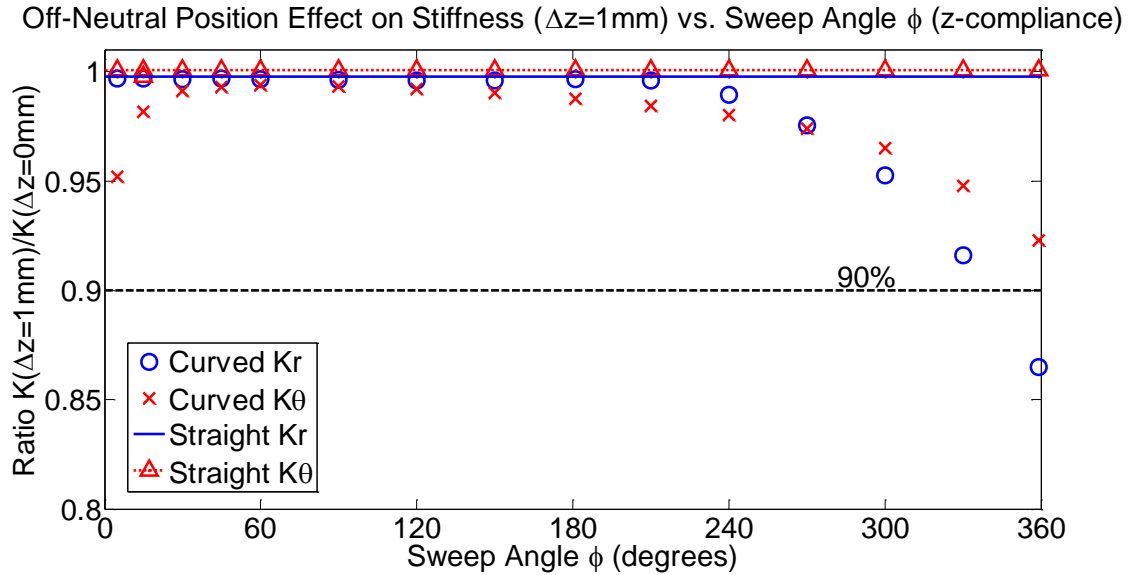


**Figure 3.32 Off-neutral position effect on the stiffness of a z-compliance flexure vs. sweep angle,  $\phi$ . Plot shows the ratio of the off-neutral position ( $\Delta z=1\text{mm}$ ) stiffness to the neutral position ( $\Delta z=0$ ) stiffness. ( $L=60\text{mm}$ ,  $t_r=10\text{mm}$ ,  $t_z=1\text{mm}$ , 7075 Aluminum)**

### 3.8 Boundary Conditions

So far all of the analysis has been conducted on fixed-free flexure blades; however, assembling flexure elements into systems imposes boundary conditions on the element's tip. It is, therefore, important to consider the effect that different boundary conditions will have on the element's performance metrics. A fixed-free element is described by a 6x6 compliance matrix; if a DOF is constrained then the compliance matrix becomes a 5x5 system. Gauss elimination can be used to remove a DOF from the compliance matrix, as shown in Figure 3.33. The boundary condition analysis presented in this section will be a key part of the system formation rules in Chapter 4. Element parasitic motions may be removed by laying out a system design such that the system imposes boundary conditions on the elements. However, one must be careful to account for the loads that are imposed on the system stages by the constraints applied on the element. This topic will be dealt with at length in Chapter 4.

<b>6x6 Fixed-free Curved Beam</b>		<b>5x5 Fixed-<math>\alpha_z=0</math> Curved Beam</b>
$\begin{pmatrix} C_{11} & C_{12} & 0 & 0 & 0 & C_{16} \\ C_{21} & C_{22} & 0 & 0 & 0 & C_{26} \\ 0 & 0 & C_{33} & C_{34} & C_{35} & 0 \\ 0 & 0 & C_{43} & C_{44} & C_{45} & 0 \\ 0 & 0 & C_{53} & C_{54} & C_{55} & 0 \\ C_{61} & C_{62} & 0 & 0 & 0 & C_{66} \end{pmatrix}$	→	$\begin{pmatrix} C_{11} - C_{61} \cdot \frac{C_{16}}{C_{66}} & C_{12} - C_{62} \cdot \frac{C_{16}}{C_{66}} & 0 & 0 & 0 \\ C_{21} - C_{61} \cdot \frac{C_{26}}{C_{66}} & C_{22} - C_{62} \cdot \frac{C_{26}}{C_{66}} & 0 & 0 & 0 \\ 0 & 0 & C_{33} & C_{34} & C_{35} \\ 0 & 0 & C_{43} & C_{44} & C_{45} \\ 0 & 0 & C_{53} & C_{54} & C_{55} \end{pmatrix}$

**Figure 3.33 Gauss elimination is used to eliminate degrees of freedom, creating the compliance matrices for elements under different boundary conditions.**

### 3.8.1 Effect on Stiffness Ratios

Imposing a boundary condition on a flexure will transform its compliance matrix as shown in Figure 3.33. This section explores the effect of imposing boundary conditions on the stiffness ratios for a  $z$ -compliance and an  $r$ -compliance element. The impact of fixing one or all of the rotations of the elements is explored because these are the DOF that are often constrained by a system. Figure 3.34 gives the stiffness ratios for a  $z$ -compliance element for different boundary conditions vs.  $\phi$ . The plot shows that constraining the parasitic rotations,  $\alpha_r$  and  $\alpha_\theta$ , of the CF increases its stiffness ratios. The magnitude of the ratios will depend on the ratio of  $t_r/t_z$  as shown in Figure 3.10; however the boundary condition effect relative to the fixed-free element will be the same. The sweep angle for which the two stiffness ratios,  $K_z/K_r$  and  $K_z/K_\theta$ , are equal is always  $\phi=122.56^\circ$  regardless of the boundary conditions.

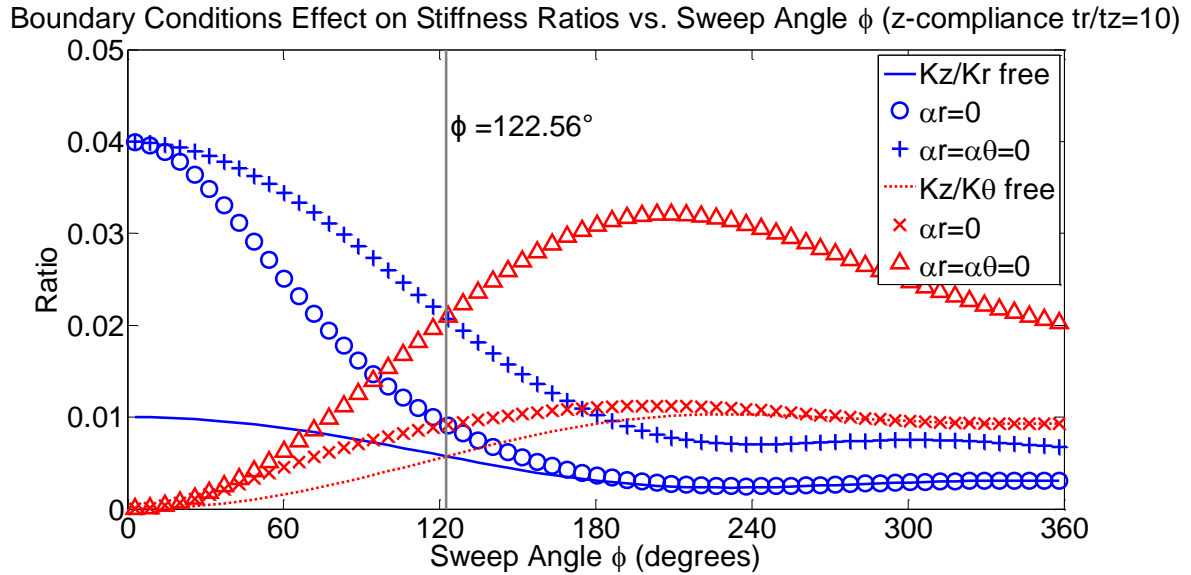


**Figure 3.34 Boundary conditions effect on stiffness ratios vs. sweep angle,  $\phi$ , for a z-compliance flexure. Plot shows that the stiffness ratios are always equal when  $\phi=122.56^\circ$ . ( $L=60\text{mm}$ ,  $t_r=10\text{mm}$ ,  $t_z=1\text{mm}$ , 7075 Aluminum)**

The effect of imposing a  $\alpha_z=0$  boundary condition on an  $r$ -compliance element is shown in Figure 3.35. The plot shows that the constrained element has higher stiffness ratios than the fixed-free element. Due to this increase in the magnitude of the stiffness ratios,  $K_r/K_\theta$  is now equal to 1 when  $\phi=90^\circ$ , and  $K_r/K_z=1$  when  $\phi=73^\circ$ . In the case of a  $\alpha_z=0$  constrained  $r$ -compliance CF the element cannot be considered a  $\theta$ -constraint when  $\phi$  is between approximately  $90^\circ$  and  $270^\circ$ . For  $\phi > 73^\circ$  the  $\alpha_z$ -constrained CF element does not act as a  $z$ -constraint. The effect of any boundary condition can be analyzed by using Gauss elimination to remove that particular DOF from the compliance matrix. When designing a flexure system the designer must recognize the boundary conditions imposed on each element and use Gauss elimination to remove those DOF that are constrained from the compliance matrix. The constrained compliance matrix should then be used in the system analysis. Appendix C presents the compliance matrices for CF elements with different tip constraints.

Boundary Conditions Effect on Stiffness Ratios vs. Sweep Angle  $\phi$  ( $r$ -compliance  $t_z/t_r=10$ )

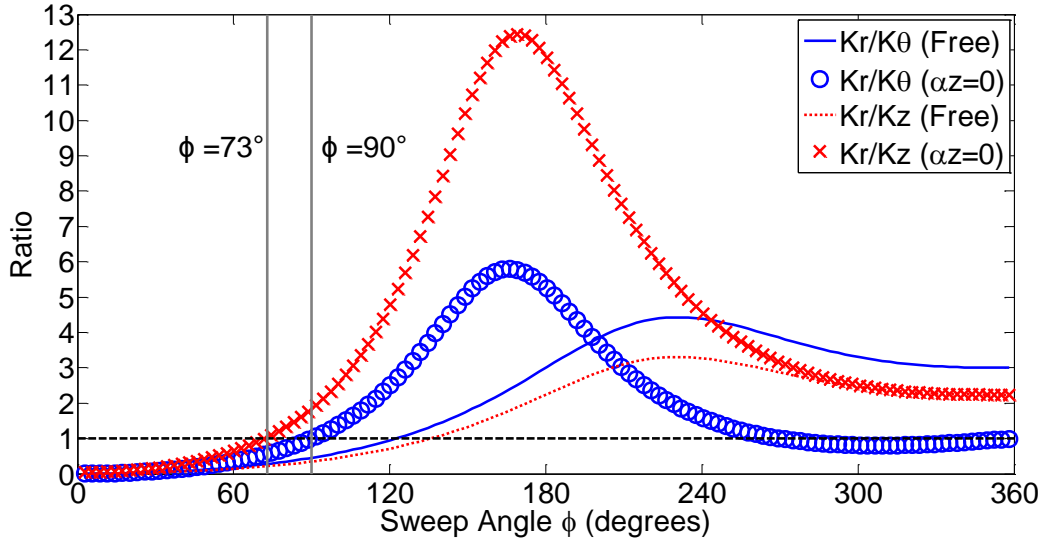


**Figure 3.35** Boundary conditions effect on stiffness ratios vs. sweep angle,  $\phi$ , for an  $r$ -compliance flexure. Plot shows that when the parasitic rotation  $\alpha_z$  is constrained, the sweep angle at which the stiffness ratio  $K_r/K_\theta=1$  decreases from  $\phi=122.6^\circ$  to  $\phi=90^\circ$ . ( $L=60\text{mm}$ ,  $t_z=10\text{mm}$ ,  $t_r=1\text{mm}$ , 7075 Aluminum)

### 3.8.2 Parasitic Ratios

Imposing boundary conditions on a compliant element will also affect its parasitic ratios. The layout of the CF system can be constructed so that it constrains a parasitic motion; however, this constraint will also have an effect on the other parasitic ratios. Figure 3.36 gives the parasitic ratios vs.  $\phi$  for a  $z$ -compliance element under two different boundary conditions. The plot shows that by constraining one of the parasitic rotations,  $\alpha_r$  or  $\alpha_\theta$ , the parasitic ratio associated with the other undesired motion increases,  $\alpha_\theta/\Delta z$  and  $\alpha_r/\Delta z$  respectively. Figure 3.37 presents the boundary conditions effect on the parasitic ratios of an  $r$ -compliance element. Setting  $\alpha_z=0$  increases the parasitic ratio of  $\Delta\theta/\Delta r$  for  $\phi$  less than approximately  $150^\circ$ . When  $90^\circ < \phi < 150^\circ$  the value for  $\Delta\theta/\Delta r$  ratio of a  $\alpha_z$ -constrained element is greater than 1, indicating a larger undesired than desired displacement.

Boundary Conditions Effect on Parasitic Ratios vs. Sweep Angle  $\phi$  (z-compliance  $t_r/t_z=10$ )

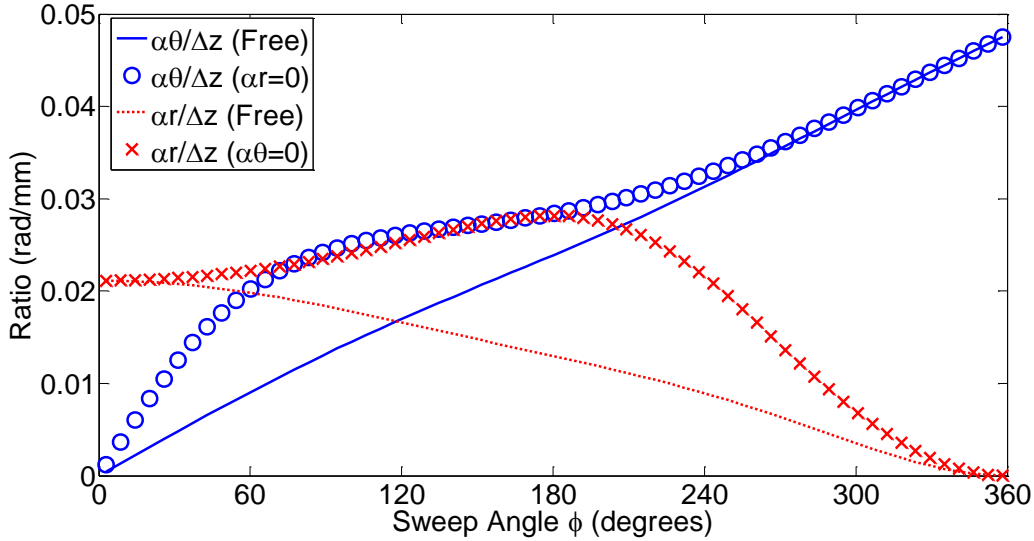


**Figure 3.36** Boundary conditions effect on the parasitic ratios vs. sweep angle,  $\phi$ , for a z-compliance flexure. Plot shows the effect that constraining one parasitic rotation has on the other parasitic ratio. ( $L=60\text{mm}$ ,  $t_r=10\text{mm}$ ,  $t_z=1\text{mm}$ , 7075 Aluminum)

Boundary Conditions Effect on Parasitic Ratios vs. Sweep Angle  $\phi$  (r-compliance  $t_z/t_r=10$ )

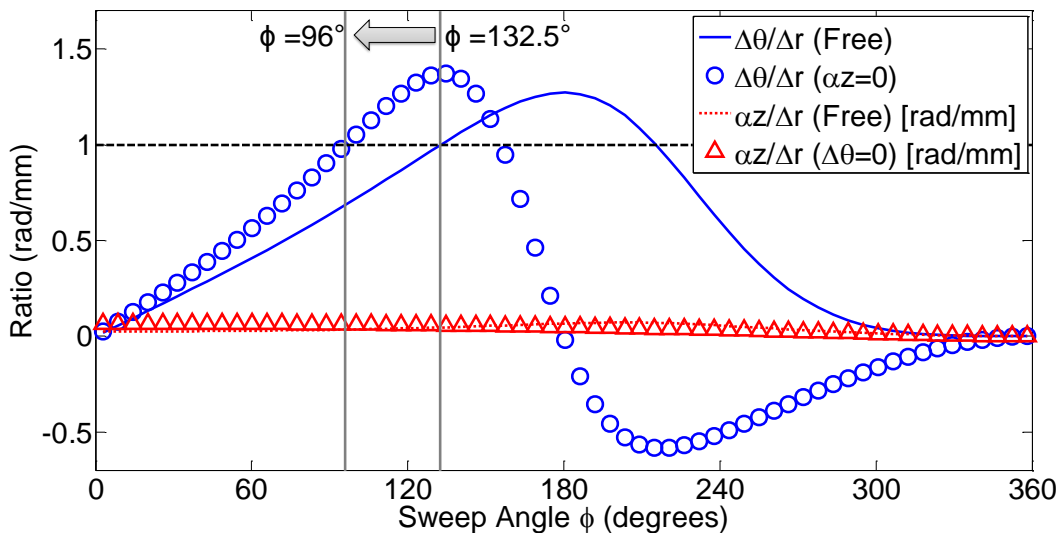


**Figure 3.37** Boundary conditions effect on the parasitic ratios vs. sweep angle,  $\phi$ , for an r-compliance flexure. Plot shows the effect that constraining the one parasitic motion,  $\alpha_z$  or  $\Delta\theta$ , has on the other parasitic ratio. For a  $\alpha_z$ -constrained element the region for which  $\Delta r > \Delta\theta$  is now limited by  $96^\circ > \phi > 150^\circ$ . ( $L=60\text{mm}$ ,  $t_z=10\text{mm}$ ,  $t_r=1\text{mm}$ , 7075 Aluminum)

### 3.9 Load location effect

Another way of removing a parasitic motion is through the location of the loading force. Essentially, if the load is applied using a lever arm both a moment and a force can be imposed on the flexure tip, as shown in Figure 3.38. The figure shows that a straight beam under an  $F_z$  will experience both the desired  $\Delta z$  and undesired  $\alpha_r$  motions. Figure 3.38b illustrates that a straight-beam under  $M_x$  will also experience two motions,  $\Delta z$  and  $\alpha_r$ . Therefore, if both an  $M_x$  and  $F_z$  are applied on the flexure's tip the  $\alpha_r$ -rotation can be removed. For a straight-beam, the  $M_x$  necessary to result in  $\alpha_r=0$  can be exerted using a single  $F_z$ , by applying the load on a stage that is  $\frac{1}{2}$  the length of the flexure, as shown in Figure 3.38c.

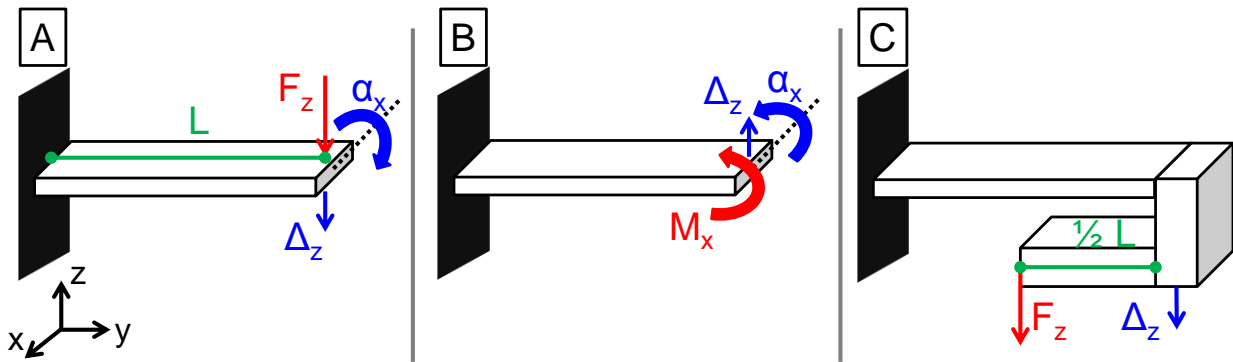


**Figure 3.38 Load location can be used to remove parasitic rotations. A) A straight-beam loaded along the  $z$ -axis experiences a desired motion,  $\Delta z$ , and a parasitic rotation,  $\alpha_x$ . B) Loading the beam with a Moment about the  $x$ -axis,  $M_x$ , at the tip of the flexure, produces a rotation,  $\alpha_x$ , and a displacement,  $\Delta z$ . C) By applying an  $F_z$  load on a stage that measures half the length,  $L$ , of the beam, an  $M_x$  moment is exerted at the tip cancelling the  $\alpha_x$  rotation. The resulting motion is a pure  $\Delta z$  displacement.**

The equation dictating the parasitic rotation for a CF can be solved to find the moment necessary to remove a parasitic rotation in terms of the applied  $F$ . For example Equation (3.16) gives the equation for the parasitic rotation  $\alpha_z$ . To find the necessary  $M_z$  to have  $\alpha_z=0$  the equation is set to equal zero and then solved for  $M_z$ . Equation (3.17) gives the required  $M_{z,\alpha_z=0}$  as a function of the applied  $F_r$  and  $F_\theta$ . In the equations  $C_{ij}$  corresponds to the  $i^{th}$  row and  $j^{th}$  column entry of the fixed-free compliance matrix. To exert the necessary moments the load on the flexure must be applied a distance from the tip of the beam. Figure 3.39 shows that the location of the load relative to the free-end of the beam is given by the radius to the load location,  $R_L$ , and the angle from the tip of the flexure to the loading point,  $\gamma$ .

$$\alpha_z = C_{61} \cdot F_\theta + C_{62} \cdot F_r + C_{66} \cdot M_z = 0 \quad (3.16)$$

$$M_{z,\alpha z=0} = \frac{-C_{61} \cdot F_\theta - C_{62} \cdot F_r}{C_{66}} \quad (3.17)$$

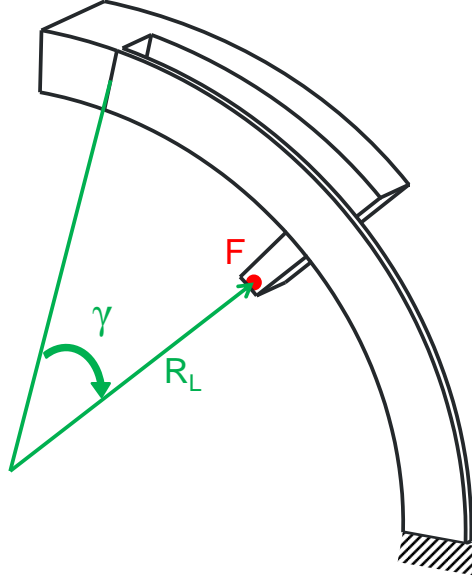


**Figure 3.39 Location of applied load on a  $z$ -compliance element. The loading point is defined by the radius to the load location,  $R_L$ , and the angle between the tip of the flexure and the loading point,  $\gamma$ .**

In the case of a  $z$ -compliance CF there are two parasitic rotations to consider,  $\alpha_r$  and  $\alpha_\theta$ . To remove these rotations the effect of both  $M_r$  and  $M_\theta$  must be considered. Equations (3.18) and (3.19) give the  $M_{r,\alpha r=\alpha\theta=0}$  and  $M_{\theta,\alpha r=\alpha\theta=0}$ , that must be applied to the tip of the flexure to remove both  $\alpha_r$  and  $\alpha_\theta$ . If the CF system in question is constructed out of cylindrical stock the load would have to be applied along  $R$  to have a monolithic system. For  $R_L=R$  Figure 3.40 shows the  $\gamma$  at which the load would have to be exerted to remove the parasitic rotations of a  $z$ -compliance element vs.  $\phi$ . The chart gives  $\gamma$  as the fraction of  $\phi$ . It is observed that  $\gamma/\phi$  for  $\alpha_r=0$  approaches 0.5 as  $\phi \rightarrow 0$ , which is consistent with the straight-beam result presented in Figure 3.38. The plot demonstrates that there is no common  $\gamma$  that would remove both  $\alpha_r$  and  $\alpha_\theta$ . Consequently, in order to remove both  $z$ -compliance parasitic rotations by load location  $R_L$  cannot equal  $R$ . Figure 3.41 gives the  $F_z$  load location necessary to set  $\alpha_z=\alpha_\theta=0$ . The location is given as the ratio of  $R_L/R$  and  $\gamma/\phi$  for different sweep angles.



$$M_{\theta, \alpha r = \alpha \theta = 0} = \left( C_{35} - C_{34} C_{55} / C_{45} \right) \cdot \left( \frac{F_z}{-C_{45} + C_{55} C_{44} / C_{45}} \right) \quad (3.18)$$

$$M_{r, \alpha r = \alpha \theta = 0} = \left( \frac{-C_{34}}{C_{45}} F_z \right) \cdot \left( \frac{C_{44}}{C_{45}} M_{\theta, \alpha r = \alpha \theta = 0} \right) \quad (3.19)$$

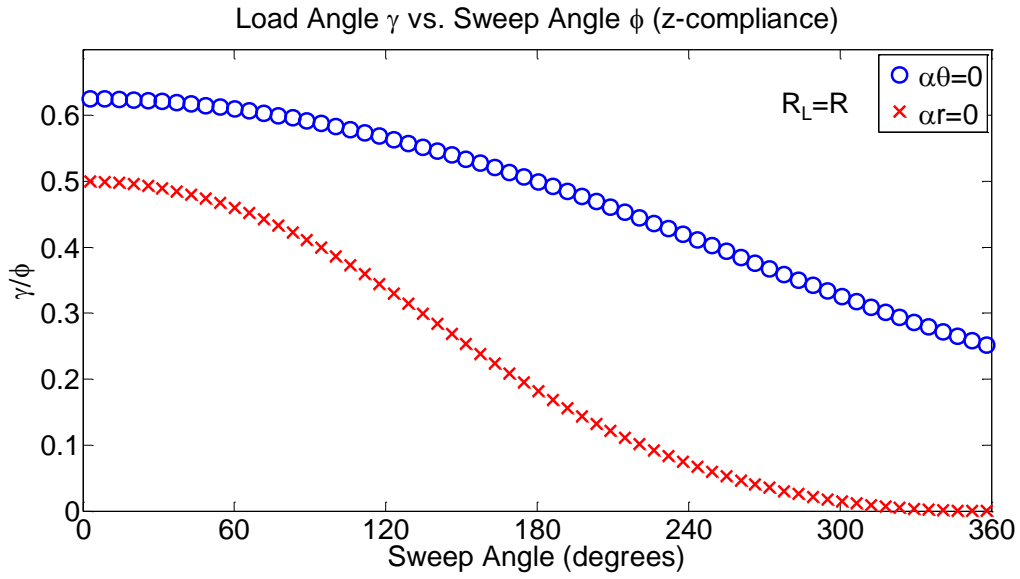


**Figure 3.40**  $F_z$  load location required to remove each parasitic rotation given  $R_L=R$ . Plot shows the ratio of  $\gamma/\phi$  vs. sweep Angle,  $\phi$ , for a z-compliance element.  $\gamma$  is measured from the tip of the flexure.

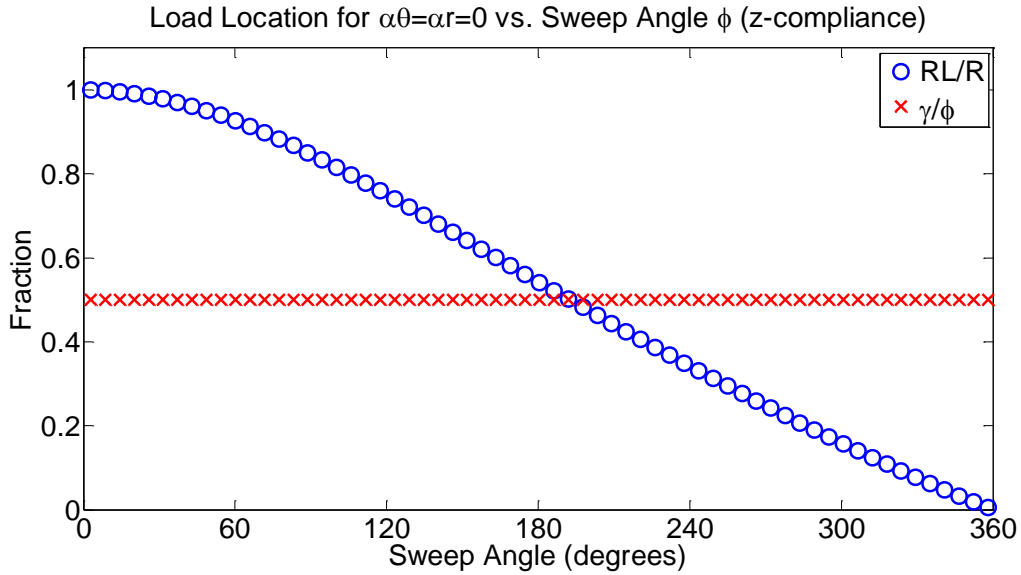


**Figure 3.41**  $F_z$  load location required to remove the element's parasitic rotations,  $\alpha_\theta$  and  $\alpha_r$ . Plot gives the ratios of  $\gamma/\phi$  and  $R_L/R$  vs. Sweep Angle,  $\phi$ , for a  $z$ -compliance element.  $\gamma$  is measured from the tip of the flexure.

To establish the load location necessary to remove the parasitic rotation of an  $r$ -compliance element, only  $M_z$  needs to be considered. Figure 3.42 gives the location  $\gamma$  of  $F_r$  necessary to result in  $\alpha_z=0$  as a function of  $\phi$ , for  $R_L=R$ . Once again, the  $\gamma/\phi$  tends to 0.5 as the curvature of the beam approaches zero. As  $\phi$  increases  $\gamma/\phi$  approaches zero because, as Figure 3.18 shows, the parasitic ratio  $\alpha_z/\Delta\theta$  tends to zero with increasing  $\phi$ .

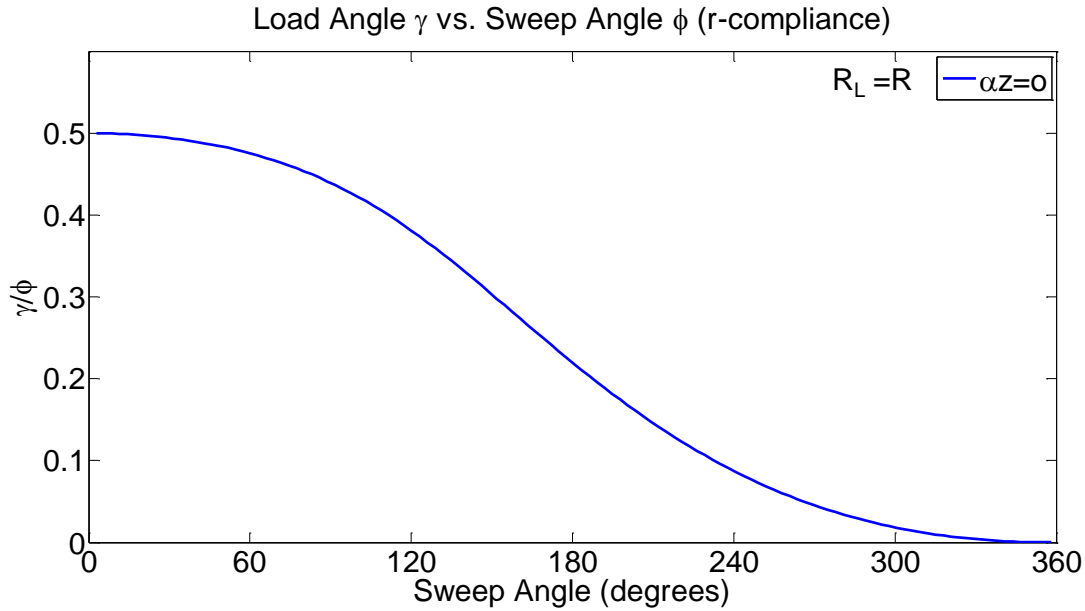


**Figure 3.42**  $F_r$  load location required to remove the element's parasitic rotation given  $R_L=R$ . Plot gives the ratio of  $\gamma/\phi$  vs. Sweep Angle,  $\phi$ , for an  $r$ -compliance element.  $\gamma$  is measured from the tip of the flexure.

### 3.10 Stress Model

The range of a flexure is determined by the maximum stress imposed on a flexure due to a load, its displacement under that load, and the flexure material's yield stress. Accurately calculating the stress on the beam is, therefore, critical in ensuring the element is not actuated past its elastic range. In the following sections the stress models for an  $r$ -compliance and a  $z$ -compliance element are presented. The stress models for CF elements are complicated by the fact that the maximum stress does not always occur at the base of the beam as it does in straight-beams. Other than that, the model for an  $r$ -compliance flexure is very similar to that of a straight-beam. The  $z$ -compliance model is more complex because as Figure 1.6 shows a  $z$ -compliance beam suffers from a stress concentration at its inner radius. This stress concentration has to be accounted for in the  $z$ -compliance stress model. The stress models presented are based on Euler-Bernoulli bending theory (thin-beams) and utilize the VonMises Yield criterion.

### 3.10.1 $r$ -Compliance and $\theta$ -Compliance

The first step in establishing the stress model for an  $r$ -compliance or  $\theta$ -compliance beam is to identify the moments acting on the beam. Figure 3.43 presents the moments resulting from: A) an  $F_r$  load and B) an  $F_\theta$  load. Both loading conditions produce a single bending moment,  $m_z$ , on the flexure. Equation (3.21) gives  $m_z$  as a function of the location,  $R\lambda$ , along the length of beam and the applied  $F_r$  and  $F_\theta$ .  $\lambda$  is measured from the free-end of the beam. The location of the maximum  $m_z$ ,  $\lambda_{max}$ , can be found by taking the derivative of Equation (3.21) with respect to  $\lambda$ . The  $\lambda$  for which  $\partial m_z / \partial \lambda = 0$  gives the location of the maximum  $m_z$ . If the  $\lambda$  calculated is greater than  $\phi$ , then  $\lambda_{max} = \phi$  and the max  $m_z$  is found at the base of the beam. Both  $r$ -compliance and  $\theta$ -compliance CF elements experience only one bending moment, therefore, the location of the max  $m_z$  is the location of the maximum stress. Figure 3.44 gives  $\lambda_{max}$  vs.  $\phi$  for an  $r$ -compliance flexure under a pure  $F_r$ . Similarly, Figure 3.45 shows  $\lambda_{max}$  as a function of  $\phi$  for a  $\theta$ -compliance beam under a pure  $F_\theta$ .

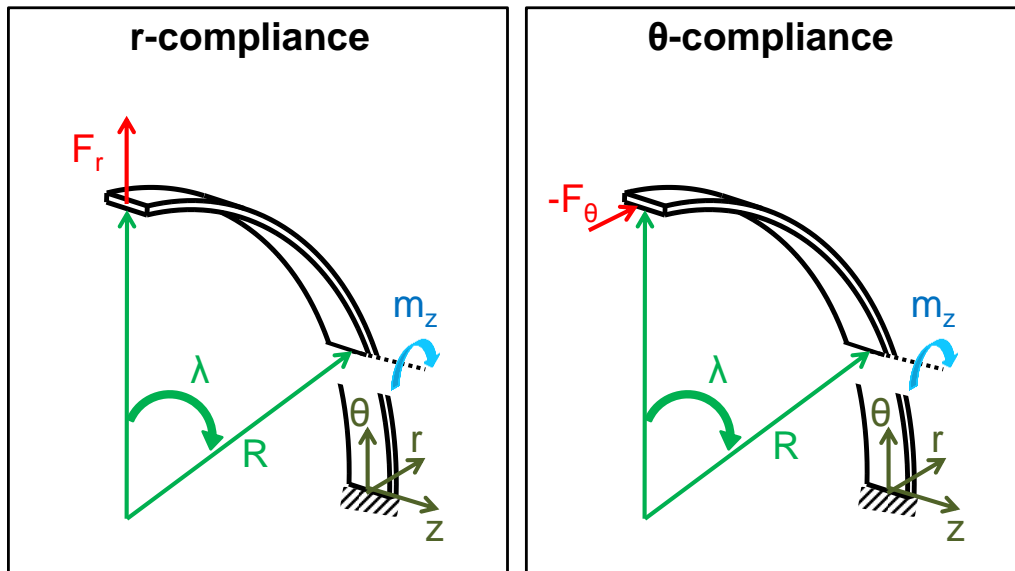


**Figure 3.43** Resulting moments on  $r$ -compliance and  $\theta$ -compliance elements as a result of loading at the tip. Both elements experience a single bending moment,  $m_z$ , when loaded under  $F_r$  and  $F_\theta$  respectively. The bending moment varies along the length of the beam. The position of the resulting moments is given by  $R\lambda$ , where  $\lambda$  is measured from the tip of the beam.

$$m_z = F_r R \sin \lambda - F_\theta R (1 - \cos \lambda), \lambda \leq \phi \quad (3.20)$$

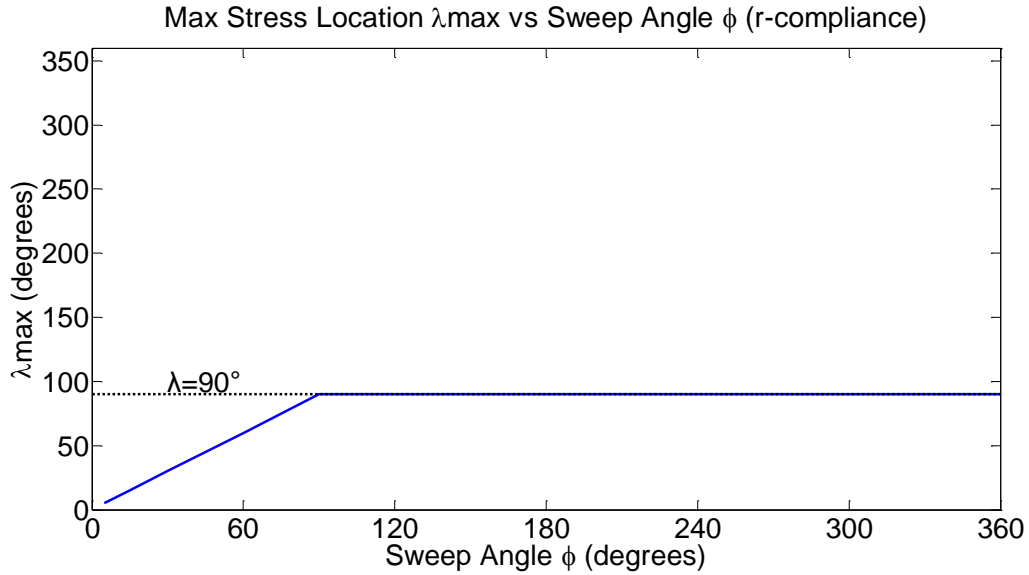


**Figure 3.44** Maximum stress location,  $\lambda_{max}$ , vs. sweep angle,  $\phi$ , for an  $r$ -compliance element under a pure  $F_r$  load.

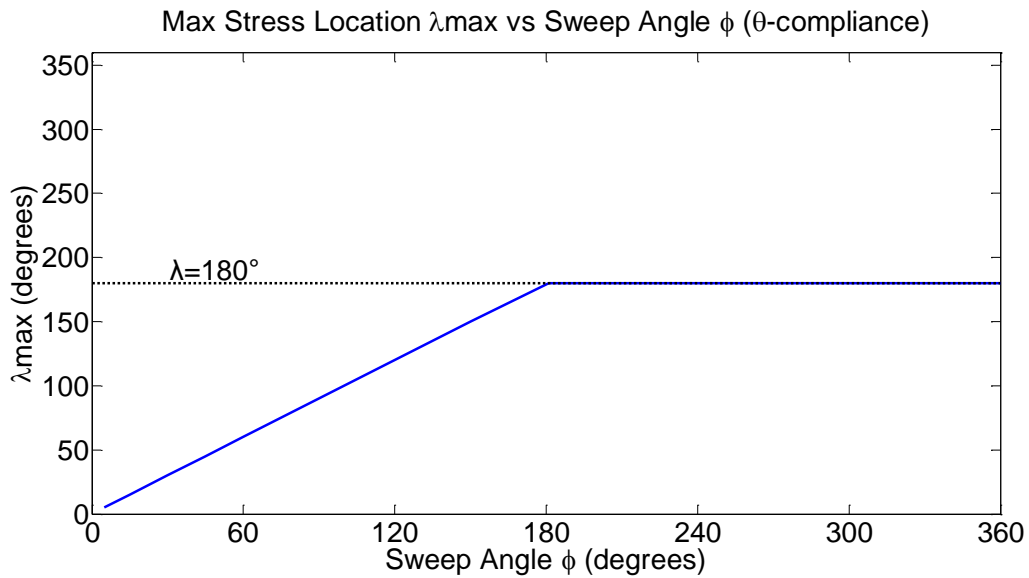


**Figure 3.45** Maximum stress location,  $\lambda_{max}$ , vs. sweep angle,  $\phi$ , for a  $\theta$ -compliance element under a pure  $F_\theta$  load.

Equation (3.21) gives the stress model,  $\sigma_{von-r}$ , for both an  $r$ -compliance and  $\theta$ -compliance beam as a function of  $m_z$  [27]. This model is compared to the FEA results for the maximum VonMises stress of an  $r$ -compliance in Figure 3.46 and a  $\theta$ -compliance element in Figure 3.47. The plots show the normalized maximum stress for flexures of different  $\phi$ . The stress is

normalized using the FEA-calculated stress for a straight-beam of the same dimensions subjected to the same load.

$$\sigma_{\theta\theta-mz} = \sigma_{von-r} = \frac{m_z t_r/2}{t_r t_z \left( R - t_r/2 \right) e} \quad (3.21)$$

$$e = t_r/2 - 2R/t_r - \frac{2}{\log\left(\frac{2R/t_r + 1}{2R/t_r - 1}\right)}$$

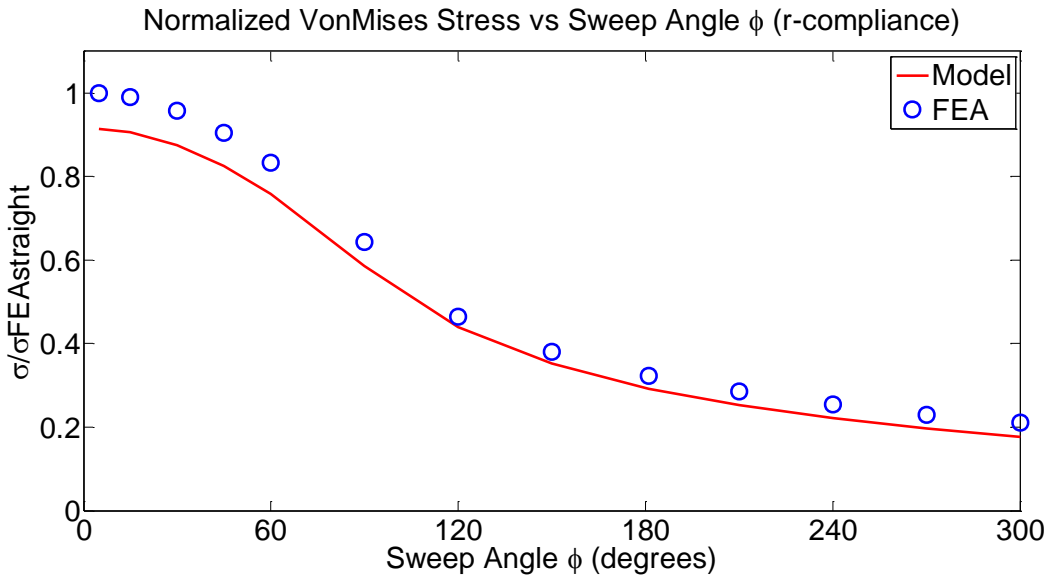


**Figure 3.46 Normalized VonMises stress vs. sweep angle,  $\phi$ , for an  $r$ -compliance element. Stress is normalized using the 3D-solid FEA stress value for a straight-beam of the same dimensions under the same load.**

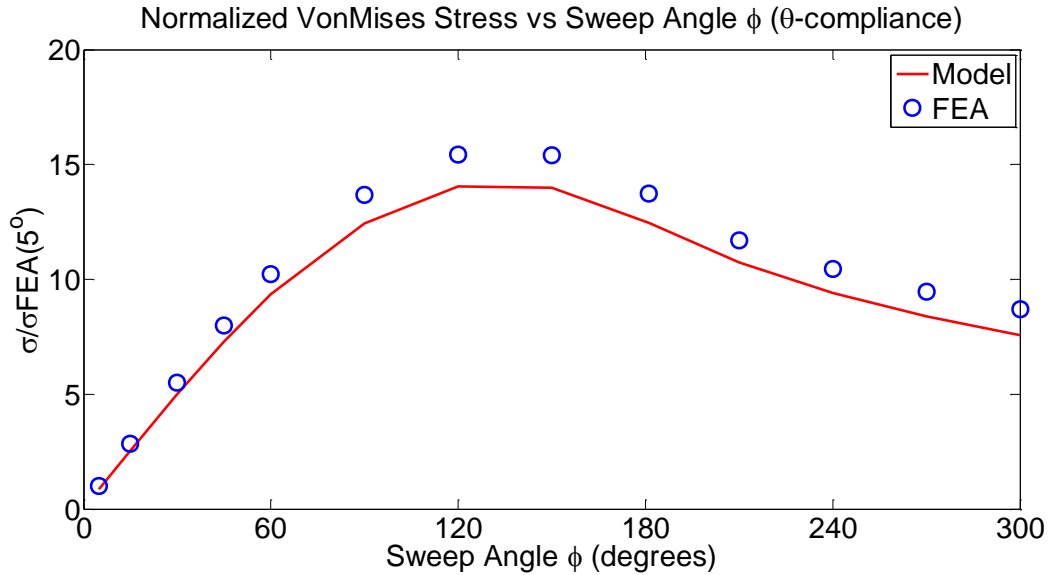


**Figure 3.47 Normalized VonMises stress vs. sweep angle,  $\phi$ , for a  $\theta$ -compliance element. Stress is normalized using the 3D-solid FEA stress value for a straight-beam of the same dimensions under the same load.**

Now that the stress model has been corroborated using FEA, the range of the elements can be calculated using the beam's compliance and the material's yield strength. Figure 3.48 gives the normalized range for an  $r$ -compliance flexure under an  $F_r$  load vs.  $\phi$ . The range for the CF is normalized using the range of a straight-beam of the same dimensions and of the same material. The dotted line in the plot indicates when the normalized range is equal to 1, below this line the range of the curved-beam is less than that of its straight-beam counterpart. For  $\phi \leq 90^\circ$  the  $r$ -compliance CF has a greater range than a straight beam. Figure 3.49 shows the effect of  $\phi$  on the normalized range of a  $\theta$ -compliance element subjected to an  $F_\theta$  load. In this plot the range is normalized using the range of the  $\phi=5^\circ$   $\theta$ -compliance element.

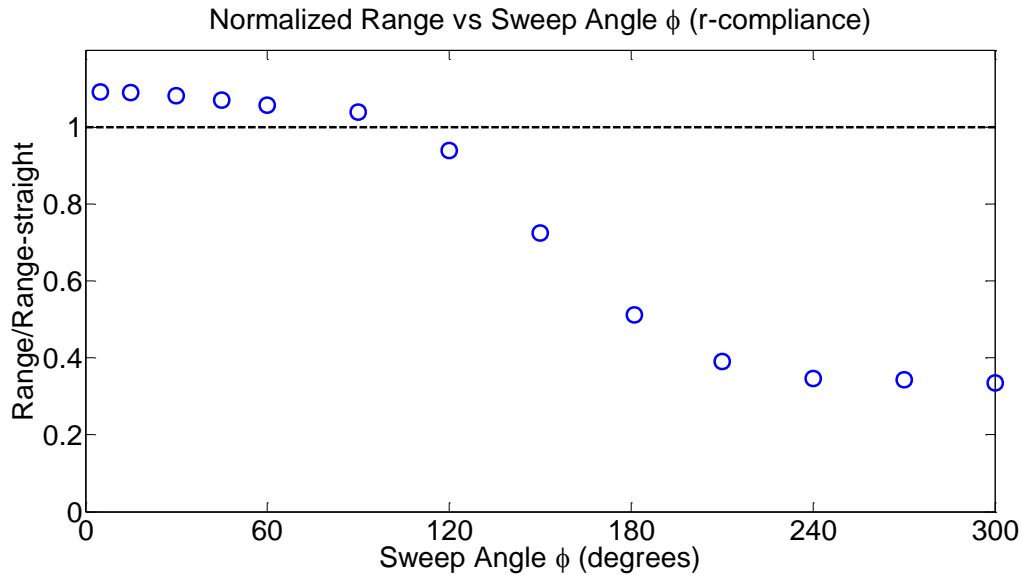


**Figure 3.48** Normalized range vs. sweep angle,  $\phi$ , for an  $r$ -compliance element under an  $F_r$  load. Range is normalized using the range value for a straight-beam of the same dimensions.

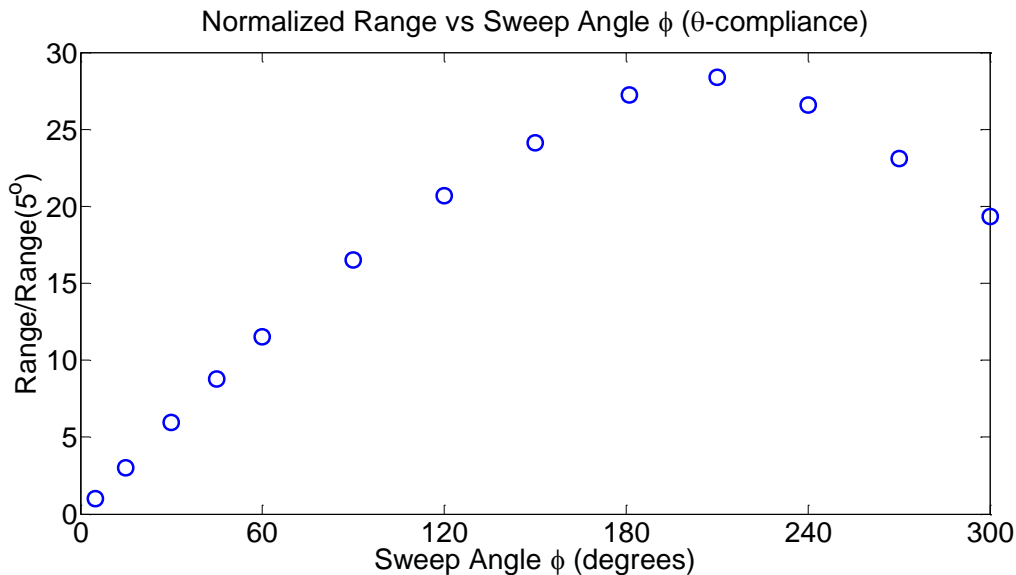


**Figure 3.49** Normalized range vs. sweep Angle,  $\phi$ , for a  $\theta$ -compliance element under an  $F_\theta$  load. Stress is normalized using the range value for a  $\phi=5^\circ$  element.

A range plot can be deceiving because it does not give any information about the length of the flexure. A better measure of the performance of the compliant element is to look at the ratio of the range to  $R$ . This ratio provides information about the flexure's range compared to its footprint. The CF's range/ $R$  ratio is compared to the straight-beam's range/ $L$  ratio. Figure 3.50 gives the range/ $R$  for an  $r$ -compliance element under  $F_r$  vs.  $\phi$ . The plot shows that for  $\phi \geq 60^\circ$  the



CF elements provide a better solution when the designer faces footprint constraints. Figure 3.51 presents the range/ $R$  for a  $\theta$ -compliance flexure loaded with  $F_\theta$  vs.  $\phi$ , and indicates that a larger  $\phi$  will result in a larger range/ $R$  ratio.

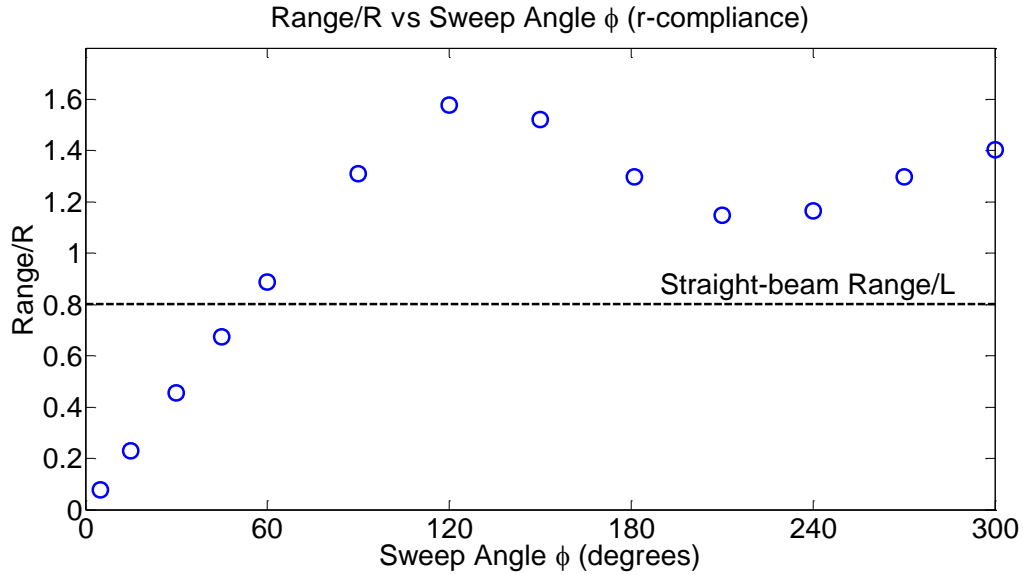


**Figure 3.50** Range/ $R$  vs. sweep angle,  $\phi$ , for an  $r$ -compliance element under  $F_r$ . Dotted line shows the range/ $L$  for a straight-beam element of the same dimensions.

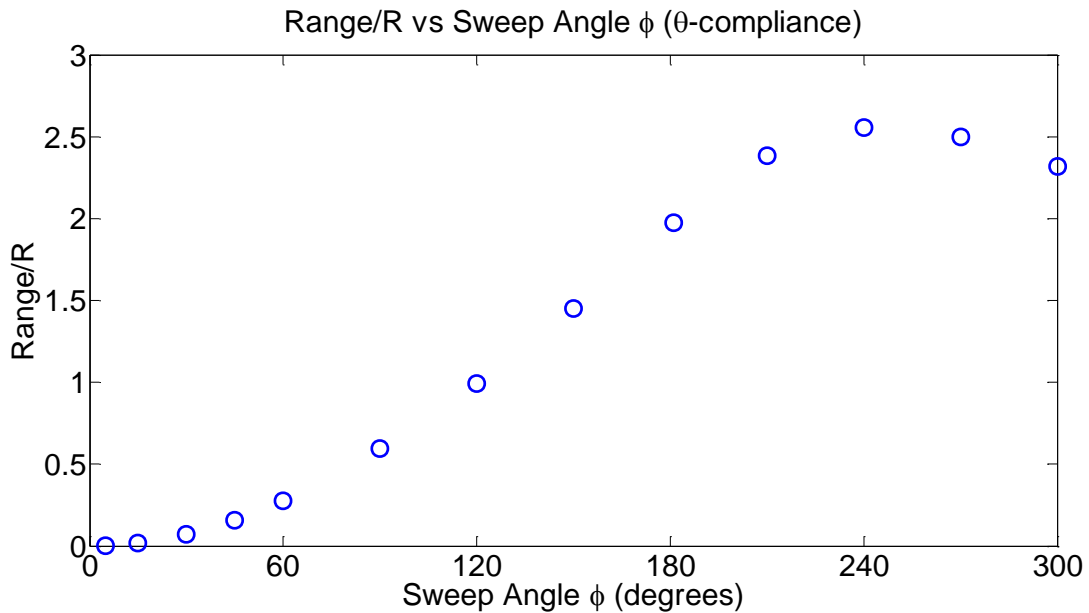


**Figure 3.51** Range/ $R$  vs. sweep angle,  $\phi$ , for a  $\theta$ -compliance element under  $F_\theta$ .

### 3.10.2 $z$ -compliance

The stress model for a  $z$ -compliance element is more complex because an  $F_z$  load results in both a bending moment,  $m_r$ , and a shear moment,  $m_\theta$ , acting on the beam, as shown in Figure 3.52. The magnitude of the resulting moments depends on where along the length of the beam,  $R\lambda$ , the analysis is conducted. Equations (3.22) and (3.23) are used to calculate  $m_r$  and  $m_\theta$ .

Finding the location of the maximum stress is not as simple in the  $z$ -compliance case as it was in the  $r$ -compliance case because there are two moments contributing to the stress on the beam. The bending moment,  $m_r$ , results in an axial stress,  $\sigma_{\theta\theta-mr}$ , given by Equation (3.24); while  $m_\theta$  produces a shearing moment  $\sigma_{\theta r-m\theta}$  expressed in Equation (3.25) [32]. In the first stress model,  $\sigma_{vonl-z}$ , only these two stresses were considered, Equation (3.26) gives the equation for  $\sigma_{vonl-z}$ . The value of  $\sigma_{vonl-z}$  for different values of  $\lambda$  was calculated to find  $\lambda_{max}$ . Figure 3.53 gives the value of  $\lambda_{max}$  as a function of  $\phi$  for a sample  $z$ -compliance beam. The plot shows that the maximum stress does not always occur at the base of the beam. The value for  $\lambda_{max}$  does not depend on the magnitude of  $F_z$ .

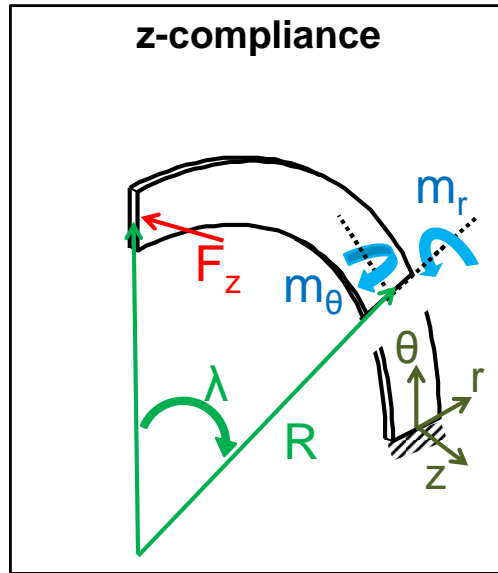


**Figure 3.52 Resulting moments on  $z$ -compliance element as a result of loading at the tip. Element experience a bending moment,  $m_r$ , and a twisting moment,  $m_\theta$ , when loaded under  $F_z$ . The resulting moments vary along the length of the beam. The position of the resulting moments is given by  $R\lambda$ , where  $\lambda$  is measured from the tip of the beam.**

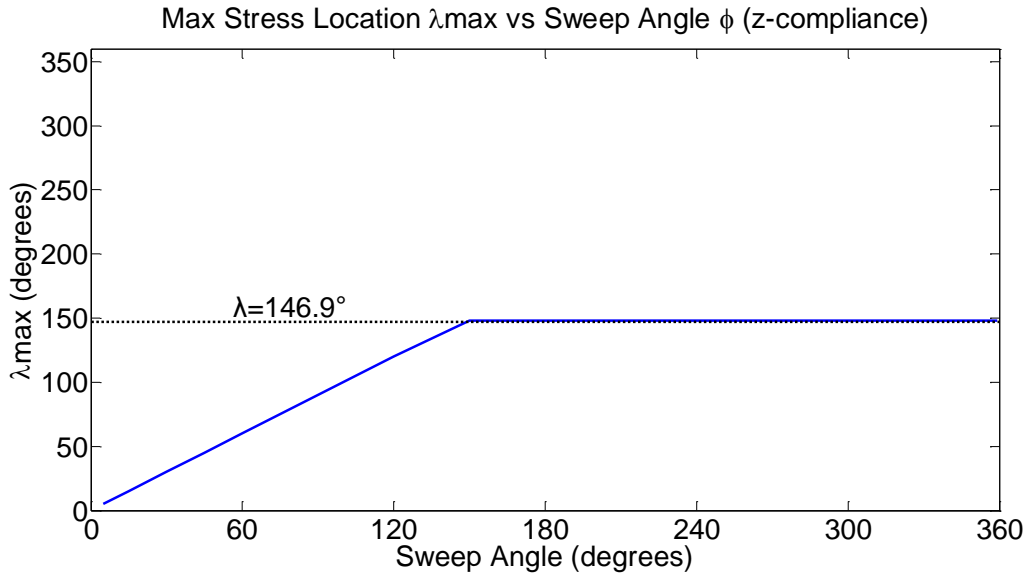
$$m_r = -F_z R \sin \lambda, \lambda \leq \phi \quad (3.22)$$

$$m_\theta = -F_z R (1 - \cos \lambda), \lambda \leq \phi \quad (3.23)$$

$$\sigma_{\theta\theta-mr} = \frac{m_r t_z / 2}{I_r} \quad (3.24)$$

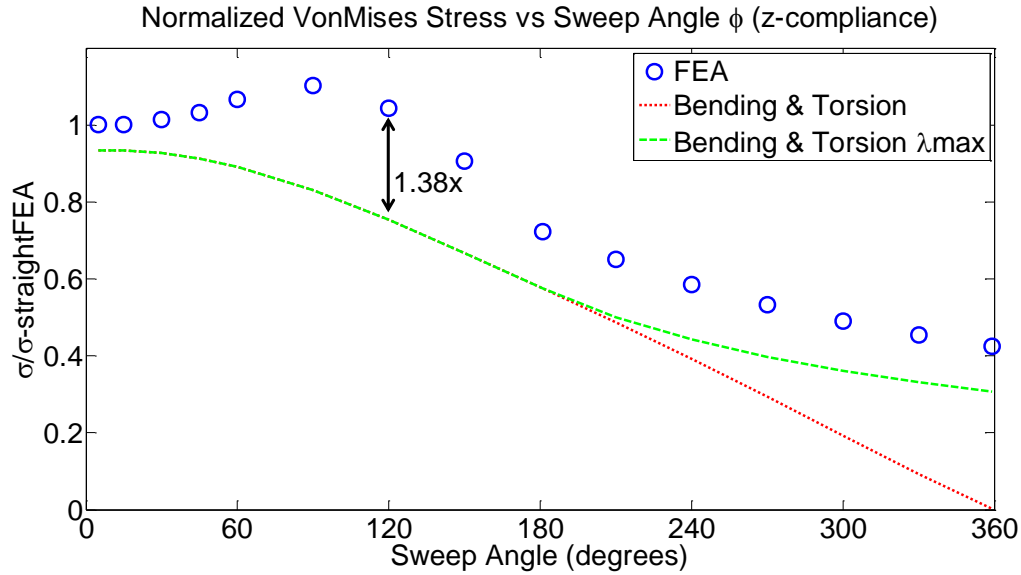
$$\sigma_{\theta r-m\theta} = \frac{m_\theta}{t_r t_z^2} \cdot \left( 3 + \frac{1.8}{t_r/t_z} \right) \quad (3.25)$$

$$\sigma_{von1-z} = \sqrt{\sigma_{\theta\theta-mr}^2 + 3(\sigma_{\theta r-m\theta})^2} \quad (3.26)$$



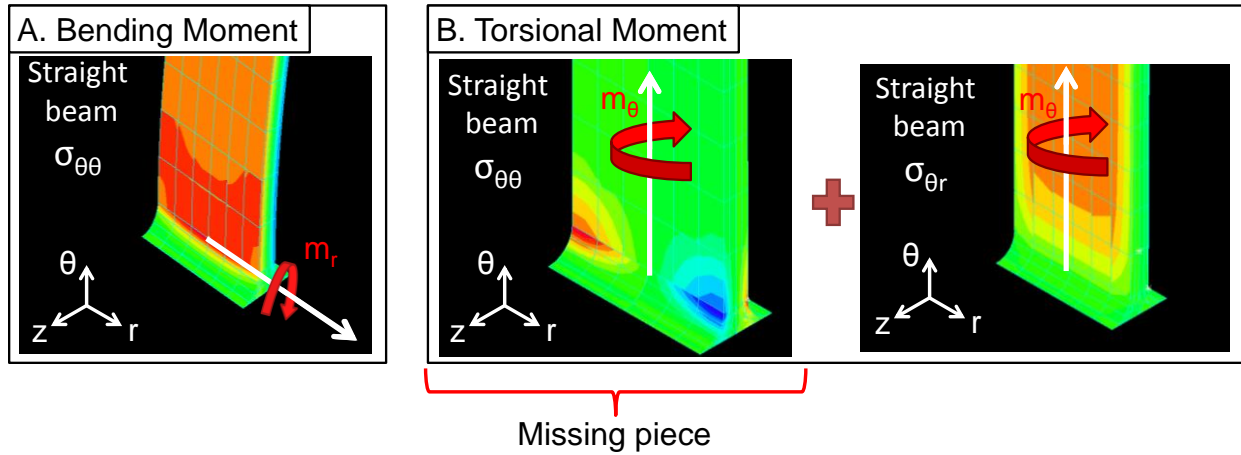
**Figure 3.53 Maximum stress location,  $\lambda_{max}$ , vs. sweep angle,  $\phi$ , for a z-compliance element under a pure  $F_z$  load. ( $L=60\text{mm}$ ,  $t_r=6.4\text{mm}$ ,  $t_z=0.6\text{mm}$  7075 Aluminum)**

Figure 3.54 shows the normalized FEA Von Mises stress vs.  $\phi$  and compares it to the value calculated using  $\sigma_{von1}$  at  $\lambda_{max}$  (Bending & Torsion  $\lambda_{max}$ ). The stress values are normalized using the FEA-stress for a straight-beam of the same dimensions under the same  $F_z$  loading. The plot also presents the  $\sigma_{von1}$  at the base of the beam (Bending & Torsion). The figure demonstrates the importance of calculating  $\sigma_{von1}$  at  $\lambda_{max}$  as opposed to assuming the max stress occurs at the base of the flexure. The plot also shows that the FEA stress is up to 1.38x the  $\sigma_{von1}$ . In other words, the stress model is incomplete because there is a stress that is not being accounted for by  $\sigma_{von1}$ .



**Figure 3.54 Normalized maximum VonMises stress vs. sweep angle,  $\phi$ , for a z-compliance element. Stress is normalized using the 3D-solid FEA stress value for a straight-beam of the same dimensions under the same load. Plot compares the FEA stress values to the stress calculated by a stress model that considers the bending axial stress and the torsion shear stress on the beam at the base of the beam (Bending & Torsion) and a stress model that gives the stress at  $\lambda_{max}$  (Bending & Torsion  $\lambda_{max}$ ).**

The missing stress component was discovered by analyzing the stress distribution of a straight beam under a bending moment and under a torsional moment. The major stress components under these two loading conditions are shown in Figure 3.55. Figure 3.55b shows that under a torsional moment the rectangular beam experiences both  $\sigma_{\theta r-m\theta}$  and  $\sigma_{\theta\theta-m\theta}$ . This  $\sigma_{\theta\theta-m\theta}$  was not considered in  $\sigma_{von1-z}$ . If all three stress distributions are summed together one can see that the  $\sigma_{\theta\theta-m\theta}$  adds to  $\sigma_{\theta\theta-mr}$  at the inner radius of the beam leading to the stress concentration.



**Figure 3.55 ADINA FEA images showing the major stress components on a straight-beam under a A) bending moment and B) a torsional moment. The axial stress,  $\sigma_{\theta\theta-m\theta}$ , due to twisting is highlighted because it is the missing component from the original stress model,  $\sigma_{von1-z}$ .**

Once the missing component of the stress model had been identified the challenge became determining what could account for  $\sigma_{\theta\theta-m\theta}$ . Non-circular beams under torsional loading with a fixed-end experience additional bending stresses. These stresses are caused by the elongation of the outer fibers during twisting and because of the warping restraint at the fixed end [27]. For a rectangular beam of closed cross-section, these warping stresses are usually small compared to the torsional shear stresses. However, in a  $z$ -compliance CF element these longitudinal warping stresses are significant because they act in conjunction with the bending stresses on the beam. A parametric study was used to create a model for the warping stress of a  $z$ -compliance element. The warping stress equations for beams with other cross-sections were used as the basis of the parametric study [27]. Table 3.4 lists the range of values of the parameters considered in the study.

**Table 3.4: Range of values used for each of the components included in the stress model parametric study.**

	$L/w$	$t_r/t_z$	$F$	Materials	$E$	$G$
<b>Range of values</b>	3-150	3-100	.001-100 N	7075 Aluminum	7.20e10 Pa	2.69e10 Pa
				Titanium-Grade 5	1.05e11 Pa	3.80e10 Pa

Equation (3.27) gives the stress model for  $\sigma_{\theta\theta-m\theta}$  at the inner radius of the beam; the model was developed through the parametric study. The original Von Mises stress model had to be updated to include the effect of the warping stress. The final model for the stress of a  $z$ -compliance element,  $\sigma_{von2-z}$ , is given by Equation (3.28). Figure 3.56 compares the normalized FEA-stress values to the final stress model,  $\sigma_{von2-z}$ , which includes the warping stress correction. The stresses are normalized using the FEA-stress value for a straight-beam with the same dimensions under the same loading conditions as the  $z$ -compliance elements. The plot shows that for this particular beam the presented stress model is able to accurately predict the stress on the beam. Figure 3.57 demonstrates that the presented stress model is able to accurately predict the stress of  $z$ -compliance elements for reasonable values of  $t_r/t_z$  and  $L/t_r$ . The plot compares FEA-stress values of beams with  $\phi=120^\circ$  with different lengths and cross-sections, to the model predicted stress.

$$\sigma_{\theta\theta-m\theta} = \frac{.6544}{\sqrt{L/10t_r}} \cdot \left(\frac{E}{G}\right)^{0.5} \cdot \sigma_{\theta r-m\theta} \cdot \left(1 + \frac{t_r}{100t_z}\right) \cdot \tanh \lambda_{max} \quad (3.27)$$

$$\sigma_{von2-z} = \sqrt{(\sigma_{\theta\theta-mr} + \sigma_{\theta\theta-m\theta})^2 + 3(\sigma_{\theta r-m\theta})^2} \quad (3.28)$$

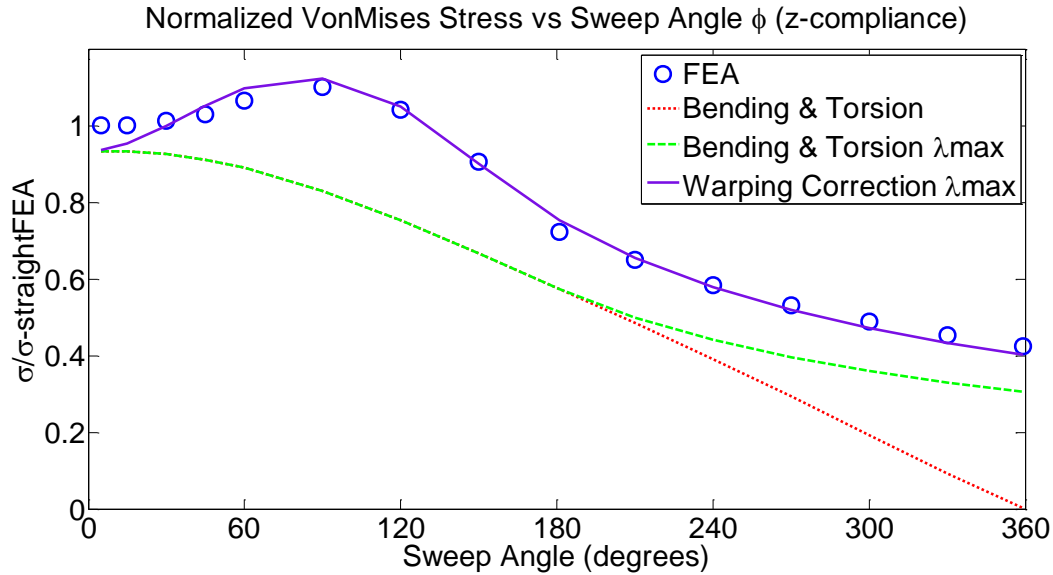


**Figure 3.56** Normalized maximum Von Mises stress vs. sweep angle,  $\phi$ , for a  $z$ -compliance element. Stress is normalized using the 3D-solid FEA stress value for a straight-beam of the same dimensions under the same load. Plot compares the FEA stress values to the stress calculated by the three stress models: (i) the bending axial and the torsion shear stress on the beam at the base of the flexure (Bending & Torsion), (ii) the bending and shear stress at  $\lambda_{max}$ ,  $\sigma_{von1-z}$  (Bending & Torsion  $\lambda_{max}$ ), and (iii) bending and shear stress at  $\lambda_{max}$  with the presented warping correction,  $\sigma_{von2-z}$  (Warping Correction  $\lambda_{max}$ ).

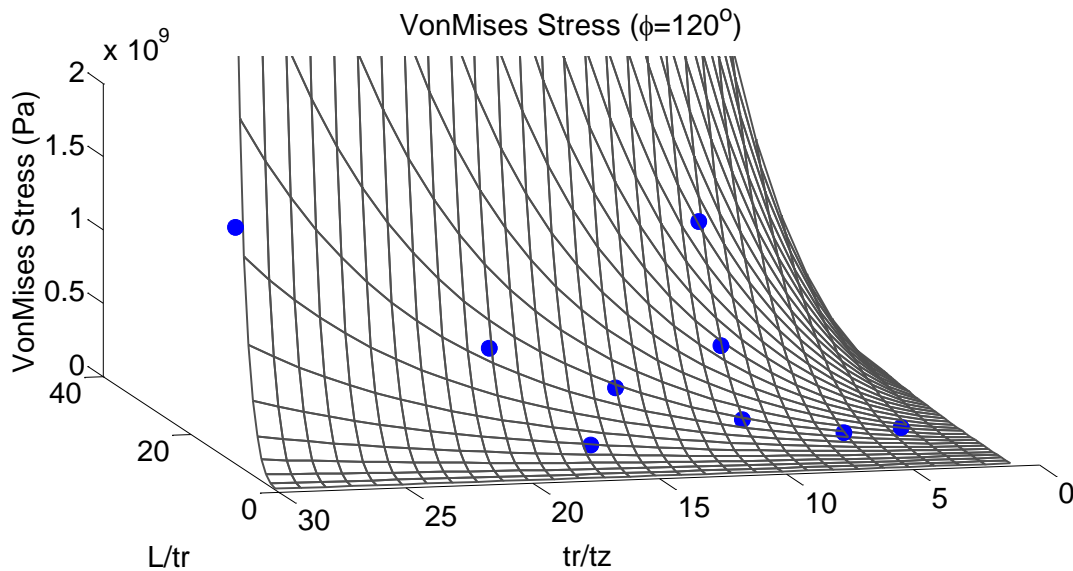


**Figure 3.57** VonMises stress for a  $\phi=120^\circ$   $z$ -compliance element. The FEA values for different length to radial-thickness,  $L/t_r$ , and radial to  $z$ -axis thickness,  $t_r/t_z$ , are plotted along the presented warping corrected stress model.



Once an accurate stress model has been established the range of the flexure can be calculated. Figure 3.58 plots the normalized range of a  $z$ -compliance element vs.  $\phi$ . The range is normalized using the range of a straight-beam of the same dimensions. The plot shows that the range for a  $z$ -compliance CF of any  $\phi$  is always less than that of a straight-beam. However, when the footprint of the flexure element is taken into consideration the CF element outperforms the straight flexure for  $\phi \geq 90^\circ$ , as shown in Figure 3.59. The chart shows how  $\phi$  affects the range/R ratio for a  $z$ -compliance element. The dashed line gives the range/ $L$  value for a straight-beam.

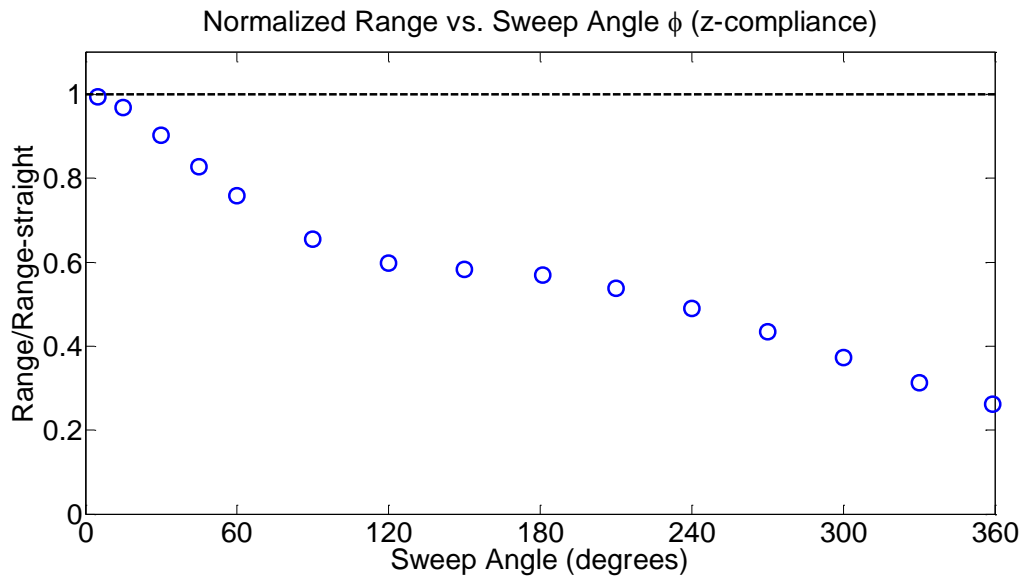


**Figure 3.58 Normalized range vs. sweep angle,  $\phi$ , for a  $z$ -compliance element. Stress is normalized using the range value for a straight-beam element of the same dimensions under the same loading.**

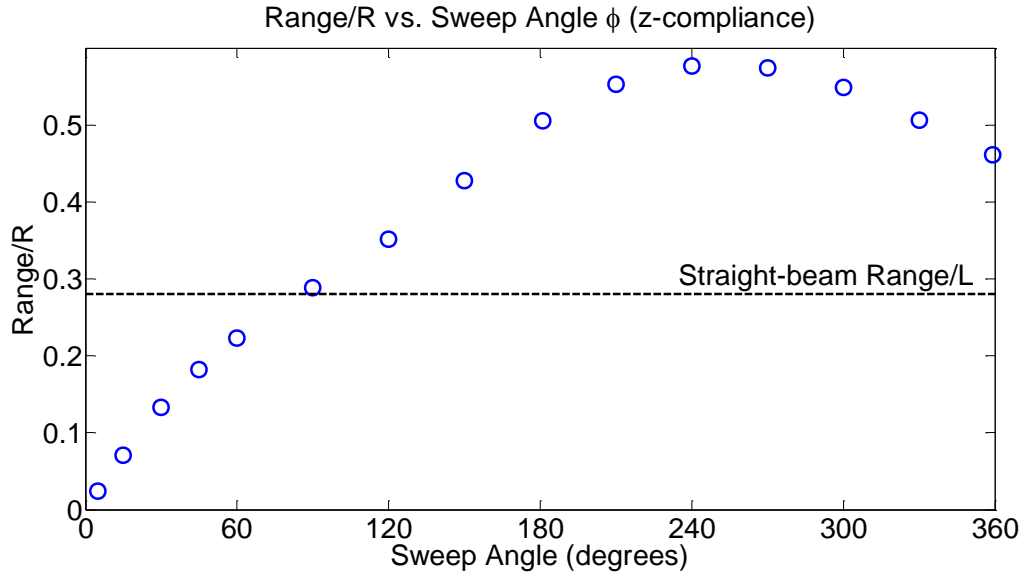


**Figure 3.59** Range/R vs. sweep angle,  $\phi$ , for a z-compliance element. Dotted line shows the range/L for a straight-beam element of the same dimensions.

### 3.11 Summary of Element Design Rules

- 1) The presented compliance matrix allows the designer to use all previous knowledge pertaining to straight-beam flexures when designing CF elements. Leaving only the effect of sweep angle,  $\phi$ , and the ratio of bending to torsional properties of the cross-section,  $\beta$ , to be considered.
- 2) The curvature adjustment factors,  $\zeta$ , facilitate the analysis of the  $\phi$  and  $\beta$  effect on the flexure performance. Different performance metrics can be used in conjunction with  $\zeta$  to establish sweep angles,  $\phi_s$ , below which the CF can be modeled as a straight-beam. In general for  $\phi \leq 15^\circ$  the beam can be modeled as a straight-beam.
- 3)  $\phi$  and  $\beta$  serve as two additional tuning knobs in the design of CFs. As a result of the increased design space, a CF may be able to meet functional requirements that cannot be met using a straight flexure.
- 4) A z-compliance CF can achieve better performance through with a lower  $K_z/K_r$  ratio than a straight-beam flexure. Increasing  $\phi$  decreases  $K_z/K_r$  as shown in Figure 3.9. The optimal  $\phi$  for minimizing both stiffness ratios is  $122.56^\circ$  regardless of  $t_r/t_z$ .
- 5) An r-compliance flexure acts as a  $\theta$ -compliance element for  $\phi > 122.56^\circ$ . For the majority of sweep angles, the r-compliance flexure has two linear DOF,  $\Delta r$  and  $\Delta \theta$ . This property

can be exploited in systems where two DOF are necessary. In straight-beam flexures the design would require two flexures in series. The designer must be aware that the  $K_r/K_z$  ratio also increases rapidly making large  $\phi$   $r$ -compliance flexures poor  $z$ -constraints.

- 6) A taper angle along the  $r$ -axis of a  $z$ -compliance flexure will increase its stiffness ratios, therefore,  $\Psi=0^\circ$  is preferable.
- 7) A  $\Psi$  along the  $r$ -axis of an  $r$ -compliance element may be used to decrease the element's  $K_r/K_z$  ratio.
- 8) The  $\alpha_r/\Delta z$  parasitic ratio for a  $z$ -compliance CF decreases with increasing  $\phi$ . This property allows the designer to create a CF with a lower  $\alpha_r/\Delta z$  than a straight-beam flexure. The optimal sweep angle for minimizing both parasitic ratios is  $\phi = 118^\circ$ .
- 9) The parasitic ratio analyses for an  $r$ -compliance and  $\theta$ -compliance elements show that for certain  $\phi$  their parasitic displacements will be larger than their desired displacements. This property can be exploited if the designer is designing a transmission element. For example, the transmission can be used to transform an  $F_\theta$  force into a  $\Delta r$  displacement.
- 10) Taper angle has a small effect on the parasitic ratios of a  $z$ -compliance flexure and no effect on the parasitic performance of an  $r$ -compliance CF.
- 11) Eigenvalue and Eigenvector analysis can be used to establish the primary and secondary compliance vectors of a CF, PCV and SCV respectively. The maximum parasitic ratio of a CF will be given by the ratio  $|SCV|/|PCV|$ .
- 12) The CF's sensitivity to a taper angle depends on  $\phi$ . A  $z$ -compliance CF has a lower sensitivity to taper angle than its straight-beam counterpart.
- 13) A deflected flexure blade has a higher susceptibility to buckling under an axial load. The off-neutral position  $K_\theta$  for a CF is within 90% of its neutral position  $K_\theta$ , except for  $\phi > 330^\circ$ .
- 14) Boundary conditions increase the magnitude of the stiffness ratios for a  $z$ -compliance beam. However,  $K_z/K_r$  will always equal  $K_z/K_\theta$  when  $\phi = 122.56^\circ$ .
- 15) An  $\alpha_z$  constraint increases the stiffness ratios for an  $r$ -compliance blade. For an  $\alpha_z$ -guided element  $K_r/K_\theta=1$  when  $\phi = 90^\circ$ , compared to  $\phi = 122.56^\circ$  for a fixed-free element. A challenge of  $\alpha_z$ -constrained elements is that their  $K_r/K_z$  is equal to 1 when  $\phi = 73^\circ$ .
- 16) For all CF elements, constraining a parasitic motion increases the other parasitic ratio.

- 17) Load location may be used to remove undesired motions. A stage may be used to exert a moment on the flexure tip in addition to the applied force. The applied moment may be used to cancel the parasitic motion. The load placement necessary to remove the parasitic rotations of the two types of CFs is given in section 3.9.
- 18) Range calculations require an accurate stress model. Loading a flexure past its elastic range will destroy the performance of the element. Unlike straight-beams the maximum stress location for a CF is not always at its base.
- 19)  $r$ - and  $\theta$ -compliance elements experience only one bending moment,  $m_z$ , under  $F_r$  and  $F_\theta$  loading. The location of the maximum  $m_z$  is the location of the max stress,  $\lambda_{max}$ .  $\lambda_{max}$  depends on  $\phi$  and the ratio of  $F_r/F_\theta$ .
- 20) The range of an  $r$ -compliance CF is greater than that of straight beam for  $\phi \leq 90^\circ$ .
- 21) The range to footprint ratio (range/ $R$ ) of an  $r$ -compliance CF is greater than that of straight-beam flexure for  $\phi \geq 60^\circ$ . If footprint is a constraint the designer may want to consider using a curved flexure.
- 22) An  $F_z$  load on a  $z$ -compliance element results in a bending moment,  $m_r$ , and a twisting moment,  $m_\theta$ , on the beam. The location of the max stress depends on  $\phi$  as well as the geometry and material of the beam and is given by  $\lambda_{max}$ .
- 23) An accurate stress model for a  $z$ -compliance blade must include a warping stress. The warping stress is due to the beam being non-circular and constrained on one end. The presented  $\sigma_{warp}$  model was developed through a parametric study, using the warping functions of other cross-sections as a starting point. The resulting model,  $\sigma_{von2}$ , is a vast improvement over the model based solely on bending and torsion.
- 24) The range of a  $z$ -compliance flexure is less than that of straight-beam for all  $\phi$ . However, the range/ $R$  of the CF can be up to twice that of a straight flexure.

# 4

## SYSTEM RULES AND MODELS

Once the designer understands how to design the CF element building blocks, the next step in the design process is to establish rules for assembling the flexural elements into systems. A compliant system consists of one or more flexures and the stages used to connect the flexures to each other or to the moving object. There are two main types of systems: parallel and serial mechanisms. This chapter will establish the rules for system creation through the development of two CF mechanism examples: a four-bar which is a parallel system, and a serial mechanism known as the compound four-bar which utilizes two four-bars in series [6]. Figure 4.1 compares the two systems and illustrates the two examples that will be analyzed.

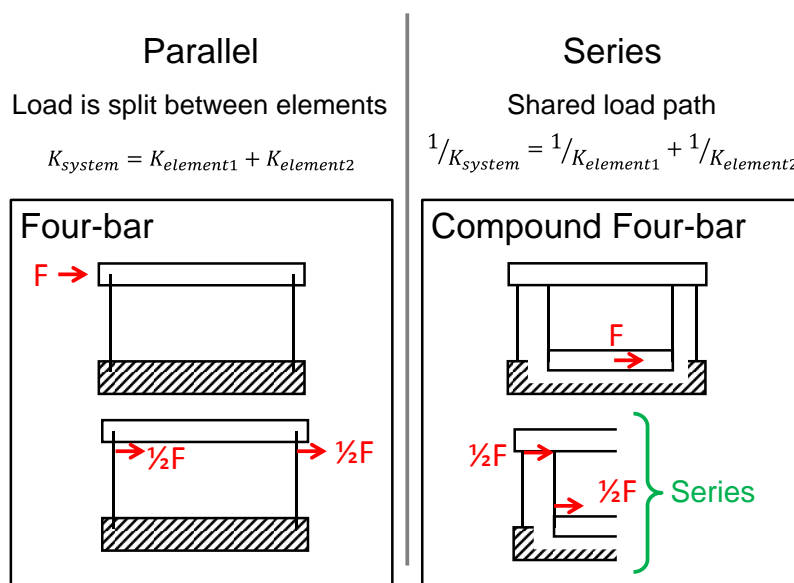


**Figure 4.1: Flexure system types: A) In a parallel system the load is split between the flexural elements. The total stiffness of the system is given by the sum of the element stiffnesses. A four-bar is an example of a parallel system. B) Serial systems are characterized by a shared load path. The compliance of the system ( $1/K_{sys}$ ) is equal to the sum of the element compliances. A compound four-bar is created by nesting two four-bars in series.**

In a parallel system the load is split between the flexural elements, therefore the stiffness of the system is the sum of the element's stiffnesses. The system's DOF are those DOF that are common to all the flexural elements [20]. In other words, the constraints of the system are the sum of the constraints of each of the elements. On the other hand, in a series system the elements share a load path, such that the compliance of the system ( $1/K_{system}$ ) is given by the sum of the compliances of the elements. To establish the system's DOF one should add the DOF of the elements in series. Therefore, the constraints of the mechanism are those constraints that are common to all the serial elements [20]. The influence of different parameters on the two sample mechanisms will be evaluated by analyzing their effect on the flexure performance metrics.

## 4.1 Parallel System Rules

The design rules for a parallel system are presented through the analysis of the four-bar mechanism. In planar compliant mechanisms a four-bar is commonly used to attain an approximate rectilinear motion [6]. The four-bar's stage is used to constrain the tip of each flexure, the motion of the four-bar is illustrated in Figure 1.14. A  $z$ -compliance CF four-bar system may be used to constrain the two tip rotations of the elements. Figure 4.2 shows the straight four-bar system parameters and motions, and compares them to those of a CF four-bar. This section will analyze how the different element and system parameters affect the performance of a curved four-bar.

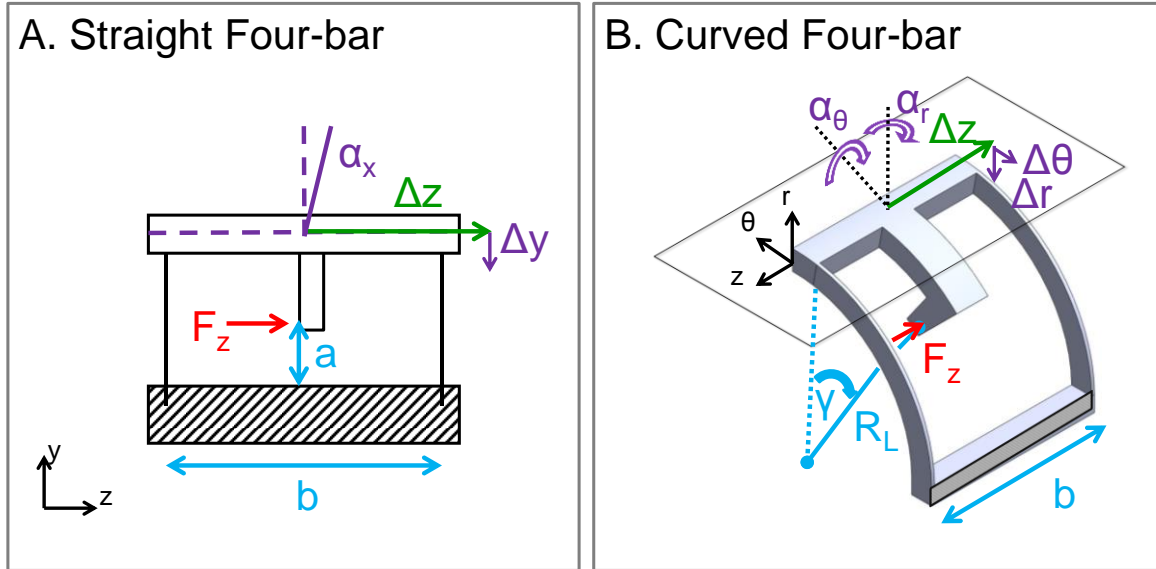


**Figure 4.2: Four-bar system parameters and motions.  $F_z$  indicates load along the  $z$ -axis and  $\Delta z$  is the desired displacement. A) Straight four-bar system: The parasitic motions are given by  $\alpha_x$  and  $\Delta y$ .  $a$  indicates the location of  $F_z$  relative to ground, and  $b$  is the distance between the two flexures. B) The curved four-bar has four undesired motions,  $\alpha_r$ ,  $\alpha_\theta$ ,  $\Delta r$ ,  $\Delta\theta$ . The location of  $F_z$  is specified using  $R_L$  and  $\gamma$ .**

#### 4.1.1 Stiffness Ratios

The stiffness analysis of the curved four-bar is simple because the coordinate systems for the flexures have the same orientation, as shown in Figure 4.3. As a result, the coordinate system for the mechanism is the same as that of the elements and the stiffnesses of the flexures can be added together to calculate the system stiffness. The stiffness ratios of the four-bar are the same as the stiffness ratios of the  $z$ -compliance elements that compose the four-bar. The  $K_z$ ,  $K_r$ , and  $K_\theta$  stiffnesses of the four-bar are twice the element's respective stiffnesses. Therefore, the effect of the different parameters on the stiffness ratios of the four-bar is given by the effect on the element's stiffness ratios described in section 3.5.

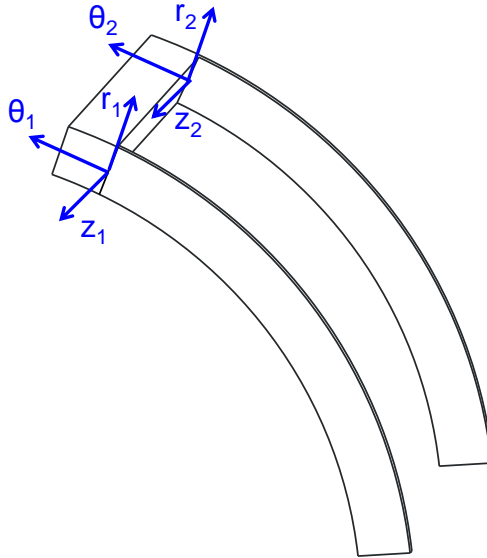


**Figure 4.3: Curved compliant four-bar mechanisms. Image shows the coordinate systems for the two flexures.**

### 4.1.2 Parasitic Rotation Ratios

The analysis of the parasitic rotation ratios of a four-bar requires an understanding of the loads and moments on both the stage and the flexures. Figure 4.4 shows the force and moment diagram for a straight four-bar. The four-bar stage constrains the parasitic rotation,  $\alpha_{x-element}$ , of its elements. However, this constraint leads to an unbalanced moment,  $M_x$ , acting on the stage. This moment has to be balanced by axial forces,  $F_y$ , on the flexures. The axial force acts in tension in one flexure and in compression on the other element, resulting in a corresponding positive or negative  $y$ -displacement,  $\Delta y$ , of the flexure tips. These axial displacements translate to a rotation of the stage,  $\alpha_x$ . The parasitic ratio of a straight four-bar is dictated by the ratio of this  $\alpha_x$  rotation to the desired displacement  $\Delta z$ . This brief analysis highlights that the parasitic ratio of the four-bar will be dictated by  $M_x$ , the distance between the flexures,  $b$ , and  $K_y$  of the elements.



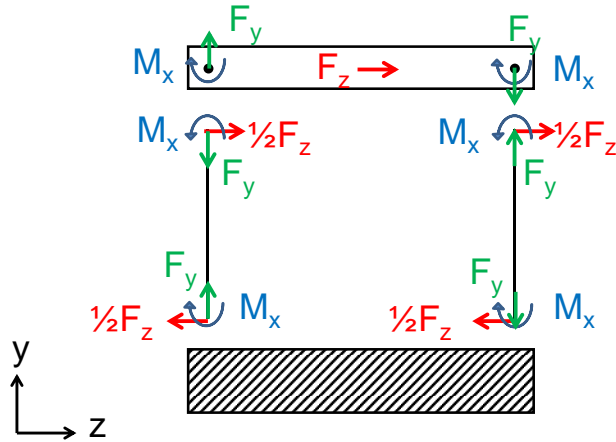


**Figure 4.4: Straight four-bar force and moment diagram. Loads and moments on the flexures and input stage are shown.  $F_z$  is the applied load, while  $M_x$  is the moment resulting from constraining the flexure tip. The axial forces,  $F_y$ , balance the  $M_x$  moments on the input stage.**

Similarly, the rotation parasitics of the curved four-bar can be established by analyzing the force and moment diagram shown in Figure 4.5. In the case of the CF mechanism the model is more complex because the stage constrains two element parasitic rotations,  $\alpha_{r-element}$  and  $\alpha_{\theta-element}$ , resulting in two unbalanced moments on the stage,  $M_r$  and  $M_{\theta}$ . The moments on the stage are given by  $M_{\theta, \alpha_r = \alpha_{\theta} = 0}$  and  $M_{r, \alpha_r = \alpha_{\theta} = 0}$  which are defined in (3.18) and (3.19), respectively. These moments are balanced by forces on the flexures,  $F_{\theta}$  and  $F_r$ . The forces lead to displacements along the direction of the force; the displacements are dictated by the element's  $K_{\theta}$  and  $K_r$ . The model for the parasitic rotations of the curved four-bar's input stage must include the effect of both the element and system parameters.

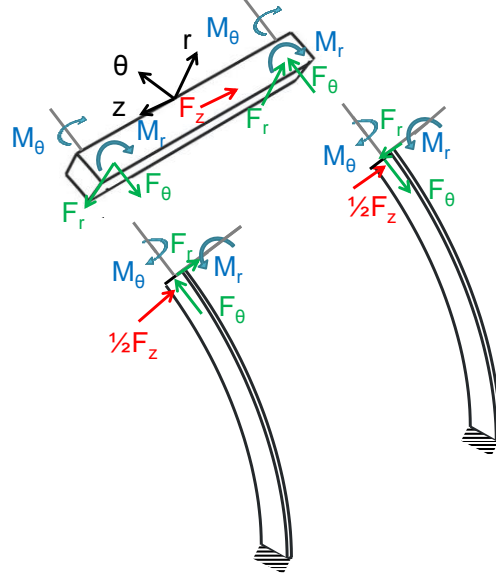


**Figure 4.5: Curved four-bar force and moment diagram. Loads and moments on one end of the flexures and input stage are shown.  $F_z$  is the applied load, while  $M_r$  and  $M_\theta$  are the moments resulting from constraining each flexure tip. The radial forces,  $F_r$ , balance the  $M_\theta$  and the axial forces,  $F_\theta$ , balance the  $M_r$  moment on the input stage.**

The curved four-bar force and moment diagram can be used alongside the force and moment balance equations to create a model for the parasitic rotations of the four-bar. The first step is to establish the moments acting on the stage; these moments are equal and opposite to the moments acting on the tip of the flexures to achieve the zero-rotation boundary conditions. These element moments are given in Equations (3.18) and (3.19). There are two flexures in the four-bar system; therefore, the net moment on the stage is twice the moment on each flexure. The stage rotations resulting from having to balance the stage moments are given by Equations (4.1) and (4.2). This model was used to establish how the parasitic rotations of the CF four-bar are affected by the sweep angle of the system,  $\phi$ , as shown in Figure 4.6. The  $\phi$  of the four-bar will affect the magnitude of the moments acting on the stage, as well as the compliance of the flexures. The plot shows that the values calculated by the model do not match the FEA results for low  $\phi$ . The discrepancy between the results suggests that the initial model for the  $\alpha_r$  and  $\alpha_\theta$  of a CF four-bar is incomplete.

$$\alpha_\theta = C_{22} \cdot \frac{M_{\theta\text{-stage}}}{0.5b^2} \quad (4.1)$$

$$\alpha_r = C_{11} \frac{M_{r-stage}}{0.5b^2} \quad (4.2)$$

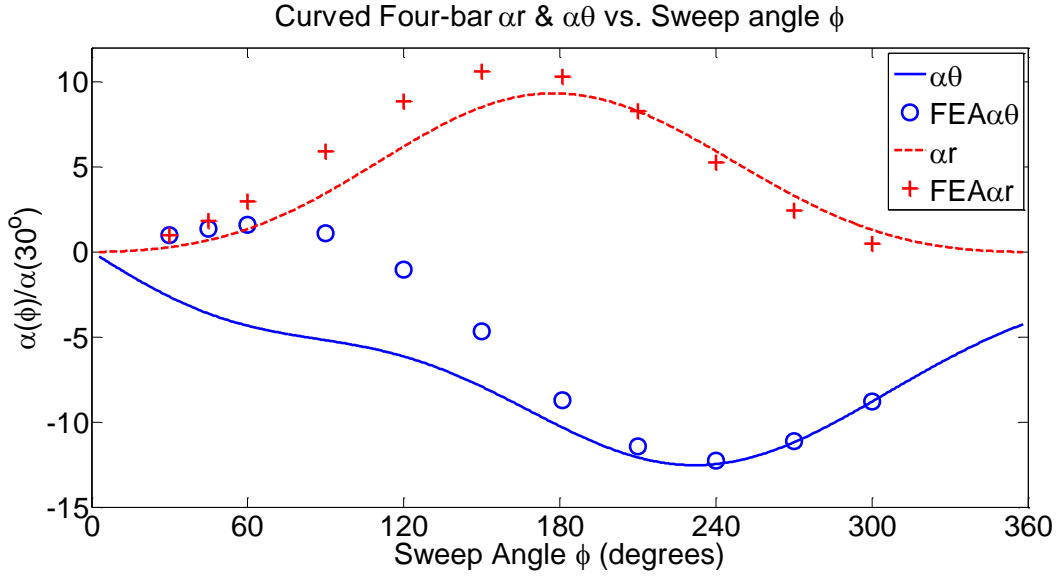


**Figure 4.6: Curved four-bar parasitics vs. sweep angle,  $\phi$ . The FEA values were calculated using a 3D-solid model. The two rotations are normalized using the FEA calculated value for  $\phi = 30^\circ$ . The plot shows that the beam-based model is inaccurate for low  $\phi$ . ( $L=60\text{mm}$ ,  $t_r=6\text{mm}$ ,  $t_z=0.6\text{mm}$ ,  $L_{stage}=6\text{mm}$ , 7075 Aluminum).**

The system FEA results presented in Figure 4.6 were calculated using a 3D-solid model. In section 3.2.1 it was shown that a beam FEA model differs from a 3D-solid model. The divergence of the models is significant in the system analysis; hence, the beam-based analytical model needs to be supplemented with adjustment factors. The first step in this rectification is to analyze which parameters result in a deviation from the beam analytical model. Previously it was established that the 3D solid model accounts for the difference in length between the inner and outer radii of the flexure. The analytical beam model does not account for this difference in length and therefore must be supplemented. This difference in length will increase as the ratio of  $L/t_r$  decreases. FEA analysis revealed that the length of the stage also affects the  $\alpha_r$  and  $\alpha_\theta$  rotations for the four-bar, as shown in Figure 4.7.

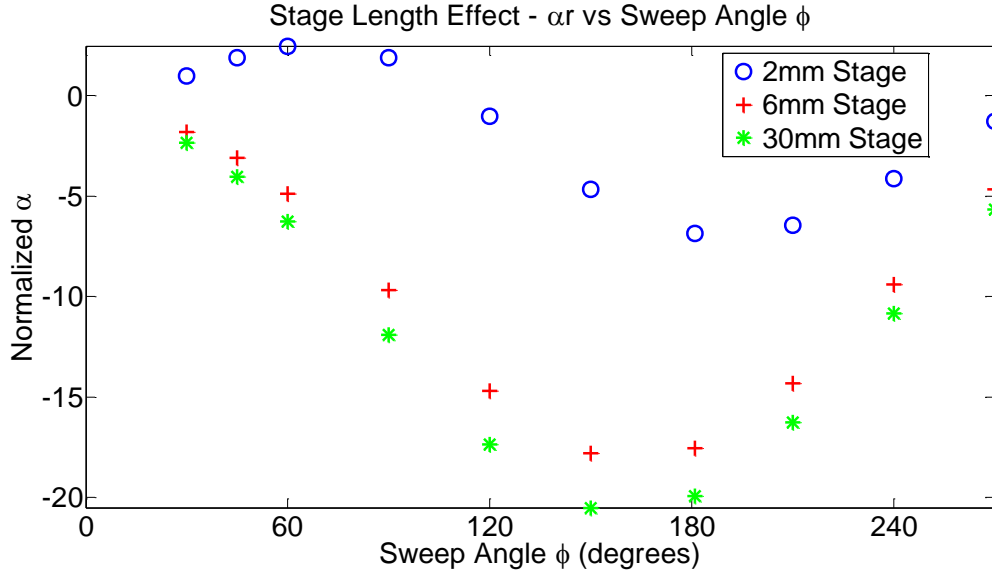


**Figure 4.7: Stage length effect on the curved four-bar parasitics vs.  $\phi$ . Values were calculated using an FEA 3D-solid model. The parasitics are normalized using the value for the  $\phi = 30^\circ$  four-bar with a 2mm stage.**

In the previous analysis of the four-bar parasitic rotations it was assumed that the axis of rotation of the stage is dictated by the flexure tip axes. However, the FEA analysis revealed that both the stage length,  $L_{stage}$ , and the  $L/t_r$  ratio of the flexure elements rotate the stage's  $r$ -axis away from the axis dictated by the flexure. Figure 4.8 illustrates the rotation of the  $r$ -axis. The angle between the element's  $r$ -axis and the system's is given by  $\omega$ .  $\omega$  is specified by an adjustment factor,  $p$ , and the sweep angle of the flexure,  $\phi$ . The effect of  $L/t_r$  and  $L_{stage}$  on  $\omega$  is shown in Figure 4.9. A preliminary model for  $\omega$ , given in Equation (4.3), was developed using the FEA results. The  $\omega$ -model is compared to the FEA values in Figure 4.9. The expression for  $\omega$  is complex; however, for large  $L/t_r$   $\omega$  approaches  $0.035\phi$ , as shown in Figure 4.9. Further work should be conducted to achieve a more robust model for  $\omega$ .

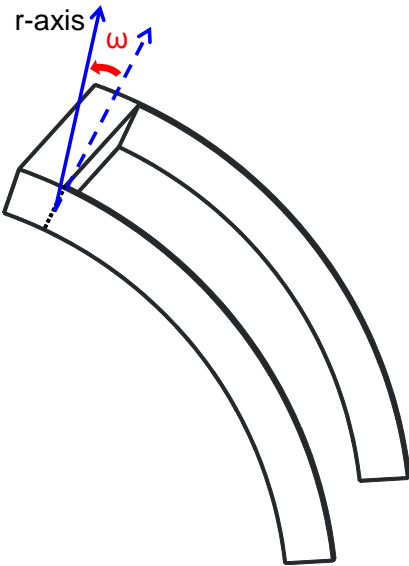


**Figure 4.8:** The curvature of the beam leads to a difference in length between the inner and outer radii. This effect in addition to the length of the stage leads to the rotation of the  $r$ -axis of the four-bar away from the  $r$ -axis of the elements. The rotation angle is given by  $\omega$ .

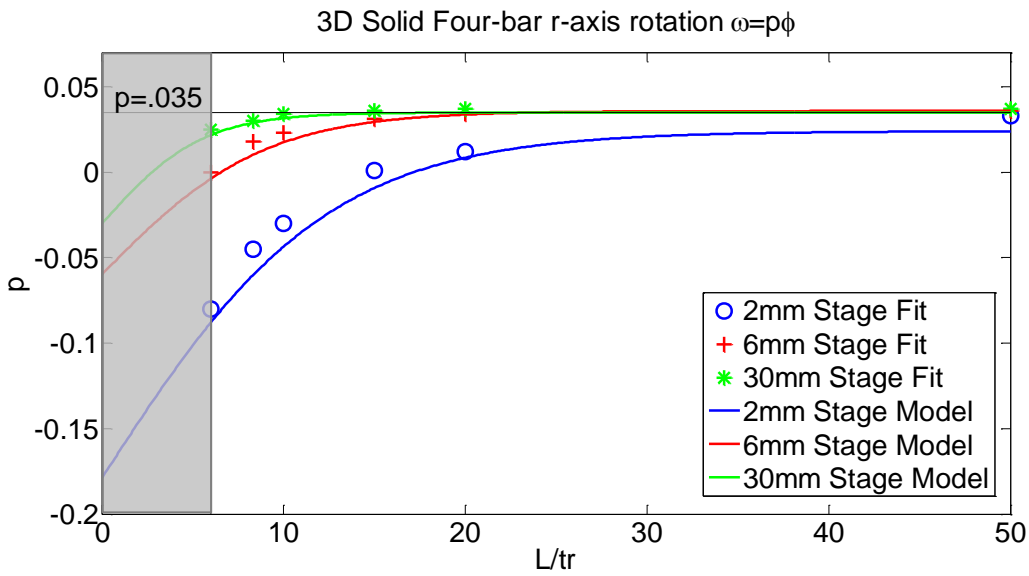


**Figure 4.9:**  $\omega$  adjustment vs.  $L/t_r$  for three different stage sizes. The plot gives the fitted values for  $p$  and the model values.  $\omega$  is given by  $p\phi$ .

$$\omega = \left[ \begin{array}{l} .0465 \left( \frac{L_{stage}}{L_{flexure}} - .0127 \right)^{-0.2} \tanh \left( \frac{L/t_r}{3.4 \left( \frac{L_{stage}}{L_{flexure}} \right)^{-0.3}} \right) \\ -.0165 \left( \frac{L_{stage}}{L_{flexure}} - .012 \right)^{-0.36} \end{array} \right] \phi \quad (4.3)$$

The  $F_r$  and  $F_\theta$  forces on the elements are dictated by the location of the stage's  $r$ -axis. Therefore, the CF four-bar's  $\alpha_r$  and  $\alpha_\theta$  will depend on  $\omega$ . Equations (4.4) and (4.5) give the adjusted four-bar rotations,  $\alpha_r'$  and  $\alpha_\theta'$ , as a function of  $\omega$ . The corrected equations for the parasitic rotations of the stage are incorporated into the compliance matrix of the CF four-bar presented in Appendix D. Figure 4.10 shows the FEA calculated rotations vs.  $\phi$  and compares them to corrected model. The dotted lines indicate the results given by the initial model with no  $\omega$  correction. Figure 4.11 and Figure 4.12 demonstrate that the  $\omega$ -model is valid for a range of  $L/t_r$  ratios. For  $L/t_r < 6$  the flexure would have to be modeled as a plate and the presented beam model would no longer apply. Similarly, Figure 4.13 and Figure 4.14 are evidence of the effect of  $L_{stage}$  on  $\omega$ . The plots show that the  $\omega=0^\circ$  model does a poor job in predicting the rotations of a four-bar with different stage lengths. The  $\omega$ -corrected model is able to accurately capture the effect of  $L_{stage}$  for stages larger than 2mm. In general larger stages are preferable because a four-bar with a small  $L_{stage}$  relative to  $L$  is vulnerable to stage deformation; this vulnerability will be discussed in section 4.1.2.2

$$\alpha_\theta' = C_{22} \frac{(M_{\theta-stage} - M_{r-stage} \sin \omega)}{0.5b^2} \quad (4.4)$$

$$\alpha_r' = C_{11} \frac{(M_{r-stage} \cos \omega)}{0.5b^2} \quad (4.5)$$

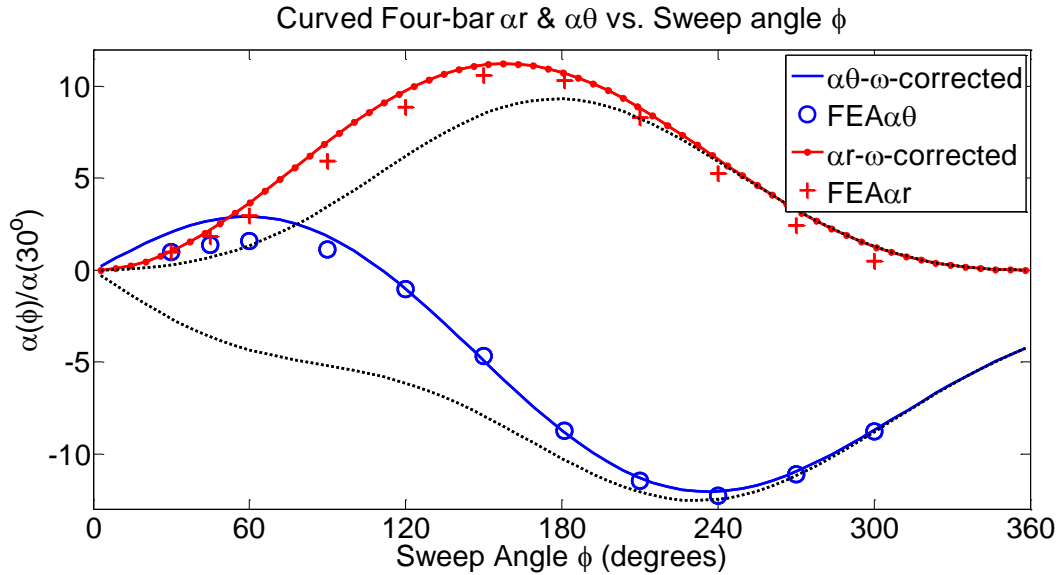


**Figure 4.10: Corrected curved four-bar parasitics vs.  $\phi$ . The rotations are normalized using the FEA values for  $\phi=30^\circ$ . The dotted lines show the  $\omega=0^\circ$  model values for  $\alpha_r$  and  $\alpha_\theta$ . ( $L=60\text{mm}$ ,  $t_r=6\text{mm}$ ,  $t_z=0.6\text{mm}$   $L_{stage}=6\text{mm}$  7075 Aluminum).**

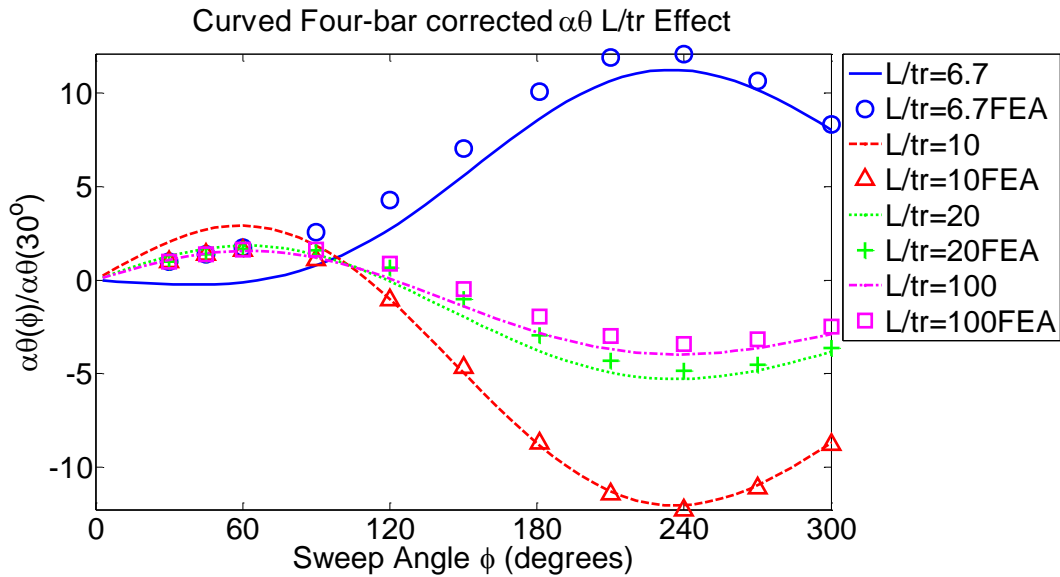


**Figure 4.11: Corrected curved four-bar  $\alpha_\theta$  vs.  $\phi$  for different  $L/t_r$  ratios.  $\alpha_\theta$  is normalized using the FEA value for  $\phi=30^\circ$ . ( $L_{stage} = 6\text{mm}$ )**

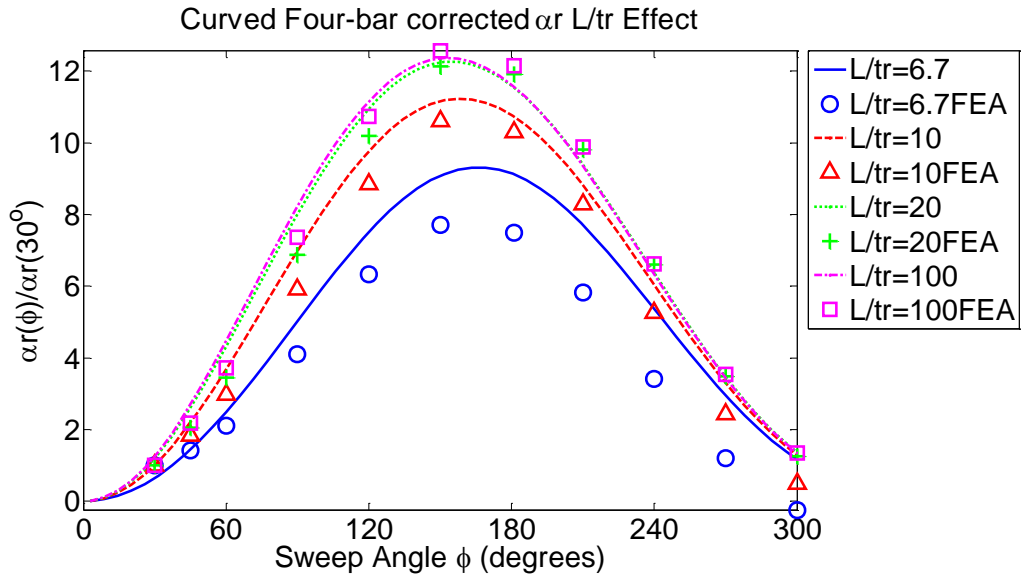


Figure 4.12: Corrected curved four-bar  $\alpha_r$  vs.  $\phi$  for different  $L/t_r$  ratios.  $\alpha_r$  is normalized using the FEA value for  $\phi=30^\circ$ . ( $L_{stage} = 6\text{mm}$ )

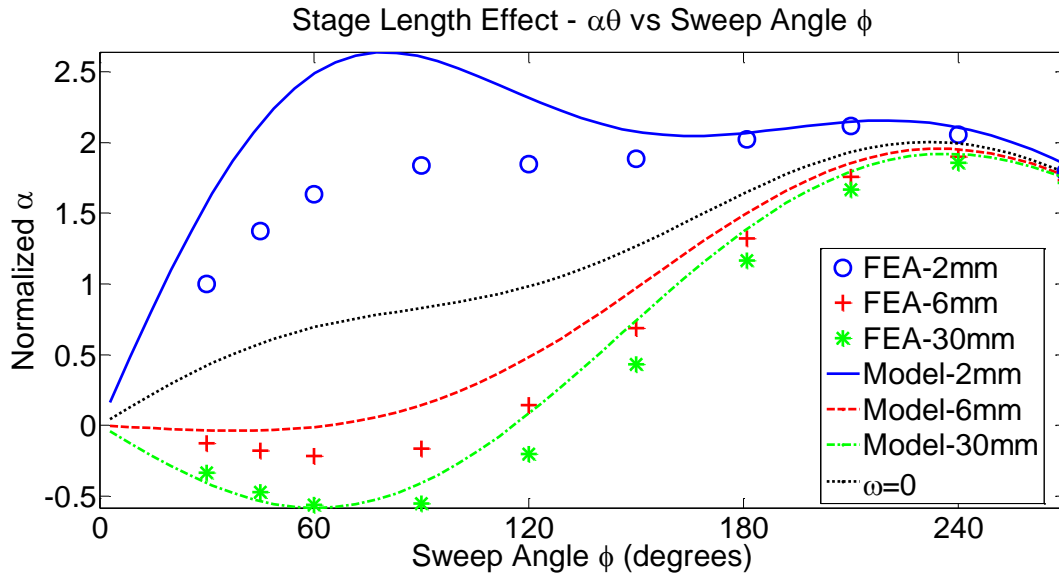
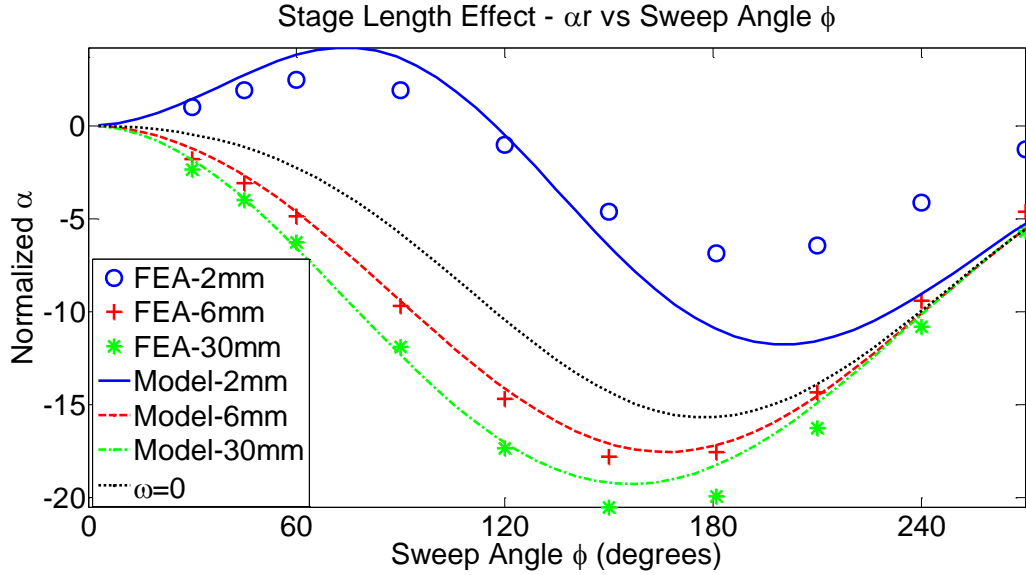


Figure 4.13: Corrected curved four-bar  $\alpha_\theta$  vs.  $\phi$  for different stage lengths.  $\alpha_\theta$  is normalized using the FEA value for  $\phi=30^\circ$  with a 2mm stage. The dotted line shows the  $\omega=0^\circ$  predicted values. ( $L/t_r=10$ )

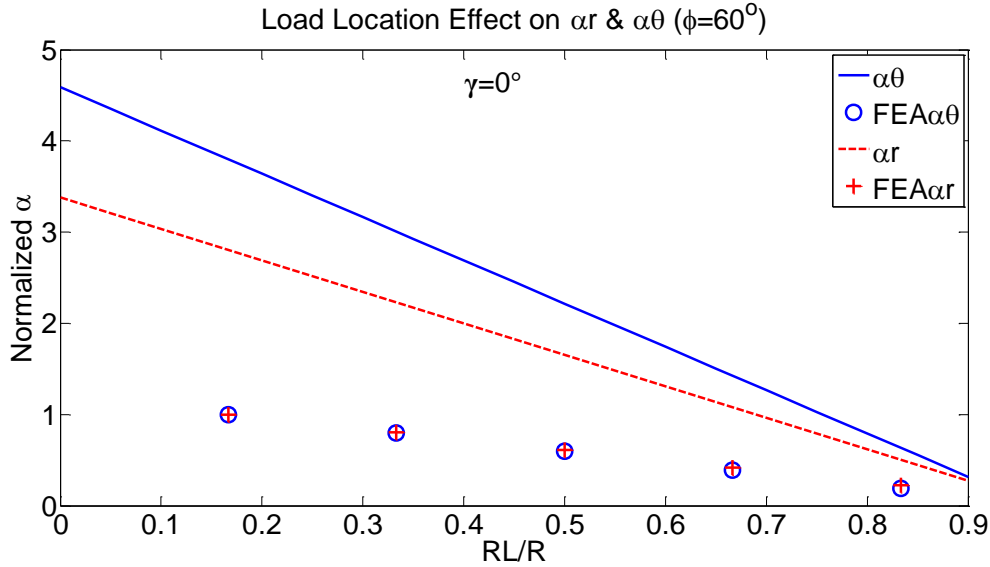




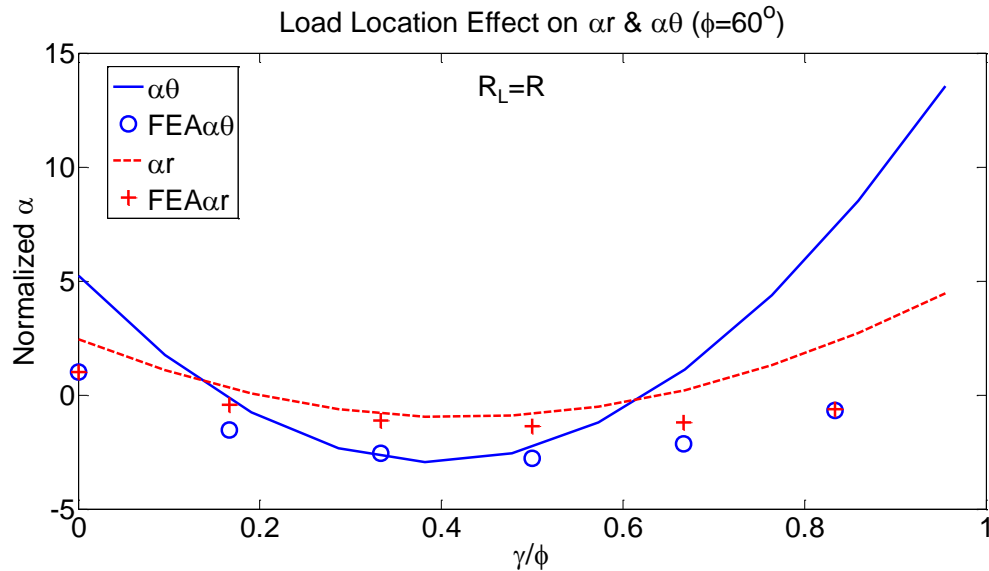
**Figure 4.14: Corrected curved four-bar  $\alpha_r$  vs.  $\phi$  for different stage lengths.  $\alpha_r$  is normalized using the FEA value for  $\phi=30^\circ$  with a 2mm stage. The dotted line shows the  $\omega=0^\circ$  predicted values. ( $L/t_r=10$ )**

#### 4.1.2.1 Load Location Effect

In section 3.9 of the element analysis, it was shown that an element's parasitic motions may be cancelled by applying a moment and a force on the flexure's tip. In the same way in the design of a compliant system, load location may be used as a way to remove or reduce the parasitic motions of the stage. To remove the parasitic rotations of the curved four-bar, the stage must be loaded with  $M_r$  and  $M_\theta$  that cancel the moments on the stage due to the flexure-tip constraint. Figure 4.2b illustrates how a four-bar system may be designed such that a single  $F_z$  load results in an  $F_z$ ,  $M_r$ , and  $M_\theta$  loading on the system stage. The location of the force relative to the flexure tip is given by  $R_L$  and  $\gamma$ . Figure 4.15 presents how the parasitics of a  $\phi=60^\circ$  four-bar vary as a function of  $R_L/R$ ; while Figure 4.16 shows the effect that locating the load  $\gamma$  degrees away from the tip has on  $\alpha_r$  and  $\alpha_\theta$ .



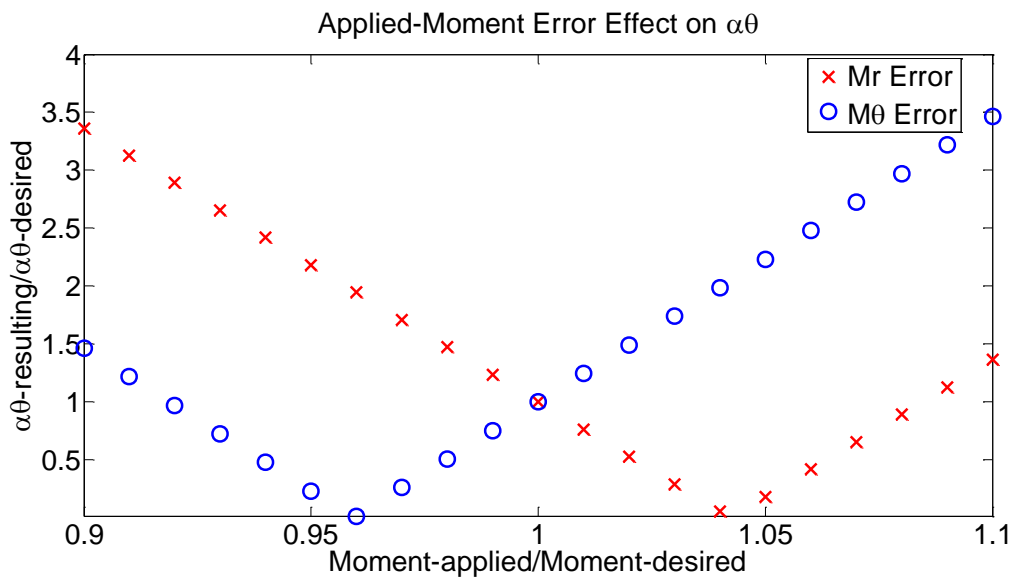
**Figure 4.15: Load location effect on the curved four-bar parasitics. Plot gives the normalized rotations vs. the ratio of  $R_L$  to  $R$  ( $\gamma=0^\circ$ ). Rotations are normalized using the FEA values for  $R_L/R=1/6$ .**



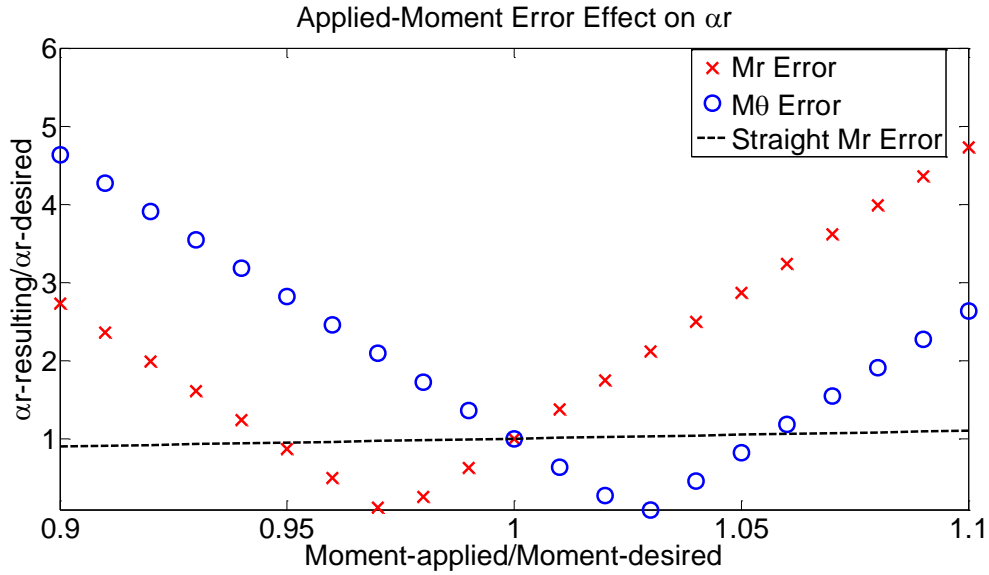
**Figure 4.16: Load location effect on curved four-bar parasitics. Plot gives the normalized rotations vs. the ratio of  $\gamma/\phi$ . Rotations are normalized using the FEA values for  $\gamma=0^\circ$ .**

Figure 4.15 and Figure 4.16 show that the  $\omega$ -corrected models capture the general effect that load placement will have on the rotations of the four-bar stage, however, the models deviate significantly from the FEA calculated values. In an effort to understand the appropriateness of the models the sensitivity of the four-bar to load location error was investigated. The goal of the

analysis was to understand if load location is a feasible way of removing the parasitic rotations of the curved four-bar given that the rotations are coupled because they both depend on  $F_z$ ,  $M_r$ , and  $M_\theta$ . Figure 4.17 gives the result of the sensitivity analysis, where the applied moments were varied by  $\pm 10\%$ . The plot shows that for a 10% error in the applied moment the  $\alpha_\theta$  rotation of the stage can be nearly 3.5 times the desired value. The  $\alpha_r$  rotation is even more sensitive to applied moment error as shown in Figure 4.18. In the case of  $\alpha_r$  a 10% error in either  $M_r$  or  $M_\theta$  results in almost 5 times the predicted  $\alpha_r$  value. The plot highlights that the sensitivity of a planar four-bar is at least an order of magnitude lower than the CF's sensitivity. Considering the high sensitivity to load location error, a superior way to remove the parasitics of a CF four-bar system is to use symmetry to cancel the rotations. A CF can be designed using two four-bars, such that the rotations of the four-bar stages cancel, as illustrated in Figure 4.19.



**Figure 4.17: Applied-moment error effect on  $\alpha_\theta$ . Plot gives the ratio of  $\alpha_\theta$ -resulting/ $\alpha_\theta$ -desired vs. the ratio of the  $M$ -applied to  $M$ -desired.**



**Figure 4.18: Applied-moment error effect on  $\alpha_r$ . Plot gives the ratio of  $\alpha_r$ -resulting/ $\alpha_r$ -desired vs. the ratio of the  $M$ -applied to  $M$ -desired. The dotted line gives the straight four-bar sensitivity to applied-moment error.**

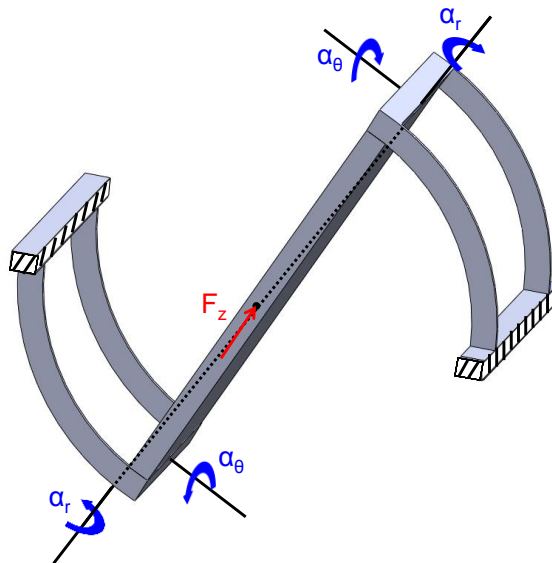


**Figure 4.19: Symmetry may be used to cancel the curved four-bar parasitic rotations.**

#### 4.1.2.2 Flexure Spacing Effect

Flexure spacing,  $b$ , has a significant effect on the parasitic ratios of a four-bar. The parasitic rotations of a CF four-bar are dictated by  $1/b^2$ , as shown in Equations (4.4) and (4.5). Figure 4.20 confirms that  $\alpha_r$  and  $\alpha_\theta$  are inversely proportional to the square of the flexure

spacing. The plot gives both the FEA calculated values and the  $\omega$ -corrected model results. Separating the flexures increases the moment arm from the center of the stage to the element tip, as a result the flexure experiences a lower force for a given moment, and similarly a displacement of the tip translates to a smaller rotation angle. The caveat to using  $b$  to decrease the rotations of the four-bar is that the stage must be able to withstand the applied moments. If the stage is not stiff enough, the stage will deform under the loads as shown in the FEA image in Figure 4.21. In CF four-bar design the engineer only has  $360^\circ$  in which to fit the flexures and the stages. This constraint limits the sweep angle that can be dedicated to the stages. Taking this into consideration the design should not rely only on flexure spacing as the only way to reduce  $\alpha_r$  and  $\alpha_\theta$ , the parasitics should be addressed in both the element and system design.

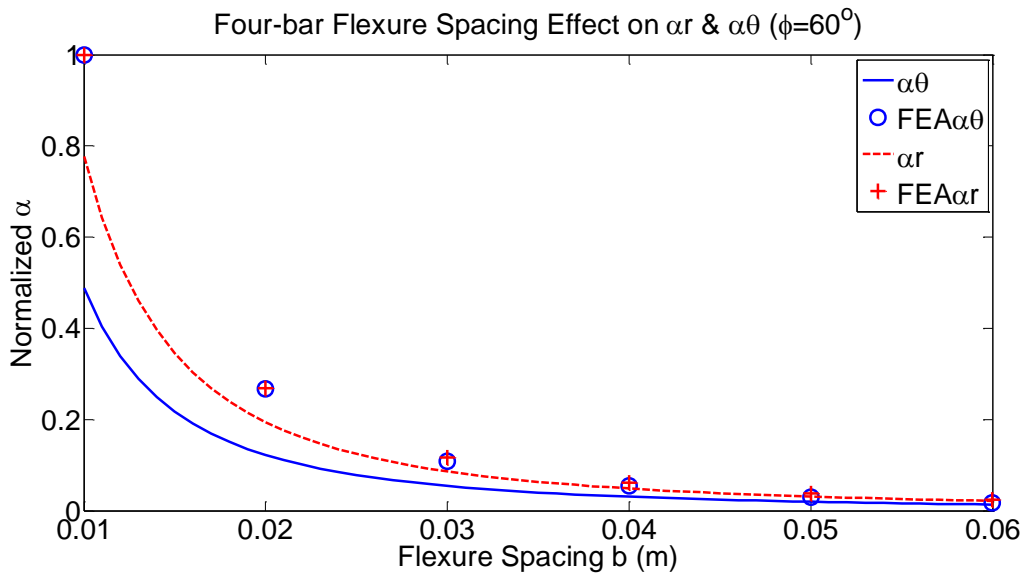


**Figure 4.20: Flexure spacing,  $b$ , effect on curved four-bar parasitic motions. Rotations are normalized using the FEA values for  $b=10\text{mm}$ . ( $\phi=60^\circ$ )**

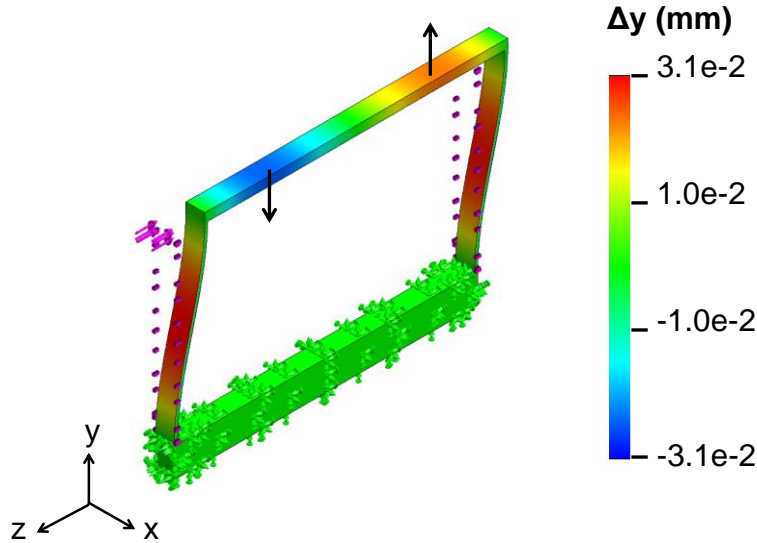


**Figure 4.21: Input stage  $\Delta y$  displacement for a straight four-bar under  $F_z$ . The four-bar's input stage can deform during operation when the spacing between the flexures is too large and the stage is not stiff enough.**

### 4.1.3 Parasitic Displacement Ratios

Planar four-bar systems suffer from a parasitic displacement in addition to the undesired rotation. This translation is a result of the geometric constraints on the flexure. Figure 4.22 illustrates how the  $\Delta z$  motion of a linear flexure is given by  $L$  and the rotation  $\alpha_x$  about the fixed-end. The free-end of the element will travel in an arc, so  $\Delta z$  is accompanied by a  $\Delta y$ . This parasitic displacement is estimated using equation (4.6) [5]. A curved four-bar exhibits two parasitic translations when loaded under  $F_z$ , as shown in Figure 1.5. These parasitic displacements were estimated by modeling the elements as a series of straight-beams. Figure 4.23 illustrates how a CF element can be modeled as a series of linear flexures. The coordinate systems of the planar-beams rotate as they follow the curvature, as a result the axial-displacements of the straight-flexures are observed as  $\Delta r$  and  $\Delta \theta$  translations of the CF tip. Figure 4.24 plots the effect of  $\phi$  on the  $\Delta r$  and  $\Delta \theta$  translations of a curved four-bar. The chart compares the large-displacement FEA values to the model results. The proposed approximation captures the trend of the  $\phi$ -effect, although it underestimates the parasitic displacements. The parasitic displacements due to geometric constraints are not captured by the compliance matrix of the four-bar, so they must be considered separately.

$$\Delta y \approx \frac{(\Delta z)^2}{2L} \quad (4.6)$$

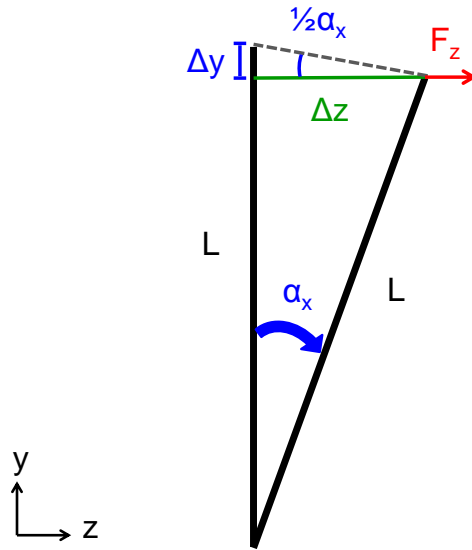


Figure 4.22: A straight-beam flexure suffers from a  $\Delta y$  displacement when loaded along  $z$ . The schematic shows the relationship between  $\Delta y$ ,  $\Delta z$ ,  $L$  and  $\alpha_x$ .

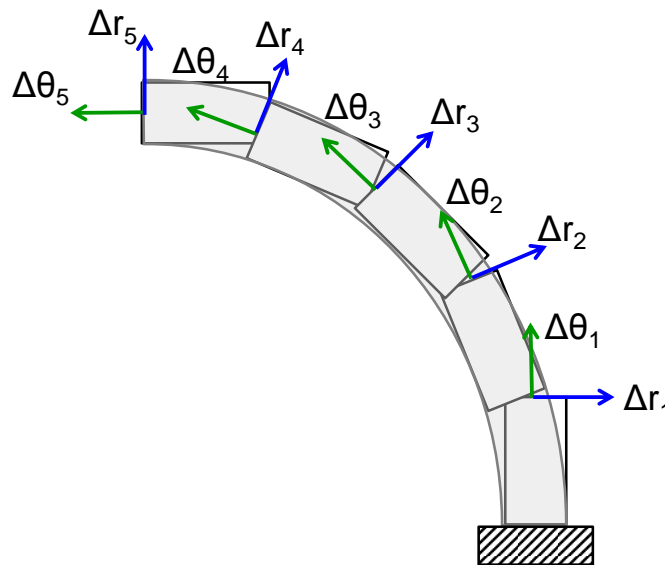
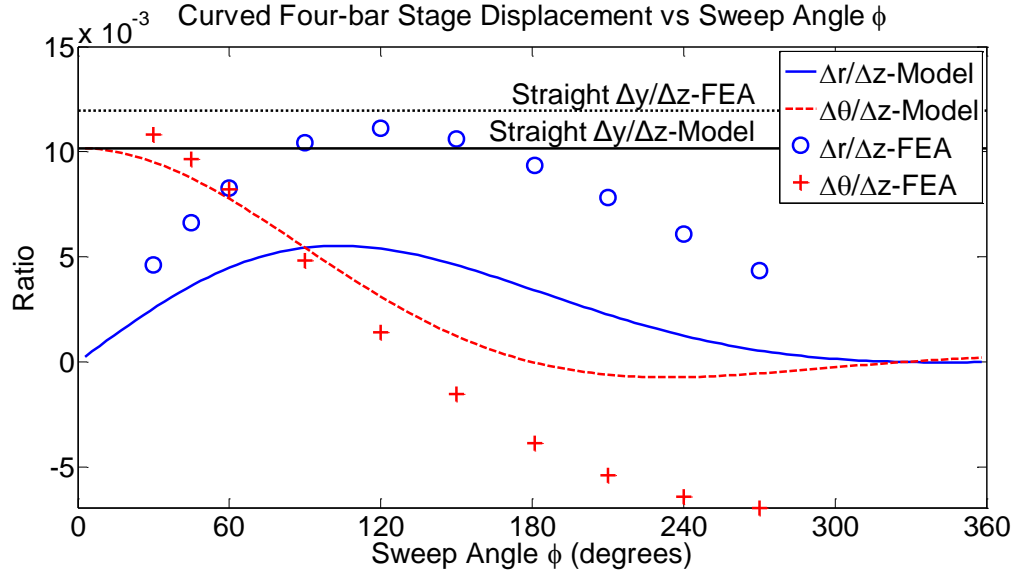


Figure 4.23: The  $\Delta r$  and  $\Delta \theta$  parasitic motions of a curved four-bar can be estimated by modeling the curved flexure as a series of straight beams.



**Figure 4.24: Curved four-bar input stage parasitic displacement ratios vs. sweep angle,  $\phi$ . The plot also compares the FEA calculated parasitic ratios to the model approximations.**

#### 4.1.4 Stress Model

The foundation of the CF four-bar stress model is the  $z$ -compliance element stress equation presented in section 3.10. In a CF four-bar the flexures are constrained by the stage, which applies a  $M_r$  and  $M_\theta$  on the flexure tip. The moments acting on the curved four-bar element are summarized in Figure 4.25. Under a negative  $F_z$  the element will experience a positive  $M_r$  and a negative  $M_\theta$ . The resulting  $m_r$  and  $m_\theta$  for a CF element under  $F_z$ ,  $M_r$ , and  $M_\theta$ , are given by equations (4.7) and (4.8). The location of the maximum stress of the four-bar is given by  $\lambda_{max}$ . Figure 4.26 shows the effect of  $\phi$  on the Von Mises stress of a CF four-bar. The plot compares the FEA calculated values to the results of both stress models: with warping,  $\sigma_{von1-z}$ , and without the warping consideration,  $\sigma_{von2-z}$ . The stress values are normalized using the stress value for a planar four-bar of the same dimensions under the same load. The chart demonstrates the importance of including warping in the stress model. The four-bar stress model allows the designer to accurately calculate the elastic range of the system.

$$m_r = -F_z R \sin \lambda + M_r \cos \lambda - M_\theta \sin \lambda, \lambda \leq \phi \quad (4.7)$$

$$m_\theta = -F_z R (1 - \cos \lambda) + M_\theta \cos \lambda + M_r \sin \lambda, \lambda \leq \phi \quad (4.8)$$



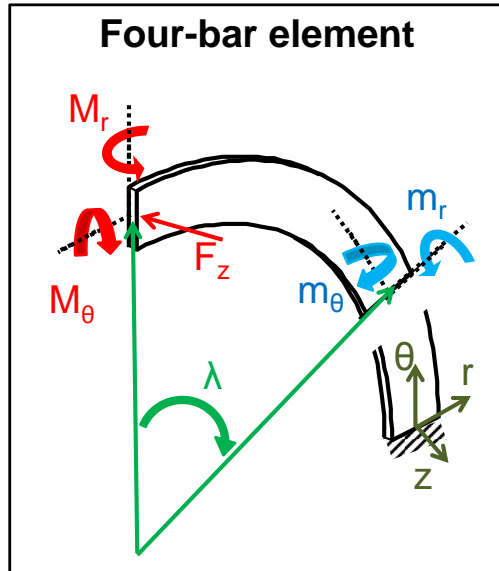


Figure 4.25: Loading conditions on a CF four-bar flexural element.  $M_r$  and  $M_\theta$  are the moments applied by the stage constraint on the flexure tip.  $F_z$  is the half the load applied on the four-bar.  $F_z$ ,  $M_r$ , and  $M_\theta$ , produce a bending moment,  $m_r$ , and a twisting moment,  $m_\theta$ , on the beam. The resulting moments vary along the length of the beam. The position of the resulting moments is given by  $R\lambda$ , where  $\lambda$  is measured from the tip of the beam.

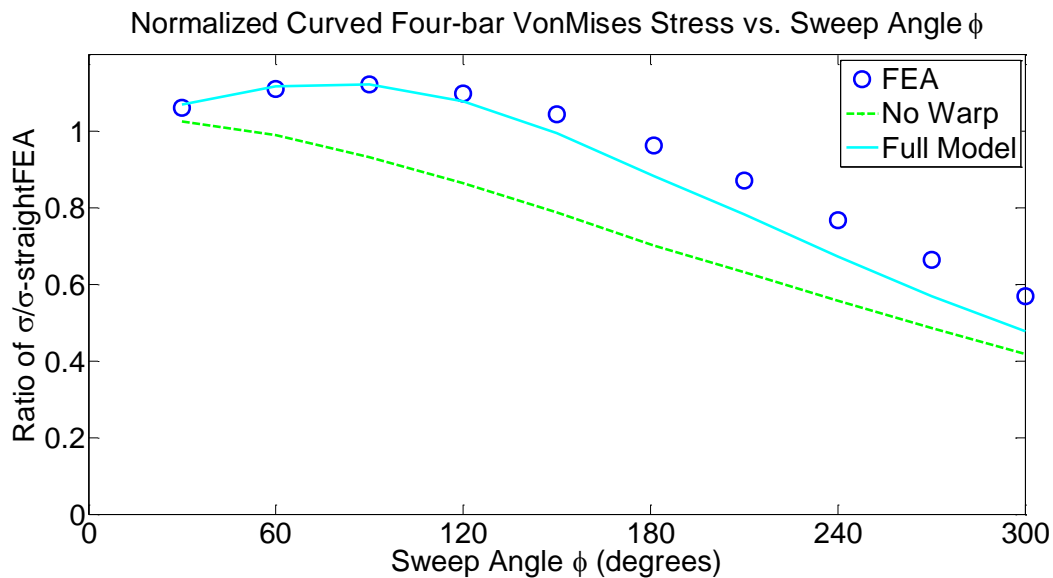
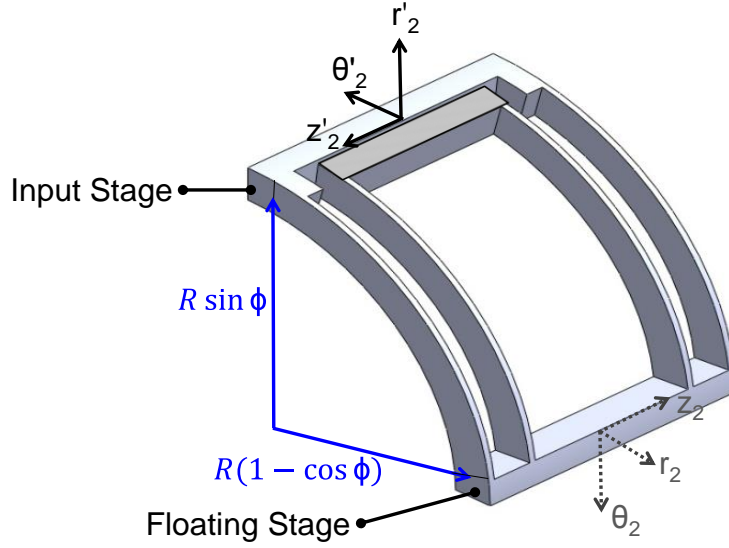


Figure 4.26: Curved four-bar Von Mises stress vs.  $\phi$ . Stress is normalized using the stress of a straight four-bar of the same dimensions under the same load. Plot shows the FEA calculated values, the stress given by a no-warp model and the values given by the full model which includes the warping correction.

## 4.2 Serial System Rules

The challenge with CF serial systems is that the curvature of the flexures leads to the translation and rotation of the elements' coordinate systems. The compound four-bar is used as the guiding example because in planar flexures it is a well-understood parallel-serial system. Compound four-bars are widely used because they double the range and decrease the parasitics of the four-bar. Figure 1.5b shows how the four-bars in a CF compound four-bar have different coordinates. The first step in assembling the serial system's compliance matrix is to establish a system coordinate matrix and transform the element compliance matrices to the system coordinates. In the case of the CF compound four-bar we choose to use the input four-bar's coordinates as the system coordinates, consequently the floating four-bar's compliance matrix needs to be transformed to the new coordinate system, as illustrated in Figure 4.27. Equation (4.9) presents the transformation matrix,  $[C_t]$ , which is used to translate the compliance matrix of the floating four-bar to the system's coordinates.  $[C_t]$  is valid for small values of  $\alpha_z$ , when  $\sin(\alpha_z) \approx \alpha_z$ . The transformed compliance matrix for a CF four-bar,  $[C'_{four-bar}]$ , is calculated using Equation (4.10).



**Figure 4.27: A CF compound four-bar is assembled by nesting two four-bars. The input and floating four-bars have different coordinate systems. If the coordinates of the input four-bar are chosen as the system coordinates, the compliance matrix of the floating four-bar must be transformed to match the system's new coordinate system  $(r'_2, \theta'_2, z'_2)$ .**

$$[C_t] = \begin{vmatrix} -\cos \phi & -\sin \phi & 0 & 0 & 0 & -R(1 - \cos \phi) \\ -\sin \phi & \cos \phi & 0 & 0 & 0 & R \sin \phi \\ 0 & 0 & -1 & 0 & 0 & 0 \\ 0 & 0 & 0 & -\cos \phi & -\sin \phi & 0 \\ 0 & 0 & 0 & -\sin \phi & \cos \phi & 0 \\ 0 & 0 & 0 & 0 & 0 & -1 \end{vmatrix} \quad (4.9)$$

$$[C'_{four-bar}] = [C_t][C_{four-bar}][C_t^T] \quad (4.10)$$

### 4.2.1 Stiffness Ratios

The compliance of a serial system is given by the sum of the compliances of its elements. Figure 4.28 illustrates why it is important to transform the element's coordinate systems to the system coordinate system. The image shows that an  $F_{r1}$  load on the input stage results in  $f_{r2}$  and  $f_{\theta2}$  forces and an  $m_{z2}$  moment on the floating stage. Another critical detail in calculating the compliance of a compound four-bar is to account for the translations of the input stage resulting

from the floating stage's rotations. The transformation matrix given in (4.9) captures the effects of the floating stage's  $\alpha_z$  by taking into account the distance between the stages. Equations (4.11)-(4.12) give the input stages displacements as a function of the floating stage's rotations.

$$\Delta\theta_{due\ to\ \alpha_z} = -R(1 - \cos \phi) \sin \alpha_z \quad (4.11)$$

$$\Delta r_{due\ to\ \alpha_z} = R \sin \phi \sin \alpha_z \quad (4.12)$$

The effect of  $\phi$  on the CF compound four-bar's stiffness ratios is shown in Figure 4.29 and Figure 4.30. The stiffness ratios for a planar compound four-bar of the same dimensions are shown for comparison. Just like in the element design, the sweep angle of the compound four-bar can be used to improve the  $K_z/K_r$  ratio in exchange for a higher  $K_z/K_\theta$  ratio. Once again, the ratios are approximately equal when  $\phi = 122^\circ$ . The difference between the model and the FEA values may be partially attributed to the four-bar parasitic rotations of the floating stage which are manifested as a  $\Delta z$  displacement of the input stage.

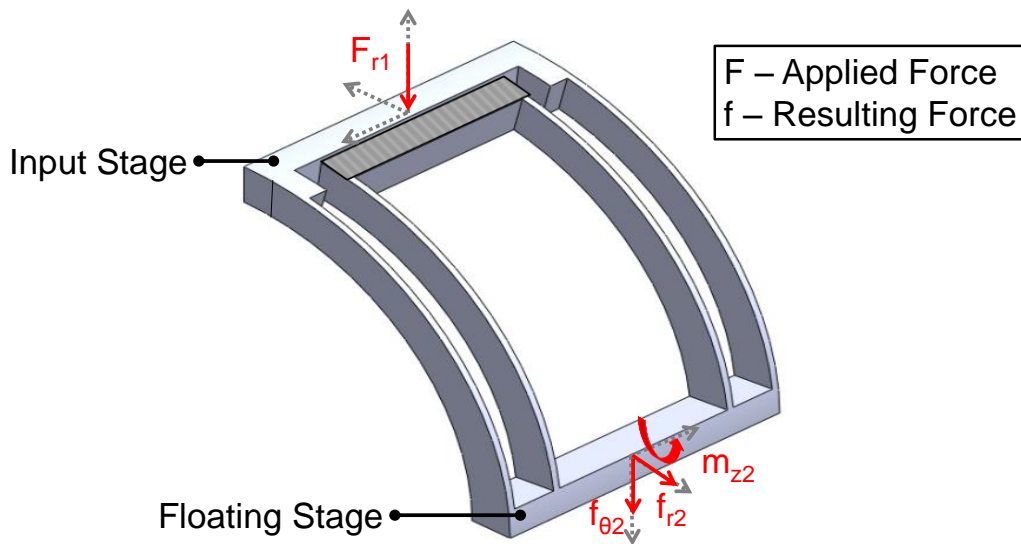


**Figure 4.28: In a compound four-bar each four-bar has a different coordinate system; therefore, an applied radial force,  $F_{r1}$ , on the input four-bar results in radial and axial forces,  $f_{r2}$  and  $f_{\theta 2}$ , and a moment about  $z$ ,  $m_z$ , on the floating four-bar.**

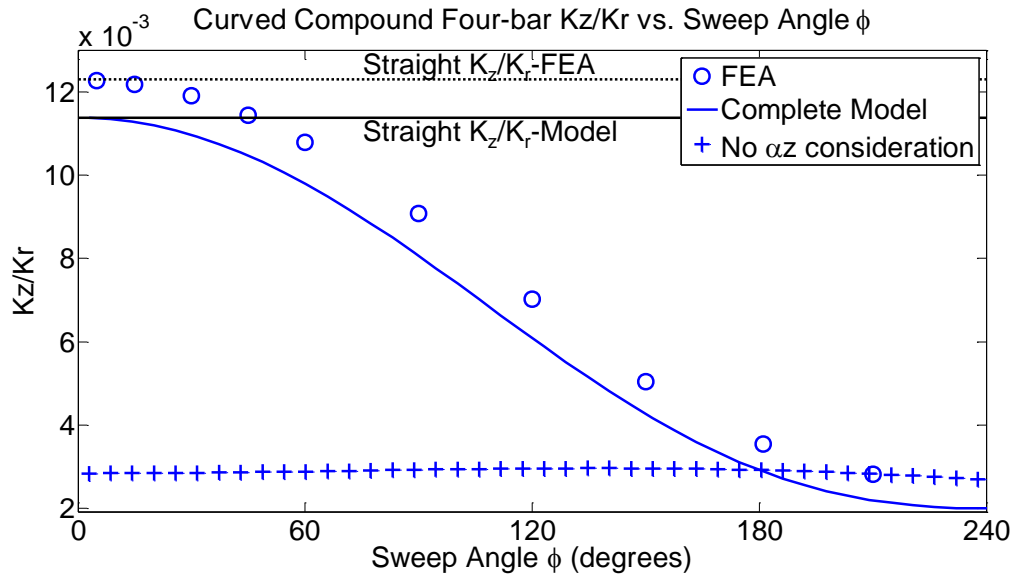


**Figure 4.29: Sweep angle,  $\phi$ , effect on the CF compound four-bar's  $K_z/K_r$  stiffness ratio. Plot shows that the ratio decreases with increasing  $\phi$ . The CF's ratio is compared to the  $K_z/K_r$  of a straight compound four-bar of the same dimensions. The graph demonstrates the importance of accounting for the effect of the  $\alpha_z$  rotation of the floating stage.**

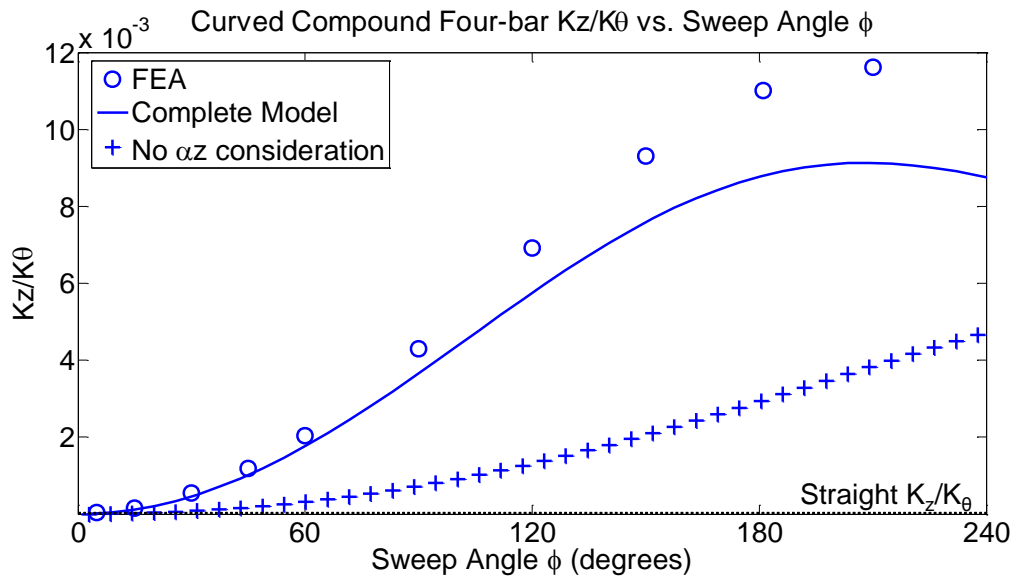


**Figure 4.30: Sweep angle,  $\phi$ , effect on the curved compound four-bar's  $K_z/K_\theta$  stiffness ratio. Plot shows that the ratio increases with increasing  $\phi$ . The CF's ratio is compared to the  $K_z/K_\theta$  of a straight compound four-bar of the same dimensions. The graph demonstrates the importance of accounting for the effect of the  $\alpha_z$  rotation of the floating stage.**

## 4.2.2 Parasitic Rotation Ratios

The planar compound four-bar is commonly used because not only does it have twice the range of a four-bar, but in addition the nesting of the four-bars decreases the input stages parasitic rotations, as shown in Figure 1.5b. The analysis of the CF compound four-bar parasitic motions is more complex because the input and floating stages are located on two different planes. The easiest way to establish the parasitic rotation ratios of the compound four-bar is through three steps: (i) first calculate the rotations of each four-bar, as shown in section 4.1.2, (ii) then transform the  $\alpha_{r2}$  and  $\alpha_{\theta2}$  of the floating stage to the coordinates of the input stage, (iii) finally add the corresponding parasitics to establish  $\alpha_r$  and  $\alpha_\theta$  for the system's input stage. This technique was used to investigate the effect of  $\phi$  on the compound's  $\alpha_r$  and  $\alpha_\theta$ , shown in Figure 4.31.

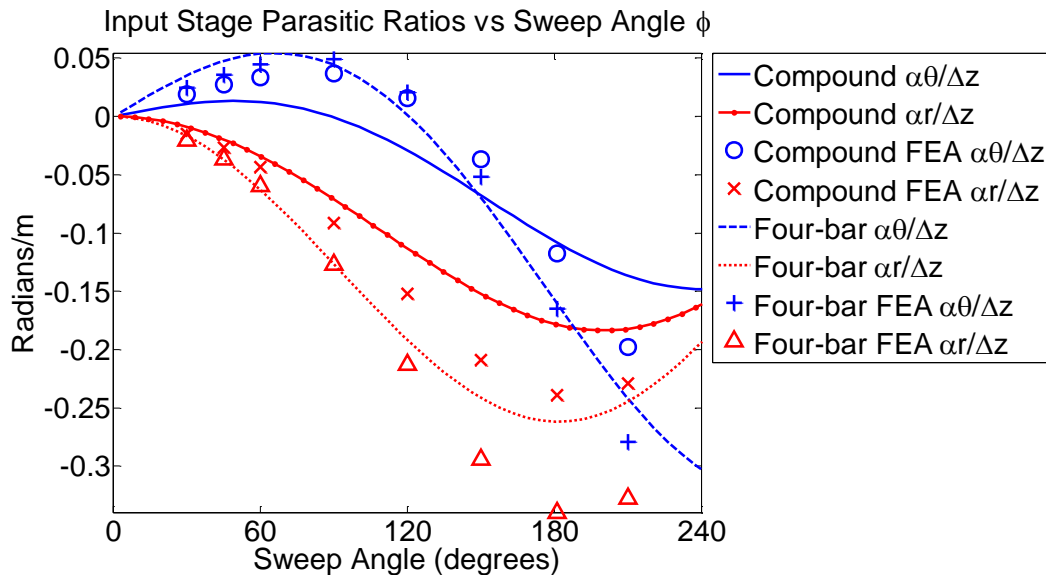


**Figure 4.31: Curved compound four-bar parasitic ratios vs.  $\phi$ . Plot compares the parasitic ratios for a compound four-bar to those of a single four-bar.**

## 4.2.3 Parasitic Displacement Ratios

In planar systems the nesting of the four-bar cancels the parasitic displacement,  $\Delta y$ , of the input stage. For CF compound four-bars there is no direct cancellation of the input stage's  $\Delta r$  and  $\Delta \theta$ . The compound four-bar's  $\Delta r$  and  $\Delta \theta$  is estimated by transforming the floating four-bar's translations to the system's coordinate system and adding them to the input four-bar's displacements. Figure 4.32 compares the parasitic displacement ratios of the compound four-

bar's input stage to those of a single four-bar. The data shows that the nesting of the four-bars does reduce the parasitics of the input stage, but does not completely cancel them for all  $\phi$ . A symmetric system design may be used to further reduce the undesired translations of the input stages. Two examples of symmetric CF compound four-bar designs are shown in Figure 4.33. In example (A) the input stage will experience an  $\alpha_z$  rotation due to the  $\Delta\theta$  movement of the compound four-bars.

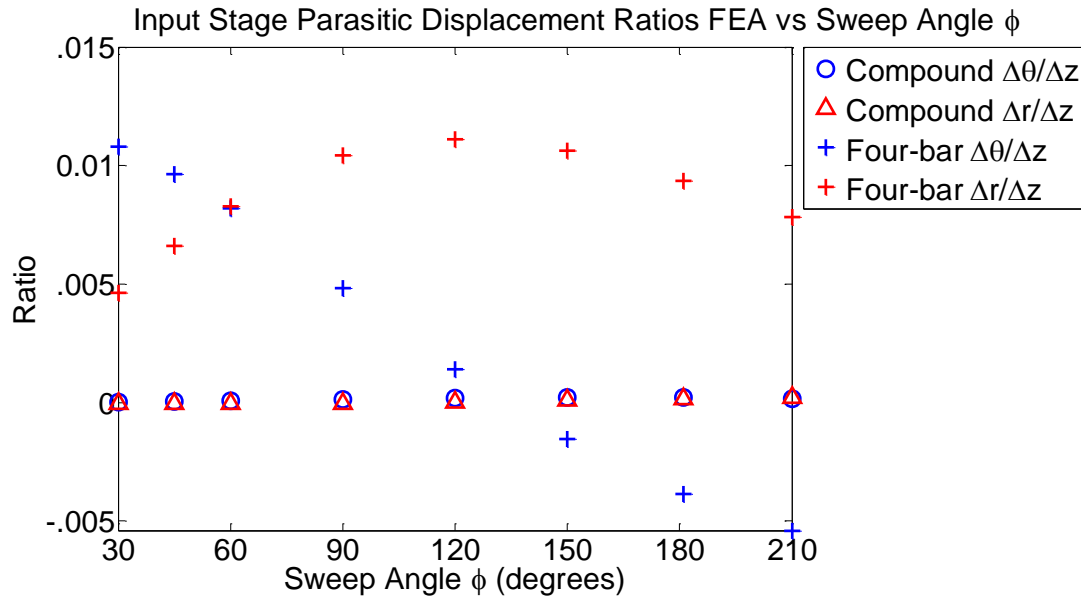


**Figure 4.32: Curved compound four-bar parasitic ratios vs.  $\phi$ . Plot compares the parasitic ratios for a compound four-bar to those of a single four-bar.**

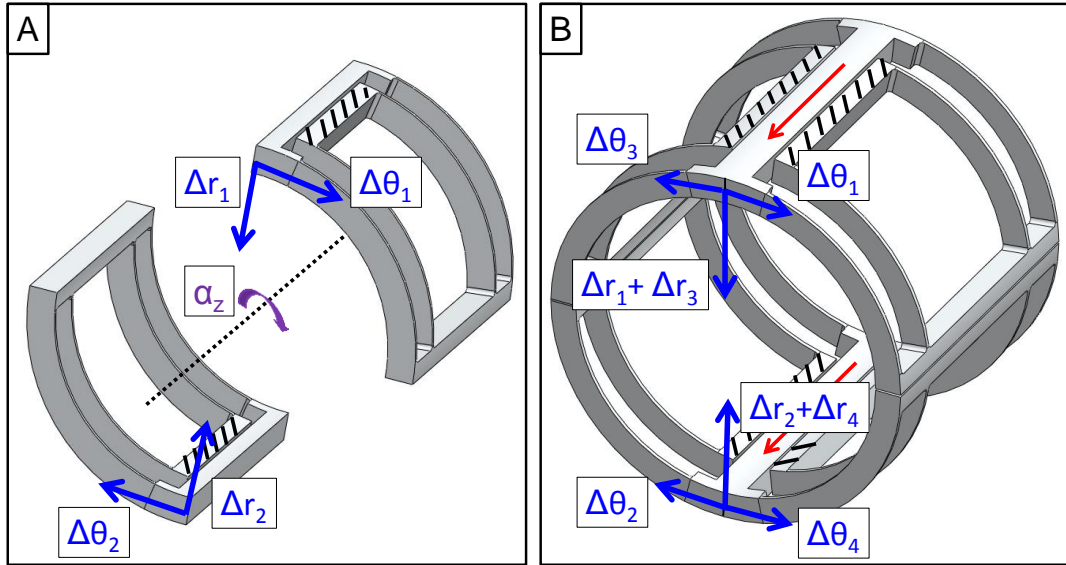


**Figure 4.33: A symmetric system design may be used to reduce or remove the parasitic displacements,  $\Delta r$  and  $\Delta \theta$ , of a compound four-bar. A) In a design with two compound four-bars separated by  $180^\circ$ , the  $\Delta r$  displacements cancel out and the  $\Delta \theta$  motions result in an  $\alpha_z$ -rotation. B) Using two double-compound four-bars leads to the cancellation of all the parasitic displacements.**

### 4.3 Summary of System Design Rules

The previous sections demonstrated how to analyze two CF systems. The basis for the creation of any CF system is the element compliance matrix. The system creation process developed in this work is generalized in the flow chart in Figure 4.34. The insights produced from the analysis of the CF four-bar and compound four-bar systems are summarized in the following rules:



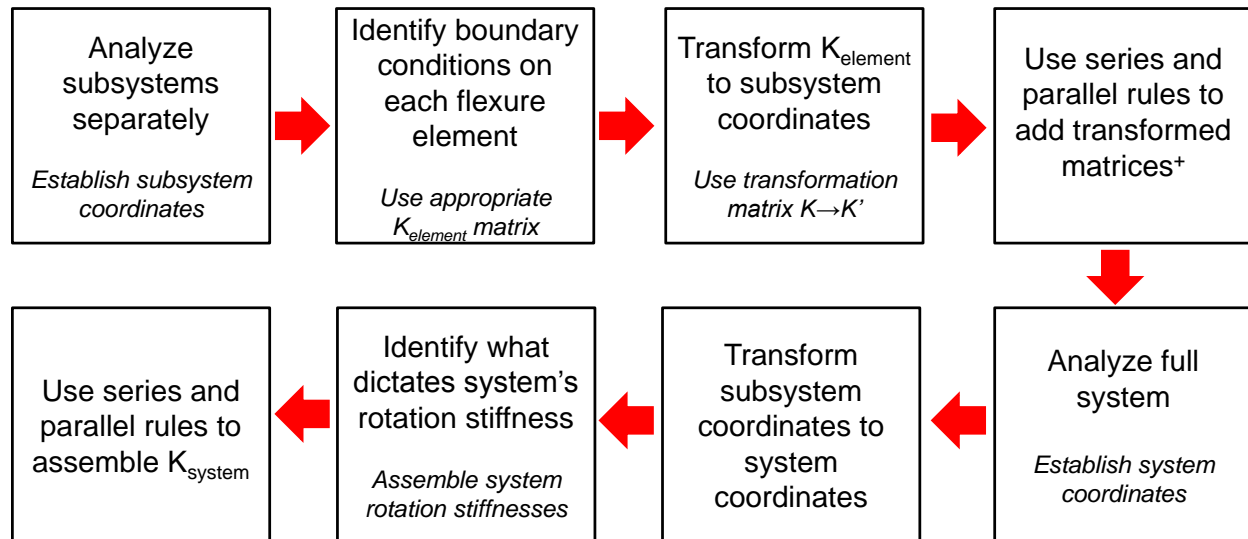


**Figure 4.34: Steps used to establish a CF system's compliance matrix. <sup>+</sup>For serial systems it may be necessary to account for the compliance due to rotations of the secondary stages.**

- 1) The curvature of the four-bar systems has a large effect on the system's performance metrics.
- 2) The curved four-bar has a larger  $K_z/K_\theta$  ratio but a better  $K_z/K_r$  ratio than a planar system. The ratios are equal when  $\phi \approx 120^\circ$ .
- 3) The 3D solid effect is significant when dealing with CF systems. In order to accurately calculate the parasitic rotations of a cylindrical four-bar the rotation of the  $r$ -axis,  $\omega$ , due to the difference in length at the inner and outer radiuses and the length of the stage must be accounted for. The presented model for  $\omega$  captures these effects and allows for the designer to accurately predict the  $\alpha_r$  and  $\alpha_\theta$  of a curved four-bar.
- 4) The parasitic rotations of the CF four-bar are highly sensitive to load location. A 10% error in the magnitude of the applied moment gives up to a 500% error in  $\alpha_r$  or  $\alpha_\theta$ . As a result, it is best to remove system parasitic rotations through a symmetric design.
- 5) In serial systems the element's or subsystem's compliance matrices must be transformed to the system's coordinates.
- 6) The  $r$ - and  $\theta$ -compliance of a curved compound four-bar is affected by the  $\alpha_z$  rotation of the floating stage.

- 7) A CF compound four-bar may be used to extend the range of the system and reduce its parasitics. However, the nesting of the four-bars does not directly cancel the undesired displacements.

# 5

## CF LINEAR GUIDE

---

A Fourier Transform Spectrometer (FTS) measures spectral components of incident radiation. One of the applications of long-wave infrared FTS is hyperspectral imaging of chemical plumes for early warning of accidental or deliberate toxic gas releases. This application requires the constant velocity translation of a mirror. The moving mirror must translate without any out-of-plane rotations to ensure the accurate reading of the spectral data [10]. MIT Lincoln Laboratory approached our lab looking for a new design to guide the moving mirror. The engineers at Lincoln had already developed a design for the guide, shown in Figure 5.1a, however the design required the assembly of 15 precision pieces making it cost prohibitive for the project. The goal of our project was to come up with a lower cost design that still met all the functional requirements. A cylindrical geometry design was first contemplated because it is (i) symmetric and therefore thermally insensitive, (ii) easily assembled with other cylinder-shaped elements (dampers, actuators, etc...), which is useful for co-axial assemblies that are common to optics, and (iii) easily made in volume with low-cost tube stock via conventional machining processes. The first CF linear guide prototype, Figure 5.1b, was designed using straight-beam guidelines and FEA. The development of the first guide highlighted the need for design rules specific to curved-flexures. The second prototype shown in Figure 5.1c was conceived using the models and guidelines presented in Chapters 3 and 4. The redesign of the linear guide using the CF design rules led to an order of magnitude improvement in system performance.

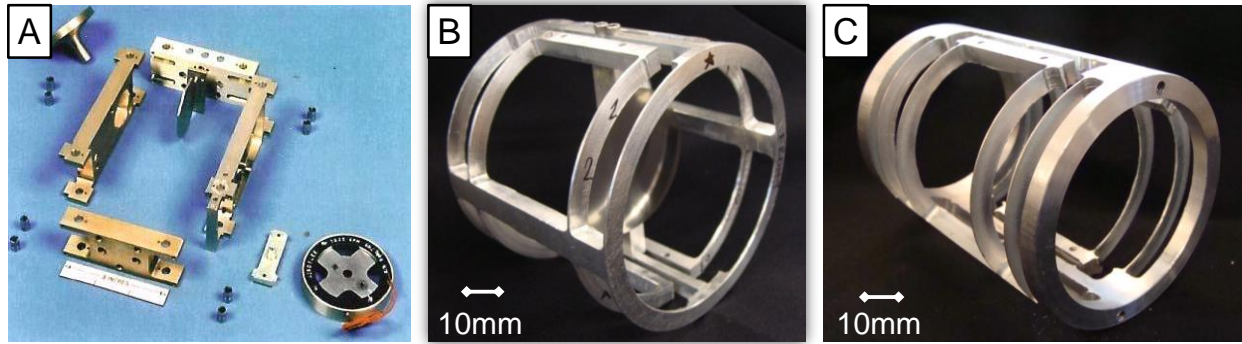


**Figure 5.1: Linear guide prototypes: A) MIT Lincoln Lab’s FTS linear guide, B)First CF linear guide, C) Second CF prototype designed using CF guidelines.**

## 5.1 Application

Lincoln’s FTS design utilizes a Michelson interferometer to capture the spectral components of the incident radiation. The operation of a Michelson interferometer is illustrated in Figure 5.2. In the FTS system one of the arms of the interferometer has a moving mirror, whose translational motion modulates the incident IR radiation. Demodulation via a Fourier transform provides the spectral information content of the incident radiation [33]. Applications of FTS include atmospheric sounding to aid numerical weather prediction, hyperspectral imaging of chemical plumes for early warning of accidental or deliberate releases, and other civilian and defense missions. In order to make accurate measurements, the mirror must translate at a constant velocity in forward and reverse linear-motion sweeps when data is collected. The optic reverses course at each end of the sweep (when no data is collected). A linear motion is required over several centimeters and this must occur with tip and tilt errors of tens of microradians or less [33]. The functional requirements for the linear guide that translates the moving mirror are given in Table 5.1.

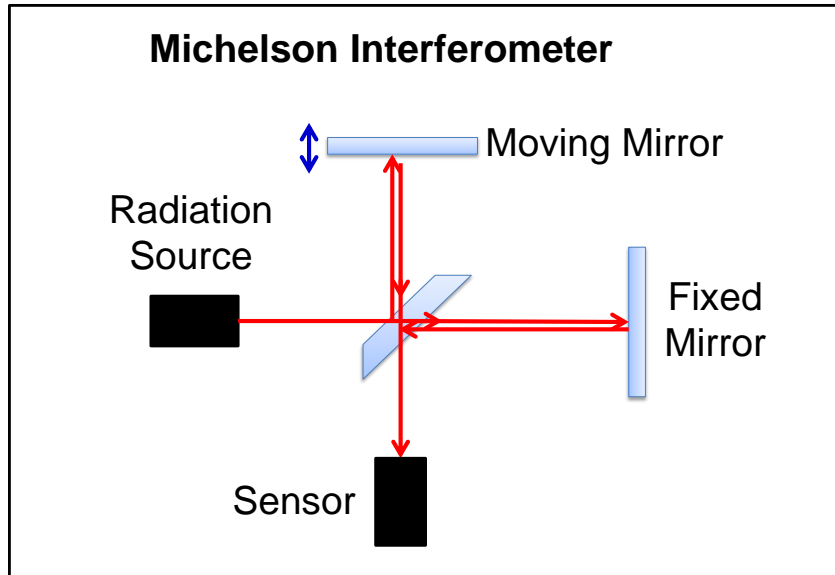


**Figure 5.2: Michelson Interferometer illustration. A linear guide is used to translate the moving mirror.**

**Table 5.1: FTS linear guide functional requirements.**

	Value	Notes
Mechanism Envelope	12x10x7 cm <sup>3</sup>	
Range	10-50 mm	FTS resolution increases with range
Tip/Tilt error	±10 μrad	Tip/Tilt error results in signal error
Cost	<\$15,000	

## 5.2 First Prototype

The original design was based on adapting the common planar compound four-bar to a cylindrical geometry. Two double compound four-bars were wrapped around to create a single cylinder as shown in Figure 5.3. A double compound four-bar is created by joining to compound four-bars at their input stages [6]. This design limits the sweep angle of the flexure blades to less than 90°. The limited sweep angle requires the use of a larger  $R$  to increase the element's length. In the presented design the flexure  $\phi$  was limited to 70° to allow space for the connecting stages.

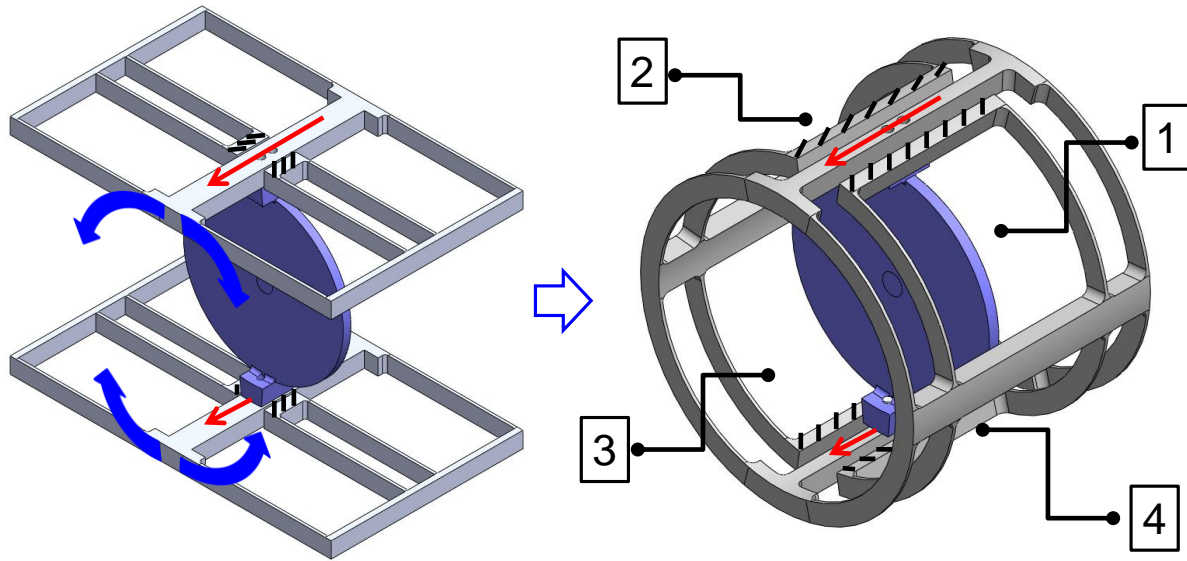


**Figure 5.3: The first CF linear guide prototype was conceived by wrapping two double compound four-bars. The floating stages of the compound four-bars were joined to create a single cylinder. The CF image highlights the four compound four-bars.**

The prototype was fabricated using a Mazak turning center shown in Figure 1.10a. The machine had never been used to cut a CF and therefore its limitations were unknown. To ease fabrication the  $t_z$  of the blades was set to 1mm. The  $t_r$  for the element was set to 6.35mm (0.25”) to match a common cylinder wall thickness. Initially the stress and range were calculated using straight-beam equations; however, FEA revealed that the calculations were inaccurate. In order to approach the volume functional requirement the CF was made out of 7075 Aluminum which has approximately an order of magnitude better yield stress to elastic modulus ratio than 6061 Aluminum. Even with this material choice, and given the chosen  $t_r$ ,  $t_z$ , and limited  $\phi$ , FEA revealed that the prototype had to have an outer diameter of 89mm to meet the desired 20mm range (each flexure blade in the compound four-bar has a range of 5mm in either direction). Table 5.2 gives the dimensions of the first prototype.

**Table 5.2: First CF linear guide prototype dimensions.**

<b>Parameter</b>	<b>Value</b>
Mid-radius ( $R$ )	41.3 mm
Sweep Angle ( $\phi$ )	70°
Element radial thickness ( $t_r$ )	6.35 mm
Element z-thickness ( $t_z$ )	1 mm
Cylinder length	76.2 mm
Number of compound four-bars	4
Material	7075 Aluminum

One of the goals of the first prototype was to demonstrate that CFs could be fabricated using conventional machining methods. The use of a standard lathe/mill reduces the cost of manufacturing the linear guides. The Mazak turning center is essentially a lathe with an actuated tool. Figure 5.4 shows the mechanism used to hold the cylindrical stock in place during machining. The cylindrical stock is slipped on a cylinder with an outer diameter nearly equal to the inner diameter of the flexure stock. The support stock is attached to a base which is then held in the lathe's spindle. The support cylinder is slightly shorter than the flexure stock so that when the cap is attached to the base the work-piece is constrained axially. The first CF linear guide prototype was successfully machined using this setup.

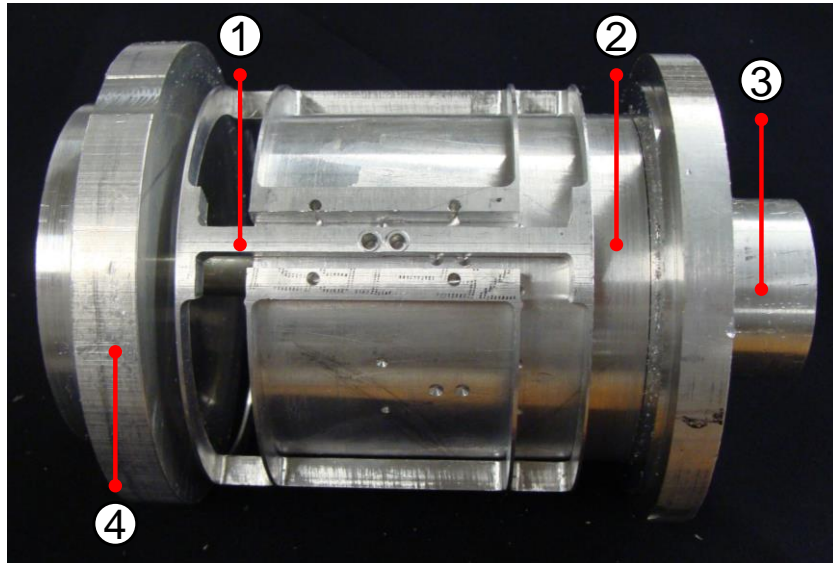


**Figure 5.4: Mechanism used to hold cylindrical stock in place during the machining process used to create the CF. The future flexure (1) is slipped onto a piece of cylindrical stock (2) which radially supports the work piece. The support stock is attached to a base (3) which is held by the lathe's spindle. The flexure stock is constrained axially with a cap (4) which is connected to the base using a bolt.**

The next step was to measure the performance of the prototype and compare the results to the functional requirements. The tip and tilt parasitic motions of the linear guide were measured using three linear optical encoders. The measurement setup is shown in Figure 5.5. The CF is held using a grinding cylinder which is attached to the optical table. The actuation load was exerted on one end of the guide using a depth micrometer. On the other end a cap with a u-channel with three scales was attached. The scales measured the displacements at: (i) the center of the flexure, (ii) the top and (iii) the side of the flexure. The distance between the center scale and the top and side scales was 50.8mm. Renishaw optical linear encoders were used to read the scales. The tip and tilt angles were calculated by computing the difference between the center and the top and side stages, respectively. Figure 5.6 and Figure 5.7 show both the unfiltered and filtered tilt and tip angles of the linear guide as it transverses 5mm. The plots indicate that the first prototype is unable to meet the functional requirement of  $\pm 10 \mu\text{radians}$  of tip/tilt over the minimum 10mm range. The unfiltered measurements display a cyclic trend approximately every 0.6mm, this trend is caused by to the rotation of the micrometer tip. The micrometer used to actuate the CF travels .025" per rotation (0.635mm). A moving average filter was used to remove the cyclic behavior imposed by the rotation of the micrometer head, the filtered data is overlaid



onto the unfiltered measurements in Figure 5.6 and Figure 5.7. For a given  $\Delta z$  position the filter averages the angles measured for all  $\Delta z \pm 0.3175\text{mm}$ . The cyclic error is not the dominant error for the first prototype, however, it became significant for the second prototype and was removed using a different setup described in section 5.3.

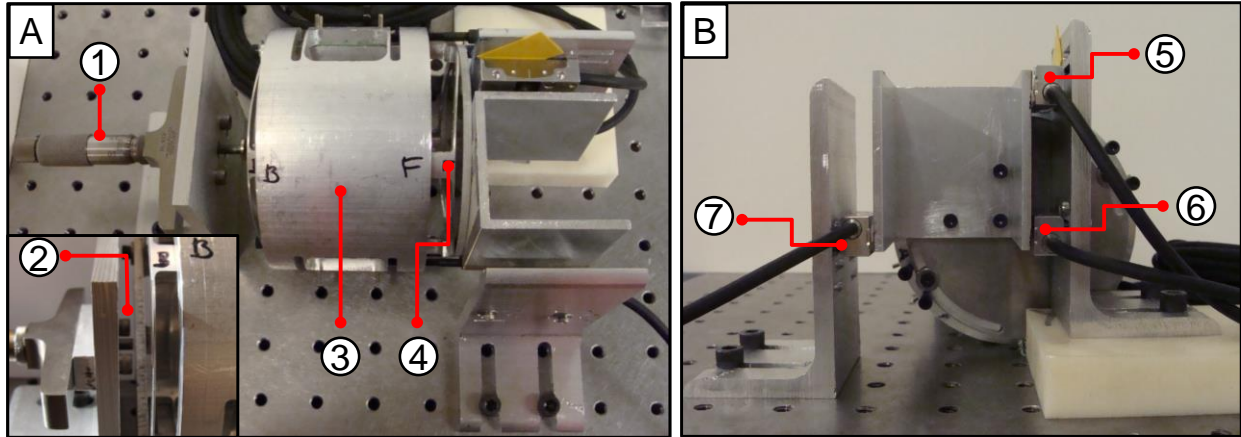


**Figure 5.5: First prototype measurement setup. A) The CF (4) is attached to a grounding cylinder (3) which is then attached to the optical table. The flexure is actuated using a depth micrometer (1) which pushes on a stage attached to the two input stages of the CF. The inset shows the tip of the micrometer (2) and the actuation stage. B) A cap with scales was attached to the flexure. The displacements of the CF were measured using optical linear encoders: (5) top, (6) center, (7) side.**

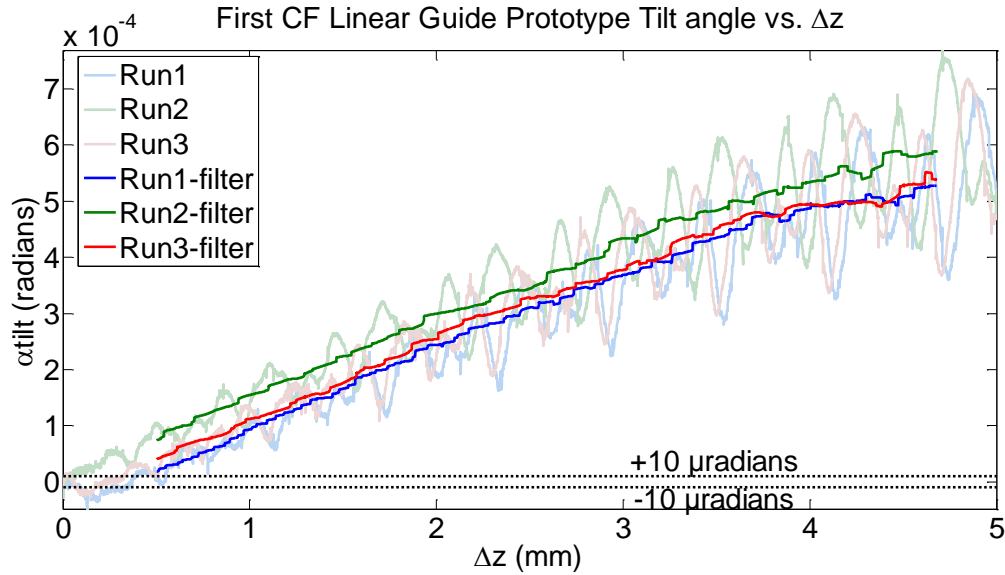


**Figure 5.6: Tilt angle vs. axial displacement ( $\Delta z$ ) for the first CF linear guide prototype. The dotted lines indicate the functional requirement of  $\pm 10 \mu\text{radians}$ . A moving average filter ( $\Delta z \pm 0.3175\text{mm}$ ) was used to remove the cyclic behavior imposed by the rotation of the micrometer head.**

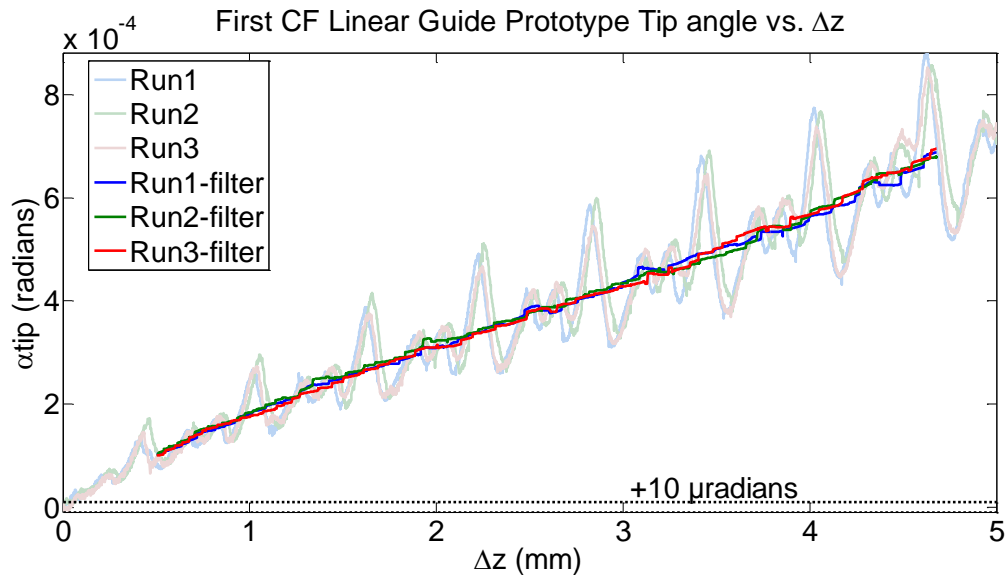


**Figure 5.7: Tip angle vs. axial displacement ( $\Delta z$ ) for the first CF linear guide prototype. The dotted line indicates the functional requirement of  $10 \mu\text{radians}$ . A moving average filter ( $\Delta z \pm 0.3175\text{mm}$ ) was used to remove the cyclic behavior imposed by the rotation of the micrometer head.**

As mentioned earlier the first CF prototype was designed without the design rules presented in this work, as a result a lot of problems with the design were overlooked. Foremost, the presented design is over-constrained. In a planar double compound four-bar the input stage has no parasitic displacements [6], however the floating stages will move along the flexure axis due to geometric constraints, as described in section 4.1.3. In the CF version the floating stages of the two double compound four-bars were connected together to create a single cylinder, and as a result their motion was constrained. Another issue with the design was that the stages were made rather small to maximize the sweep angle of the flexures. In section 4.1.2.2 it was shown that if the four-bar spacing is large enough and the connecting stage is not stiff enough the stage will deform as it attempts to constrain the parasitic rotations of the four-bar. FEA analysis of the first CF design revealed that the input stages were deforming during actuation, this is illustrated in Figure 5.8. The deformation of the stages may help explain why the performance of the linear guide was poor.

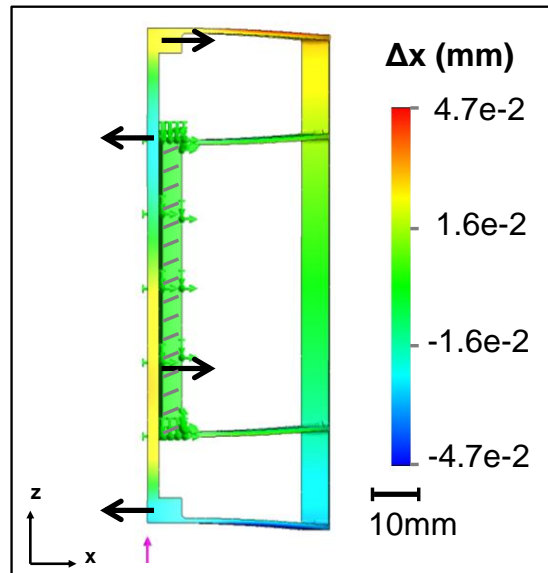


**Figure 5.8: FEA analysis of one of the compound four-bars of the first CF linear guide design shows that the input stage deforms during actuation.**

Table 5.3 compares the performance of the first CF linear guide design to the FTS functional requirements. Working through the design, fabrication, and measurement of the first prototype emphasized the need for the development of design rules and guidelines. The design of this prototype was inefficient and limited because it relied heavily on FEA. The FEA

optimization was tedious because there was little understanding as to how the CF factors affected the performance of the CF.

**Table 5.3: First CF linear guide prototype performance. <sup>+</sup>Error over 5mm range.**

	<b>Required</b>	<b>First prototype</b>
Mechanism Envelope	12x10x7 cm <sup>3</sup>	8.9x7.6x7.6 cm <sup>3</sup>
Range	10-50 mm	20 mm
Tip error	±10 μrad	700 μrad <sup>+</sup>
Tilt error	±10 μrad	600 μrad <sup>+</sup>
Cost	<\$15,000	<\$500

### 5.3 Second Prototype

The design and fabrication of the first cylindrical linear guide demonstrated the need for design rules for CFs. The second prototype was developed once the element and system guidelines had been established. The analytical models presented in this work enabled the efficient design of an improved linear guide design. The first step in the redesign was to remove the over-constraint of the floating stages. Figure 4.33 showed that a symmetric design of two compound four-bars spaced 180° apart theoretically has only one parasitic rotation,  $\alpha_z$ . This is a feasible design for the linear guide because the rotation about the CF's  $z$ -axis does not affect the performance of the FTS system. The next step was to reduce the design volume to meet the space constraints while still achieving the desired range. Ideally the design would also be able to be constructed out of 6061 Aluminum stock because it is more widely available in different stock sizes. The substitution from 7075 to 6061 Aluminum meant an order of magnitude decrease in  $\sigma_y/E$  and therefore in the range of the system. To offset this loss in range, the  $t_z$  of the flexures was reduced to 0.5mm. Testing of the capabilities of the Mazak turning center had revealed that the machine would be able to fabricate flexures of that thickness.

Once the material and  $t_z$  of the CF's elements had been established the challenge was to meet the desired range while staying within the design volume. The chosen concept is composed of only two compound four-bars, this design allows for  $\phi$  to be greater than  $90^\circ$ . The stress and displacement models for a four-bar developed in this work were used to find the minimum  $\phi$  required to meet the desired range (5mm per four-bar) given the volume, material,  $t_z$  and  $t_r$  constraints. The FTS functional requirements set the minimum system dimension at 70mm. In chapter 4 it was established that the four-bar's parasitics decrease with the square of the flexure spacing. In order to benefit from the maximum flexure spacing the longest dimension (120mm) was chosen as the constraint for the length of the cylinder. As a result the limit for the diameter of the CF was set at 70mm. The range vs.  $\phi$  is presented in Figure 5.9. The plot shows that for  $\phi > 91^\circ$  the four-bars are able to achieve the minimum 5mm range. A safety factor of 1.55 was applied to the range requirement to ensure that the CF system will not fail due to fabrication tolerances. The safety factor brings the minimum  $\phi$  to  $115^\circ$ .

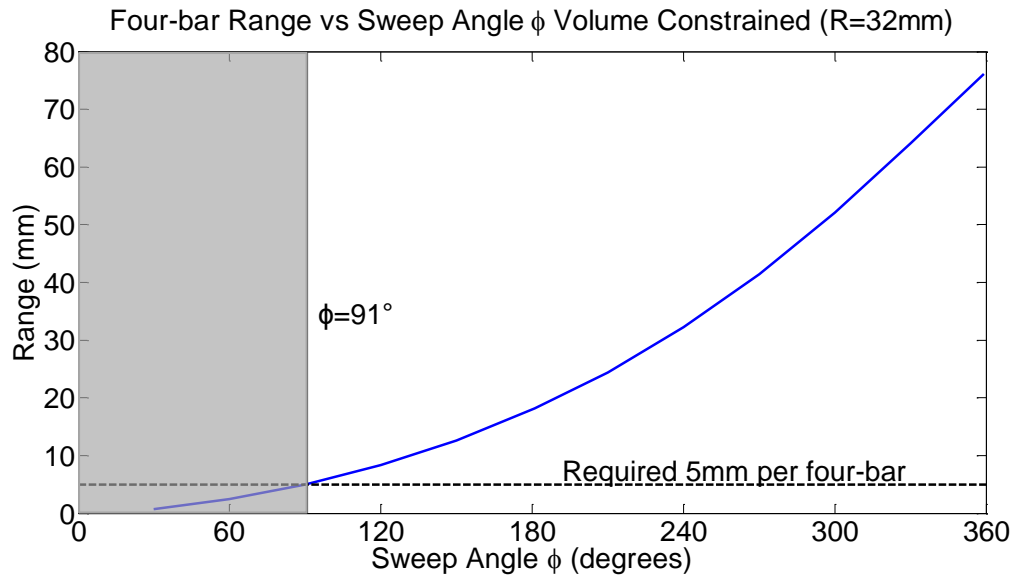


**Figure 5.9: Range vs. sweep angle,  $\phi$ , for a 6061 Aluminum four-bar with  $R=32\text{mm}$ ,  $t_r=6.35\text{mm}$ , and  $t_z=0.5\text{mm}$ . The minimum range required for the FTS system is 5mm per four-bar which is achieved for  $\phi > 91^\circ$ . An  $R$  of 31.75mm corresponds to an outer diameter of 69.85mm (2.75”).**

Once the minimum sweep angle required to meet the volume and range constraints was established, the next step was to analyze the design parameters effect on the CF's parasitic tip/tilt rotations. In chapter 3 it was established that the optimal  $\phi$  for reducing  $\alpha_r$  and  $\alpha_\theta$  of a z-

compliance element is  $\phi=118^\circ$ . Meanwhile chapter 4 presented models to calculate the parasitic rotations of a compound four-bar. Figure 5.10 shows how  $\phi$  affects  $\alpha_r$  and  $\alpha_\theta$  of a 6061 Al compound four-bar with the chosen  $t_r$  and  $t_z$ . In the plot the sweep angles below  $\phi=91^\circ$  have been shaded because these do not meet the minimum range requirement. The model predicts that the parasitic rotations increase with  $\phi$  and therefore a sweep angle as small as possible should be chosen for the design. Considering the range safety factor the element's  $\phi$  was set to  $115^\circ$ . A single compound four-bar will not meet the required parasitic ratio; however, a system composed of two compound four-bars spaced  $180^\circ$  apart will lead to a cancellation of the  $\alpha_r$  and  $\alpha_\theta$ . The challenge of joining the subsystems to create a single cylinder was solved by using two connecting rings to link the two input stages as shown in Figure 5.11. Table 5.4 lists the dimensions of the second CF linear guide prototype.

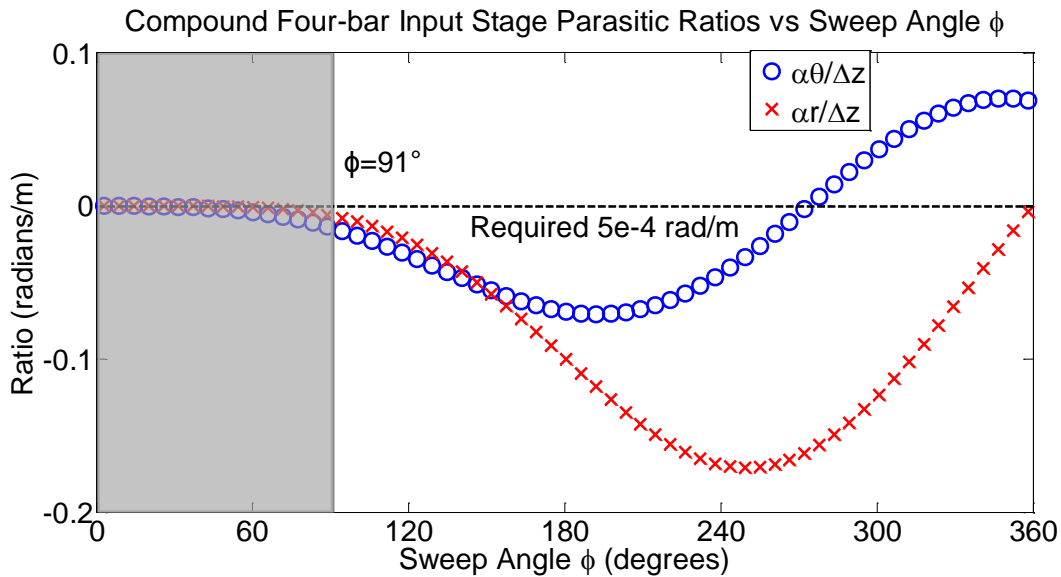


**Figure 5.10: Input stage parasitic rotation ratios vs. sweep angle,  $\phi$ , for a 6061 Aluminum compound four-bar with  $R=32\text{mm}$ ,  $t_r=6.35\text{mm}$ , and  $t_z=0.5\text{mm}$ . Angles below  $91^\circ$  are shaded because they do not meet the minimum 5mm range constraint. The dotted line indicates the FTS  $5\text{e-}4$  rad/m parasitic ratio requirement.**

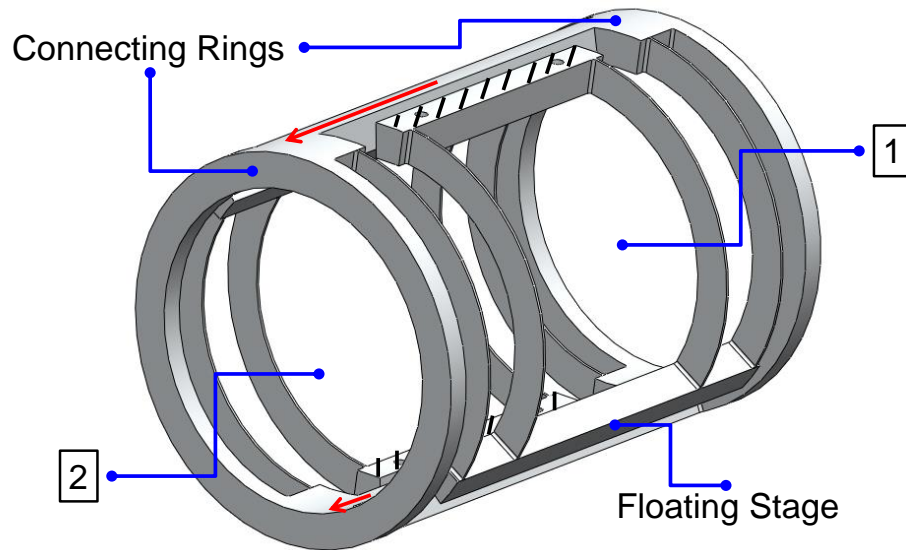


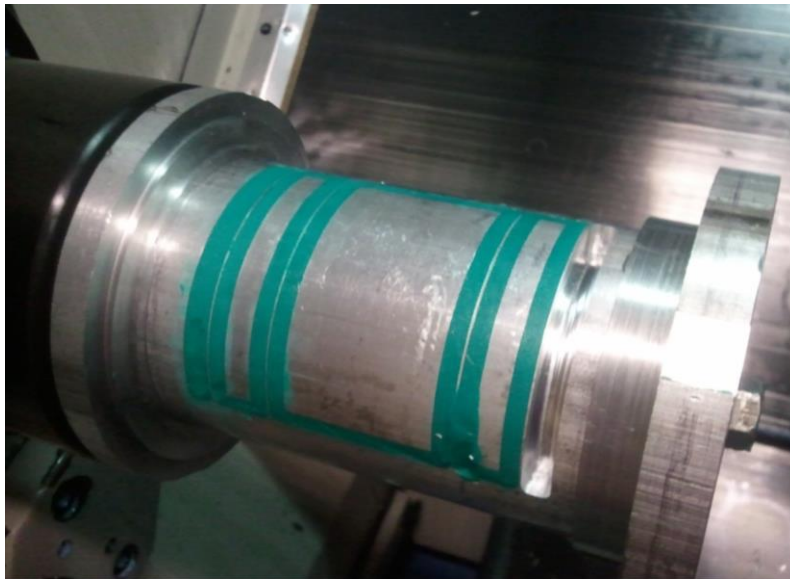
**Figure 5.11: CAD model of the second CF linear guide design. The concept is composed of two compound four-bars which are labeled in the picture. The design allows for the floating stages to translate and rotate freely. The two compound four-bars' input stages are joined using connecting rings at the front and back of the cylinder.**

**Table 5.4: Second CF linear guide prototype dimensions.**

Parameter	Value
Mid-radius ( $R$ )	31.75 mm
Sweep Angle ( $\phi$ )	115°
Element radial thickness ( $t_r$ )	6.35 mm
Element z-thickness ( $t_z$ )	0.5 mm
Cylinder length	100 mm
Number of compound four-bars	2
Material	6061 Aluminum

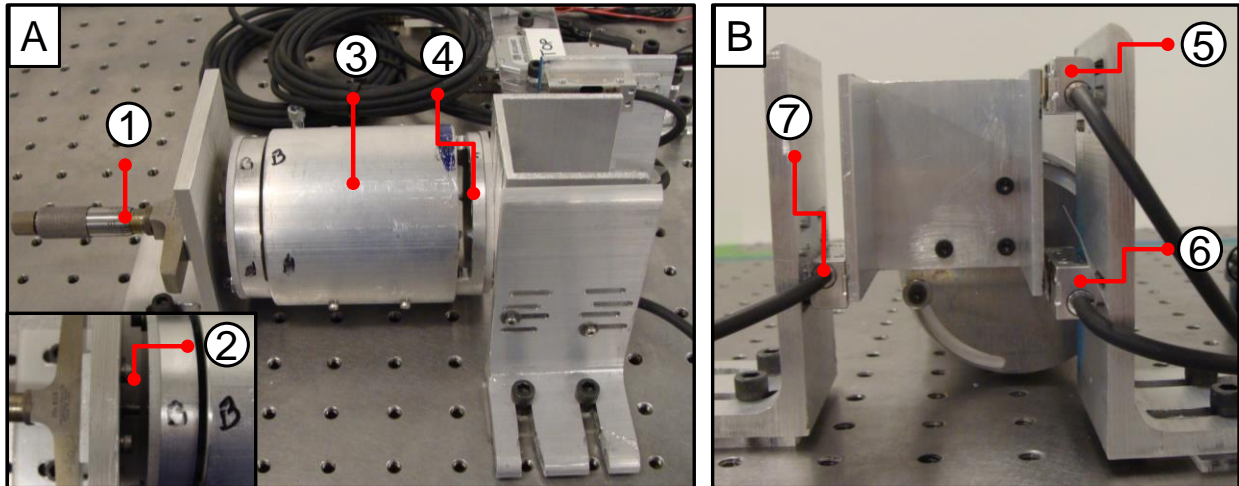
## 5.4 Fabrication and Testing

The second prototype was fabricated using the same Mazak turning center and fabrication setup. Once a pocket was milled it was filled with putty before the next pocket was cut. The putty helps reduce vibrations of the flexure elements during cutting. Figure 5.12 shows the partially machined prototype filled with putty. The pockets were also not cut all the way through; instead a 100 $\mu$ m web was left to keep the flexures attached and help reduce the vibrations. The web was removed using an exacto knife post machining. The performance of the second prototype was measured using the same setup that was used for the initial linear guide. The redesigned linear guide is shown in the measurement setup in Figure 5.13. The image shows the depth micrometer that was used to actuate the flexure, as well as the optical linear encoders used to measure the displacements at the top, side, and center of the CF.



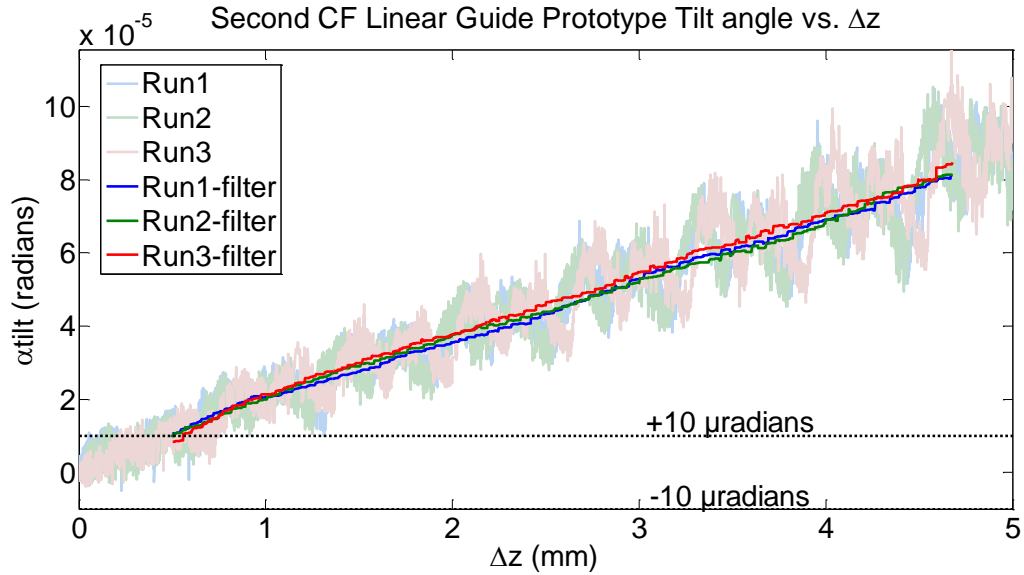
**Figure 5.12: Each pocket of the second prototype was filled with putty before the next one was cut. The putty helps reduce the vibrations of the flexure elements during cutting.**



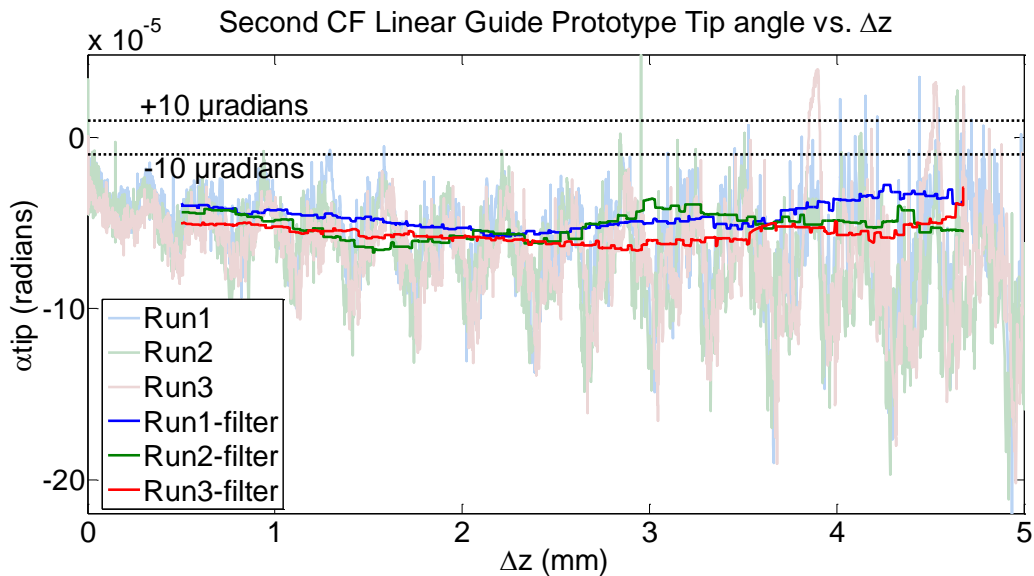


**Figure 5.13: Second prototype measurement setup. A) The CF (4) is attached to a grounding cylinder (3) which is then attached to the optical table. The flexure is actuated using a depth micrometer (1) which pushes on a cap attached to the connecting ring of the CF. The inset shows the tip of the micrometer (2) and the actuation cap. B) Another cap with scales was attached to the front of the flexure. The displacements of the CF were measured using optical linear encoders: (5) top, (6) center, (7) side.**

Figure 5.14 and Figure 5.15 plot both the unfiltered and filtered tilt and tip angle of the CF stage as a function of its  $z$ -axis displacement. The charts show that the tip and tilt error measured using the micrometer setup is an order of magnitude lower for the second concept compared to the initial CF design. Once again the data has a cyclic trend approximately every 0.6mm, which is associated with the rotation of the micrometer head. The cyclic error was removed using a moving average filter. For every  $\Delta z$  position the filter calculates the mean of all tip or tilt measurements at  $\Delta z \pm 0.3175\text{mm}$ . In the case of the performance of the second prototype the error associated with the micrometer rotation is significant, particularly in the measurement of the tip angle. In view of this observation it was decided that the prototype performance should be measured using a better setup.



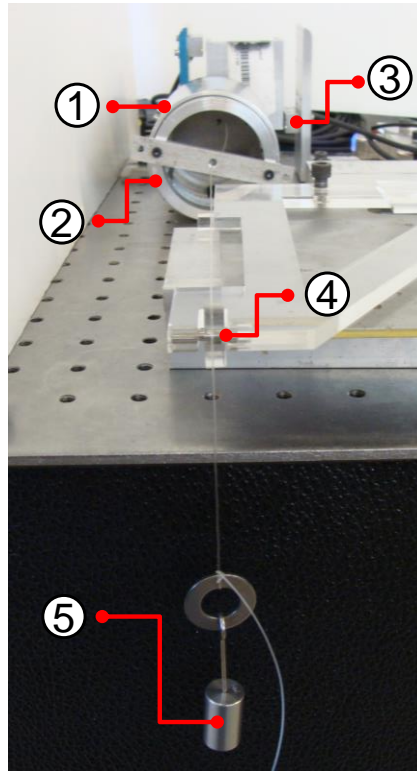
**Figure 5.14: Tilt angle,  $\alpha_{tilt}$ , vs. axial displacement ( $\Delta z$ ) for the second CF linear guide prototype. The dotted lines indicate the functional requirement of  $\pm 10 \mu\text{radians}$ . The flexure was actuated using a micrometer. A moving average filter ( $\Delta z \pm 0.3175\text{mm}$ ) was used to remove the cyclic behavior imposed by the rotation of the micrometer head.**



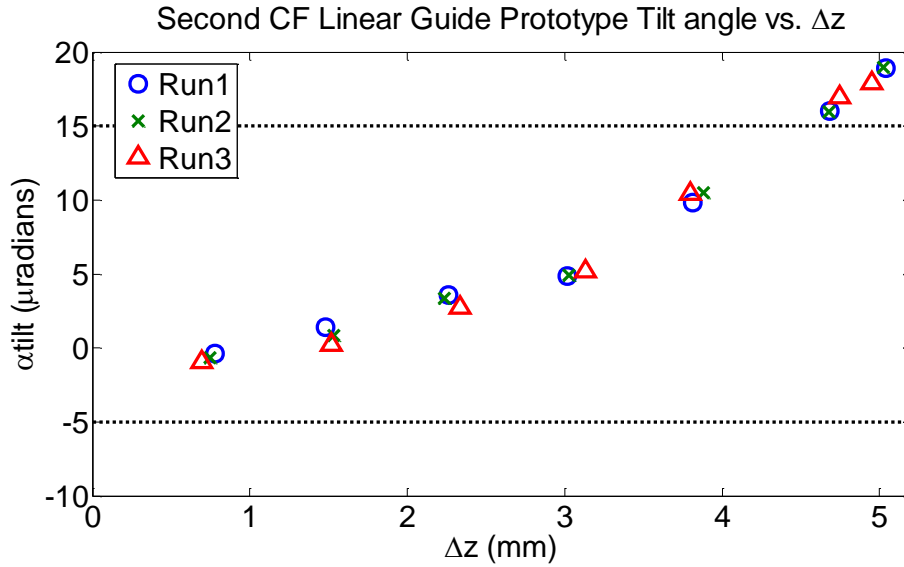
**Figure 5.15: Tip angle,  $\alpha_{tip}$ , vs. axial displacement ( $\Delta z$ ) for the second CF linear guide prototype. The dotted lines indicate the functional requirement of  $\pm 10 \mu\text{radians}$ . The flexure was actuated using a micrometer. A moving average filter ( $\Delta z \pm 0.3175\text{mm}$ ) was used to remove the cyclic behavior imposed by the rotation of the micrometer head.**

The solution to the micrometer error was to load the CF using masses on a low-friction pulley as shown in Figure 5.16. The flexure was loaded using increments of 50g, which resulted

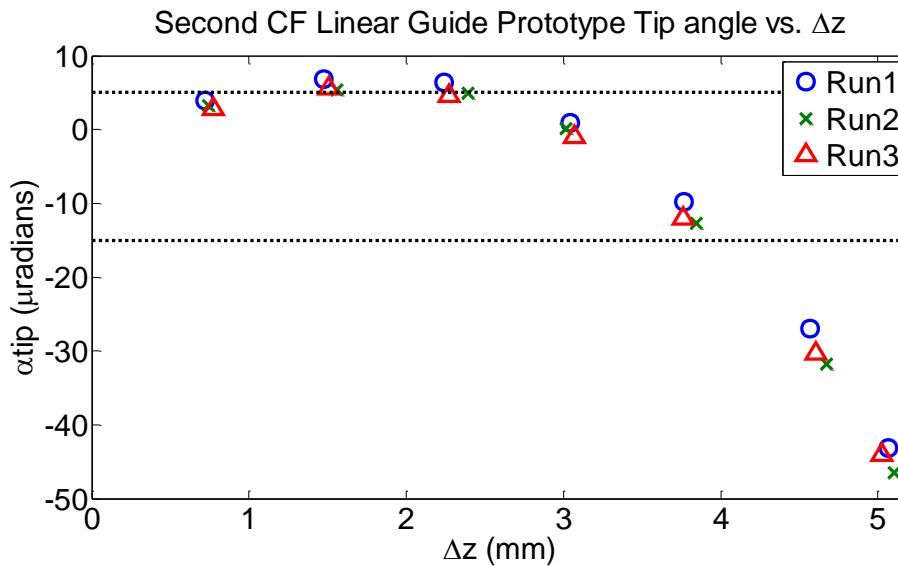
in discrete data points for the tip/tilt error of the system. Figure 5.17 and Figure 5.18 present the measured tilt and tip error for the second prototype using the new measurement setup. The tilt plot shows that the tilt error is nearly within the required  $\pm 10 \mu\text{radians}$  for the measured 5mm range. The tip error is higher but of the same order of magnitude.



**Figure 5.16: Weight loading measurement setup. The flexure (2) is attached to the table using a grounding cylinder (1). The CF is loaded using a mass (5) on a low-friction pulley (4). The displacements are measured using the same three optical linear encoders (3).**



**Figure 5.17: Tilt angle,  $\alpha_{tilt}$ , vs. axial displacement ( $\Delta z$ ) for the second CF linear guide prototype. The dotted lines indicate the functional requirement of  $\pm 10\mu$ radians from the average tilt error. The flexure was actuated by hanging masses.**



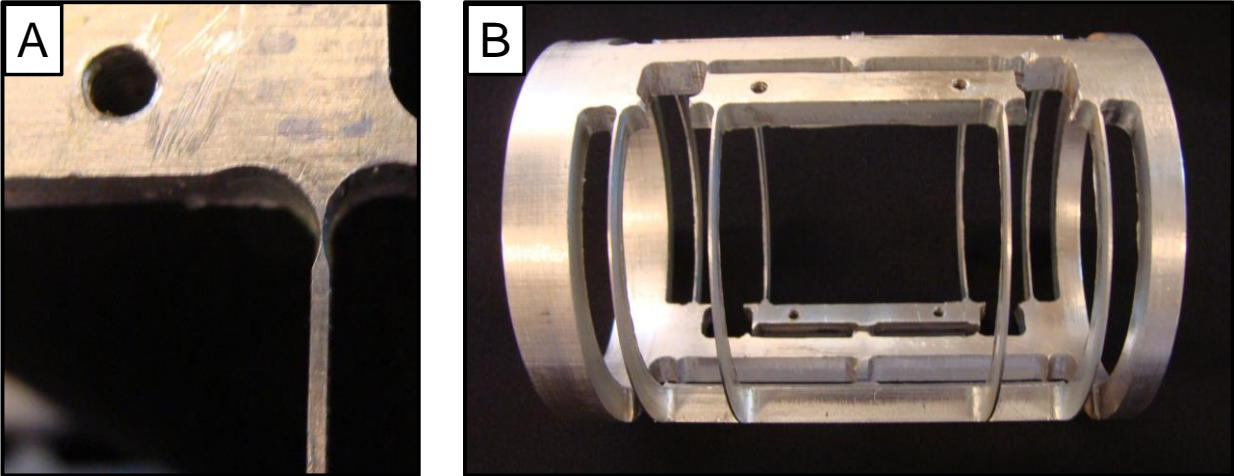
**Figure 5.18: Tip angle,  $\alpha_{tip}$ , vs. axial displacement ( $\Delta z$ ) for the second CF linear guide prototype. The dotted lines indicate the functional requirement of  $\pm 10\mu$ radians from the average tip error. The flexure was actuated by hanging masses.**

Table 5.5 compares the measured performance of the second prototype to the FTS functional requirements as well as the FEA projections. The FEA of the CF predicts a lower

tip/tilt error for the design, which suggests that there may be some external sources of error. A mistake was made when machining the prototype which resulted in certain flexures being thinner at their base as shown in Figure 5.19a. The travel limits of the machine also resulted in one connecting ring being larger than the other as highlighted in Figure 5.19b. These machining oversights resulted in the design no longer being symmetric. Another source of error is the location of the load; FEA shows a tip/tilt error of  $9.5\mu\text{radians}$  over the 5mm range when the load is applied 1mm from the center. Finally, the measurement setup is also asymmetric, the weight of the u-channel that holds the encoder scales applies a moment on the front of the flexure. This moment may explain why the tip error is larger than the tilt error. FEA predicts a  $10\mu\text{radian}$  tip angle for a 10 gram (0.1N) mass placed on one of the connecting rings. Table 5.6 summarizes the possible sources of error.

**Table 5.5: Second CF linear guide prototype performance. <sup>+</sup>Error over 5mm range.**

	<b>Required</b>	<b>Measured</b>	<b>FEA</b>
Mechanism Envelope	$12 \times 10 \times 7 \text{ cm}^3$	$10 \times 7 \times 7 \text{ cm}^3$	$10 \times 7 \times 7 \text{ cm}^3$
Range	10-50 mm	20 mm	20 mm
Tip error	$\pm 10 \mu\text{rad}$	$45 \mu\text{rad}^+$	$< 2 \mu\text{rad}^+$
Tilt error	$\pm 10 \mu\text{rad}$	$19 \mu\text{rad}^+$	$< 1 \mu\text{rad}^+$
Cost	$< \$15,000$	$< \$500$	-



**Figure 5.19: Machining errors: A) Tool lead-in error resulted in some of the flexure elements being thinner at their base. B) The back connecting ring is larger than the front because of the machine’s travel limit.**

**Table 5.6: Possible sources of tip/tilt error. <sup>+</sup>Error over 5mm range.**

Source	Notes
Machining error	Unsymmetric design
Load misalignment	9.5 $\mu\text{rad}^+$ error per 1mm misalignment
Weight imbalance	10 $\mu\text{rad}$ error per 0.1N imbalance

The guidelines and rules presented in this work were used to create a design with an order of magnitude lower tip/tilt error than the concept created using straight-beam rules and FEA. The CF linear guide performance may be further improved by reducing the sources of error or making the design less sensitive to these errors. The current design should be able to meet the FTS requirements according to FEA if the machining oversights are eliminated, the accuracy of the load location is improved, and the measurement setup is made symmetric such that there is no weight imbalance. A better way to fix the actuator to the system would be to attach it to the grounding cylinder as opposed to the table. One way to decrease the sensitivity of the design is through Saint-Venant’s principle [34]. If two linear bearings are used instead of a single linear guide, then the spacing of the guides may be used to decrease the tip/tilt error of the moving

mirror. Figure 5.20 shows a monolithic design for a two bearing CF linear guide. The actuator may be placed between the two bearings to reduce the overall length of the system.

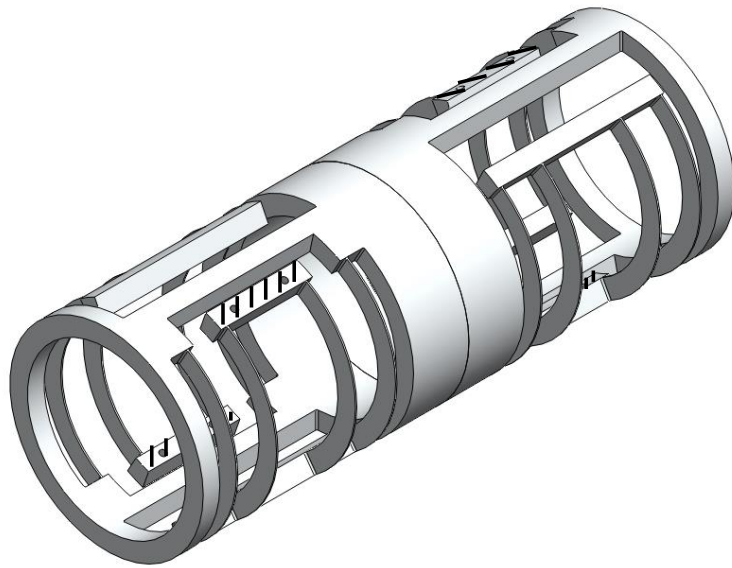


**Figure 5.20: Linear guide constructed using two CF bearings.**





# 6

## CF X-Y- $\theta_z$ STAGE

---

Dip Pen Nanolithography (DPN) utilizes atomic force microscope cantilevered tips as pens to write nano-patterns. The scale of the tips allows for feature sizes ranging from 50nm to 10 $\mu$ m. DPN's resolution enables it to print user-defined organic, inorganic, and biological materials. The challenge with DPN is that the disposable cantilever tips have to be aligned to the machine. The alignment requires 1 $\mu$ m accuracy and 0.1 $\mu$ m repeatability [35]. Last year Marcel Thomas, a student in the PCSL lab, designed an x-y- $\theta_z$  stage to align the tips to the DPN machine; his design is shown in Figure 61a. The primary goal of the second case study was to demonstrate the usability of the presented design rules and guidelines during the design process for a CF *r*-compliance stage that met the DPN requirements. To this end the stage was designed in collaboration with an undergraduate senior thesis student. The student was introduced to the rules and models presented in this work and guided throughout the design process. The result of this collaboration is the system shown in Figure 61b. The CF design presents an alternative x-y- $\theta_z$  stage design with comparable performance but it has the advantage that it can be fabricated out of a single piece of stock.

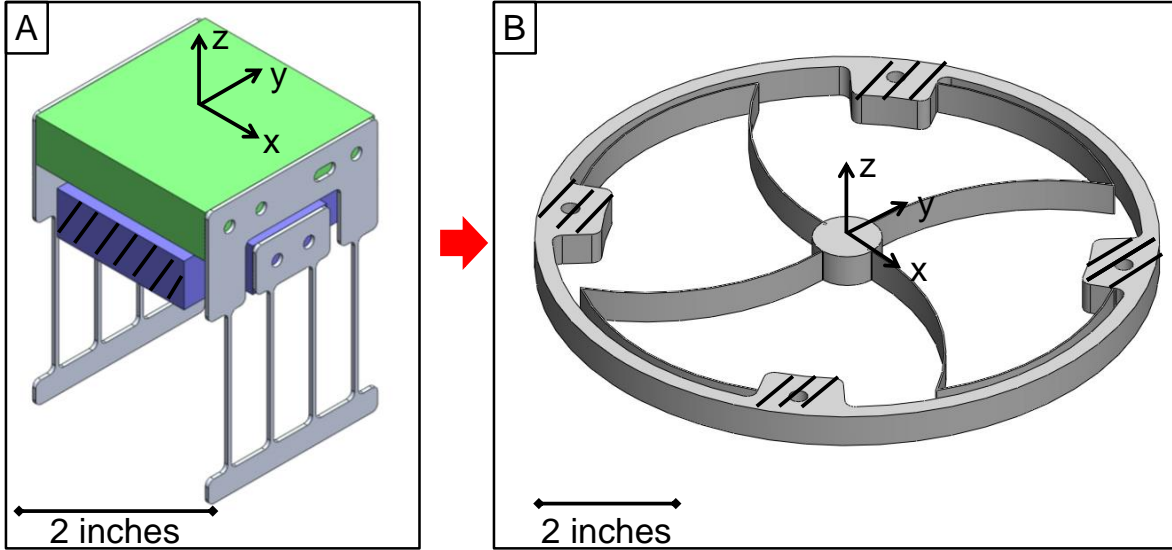


**Figure 61: A) Thomas' current straight-beam  $x$ - $y$ - $\theta_z$  stage [35]. B) Proposed CF  $r$ -compliance  $x$ - $y$ - $\theta_z$  stage.**

## 6.1 Application

The state of the art NanoInk DPN machine requires manual alignment of the tip to the machine. Manually aligning the tip to the machine is time and labor intensive; in some cases the time to set-up the machine is greater than the print time. In his thesis Thomas proposes a system, shown in Figure 6.2, to automate the alignment process using his  $x$ - $y$ - $\theta_z$  stage, three voice coils, and a camera. The camera is used to establish the position of the DPN tip. The camera image is analyzed using Matlab to determine the  $\Delta x$ ,  $\Delta y$ , and  $\theta_z$  stage displacements required to move the tip to the desired location. The voice coils are then used to control the position of the stage. Once the actuation is complete, the camera takes another picture to evaluate the new position of the tip. The feedback loop is repeated until the DPN tip has been aligned correctly [35]. Table 6.1 summarizes the current alignment system attributes. The CF stage will be actuated using the same voice coils, therefore its in-plane stiffnesses need to be similar to those of the current stage. The performance of the CF  $x$ - $y$ - $\theta_z$  stage will be evaluated relative to the performance of the straight-beam stage.

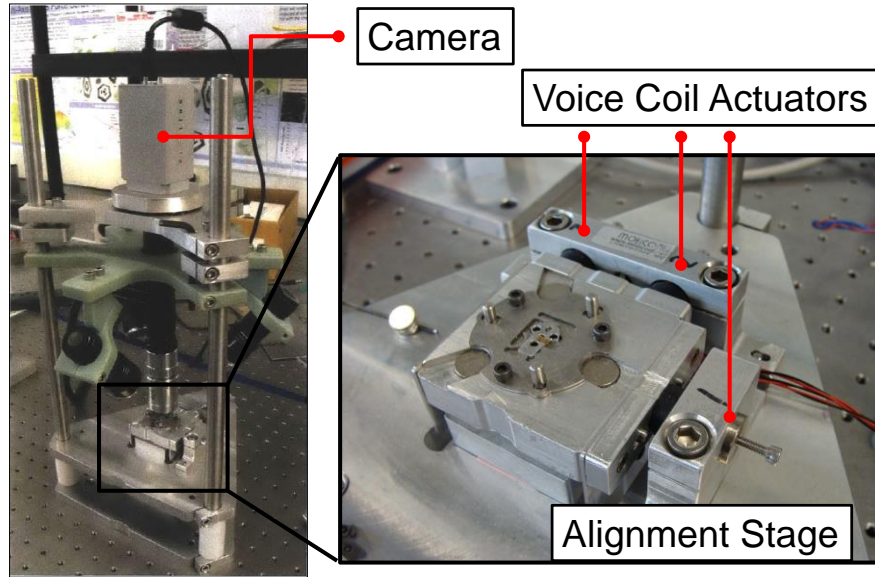


**Figure 6.2: DPN alignment mechanism with the straight-beam x-y- $\theta_z$ -stage [35]. The camera is used to determine the position of the DPN tip, while the voice coil actuators are used to position the tip.**

**Table 6.1: DPN x-y- $\theta_z$ -stage attributes.**

Attribute (required)	Straight-beam Flexure Stage (FEA results)
$K_x$	1.7 N/mm
$K_y$	2.3 N/mm
$K_{\theta_z}$	2 Nm/rad
$K_y/K_z$	$1.4 \times 10^{-3}$
$K_{\theta_z}/K_{\theta_x}$	$9.1 \times 10^{-3}$
$\Delta x$ -range ( $\pm 272 \mu\text{m}$ )	$\pm 5.99$ mm
$\Delta y$ -range ( $\pm 272 \mu\text{m}$ )	$\pm 4.18$ mm
$\theta_z$ -range ( $\pm 0.2$ rad)	$\pm 0.37$ rad
Volume	5.1x5.3x7.6 cm ( $205 \text{cm}^3$ )

## 6.2 CF Design Process

### 6.2.1 Concept Generation

The idea to design a CF x-y- $\theta_z$  stage was driven by the observation that for certain sweep angles  $r$ -compliance elements can behave as having 2-DOF,  $\Delta r$  and  $\Delta\theta$ . This property makes it possible to use a single flexure blade to guide the  $x$ - $y$  motions. The challenge with using  $r$ -compliance flexures to create an x-y- $\theta_z$  stage is that both their  $K_r/K_\theta$  and  $K_r/K_z$  stiffness ratios rise quickly with increasing  $\phi$ , as shown in Figure 3.11. As a result the sweep angle must be carefully chosen to ensure that the elements provide a  $z$ -constraint but allow for  $x$ - $y$  travel.

Figure 6.3 presents the preliminary concept layouts conceived during the concept generation phase. The rules and guidelines presented in this thesis made it possible to quickly sketch these concepts and to analyze their performance. The concepts were evaluated on their ability to guide the required translations,  $\Delta x$  and  $\Delta y$ , and rotation,  $\theta_z$ . In all of the designs it is assumed that the stage constrains all the rotations of the flexure tips. Figure 6.3 summarizes the resulting displacements for each flexure tip under two loading conditions  $F_y$  and  $M_z$ . The desired translations are presented in green and the parasitics are given in purple. Table 6.2 summarizes the advantages and disadvantages of each of the layouts.

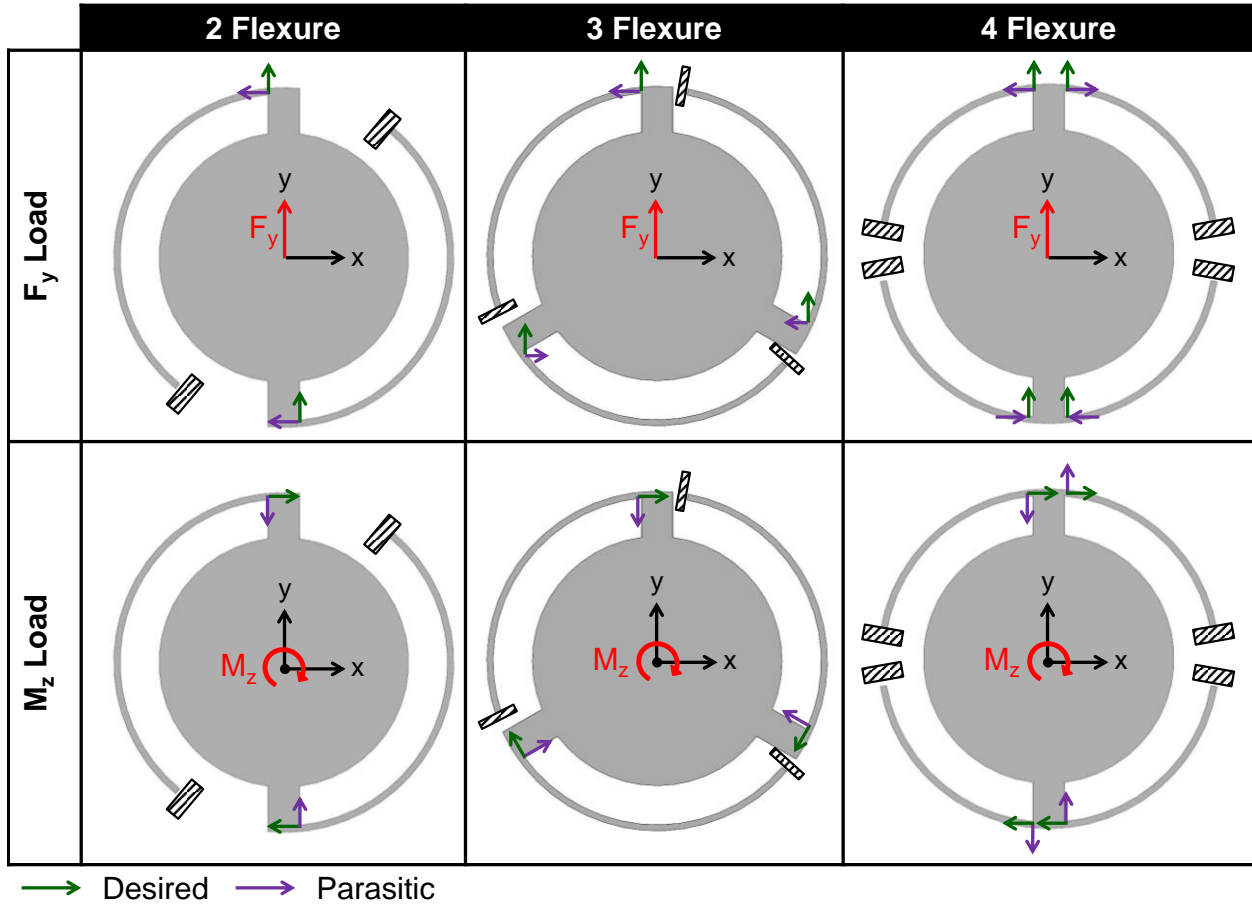


**Figure 6.3: Preliminary CF x-y- $\theta_z$  stage concepts.** The table compares the motions of the three layouts under  $F_y$  and  $M_z$  loads. The desired displacements are indicated in green, while the parasitic motions are given in purple.

**Table 6.2: Advantages and disadvantages of the preliminary CF x-y- $\theta_z$  stage concepts.**

2 Flexure Concept	3 Flexure Concept	4 Flexure Concept
Advantages	Advantages	Advantages
<ul style="list-style-type: none"> <li>• Lowest <math>K_{\theta_z}</math></li> <li>• Large <math>\phi</math> possible</li> </ul>	<ul style="list-style-type: none"> <li>• <math>\phi_{\max} = 120^\circ</math></li> </ul>	<ul style="list-style-type: none"> <li>• Highest <math>K_{\theta_x}</math> and <math>K_{\theta_y}</math></li> <li>• Balanced parasitics</li> </ul>
Disadvantages	Disadvantages	Disadvantages
<ul style="list-style-type: none"> <li>• Lowest <math>K_{\theta_x}</math> and <math>K_{\theta_y}</math></li> <li>• Unbalanced Parasitics</li> </ul>	<ul style="list-style-type: none"> <li>• Unbalanced Parasitics</li> </ul>	<ul style="list-style-type: none"> <li>• <math>\phi_{\max} = 90^\circ</math></li> <li>• Highest <math>K_{\theta_z}</math></li> </ul>

A design with balanced parasitic motions is preferred because it simplifies the control of the stage. The four-flexure concept was selected as the most promising layout because of the cancellation of the parasitic displacements. The drawback of the four-flexure concept is its high  $K_{\theta_z}$  stiffness. In order to create a four-flexure design with a  $\theta_z$ -DOF the flexure layout has to be

rearranged. Figure 6.4 presents the rearranged four-flexure spider concept. The diagrams show that the spider layout enables the required  $\theta_z$  rotation and has balanced parasitic motions. Another advantage of the spider design is that the flexure elements are not concentric, which allows for  $\phi > 90^\circ$ .

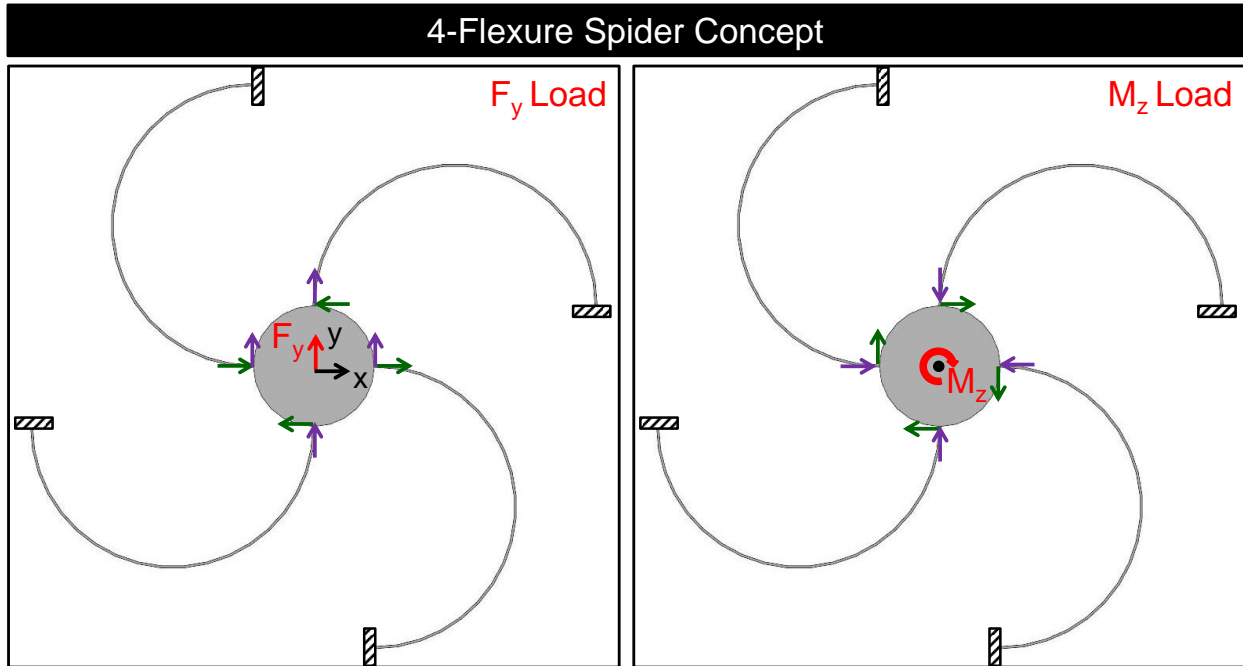


**Figure 6.4: 4-Flexure spider concept. Axi-symmetric layout of the flexures reduces  $K_{\theta_z}$ . In this design the flexures are not concentric which allows for  $\phi > 90^\circ$ .**

### 6.2.2 Concept Analysis and Optimization

Once the most promising concept has been selected the next step in the design process is to analyze the effect of the different design parameters on the performance of the system. Figure 6.5 defines the 4-flexure spider design system and element parameters. Equation (6.1) defines the radius of the flexures,  $R$ , which is set by the system radius,  $R_{sys}$ , the stage radius,  $R_{stage}$ , and the flexure span. The span of the flexure is defined in equation (6.2). Equation (6.1) slightly underestimates the maximum  $R$  allowable for a set  $R_{sys}$ .

$$R = \frac{R_{sys} - R_{stage}}{span} \quad (6.1)$$

$$span = \sqrt{(R \sin \phi)^2 + (R(1 - \cos \phi))^2}, \text{ for } \phi \leq 180^\circ \quad (6.2)$$

$$span = 2R, \text{ for } \phi > 180^\circ$$

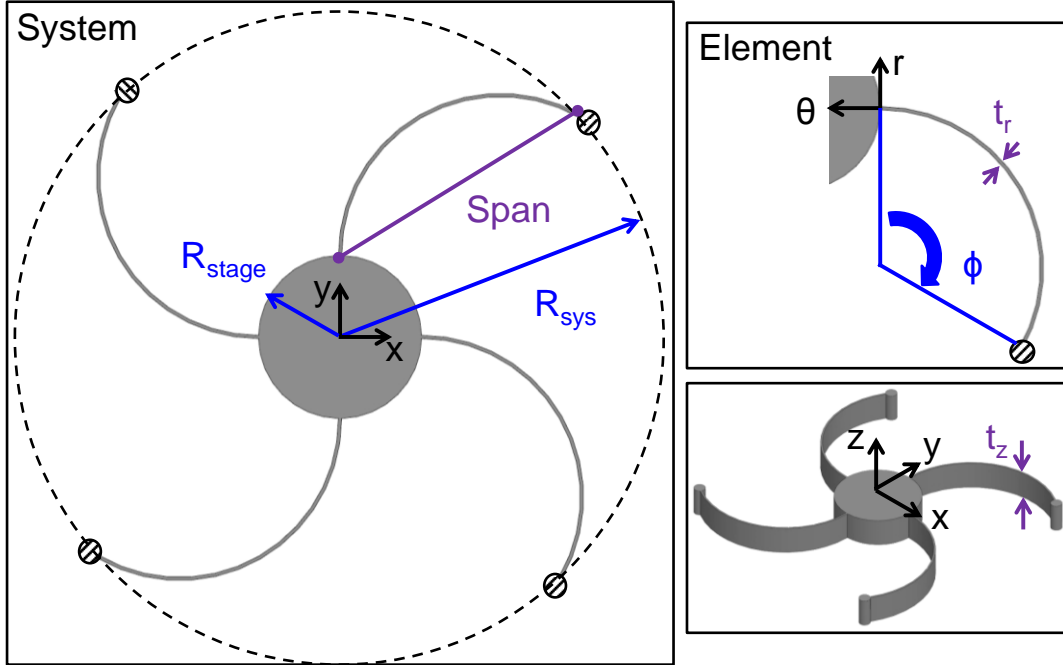


**Figure 6.5: 4-flexure spider concept system and element parameters.  $R_{sys}$  and  $R_{stage}$  define the radius of the system and stage respectively. The element span gives the maximum distance between the tip of flexure and any point along the beam. The element parameters are the sweep angle of the flexure,  $\phi$ , the radial thickness,  $t_r$ , and the  $z$ -axis thickness,  $t_z$ . The figure also shows the system and element coordinate systems.**

The 4-flexure spider concept system stiffness matrix was established following the flow chart presented in Figure 4.34. The first step was to identify the boundary conditions placed on the elements. In the case of the spider design the stage constrains all three flexure tip rotations ( $\alpha_r$ ,  $\alpha_\theta$ , and  $\alpha_z$ ), resulting in a 3DOF stiffness matrix. Appendix C gives the element compliance matrix for these boundary conditions. Next, we can use parallel system rules to determine the system's stiffnesses which are given in Equations (6.3)-(6.6). The symmetric design results in  $K_x=K_y$  and  $K_{\theta_x}=K_{\theta_y}$ . Once the system stiffness matrix has been established we can analyze the effect of the different element and system parameters on the performance of the spider flexure concept. The three main concerns for this design were to minimize the in-plane to out-of-plane stiffness ratios,  $K_x/K_z$  and  $K_{\theta_z}/K_{\theta_x}$ , minimize the in-plane stiffnesses,  $K_x$  and  $K_{\theta_z}$ , and achieve the required range,  $\Delta x$  and  $\theta_z$ . The following limits set the design space: (i) the  $t_r$  of the elements

must be at least .02” so that the system could be fabricated using an abrasive waterjet, (ii)  $R_{stage} \geq 0.5$ ” to allow room for the DPN tip holding mechanism. The first performance analysis was performed with  $R_{sys}=3$ ” and  $t_z=0.5$ ” which would result in a system of roughly the same volume as the current DPN straight-beam x-y- $\theta_z$  stage.

$$K_x = K_y = 2K_{r-element} + 2K_{\theta-element} \quad (6.3)$$

$$K_z = 4K_{z-element} \quad (6.4)$$

$$K_{\theta z} = 4K_{r-element} \cdot r_{stage}^2 \quad (6.5)$$

$$K_{\theta x} = K_{\theta y} \approx 2K_{z-element} \cdot r_{stage}^2 \quad (6.6)$$

The sweep angle,  $\phi$ , of the spider concept elements is not limited by volume or manufacturing constraints. Therefore, the performance of the spider concept design was analyzed to determine the optimal  $\phi$ . Figure 6.6 gives the stiffness ratios for the spider concept system vs. the element sweep angle. The plot shows that the system’s stiffness ratios are equal when  $\phi = 60^\circ$ . The stiffness ratios rise quickly with  $\phi$ ; when  $\phi \geq 135^\circ$   $K_{\theta z} > K_{\theta x}$  which indicates that for an x-y- $\theta_z$  stage the spider concept element’s  $\phi$  must be less than  $135^\circ$ . The other performance metric that must be considered is the magnitude of the system’s in-plane stiffnesses. The plot in Figure 6.7 shows how the in-plane system stiffnesses vary with  $\phi$ . The chart shows that for a system with  $R_{sys}=3$ ”,  $R_{stage}=0.5$ ”,  $t_z=0.5$ ”,  $t_r=0.03$ ”, made out of 6061-T6 Aluminum the sweep angle must be greater than  $285^\circ$  in order to have a  $K_x$  stiffness less than or equal to the desired 1700Nm stiffness. The analysis of the spider concept has demonstrated that the current design cannot meet the functional requirements for the x-y- $\theta_z$  DPN stage.



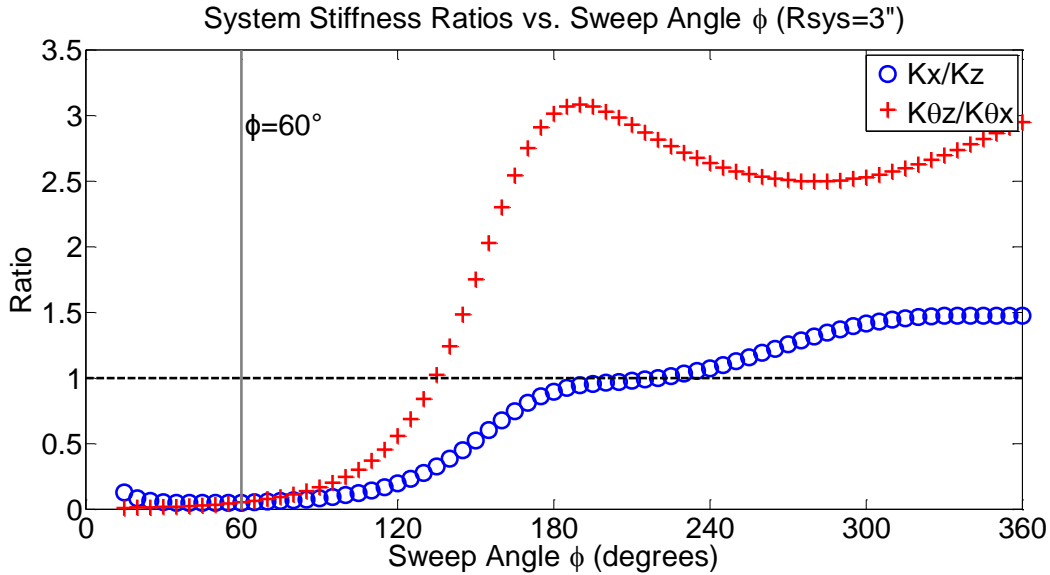


**Figure 6.6: Spider concept stiffness ratios vs. element sweep angle,  $\phi$ .** Plot shows that  $K_x/K_z = K_{\theta z}/K_{\theta x}$  when  $\phi = 60^\circ$ . ( $R_{sys}=3''$ ,  $R_{stage}=0.5''$ ,  $t_z=0.5''$ ,  $t_r=0.03''$ , 6061-T6 Al).

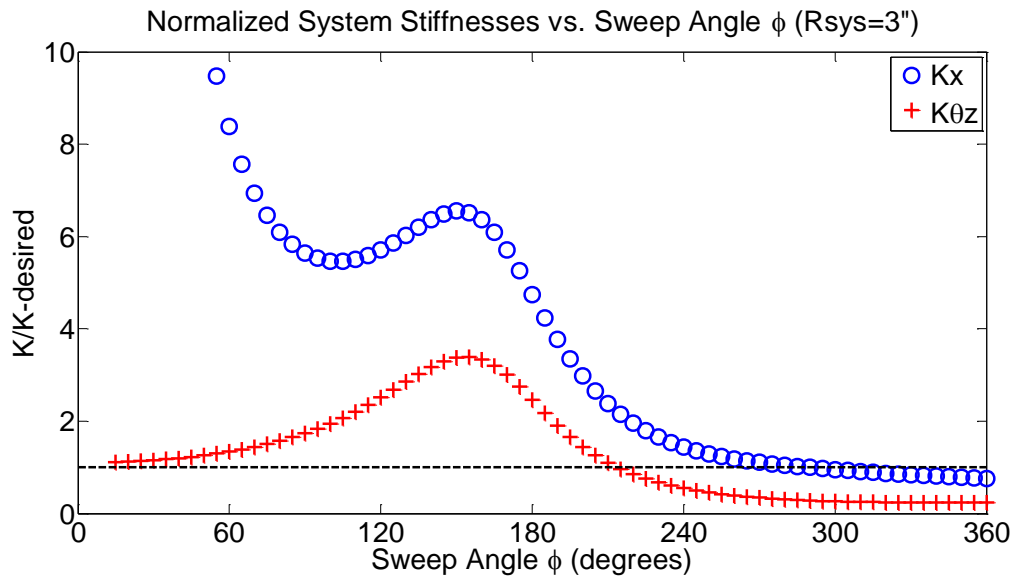


**Figure 6.7: Spider concept in-plane stiffnesses vs. element sweep angle,  $\phi$ .** The stiffnesses are normalized using the desired stiffness value,  $K_x\text{-desired}=1700\text{N/m}$ ,  $K_{\theta z}\text{-desired}=2\text{Nm/rad}$ . ( $R_{sys}=3''$ ,  $R_{stage}=0.5''$ ,  $t_z=0.5''$ ,  $t_r=0.03''$ , 6061-T6 Al).

Figure 6.6 shows that the spider system stiffness ratios are minimized when  $\phi=60^\circ$ ; however, the resulting in-plane stiffnesses are too high for the DPN application. In straight-beam applications this conflict could be addressed by increasing  $t_z$  to decrease  $K_x/K_z$ . The same is not true for CFs where  $t_z$  has a reduced effect on  $K_x/K_z$  because  $K_z$  is dictated not only by bending but

by twisting. Section 3.5.1 provides a detailed analysis of the effect of  $t_z$  on the stiffness ratios of an  $r$ -compliance CF. The in-plane stiffnesses of the spider design can be reduced by increasing  $R_{sys}$ , but this is not very efficient in terms of system volume. The best approach to reducing the stiffness of the design is through a serial design. Figure 6.8 shows the serial spider concept, each leg of the system is composed of two  $60^\circ$  flexures connected in series. In the serial design the bottom stage is grounded while the upper stage is actuated.

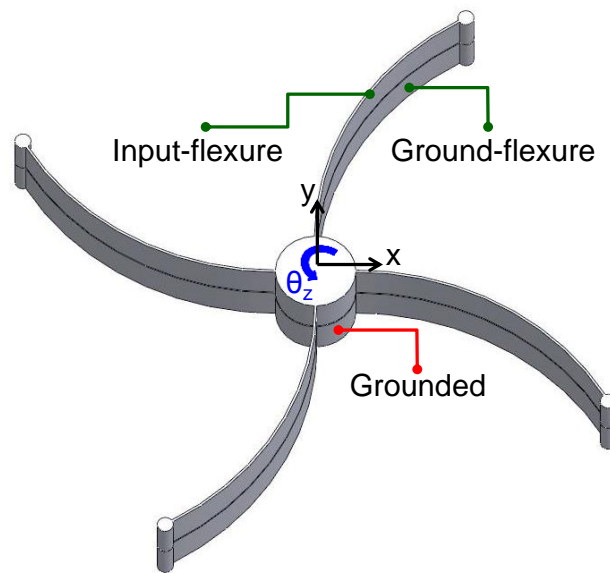


**Figure 6.8: Serial spider concept design. System is composed of two spider designs connected in series. The top stage is actuated while the bottom stage is grounded. Each leg of the system is composed of two  $r$ -compliance elements connected in series.**

The volume of the serial spider design can be reduced by changing the angle between the two flexures,  $\nu$ , so that the two flexures may be located in a single plane, as illustrated in Figure 6.9. A single plane design eliminates the need for assembly as the system can now be cut out of a single piece of aluminum stock. The analysis of the serial system is simplified by examining the performance of the subsystem identified in Figure 6.9. The subsystem analysis identifies the relative effect of the system and element parameters on the performance of the system.

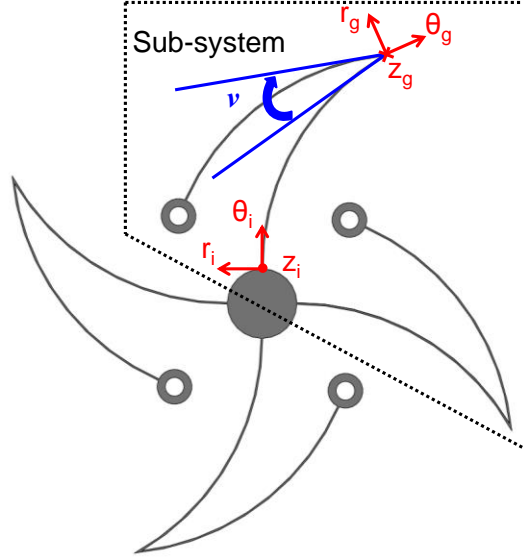


**Figure 6.9: Single plane serial spider design. The attachment angle between the serial flexures is given by  $\nu$ . The coordinate system for the input-flexure is given by  $r_i, \theta_i, z_i$ , while  $r_g, \theta_g, z_g$  designate the coordinate system for the ground-flexure. The dotted lines delineate the subsystem for which the analysis and optimization was performed.**

The analysis of the serial design requires that the compliance matrix of the ground-flexure be transformed to the input-flexure's coordinate system. In the serial design it is assumed that the connection between the flexures does not impose any boundary conditions on the ground-flexure. Therefore, the ground-flexure is modeled as having 6-DOF. Equation (6.7) gives the rotation matrix used to transform the ground-flexure compliance matrix to the input flexure's coordinates. The distance between the flexure tips dictates the moments on the ground-flexure resulting from forces on the stage. The moment arm also determines the displacements of the stage due to the rotation of the ground-flexure's tip. The rotation matrix,  $[C_s]$ , in equation (6.7) captures these effects.  $[C_s]$  is valid for small flexure tip rotations when  $\sin(\alpha) \approx \alpha$ . The transformed compliance matrix is calculated using (6.8).

$$[C_s] = \begin{vmatrix} -\cos(\phi + \nu) & -\sin(\phi + \nu) & 0 & 0 & 0 & -R(1 - \cos \phi) \\ -\sin(\phi + \nu) & \cos(\phi + \nu) & 0 & 0 & 0 & R \sin \phi \\ 0 & 0 & -1 & -R \begin{pmatrix} (1 - \cos \phi) \cos \nu \\ + \sin \phi \sin \nu \end{pmatrix} & R \begin{pmatrix} \sin \phi \cos \nu \\ -(1 - \cos \phi) \sin \nu \end{pmatrix} & 0 \\ 0 & 0 & 0 & -\cos(\phi + \nu) & -\sin(\phi + \nu) & 0 \\ 0 & 0 & 0 & -\sin(\phi + \nu) & \cos(\phi + \nu) & 0 \\ 0 & 0 & 0 & 0 & 0 & -1 \end{vmatrix} \quad (6.7)$$

$$[C'_{ground-flexure}] = [C_s][C_{ground-flexure}][C_s]^T \quad (6.8)$$

The serial spider flexure leg compliance is calculated by adding the transformed ground-flexure compliance to the input-flexure compliance. The compliances of the elements are added because the flexures are connected in series. The subsystem's stiffnesses are calculated using equations (6.9)-(6.12), where  $C$  corresponds to the element compliance. Once the subsystem's stiffnesses have been established the next step is to analyze the effect of the flexure attachment angle,  $\nu$ , on the subsystem's performance. Figure 6.10 shows the effect of  $\nu$  on the in-plane stiffnesses. The stiffnesses are normalized to the stiffness value for  $\nu=0^\circ$ . The plot indicates that both  $K_x$  and  $K_{\theta z}$  decrease with  $\nu$ . The flexure attachment angle must be less than or equal to  $60^\circ$  for both flexures to fit within  $R_{sys}$ . Similarly Figure 6.11 gives the effect of  $\nu$  on the subsystem's stiffness ratios. Finally, Figure 6.12 plots the in-plane ranges for the subsystem as a function of  $\nu$ .

$$K_{x-subsystem} = K_y = (C_r + C'_r)^{-1} + (C_\theta + C'_\theta)^{-1} \quad (6.9)$$

$$K_z = 2(C_z + C'_z)^{-1} \quad (6.10)$$

$$K_{\theta z-subsystem} = 2(C_r + C'_r)^{-1} \cdot r_{stage}^2 \quad (6.11)$$

$$K_{\theta x} = K_{\theta y} \approx (C_z + C'_z)^{-1} \cdot r_{stage}^2 \quad (6.12)$$

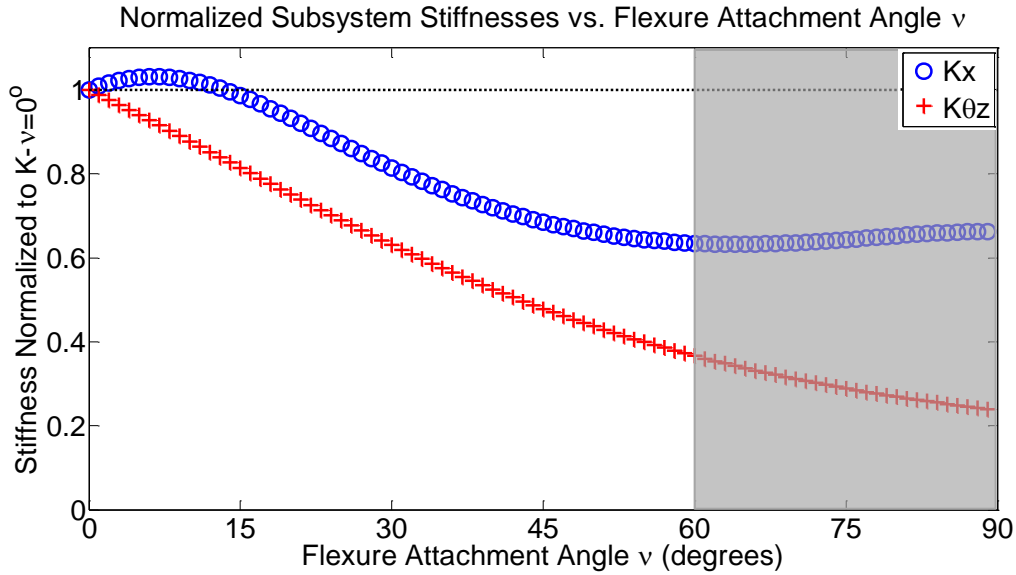


**Figure 6.10: Flexure attachment angle,  $\nu$ , effect on the serial spider concept subsystem in-plane stiffnesses. The stiffnesses are normalized using the corresponding stiffness value for  $\nu=0^\circ$ .  $\nu$  must be less than or equal to  $60^\circ$  for both flexures to fit within  $R_{sys}$ . The plot corresponds to a design with  $\phi=60^\circ$ .**

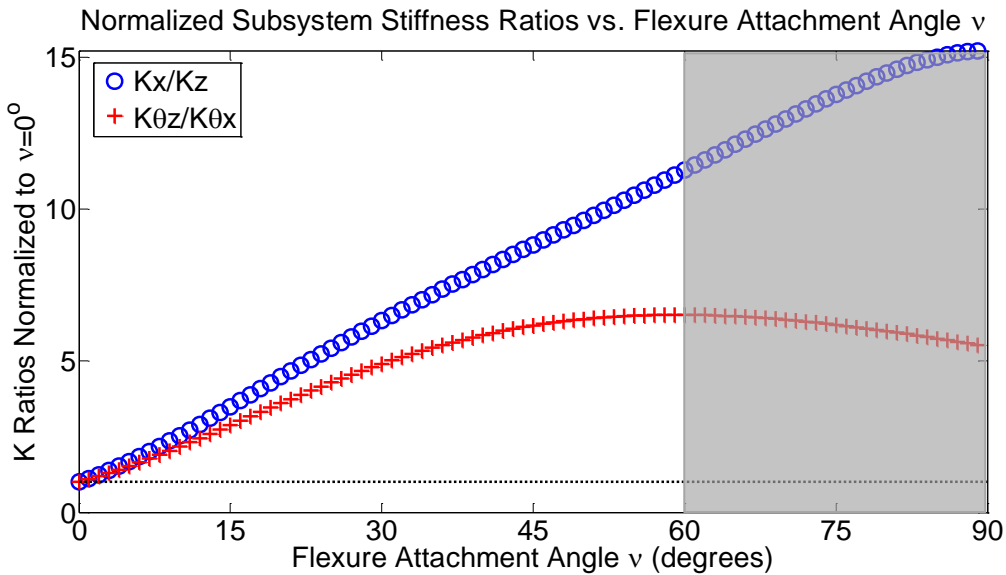


**Figure 6.11: Flexure attachment angle,  $\nu$ , effect on the serial spider concept subsystem stiffness ratios. The ratios are normalized using the corresponding ratio value for  $\nu=0^\circ$ .  $\nu$  must be less than or equal to  $60^\circ$  for both flexures to fit within  $R_{sys}$ . The plot corresponds to a design with  $\phi=60^\circ$ .**

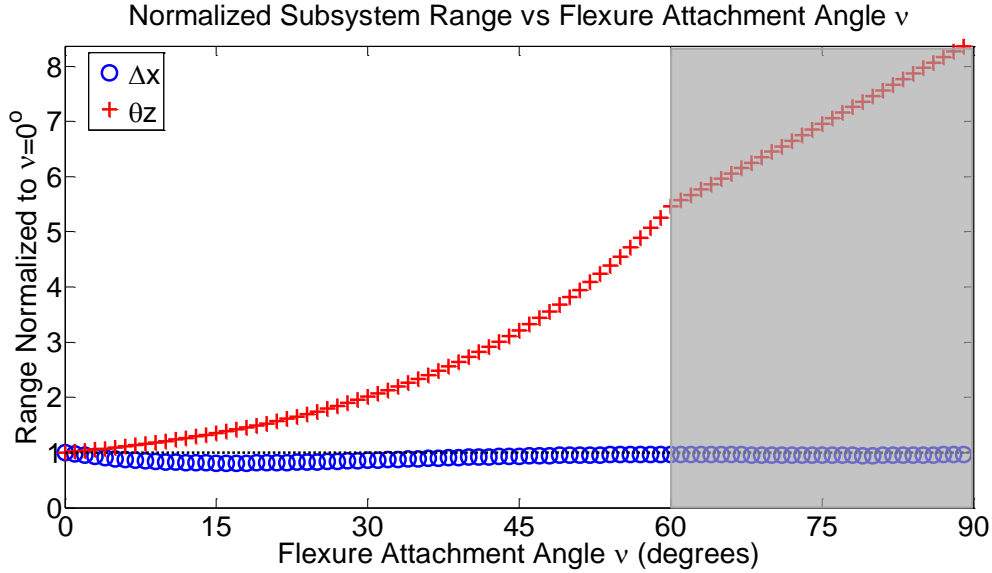


**Figure 6.12: Flexure attachment angle,  $\nu$ , effect on the serial spider concept subsystem in-plane range. The ranges are normalized using the corresponding range value for  $\nu=0^\circ$ .  $\nu$  must be less than or equal to  $60^\circ$  for both flexures to fit within  $R_{sys}$ . The plot corresponds to a design with  $\phi=60^\circ$ .**

Figure 6.10 indicates that increasing  $\nu$  will decrease the x-y- $\theta_z$  in-plane stiffnesses. On the other hand the analysis shows that the stiffness ratios of the subsystem increase with  $\nu$ . These effects would mandate that the designer trade-off decreasing in-plane stiffness for increasing stiffness ratios. However, it is important to remember that the analysis presented pertains to the subsystem. The  $K_z$  stiffness of the system will be more than twice that of the subsystem because the  $\theta_x$  and  $\theta_z$  rotations of the stage will be constrained by the symmetry of the system. Figure 6.13 compares the FEA displacements of the subsystem under an  $F_z$  load, to those of the full system under the same loading. The image shows the  $\theta_x$  and  $\theta_y$  rotations of the subsystem stage. FEA analysis of the complete system shows that the stiffness ratios decrease with increasing  $\nu$ . The flexure attachment angle was set to  $60^\circ$  to minimize the in-plane stiffnesses and ensure that the ground-flexures fit within  $R_{sys}$ .

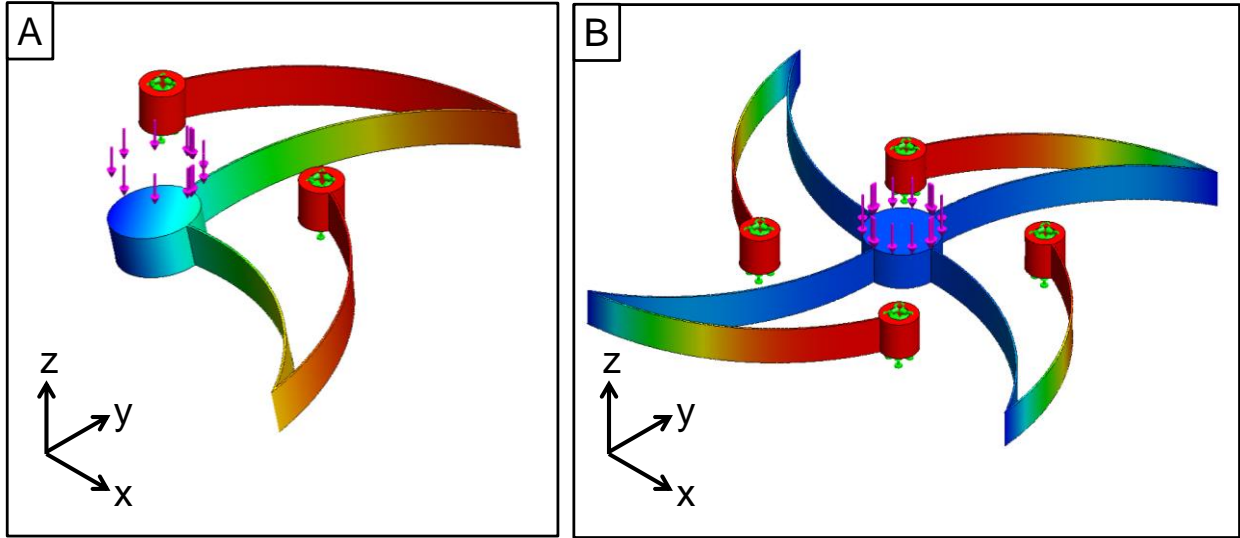


**Figure 6.13: A) Subsystem  $\Delta z$  displacement under an  $F_z$  load. FEA image shows the  $\theta_x$  and  $\theta_y$  rotations of the subsystem's stage. B) Full system  $\Delta z$  displacement under an  $F_z$  load. The system's stage does not experience a  $\theta_x$  or  $\theta_y$  rotation.**

The foot print of the serial plane spider design can be reduced by changing the attachment angle between the input-flexures and the stage. The stage attachment angle,  $\eta$ , is defined in Figure 6.14. Increasing  $\eta$  allows for either a larger  $R$  for a given  $R_{sys}$  or a smaller  $R_{sys}$  for a given  $R$ . In the subsystem analysis  $R_{sys}$  is held constant and  $R$  increases with  $\eta$ . Equation (6.13) gives  $R$  as a function of  $R_{sys}$ ,  $span$ ,  $R_{stage}$ , and  $\eta$ . The flexure span is calculated using equation (6.2). Figure 6.15 looks at the effect of the attachment angle on the performance of the  $\nu=60^\circ$  serial spider design. The  $\eta$  effect on the subsystem stiffness ratios is shown in Figure 6.16. For the final design an stage attachment angle of  $0^\circ$  was chosen to avoid the large increase in  $K_{\theta_z}$  associated with  $\eta>0^\circ$ .

$$R = \frac{R_{sys} - R_{stage}(1 - \sin \eta)}{span} \quad (6.13)$$

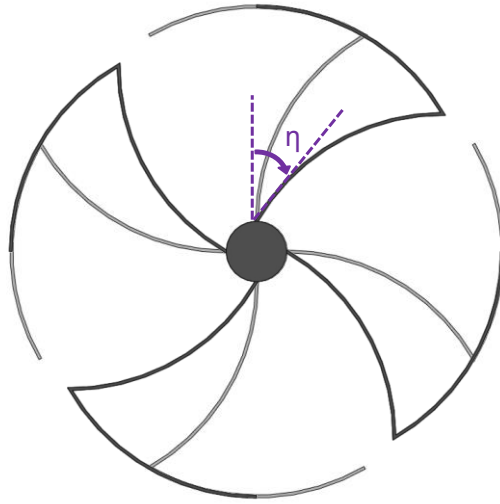


**Figure 6.14: Stage attachment angle definition. The attachment angle between the stage and the input-flexure is given by  $\eta$ .**

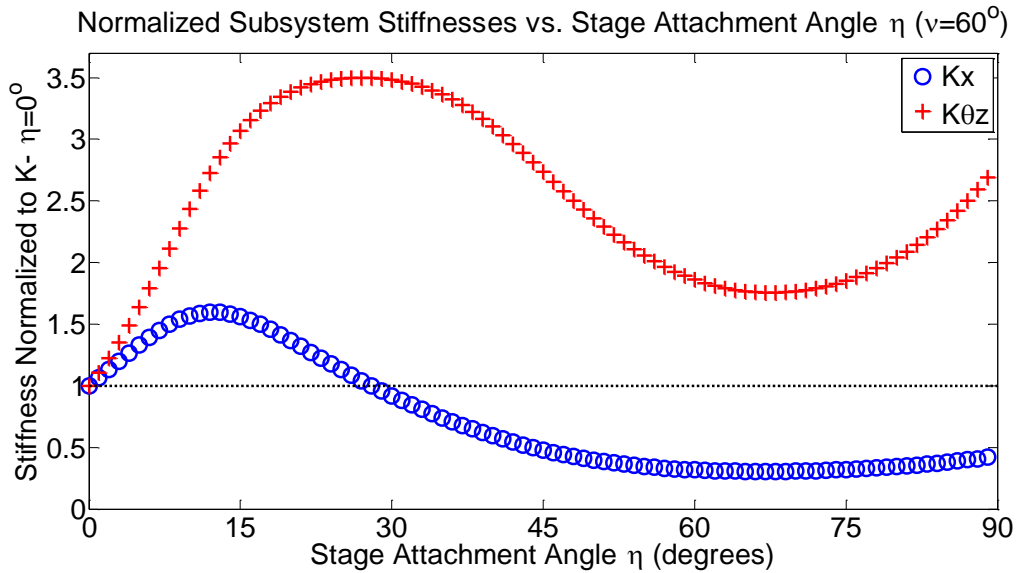


**Figure 6.15: Stage attachment angle,  $\eta$ , effect on the serial spider concept subsystem in-plane stiffnesses. The stiffnesses are normalized using the corresponding stiffness value for  $\eta=0^\circ$ . The plot corresponds to a design with  $\phi=60^\circ$  and  $\nu=60^\circ$ .**



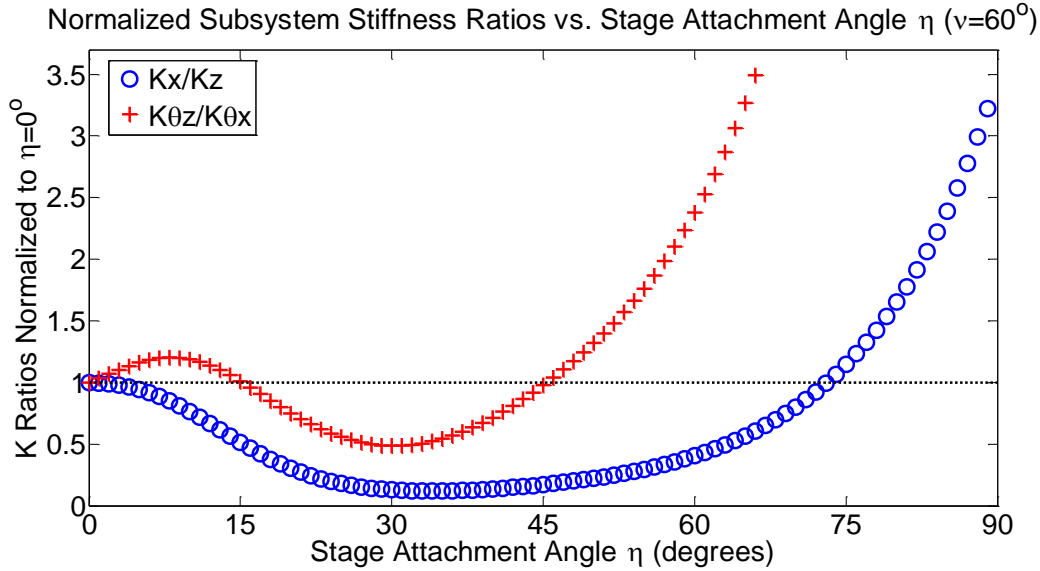


**Figure 6.16: Stage attachment angle,  $\eta$ , effect on the serial spider concept subsystem stiffness ratios. The ratios are normalized using the corresponding ratio value for  $\eta=0^\circ$ . The plot corresponds to a design with  $\phi=60^\circ$  and  $\nu=60^\circ$ .**

The analysis of the spider concept design and the serial subsystem was used to optimize the performance of the CF x-y- $\theta_z$  stage. In section 3.5 it was shown that the stiffness ratios of an  $r$ -compliance flexure may be decreased by applying a taper angle,  $\Psi$ , along the  $r$ -axis of the element. Unfortunately, fabricating the spider design using a water-jet results in a  $\Psi$  along the element's  $z$ -axis. As a result, the performance of the stage cannot be improved using the taper angle. Table 6.3 summarizes the system and element parameters of the final design. The final design was analyzed using FEA to check the performance of the entire system. Table 6.4 summarizes the FEA results and compares them to the FEA values for the original DPN stage design.

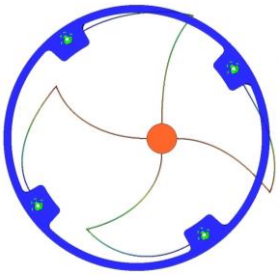
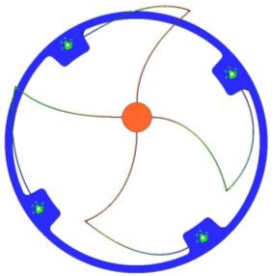
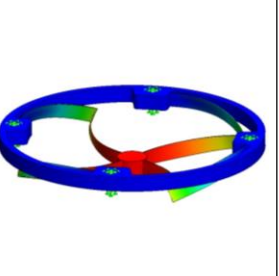
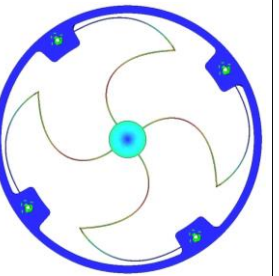
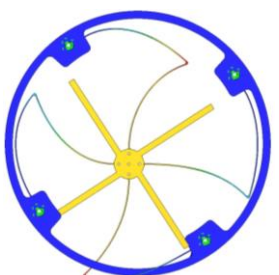
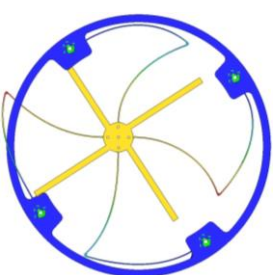
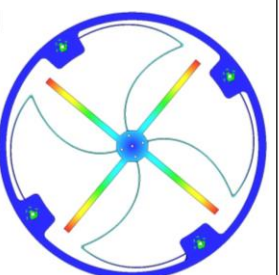
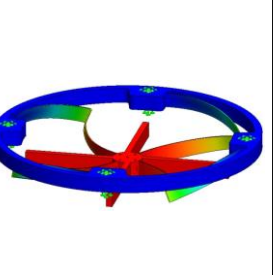
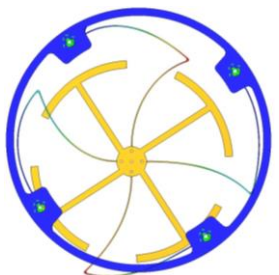
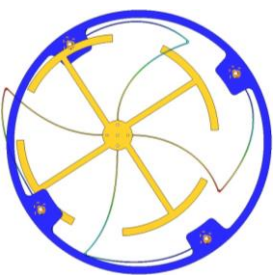
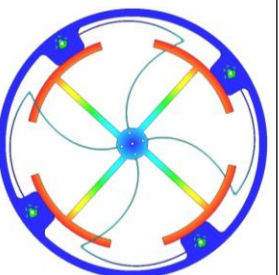
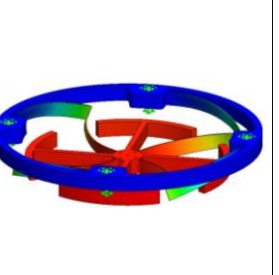
**Table 6.3: Final CF x-y- $\theta_z$ -stage element and system parameters.**

Element radial thickness, $t_r$	0.024 inches
System z-thickness, $t_z$	0.5 inches
System radius, $R_{sys}$	4 inches
Stage radius, $R_{stage}$	0.5 inches
Element sweep angle, $\phi$	$60^\circ$
Stage attachment angle, $\eta$	$0^\circ$
Flexure attachment angle, $\nu$	$60^\circ$
Material	6061-T6 Aluminum

**Table 6.4: Performance comparison for the straight-beam and CF x-y- $\theta_z$ -stages.**

Attribute (required)	Straight-beam flexure (FEA results)	CF Design (FEA results)
$K_x$	1.7 N/mm	.612 N/mm
$K_y$	2.3 N/mm	.612 N/mm
$K_{\theta_z}$	2 Nm/rad	2.85 Nm/rad
$K_y/K_z$	$1.4 \times 10^{-3}$	$1.7 \times 10^{-1}$
$K_x/K_z$	$1.0 \times 10^{-3}$	$1.7 \times 10^{-1}$
$K_{\theta_z}/K_{\theta_x}$	$9.1 \times 10^{-3}$	$1.3 \times 10^{-1}$
$K_{\theta_z}/K_{\theta_y}$	$1.8 \times 10^{-3}$	$1.3 \times 10^{-1}$
$\Delta x$ -range ( $\pm 272\mu\text{m}$ )	$\pm 5.99$ mm	$\pm 17.53$ mm
$\Delta y$ -range ( $\pm 272\mu\text{m}$ )	$\pm 4.18$ mm	$\pm 17.53$ mm
$\theta_z$ -range ( $\pm 0.2$ rad)	$\pm 0.37$ rad	$\pm 0.26$ rad
Volume	5.1x5.3x7.6 cm (205cm <sup>3</sup> )	22.6x22.6x1.27cm (666cm <sup>3</sup> )
$\Delta x$ -range/L	0.079	0.078

A modal analysis of the design reveals that the first three frequency modes of the CF x-y- $\theta_z$  stage are its three translations. Figure 6.17a presents the first four FEA calculated modes. These results indicate that the CF stage should be classified as an x-y-z stage in accordance with its three lowest modes. The mode shapes of a system are set by its stiffness and mass distribution. Since the system and element parameters were optimized to decrease the stiffness ratios of the CF stage, we utilize mass distribution to decrease the frequency of the  $\theta_z$ -mode. Figure 6.17b shows how adding four radial arms to the stage lowers the frequency of all the modes, but more importantly results in the  $\theta_z$ -mode having the third lowest frequency. The ratio between the third and fourth frequency modes can be improved by adding masses at the end of the arms as shown in Figure 6.17c. Overall it is important to note that the third and fourth frequency modes are close together even after adding the overhanging masses. These results indicate that the CF design acts as a poor out-of-plane constraint, which suggests that radial compliance CF elements may be best suited for 6-DOF applications.

	1 <sup>st</sup> Mode	2 <sup>nd</sup> Mode	3 <sup>rd</sup> Mode	4 <sup>th</sup> Mode
A. No added mass				
	26.52 Hz	26.54 Hz	79.54 Hz	123.51 Hz
B. Addition of 4 arms				
	20.67 Hz	20.69 Hz	33.82 Hz	54.03 Hz
C. 4 arms with masses				
	14.84 Hz	14.85 Hz	16.39 Hz	37.10 Hz

**Figure 6.17: CF stage first four frequency modes: A) Original design, B) Design with four radial arms, and C) Design with four arms with masses.**

### 6.3 Fabrication and Testing

The CF DPN stage was fabricated using an abrasive water-jet. Figure 6.18 shows an image of the final prototype. The stage has four radial arms which serve to decrease the  $\theta_z$  frequency mode and were used to ground the stage during cutting. The radial arms were separated from the grounding ring after the water-jet operation was completed. The final prototype has an average flexure radial thickness,  $t_r$ , of .029 inches compared to the designed .024 inches, therefore we expect the flexure to be stiffer than what was predicted by the models

and the FEA. The error in  $t_r$  was due to limitations of the water-jet kerf size and positioning resolution. The flexures also had an average taper angle of  $0.36^\circ$  on either side of the flexure. The performance of the system was measured using the measurement setup shown in Figure 6.19. The system was actuated by hanging masses off of the stage and the displacements were measured off the attached block using capacitance probes. Probe 1 was used to measure the  $\Delta z$  displacement, the out of plane rotation  $\theta_x$  was calculated by taking the difference between the probe 1 and probe 2 measurements and the distance between the probes. Similarly,  $\theta_y$  was measured by taking the difference between the probe 1 and probe 3 measurements. The in-plane displacements  $\Delta x$  and  $\Delta y$  are given by probes 4 and 5 respectively. Finally,  $\theta_z$  is measured by taking the difference between the probe 5 and 6 measurements and the distance between the measurement points. The performance of the prototype is summarized in Table 6.5.

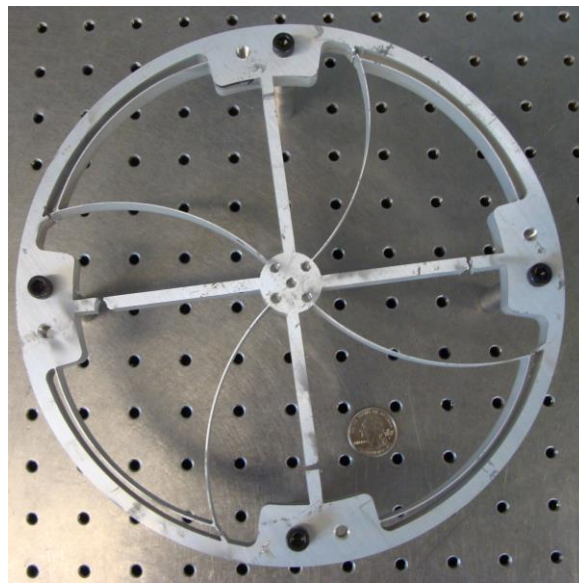


**Figure 6.18: Final CF x-y- $\theta_z$  DPN stage prototype. System was fabricated using an abrasive water-jet.**

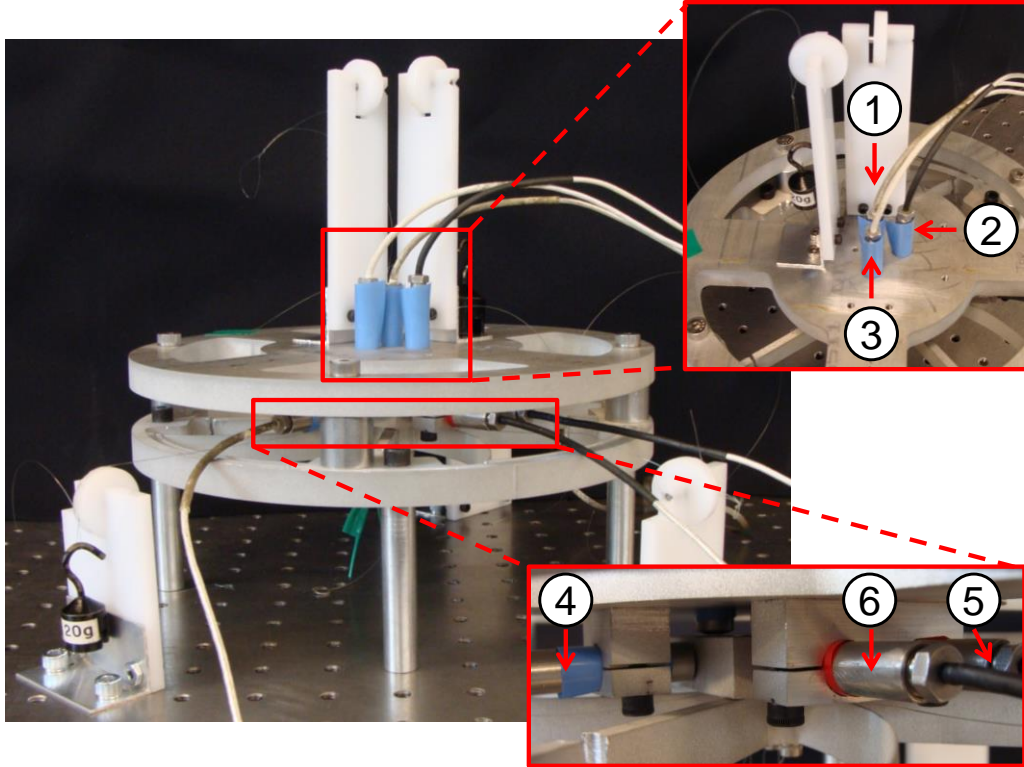


**Figure 6.19: CF x-y- $\theta_z$  DPN stage measurement setup. Six capacitance probes (1-6) are used to measure the three displacements,  $\Delta x$ ,  $\Delta y$ , and  $\Delta z$ , and three rotations,  $\theta_x$ ,  $\theta_y$ , and  $\theta_z$ , of the stage. The system is actuated by hanging masses off the stage.**

**Table 6.5: CF DPN x-y- $\theta_z$  stage performance.**

Attribute	Measured values
$K_x$	.735 N/mm
$K_y$	.880 N/mm
$K_{\theta_z}$	4.69 Nm/rad
$K_x/K_z$	$1.49 \times 10^{-1}$
$K_x/K_z$	$1.79 \times 10^{-1}$
$K_{\theta_z}/K_{\theta_x}$	$1.68 \times 10^{-1}$
$K_{\theta_z}/K_{\theta_y}$	$1.60 \times 10^{-1}$

The guidelines and models developed in this thesis enabled the efficient design of the CF x-y- $\theta_z$  stage; without them, the designer would have had to rely solely on FEA and straight-beam design rules. An example of the significant limitations of this approach is the effect that  $t_z$  has on

the performance of the system. The straight-beam analysis would indicate that  $t_z$  has a significant effect on the stiffness ratios, when in reality for  $r$ -compliance CF elements  $t_z$  plays only a minor role. The undergraduate student was able to quickly analyze the 3 original concepts and identify the most promising design. The models then allowed the designer to realize that the spider concept would not be able to meet the DPN functional requirements. The student and the author used the rules in Chapter 4 to create the serial spider design. The element and system models allowed us to explore the effect of  $\phi$ ,  $v$ ,  $\eta$ , and other parameters, without FEA.

The DPN case study highlights that the main challenge with  $r$ -compliance CFs is their high  $K_x/K_z$  ratios. The rules developed in this thesis made it possible to overcome this hurdle and design a system with acceptable performance. Even after optimization the CF  $x$ - $y$ - $\theta_z$  stage has significantly lower stiffness ratios than its straight-beam counter-part, which may be problematic for applications that rely on the out-of-plane motions being constrained. The  $r$ -compliance elements may be better suited for 6-DOF stages. The CF DPN stage design does present some advantages over the straight-beam design, for example the curved beam stage's  $K_x=K_y$  and these are a little over a quarter of the straight-beam  $K_y$ . Another benefit could be the reduction in  $z$ -axis depth that the CF provides; the CF is only 0.5" thick compared to the 3" of the Thomas stage.

# 7

## CONCLUSIONS

---

Straight-beam flexures are common in precision engineering applications because design rules have been established which enable their effective design. These guidelines inform the designer on how to design the straight-beam flexure to obtain the correct kinematics and ensure that the element achieves the desired range. Up until now no such rules existed for the curved-beam elements utilized in cylindrical flexures (CFs), and therefore the design process was impeded. CFs present a challenge because their mechanics differ from those of straight beams, and although the modeling of curved beams has been researched in detail [1–4], it has yet to be distilled into compliant element and system creation rules. The lack of relevant design rules has inhibited the design and optimization of CF systems, preventing these systems from becoming pervasive in engineering applications. The design guidelines developed in this work enable (i) the rapid generation of multiple concepts, (ii) more efficient analysis of different designs, (iii) the selection of the best design, and (iv) more effective optimization of the chosen concept.

The first step in developing the design guidelines was to establish the compliance matrix for a curved-beam. This analytical model was used to characterize the effect of different parameters on the behavior of the CF elements. The flexure's sweep angle,  $\phi$ , and ratio of bending to torsional properties,  $\beta$ , were established as the only two parameters that differentiate the kinematics of a curved-beam from those of a straight-beam. Chapter 3 characterizes the effect of these two parameters on the element performance metrics. In the following chapter, the system creation guidelines are established through the analysis of two CF subsystems. Finally, helpful fabrication tips were presented in the context of the creation of the two CF system prototypes.

The importance of this work is demonstrated in the two case studies. The CF guidelines and rules made it possible to create a linear guide with an order of magnitude lower tip/tilt error than the concept created using straight-beam rules and FEA. The CF design rules and models also enabled the efficient design of the CF  $x$ - $y$ - $\theta_z$  stage. A great example of the significant limitations of using straight-beam guidelines to model CFs is the misrepresentation of the effect of  $t_z$  on the performance of the  $x$ - $y$ - $\theta_z$  stage. The straight-beam analysis would indicate that  $t_z$  would have a significant effect on the system's stiffness ratios, when in reality for an  $r$ -compliance CF system  $t_z$  plays only a minor role. For both of the case studies the CF element and system rules made it possible to quickly analyze the original concepts and identify the most promising design. The analytical models allowed us to explore the effect of different parameters efficiently without having to rely on FEA.

Now that design guidelines and models have been created for curved-beam flexure systems, the design of new CF systems will be facilitated. These new mechanisms could fill the gaps that current planar flexures fail to meet. Some of the CF benefits include: (i) the availability of precision round stock, means reduced fabrication variations and (ii) reduced cost, (iii) compatibility with cylindrical applications, (iv) higher stability due to symmetry, (v) ease of assembly of concentric tubes, (vi) larger range to footprint ratio, and (vii) an increased design space which can lead to designs that meet currently unreachable functional requirements. CF's most attractive quality is their compatibility with applications that benefit from a cylindrical geometry, for instance rotating systems, optical mechanisms, and laparoscopic tools. The use of cylindrical flexures in these applications will result in more compact systems with higher precision and lower cost. The axial symmetry of cylindrical systems may be used to achieve thermocentricity, and it serves to decrease the effects of manufacturing and load placement errors. Monolithic CF systems can be created out of a single piece of round stock reducing assembly cost and errors. The cylindrical geometry may also serve to reduce the footprint and therefore the volume of the system.

This thesis demonstrated that CF systems may achieve a greater range to footprint ratio than its planar counterparts. The configuration of the compliance matrix of the CF element enables the designer to use all previous knowledge pertaining to straight-beam flexures when



designing CF elements. The element analysis demonstrated that  $\phi$  and  $\beta$  serve as two additional tuning knobs in the design of CFs. As a result of the increased design space, a CF may be able to meet functional requirements that cannot be met using a straight flexure. Some of the other advantages that CFs have over straight-beam flexures are: (i) a  $z$ -compliance CF can achieve better performance through with a lower  $K_z/K_r$  ratio than a straight-beam flexure, (ii) certain curved-beams have a lower  $\alpha_r/\Delta z$  parasitic ratio than a straight-beam flexure, and (iii) CFs also have a lower sensitivity to taper angle.

## 7.1 Future Work

This thesis presented the detailed analysis of the different curved-beam elements as well as two CF subsystems: (i) the curved four-bar, and (ii) the compound four-bar. The detailed characterization of different building blocks allows the engineer to quickly create more complicated systems using these blocks as subsystems. The analysis of the larger system is facilitated because the kinematics and stress distribution of the blocks is well-known. The CF  $x$ - $y$ - $\theta_z$  stage in chapter 6 was designed using two  $r$ -compliance elements in series. This flexure layout should be further characterized to create a new building block. The models and guidelines presented in chapters 3 and 4 will serve as the foundation for the development of new CF subsystems.

During the analysis of the parasitic rotations of a curved four-bar it was discovered that the  $r$ -axis of the system rotates away from the axis defined by the element. This rotation is due to the fact that the length of the beam varies between the inner and outer radiuses of the beam, and the added length of the four-bar stage. Chapter 4 presented a preliminary model for the rotation of a curved four-bar's  $r$ -axis,  $\omega$ . This model should be further developed using solid mechanics analysis, which is out of the scope of this thesis.

Over the last few years the FACT synthesis approach for compliant mechanism design has proven itself to be efficient and powerful. FACT proposes using freedom, constraint, and actuation topologies to design any flexure system [24], [25]. FACT utilizes the principles of exact-constraint based design and the mathematics of screw theory to create visual spaces for

where constraints should be placed to achieve the desired DOF. The design process is enhanced by FACT because it presents the designer with a quick way to consider all possible constraint locations. In order to design CF systems using FACT we need to establish the constraints that each CF element imposes such that the engineer may quickly layout curved-beam elements in the constraint spaces. The FACT analysis tool also needs to be augmented to include the compliance matrices for curved-beams elements so that the CF element does not need to be modelled as a series of straight-beams. The use of the curved flexure compliance matrix instead of a system of straight-beams increases the accuracy of the kinematic calculations and reduces the required computational power. By enhancing FACT with the CF knowledge generated in this thesis we will enable the engineer to consider both straight and curved beam flexures simultaneously during the design process.

# REFERENCES

---

- [1] S. Timoshenko, *Strength of Materials Part II*, 2nd ed. Lancaster: Lancaster Press, 1941.
- [2] H. C. Martin, *Introduction to matrix methods of structural analysis*, First. United States: McGraw-Hill, 1966, pp. 136–155.
- [3] H.-P. Lee, “Generalized stiffness matrix of a curved-beam element,” *AIAA Journal*, vol. 7, no. 10, pp. 2043–2045, Oct. 1969.
- [4] R. Palaninathan and P. S. Chandraekharan, “Curved beam element stiffness formulation,” *Computers & Structures*, vol. 21, no. 4, pp. 663–669, 1985.
- [5] A. H. Slocum, *Precision Machine Design*. Dearborn: Society of Manufacturing Engineers, 1992.
- [6] S. T. Smith, *Flexures: Elements of elastic mechanisms*, 1st ed. USA: CRC Press LLC, 2000.
- [7] M. J. Telleria and M. L. Culpepper, “Understanding the drivers for the development of design rules for the synthesis of cylindrical flexures,” *Mechanical Sciences*, vol. 3, no. 1, pp. 25–32, Apr. 2012.
- [8] A. Ertas and J. C. Jones, *The Engineering Design Process*, 2nd ed. John Wiley & Sons, 1996.
- [9] R. J. Eggert, *Engineering Design*. Upper Saddle River: Prentice Hall, 2005.
- [10] M. J. Telleria, M. L. Culpepper, and D. Weitz, “Design of a monolithic cylindrical flexure for precision motion guidance,” in *Proceedings of the 2010 ASPE Annual Meeting*, 2010.
- [11] O. Corporation, “OMAX Rotary axis,” *Accessory Specifications*. [Online]. Available: <http://www.omax.com/waterjets/rotary-axis>.
- [12] M. J. Telleria, M. L. Culpepper, and D. Weitz, “Low-cost Precision Motion Control with Cylindrical Flexures,” in *Proceedings of the 2010 Machine Tool Technology Research Foundation*, 2010, pp. 63–66.
- [13] M. J. Telleria, M. Culpepper, and J. Chun, “Cylindrical Flexures as Transmission Elements and Bearings in cm-scale Robotic Systems,” in *Proceedings of the 2011 Machine Tool Technology Research Foundation*, 2011.

- [14] S.-C. Chen and M. L. Culpepper, “Design of Contoured Microscale Thermomechanical Actuators,” *Journal of Microelectromechanical Systems*, vol. 15, no. 5, pp. 1226–1234, Oct. 2006.
- [15] M. I. Frecker, G. K. Ananthasuresh, S. Njshiwaki, N. Kikuchi, and S. Kota, “Topological Synthesis of Compliant Mechanisms Using Multi-Criteria Optimization,” *Journal of Mechanical Design*, vol. 119, no. June, pp. 238–245, 1997.
- [16] C. M. DiBiasio, “Concept synthesis and design optimization of meso-scale, multi-degree-of-freedom precision flexure motion systems with integrated strain-based sensors,” Ph. D. Thesis, Massachusetts Institute of Technology, 2010.
- [17] L. L. Howell, *Compliant mechanisms*, 1st ed. USA: Wiley-Interscience, 2001.
- [18] J. C. Maxwell, *General considerations concerning scientific apparatus: The scientific papers of James Clerk Maxwell*, Reprinted . Dover Press, 1890.
- [19] D. L. Blanding, *Exact constraint: Machine design using kinematic principles*. New York: ASME Press, 1999.
- [20] L. C. Hale, “Principles and techniques for designing precision machines,” Ph. D. Thesis, Massachusetts Institute of Technology, 1999.
- [21] S. Awtar and A. H. Slocum, “Constraint-Based Design of Parallel Kinematic XY Flexure Mechanisms,” *Journal of Mechanical Design*, vol. 129, no. 8, p. 816, 2007.
- [22] M. L. Culpepper, “Design of quasi-kinematic couplings,” *Precision Engineering*, vol. 28, no. 3, pp. 338–357, Jul. 2004.
- [23] C. J. Kim, Y.-M. Moon, and S. Kota, “A Building Block Approach to the Conceptual Synthesis of Compliant Mechanisms Utilizing Compliance and Stiffness Ellipsoids,” *Journal of Mechanical Design*, vol. 130, no. 2, p. 022308, 2008.
- [24] J. B. Hopkins, “Design of Parallel Flexure Systems via Freedom and Constraint Topologies ( FACT ),” S. M. Thesis, Massachusetts Institute of Technology, 2007.
- [25] J. B. Hopkins, “Design of Flexure-based Motion Stages for Mechatronic Systems via Freedom, Actuation and Constraint Topologies (FACT),” Ph. D. Thesis, Massachusetts Institute of Technology, 2010.
- [26] L. Y. Matloff, “Design and Optimization of x-y-θz Cylindrical Flexure Stage,” S. B. Thesis, Massachusetts Institute of Technology, 2013.
- [27] W. C. Young and R. G. Budynas, *Roark’s formulas for stress and strain*, 7th ed. Singapore: McGraw-Hill, 2002, pp. 297–380.

- [28] S. Awtar and A. H. Slocum, “Flexure Systems based on a Symmetric Diaphragm Flexure,” in *ASPE Annual Meeting*, 2005.
- [29] D. Vukobratovich, R. M. Richard, J. P. Mcniven, and L. Sinclair, “Slit Diaphragm Flexures for Optomechanics,” in *SPIE’s 1995 International Symposium on Optical Science, Engineering, and Instrumentation*, 1995.
- [30] S. Chen, A. Herrmann, D. Golda, and A. H. Slocum, “Design of an Ultra Precision Diaphragm Flexure Stage for Out-of-plane Motion Guidance,” in *Proceedings of DETC’04*, 2004, pp. 1–7.
- [31] D. M. Ljubicic, “Design and Analysis of a Monolithic Flexure Atomic Force Microscope,” S. M. Thesis, Massachusetts Institute of Technology, 2008.
- [32] J. E. Shigley, C. R. Mischke, and R. G. Budynas, *Mechanical engineering design*, 7th ed. New York: McGraw-Hill, 2004.
- [33] P. Griffiths and J. A. De Haseth, *Fourier Transform Infrared Spectrometry. Vol. 171*. Wiley-Interscience, 2007.
- [34] A. H. Slocum, *FUNdaMENTALS of Design*. 2005, p. Topic 3 FUNdaMENTAL Principles.
- [35] M. A. C. Thomas, “Design, Fabrication and Implementation of a Flexure-based Micropositioner for Dip Pen Nanolithography,” S. B. Thesis, Massachusetts Insitute of Technology, 2012.



## A

# FEA CORROBORATION OF CF COMPLIANCE MATRIX

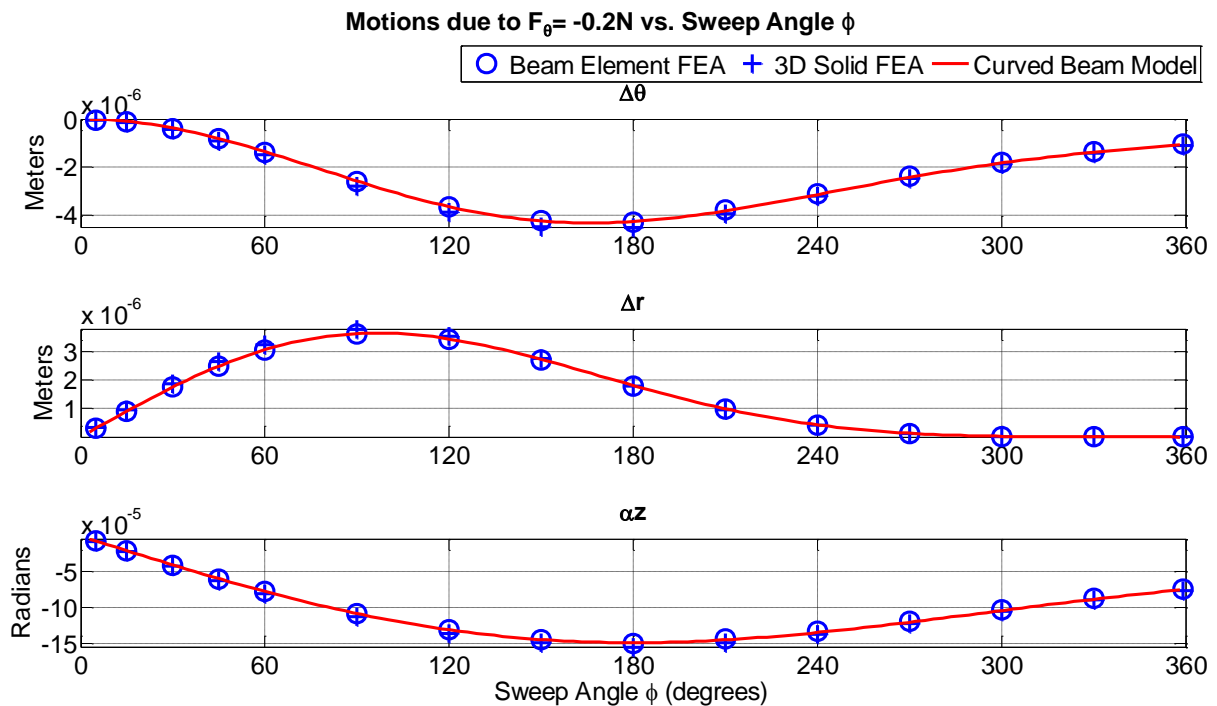


**Figure A.1: FEA corroboration of compliance matrix, predicted displacements under  $-0.2N$   $F_\theta$  load vs. sweep angle,  $\phi$ . The plot compares the curved beam model to an FEA Beam Element model and an FEA 3D solid model. ( $L=60\text{mm}$ ,  $t_r=6.35\text{mm}$ ,  $t_z=1\text{mm}$ , 7075Aluminum).**

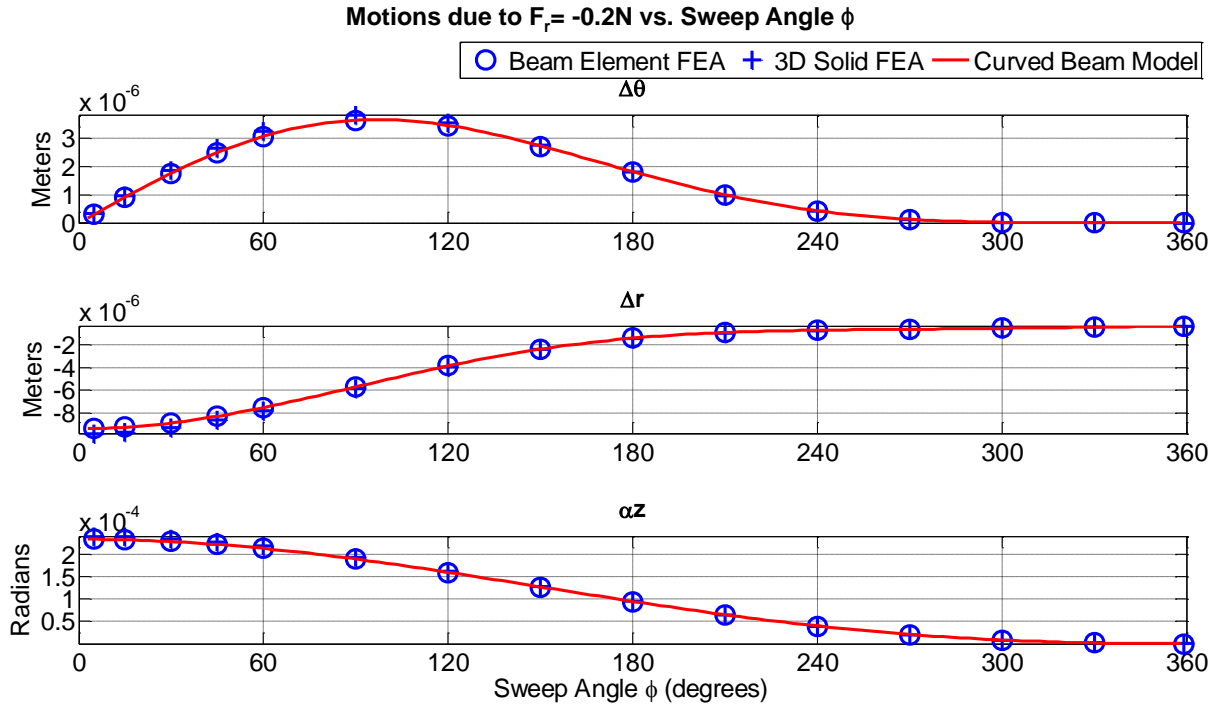


**Figure A.2: FEA corroboration of compliance matrix, predicted displacements under  $-0.2N$   $F_r$  load vs. sweep angle,  $\phi$ . The plot compares the curved beam model to an FEA Beam Element model and an FEA 3D solid model. ( $L=60\text{mm}$ ,  $t_r=6.35\text{mm}$ ,  $t_z=1\text{mm}$ , 7075Aluminum).**



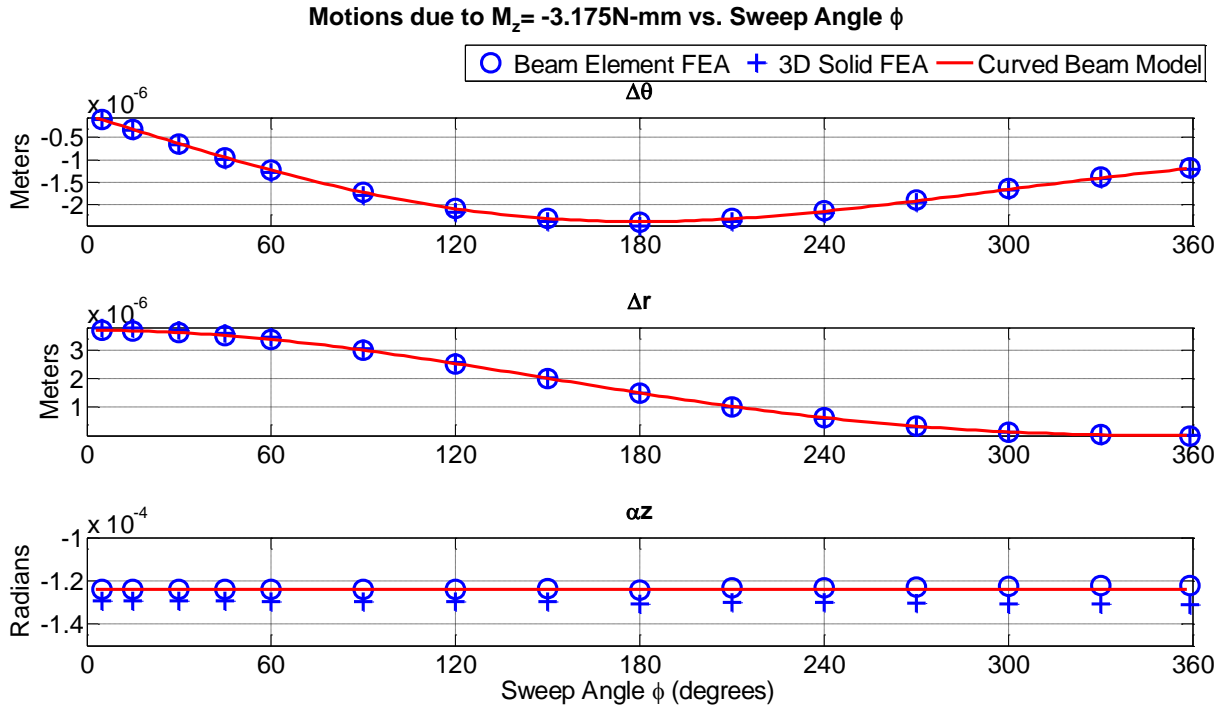


**Figure A.3: FEA corroboration of compliance matrix, predicted displacements under  $-3.175\text{Nmm}$   $M_z$  vs. sweep angle,  $\phi$ . The plot compares the curved beam model to an FEA Beam Element model and an FEA 3D solid model. ( $L=60\text{mm}$ ,  $t_r=6.35\text{mm}$ ,  $t_z=1\text{mm}$ , 7075Aluminum).**

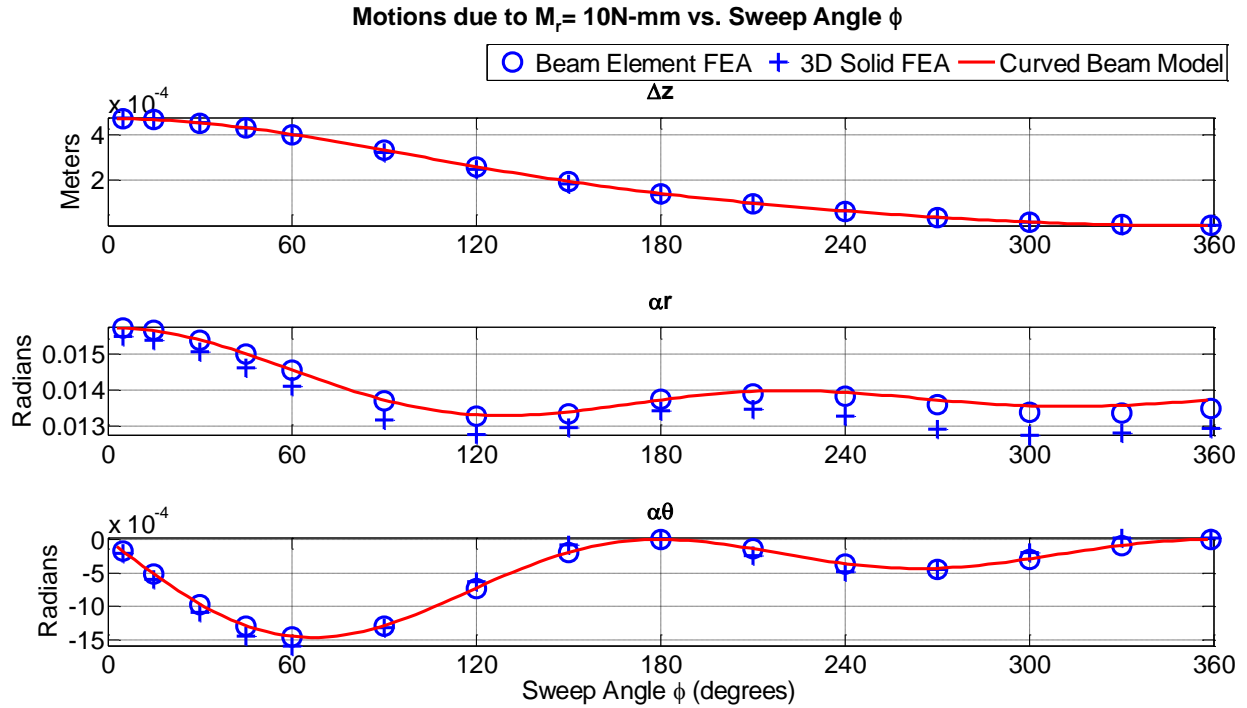


**Figure A.4: FEA corroboration of compliance matrix, predicted displacements under 10Nmm  $M_r$  vs. sweep angle,  $\phi$ . The plot compares the curved beam model to an FEA Beam Element model and an FEA 3D solid model. ( $L=60\text{mm}$ ,  $t_r=6.35\text{mm}$ ,  $t_z=1\text{mm}$ , 7075Aluminum).**

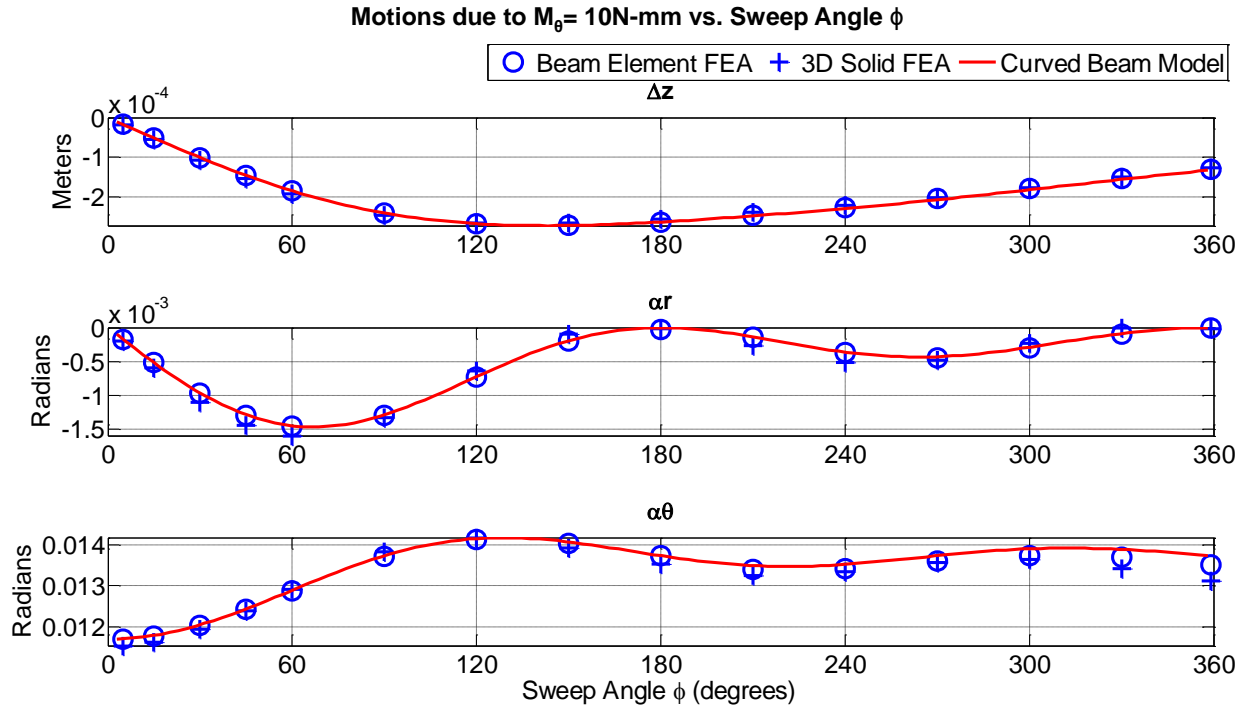


**Figure A.5: FEA corroboration of compliance matrix, predicted displacements under 10Nmm  $M_\theta$  vs. sweep angle,  $\phi$ . The plot compares the curved beam model to an FEA Beam Element model and an FEA 3D solid model. ( $L=60\text{mm}$ ,  $t_r=6.35\text{mm}$ ,  $t_z=1\text{mm}$ , 7075Aluminum).**



## B

# TORSIONAL STIFFNESS CONSTANT FOR AN *r*-COMPLIANCE ELEMENT

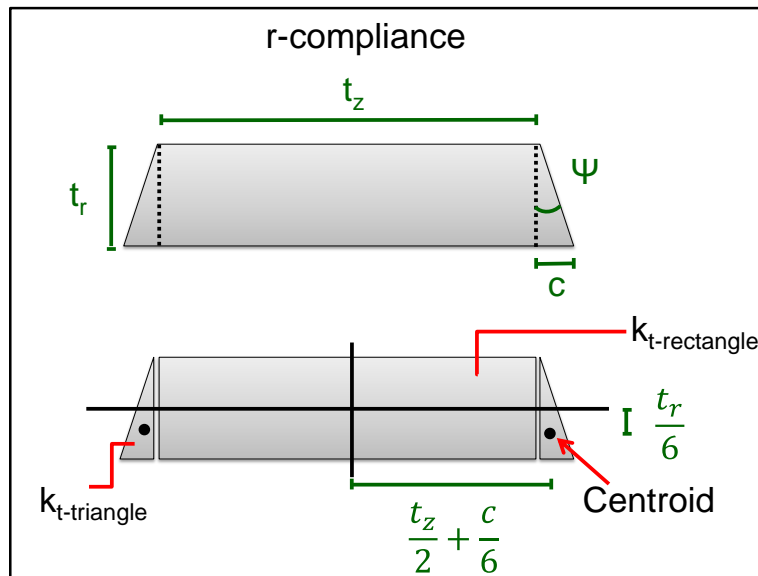


Figure B.1: *r*-compliance element cross-section parameter definitions. The taper angle is given by  $\Psi$ .

$$k_{t-rcomp} = k_{t-rectangle} + 2k_{t-triangle} + 2 \left\{ A_{triangle} \cdot \left[ \left( \frac{t_z}{2} + \frac{c}{3} \right)^2 + \left( \frac{t_r}{6} \right)^2 \right] \right\} \quad (B.1)$$

$$c = t_r \sin \Psi \quad (B.2)$$

$$k_{t-rectangle} = t_z t_r^3 \left[ \frac{1}{3} - .21 \frac{t_r}{t_z} \left( 1 - \frac{t_r^4}{12 t_z^4} \right) \right] \quad (B.3)$$

$$k_{t-triangle} = 0.0261 t_r^4 \quad (B.4)$$

Equations (B.3) and (B.4) are given in Roark [27]. Equation (B.4) is valid for right triangles.



## C

## ELEMENT COMPLIANCE MATRICES FOR DIFFERENT BOUNDARY CONDITIONS

---

The matrices below correspond to the compliance matrices for a curved beam element under different boundary conditions.  $C_{ij}$  corresponds to the  $i^{\text{th}}$  row and  $j^{\text{th}}$  column of the fixed-free 6-DOF compliance matrix  $[C]$ . The constrained matrices are calculated using Gauss elimination.

1) Constrained  $\alpha_z$

$$[A]= \begin{vmatrix} C_{11} - C_{61} \frac{C_{16}}{C_{66}} & C_{12} - C_{62} \frac{C_{16}}{C_{66}} & 0 & 0 & 0 \\ C_{21} - C_{61} \frac{C_{26}}{C_{66}} & C_{22} - C_{62} \frac{C_{26}}{C_{66}} & 0 & 0 & 0 \\ 0 & 0 & C_{33} & C_{34} & C_{35} \\ 0 & 0 & C_{43} & C_{44} & C_{45} \\ 0 & 0 & C_{53} & C_{54} & C_{55} \end{vmatrix}$$

2) Constrained  $\alpha_\theta$

$$[B]= \begin{vmatrix} C_{11} & C_{12} & 0 & 0 & C_{16} \\ C_{21} & C_{22} & 0 & 0 & C_{26} \\ 0 & 0 & C_{33} - C_{43} \frac{C_{34}}{C_{44}} & C_{35} - C_{45} \frac{C_{34}}{C_{44}} & 0 \\ 0 & 0 & C_{53} - C_{43} \frac{C_{54}}{C_{44}} & C_{55} - C_{45} \frac{C_{54}}{C_{44}} & 0 \\ C_{61} & C_{62} & 0 & 0 & C_{66} \end{vmatrix}$$

3) Constrained  $\alpha_r$

$$[D]= \begin{vmatrix} C_{11} & C_{12} & 0 & 0 & C_{16} \\ C_{21} & C_{22} & 0 & 0 & C_{26} \\ 0 & 0 & C_{33} - C_{53} \frac{C_{35}}{C_{55}} & C_{34} - C_{54} \frac{C_{35}}{C_{55}} & 0 \\ 0 & 0 & C_{43} - C_{53} \frac{C_{45}}{C_{55}} & C_{44} - C_{54} \frac{C_{45}}{C_{55}} & 0 \\ C_{61} & C_{62} & 0 & 0 & C_{66} \end{vmatrix}$$

4) Constrained  $\alpha_r$  and  $\alpha_\theta$

$$[E]= \begin{vmatrix} C_{11} & C_{12} & 0 & C_{16} \\ C_{21} & C_{22} & 0 & C_{26} \\ 0 & 0 & D_{33} - D_{43} \frac{D_{34}}{D_{44}} & 0 \\ C_{61} & C_{62} & 0 & C_{66} \end{vmatrix}$$

5) All  $\alpha$  constrained ( $\alpha_z = \alpha_r = \alpha_\theta = 0$ )

$$[F]= \begin{vmatrix} C_{11} - C_{61} \frac{C_{16}}{C_{66}} & C_{12} - C_{62} \frac{C_{16}}{C_{66}} & 0 \\ C_{21} - C_{61} \frac{C_{26}}{C_{66}} & C_{22} - C_{62} \frac{C_{26}}{C_{66}} & 0 \\ 0 & 0 & D_{33} - D_{43} \frac{D_{34}}{D_{44}} \end{vmatrix}$$



# D

## CF FOUR-BAR COMPLIANCE MATRIX

The stage of the CF four-bar constrains the  $\alpha_r$  and  $\alpha_\theta$  rotations of the flexural elements. As a result, the compliance matrix of the four-bar,  $[C_{four-bar}]$ , is dictated by the  $\alpha_r$ - $\alpha_\theta$ -constrained element matrix  $[E]$ .  $[C_{four-bar}]$  calculates the resulting displacements and rotations of the stage due to the forces and moments on the four-bar. The matrix is valid for small rotations when  $\sin(\alpha_r) \approx \alpha_r$ .

$$[C_{four-bar}] = \begin{vmatrix} \frac{E_{11}}{2} & \frac{E_{12}}{2} & 0 & 0 & 0 & \frac{E_{16}}{2} \\ \frac{E_{21}}{2} & \frac{E_{22}}{2} & 0 & 0 & 0 & \frac{E_{26}}{2} \\ 0 & 0 & \frac{E_{33}}{2} & 0 & 0 & 0 \\ 0 & 0 & C_{fb,43} & \frac{E_{22}}{0.5b^2} & \frac{E_{21}}{0.5b^2} & 0 \\ 0 & 0 & C_{fb,53} & \frac{E_{12}}{0.5b^2} & \frac{E_{11}}{0.5b^2} & 0 \\ \frac{E_{61}}{2} & \frac{E_{62}}{2} & 0 & 0 & 0 & \frac{E_{66}}{2} \end{vmatrix}$$

$$C_{fb,43} = C_{22} \frac{(M_{\theta-stage} - M_{r-stage} \sin \omega)}{0.5b^2 F_z}$$

$$C_{fb,53} = C_{11} \frac{(M_{r-stage} \cos \omega)}{0.5b^2 F_z}$$

$$M_{\theta, \alpha_r = \alpha_\theta = 0} = \left( C_{35} - C_{34} C_{55} / C_{45} \right) \cdot \left( \frac{F_z}{-C_{45} + C_{55} C_{44} / C_{45}} \right)$$

$$M_{r, \alpha_r = \alpha_\theta = 0} = \left( \frac{-C_{34}}{C_{45}} F_z \right) \cdot \left( \frac{C_{44}}{C_{45}} M_{\theta, \alpha_r = \alpha_\theta = 0} \right)$$

